Universality in the Evolution of Molecular Phenotypes

Inaugural-Dissertation

zur

Erlangung des Doktorgrades

der Mathematisch-Naturwissenschaftlichen Fakultät

der Universität zu Köln

vorgelegt von

Torsten Held

aus Münster

Köln, 2018

Berichterstatter: Prof. Dr. Michael Lässig

Prof. Dr. Johannes Berg

Prof. Dr. Erwin Frey

Tag der mündlichen Prüfung: 19.07.2018

Abstract

With massive growth of biological sequence data and evolutionary experiments the quantitative modeling of evolutionary processes is made possible. These models aim to quantify the degree of conservation and the speed of adaptation in the evolution of biological systems. Evolutionary processes are driven by mutations, selection, and genetic drift. Mutations generate new variants, natural selection favors some of these, and genetic drift is the randomness in their reproduction success. In the early days of population genetics, it was identified that these processes can be described by employing mathematical models from statistical mechanics such as diffusion equations. Recent theoretical studies modeled and solved the dynamics for complex, interacting systems. The complexity arises through evolutionary interaction. On the one hand, mutations interact in their effect on selection. On the other hand, there is competing co-evolution of variants, if recombination cannot break up genomic links. Both problems arise naturally when considering the evolution of molecular phenotypes such as gene expression levels, protein stabilities, or biophysical binding properties. The inheritable information of these phenotypes is constituted by many sites of the DNA sequence. These sites give a large target to new mutational variants and, hence, a number of competing mutations. Since the sites are often confined to small regions of the DNA, beneficial variants in different individuals cannot be recombined through forms of horizontal gene transfer. Selection is further shaped by generically non-linear fitness landscapes, which is the mapping from the phenotypes to biological growth rates. Recent theoretical breakthroughs allowed for the description of the phenotypic dynamics decoupled from plenty of genomic details. These dynamics were solved in evolutionary equilibrium.

In this thesis, we take up these models to describe various modes of their evolution, which are scenarios of time-dependent selection and in the co-evolution with other genes. We study for the first time the phenotypic evolution in time-dependent fitness landscapes, so called fitness seascapes, with underlying genomic sites that are genetically linked. We find universal properties that break down the relevant parameters to the stabilizing strength and the driving rate of the fitness seascape. These determine the divergence pattern on the phenotypic scale and the fitness flux, which is a measure for deviations from detailed balance and adaptation, on macro-evolutionary timescales. Therefore, we can read off the stabilizing strength and the fitness flux from the time-dependent phenotypic divergence/diversity ratio. Moreover, we study the impact of short-term constraining phenotypic selection on correlations in their constituting sequences. These correlations arise because sites compensate for the destructive effect from adaptation and genetic drift of other sites. We find that phenotypic evolution generates broad epistasis and correlation matrices across all trait sites, which are of low dimension. This kind of universality allows to read off from sequence correlations alone the number of traits under selection,

the genotype–phenotype map, and single site adaptation. The latter can be identified from the asymmetry of time-ordered correlation measures, i.e. deviations from detailed balance. Furthermore, we join the dynamics with recent theories of asexual evolution. These showed universality in the scaling laws of fitness statistics under large mutational influx. With this, we make the step towards systems biology by studying for the first time the asexual co-evolution of biophysical phenotypes on a genome-wide level. We again find universality in the scaling of fitness statistics with the genome size, which decouples from the details of selection. This evolutionary mode induces a so far unknown and dramatic long-term cost of complexity, which can be overcome with small rates of horizontal gene transfer. Comparing this cost to actual biological genome sizes and recombination rates, this offers a new, feasible pathway for the evolution of sex.

In all these modes we find so-far unknown laws of universality. These reduce the complexity of the processes on the higher level, e.g. the phenotypic or the overall fitness level and allow the inference of relevant parameters shaping the dynamics or to quantify scalings. Moreover, universalities are strongly related to the predictability of the evolutionary process.

Kurzzusammenfassung

Die stark wachsende Anzahl biologischer Sequenzdaten und evolutionärer Experimente ermöglicht die quantitative Modellierung evolutionärer Prozesse. Diese Modelle zielen darauf ab, den Grad der Erhaltung und die Geschwindigkeit der Anpassung in der Evolution biologischer Systeme zu bestimmen. Der evolutionäre Prozess wird durch Mutationen, Selektion und genetischen Drift bestimmt. Mutationen erzeugen neue Variationen, natürliche Selektion bevorzugt einige hiervon, und genetischer Drift ist der Zufall im Reproduktionserfolg. Man hat früh erkannt, dass dieser Prozess durch den Einsatz von mathematischen Modellen aus der statistischen Physik, wie etwa Diffusionsgleichungen, beschrieben werden kann. Neuere theoretische Erkenntnisse erlauben die Modellierung der Dynamik komplexer, interagierender Systeme. Die Komplexität entsteht durch evolutionäre Interaktion. Einerseits interagieren Mutationen in ihren Fitnesseffekten. Andererseits existiert eine konkurrierende Koevolution verschiedener Varianten, wenn Rekombination die genomischen Verbindungen nicht aufbrechen kann. Beide Probleme treten auf, wenn man die Entwicklung molekularer Phänotypen wie Genexpressionslevels, Proteinstabilitäten oder biophysikalische Bindungseigenschaften betrachtet. Die vererbbare Information dieser Phänotypen besteht aus vielen Positionen der DNA-Sequenz. Diese geben ein großes Angriffsziel für neue Mutationsvarianten und damit eine Reihe von konkurrierenden Mutationen. Da sie oftmals auf kleine Bereiche der DNA beschränkt sind, können vorteilhafte Varianten bei verschiedenen Individuen nicht durch horizontalen Gentransfer rekombiniert werden. Die Selektion wird weiterhin generisch durch nichtlineare Fitnesslandschaften geprägt. Diese sind die Abbildung von den Phänotypen auf Wachstumsraten. Neuere theoretische Erkenntnisse erlauben es, diese phänotypische Dynamik losgelöst von vielen genomischen Details zu beschreiben.

Hier greifen wir dies auf, um verschiedene Formen phänotypischer Evolution zu betrachten. Wir untersuchen zum ersten Mal die phänotypische Evolution in zeitabhängigen Fitnesslandschaften, so genannten Fitness-'seascapes', mit zugrunde liegenden genomischen Sequenzen, die genetisch zusammenhängend sind. Wir finden universelle Eigenschaften, welche die relevanten Parameter auf die Stärke stabilisierender Selektion und die zeitliche Änderungsrate der Fitness-'seascape' reduzieren. Diese bestimmen das Divergenzverhalten auf der phänotypischen Skala und den generierten Fitness Fluss, welcher die Abweichung vom detaillierten Gleichgewicht und die Stärke der Adaptation misst. Daher können die stabilisierende Selektion und die Adaptation vom zeitlich aufgelösten Divergenz-Diversitätsverhältnis bestimmt werden. Weiterhin untersuchen wir den Einfluss von stabilisierender phänotypischer Selektion auf die Korrelationen in diesen Sequenzen. Diese Korrelationen entstehen durch die Kompensation schadhafter Mutationen anderer DNA Positionen des Phänotypen, welche durch genetischen Drift oder Adaptation auftreten können. Wir lernen, dass phänotypische Evolution Epistasis und Korrelationen

generiert, die all diese Positionen umfassen. Nichtsdestotrotz sind diese von niedriger Dimension. Diese Universalität ermöglicht es von Sequenzkorrelation die Anzahl selektionsrelevanter Phänotypen, ihre Genotyp-Phänotyp-Abbildungen sowie Adaptation bestimmter Positionen zu erlernen. Letztere kann aus der Asymmetrie der zeitabhängigen Korrelationen identifiziert werden, welche Abweichungen des detaillierten Gleichgewichts messen. Schließlich begeben wir uns in die Systembiologie, indem wir erstmals die asexuelle Koevolution biophysikalischer Phänotypen auf genomweiter Ebene untersuchen. Wir finden universelle Skalierungsgesetze für die genomweite Fitnessstatistik, welche von Details der Selektion entkoppeln. Wir zeigen, dass diese zu dramatischen Kosten in der Genomgröße führen. Beim Vergleich unserer Ergebnisse mit realen biologischen Daten identifizieren wir einen neuen, selektiv praktikablen Weg für die Evolution zur Ausbildung der Geschlechter.

In all diesen Modi finden wir Universalitäten. Diese reduzieren die Komplexität der Prozesse auf der höheren Ebene, z. B. der phänotypische Ebene oder der Gesamtfitness. Die Universalitäten erlauben die Inferenz relevanter Parameter, welche die Dynamik von Phänotypen beeinflussen, sowie die Identifizierung von Skalierungsgesetzen. Weiterhin stehen sie im engen Zusammenhang zur Vorhersagbarkeit des evolutionarären Prozesses.

Financial support. My work has been supported by the Deutsche Forschungsgemeinschaft, grant SFB 680, by the Bonn-Cologne Graduate School for Physics and Astronomy, and by the Kavli Institute for Theoretical Physics.

Collaboration. Parts of the work in Chapter 2, i.e. the biophysical modeling, has been work under equal contribution by Daniel Klemmer. The work presented in Chapter 3 has been done in collaboration with Dr. Armita Nourmohammad. Here both, analytical theory and simulations were essentially my work, with valuable ideas and interpretations by Dr. Nourmohammad. Chapter 4 has been done in collaboration with Dr. Simone Pompei. Analytical theory and simulations were essentially my work, with valuable ideas and interpretations by Dr. Pompei. The work in Chapter 5 was under equal contribution from Daniel Klemmer: the theory has been developed together under equal contribution. The presented simulations were performed and data processed by me. The ideas and the interpretations of the simulations were under equal contribution.

Publications & preprints. Parts of the material in Chapters 2 and 3 have been published in [1]. Some conclusions of this Chapter have been discussed in [2]. The method has been applied to the divergence of gene expression levels of *Drosophila*, which is discussed in [3], but not the focus of this thesis and neither under my first-authorship. Parts of Chapters 2 and 5 are available as preprint [4].

Contents

List of Figures

List of Tables

Chapter 1

Introduction

The evolutionary process is driven by the appearance of new mutational variants. These variants often show growth rate difference, called fitness, that allows the spread of the fitter individuals in the population. An effect that is well-known as natural selection. Genetic drift adds stochasticity to this reproduction success. Population genetics aims at describing this evolutionary process and its mechanisms. Early in the field, [5] identified the use of diffusion equations for the stochastic process, if generated by incremental changes on the timescale of a generation. Nowadays, the exponentially growing availability of genomic sequence data and high-throughput evolutionary experiments technology, also in natural environments, permits the testing of these models. Methods from statistical mechanics allow for the quantitative modeling of complex systems and can quantify the degree and speed of adaptation in the evolution of biological systems. Moreover, these models can be supported by extensive numerical simulations.

A quantitative understanding of population genetics will supposedly give diverse and very powerful applications among others for human health. These are for instance the co-evolution of immune systems with pathogens to optimize treatments or vaccines [6–12], from which some already proved powerful [7, 8, 11]. Promising laboratory and theoretical attempts were made to use growth rate trade-offs to control antibiotic resistances [13], and control theory has been suggested to direct the somatic evolution of cancers [14]. Some of these applications depend on the identification and evolution of the underlying molecular and biophysical phenotypes. These are organismic functions, such as outcomes of regulatory pathways, i.e. gene expression levels, protein stabilities, biophysical binding affinities, or allosteric mechanisms. A typical physical example for such a quantitative trait is the binding energy between proteins depending on multiple binding sites such as regulatory binding motifs modeled in [15–17]. The inheritable component of quantitative phenotypes is genetically encoded in multiple positions of the genomic sequence, the DNA sequence also called genotype. Mutations on these sequences compete in a complex way with long-range correlations and interactions through non-linear fitness functions. Moreover, biological processes are out of equilibrium from cellular to evolutionary scales [18–21]. All these make the dynamics appear noisy on the sequence level. However reproducible evolution has widely been observed on a functional level [20, 22, 23] such as the re-occurrence of drug resistance by mutations targeting the same gene [23]. These problems and observations of

predictability on higher-levels are well-known and tackled in statistical mechanics. The evolution and the co-evolution of complex phenotypes and their impact on the sequence evolution in various evolutionary modes can be described with mathematical instruments borrowed from statistical physics [19, 24–29]. The identification of universal properties can improve the predictions of the evolutionary process [7, 10, 11, 30] and hence improve the applications discussed.

The evolutionary fate of independent mutations is well described by classical population genetics [31–34]. Available theory still lacks sophisticated description of evolving complex phenotypes. On the one hand, phenotypes evolve in non-linear fitness landscapes, which is the map from the trait value to the fitness. They lead to fitness interactions between mutations, so called fitness epistasis. On the other hand, the large genomic basis of quantitative traits, the so called quantitative trait loci (QTL), depends on tens to hundreds of sites. They offer a large target for mutations altering the sequence and producing new trait variants. Therefore, various beneficial mutations evolve, competing for a fixation in the population if they are in distinct individuals, or they trail deleterious mutations on their way to fixation. This effect is called clonal interference and has been widely observed in experiments [20, 21, 35–42]. Horizontal gene transfer can recombine beneficial parts of two genome and break up these links. Classical theoretical work by [31, 43–51] used the assumption of linkage equilibrium, which is a misleading term for omitting interference correlations with the argument of high recombination rates, or assumed a low mutation rate to ignore interference. However, QTL are located in a confined genomic region with at least partial genetic linkage even under sexual evolution [52]. Recent theoretical breakthroughs by [53] and the generalization to a phenotype under external interference [54] could bring the dynamics of non-recombining sequences to the phenotypic level. Fokker-Planck equations, which are well-known in statistical mechanics, describe the evolution of the mean and the variance of the trait distribution in a population. The authors also solved the trait statistics in evolutionary equilibrium of the trait dynamics and discussed stabilizing selection by a quadratic fitness landscapes penalizing deviations from the trait optimum.

However, a difficulty arises because of the ubiquitous non-equilibrium of biological processes. These arise on short, cell cycle timescales [18] due to changing demand of protein functions and the regulation of genes. Biophysical ideas are based so far on the assumption of thermodynamic equilibrium [55,56] and have hence similarly been used to build fitness landscapes [57,58]. However, the function of a biophysical traits does not only depend on its equilibrium thermodynamics, but non-equilibrium processes need to be considered carefully. These shape the fitness landscapes, which serves as input to the evolutionary trait dynamics. On long, evolutionary timescales the ecological environment as well as epistatic interaction with other genes change fitness landscapes. So called fitness seascapes trigger adaptation through time-dependent selection [59]. Strong adaptation can generate a very substantial non-equilibrium processes as biological data show [19–21]. This is especially the case for quickly evolving viruses, which adapt to change the recognition by the host's immune system. A model for the evolution of Mendelian traits in fitness seascapes has been introduced in [19]. For phenotypic fitness seascapes, the dynamics of [53] are usable, but have not yet been solved. As a measure for adaptation, the fitness flux got introduced by [60]. It measures the average adaptive steps that the population

dynamics make uphill in a fitness land- or seascape. In a stationary non-equilibrium state, it measures hence the compensation for the environmental changes of the fitness seascape. The fitness flux has its physical equivalent in the heat of non-equilibrium systems. Therefore, it is a measure for the deviations from detailed balance defining equilibrium.

Another difficulty prevails because clonal interference also arises on the systems biology scale under asexual evolution, which does not allow the assumption of linkage equilibrium. For Mendelian traits, the destructive effect of asexual evolution on long genome sizes has been described with Eigen's quasi-species model or the dynamics of Muller's ratchet [61–64]. Recent publications described the fitness statistics of competing mutations [64–71] and quantified the adaptation in these. A model from statistical physics, namely universality in the front propagation of a wave of hopping particles [72], was used to derive a traveling wave theory for the adaptation in asexual evolution [64, 66, 67, 69–71, 73]. They show arising universality in the fitness statistics in a population, if the effect of a mutation is small and the rate of new mutations is high. Particularly, the variance of fitness is determined by the rate and the average fitness effect of mutations, but not by the particular distribution of the fitness effects. However, these models ignore the genomic details for the mutational input that generates the mutation rate and and the mean fitness effect inhered in the system. Without fitness epistasis, i.e. for Mendelian traits, the genomic relation to mutation rates has destructive consequences to the genome in a stationary fitness wave, which we discuss in another paper [74]. However, the question how the non-linear selection of quantitative traits changes the mean selective effect of a mutation and hence the scaling laws of the fitness statistics has not yet been addressed. The findings by [54] allow this by describing the impact of interference selection on the dynamics of quantitative traits.

For some molecular traits, data sequencing and high-throughput trait measurements allowed establishing a variety of genotype–phenotype maps, which associate a phenotype to the underlying DNA sequences. However, for the vast majority of complex traits, these are out of reach. Often, neither the number nor the position of trait loci is known. Therefore, the effect of mutations on trait values is rarely known. However, as mentioned above, the evolution of functions turned out to be repeatable in experiments, whereas sequence evolution diverged [20,22,23]: the many degrees of freedom on the microscopic level allow us to adapt on various pathways on the functional level. Hence, there is, as statistical mechanics taught us, hope for universal pattern on mesoscopic trait or macroscopic systems-biology levels. The tenet behind universalities is the very stochastic fate of the microscopic items [75], but their integral effect is shaped by selection on different scales and follows more predictable rules. As the recent theoretical work by [53] identified, these plenty degrees of freedom indeed generate universality on the mesoscopic, the trait level. They identify that the trait divergence, the variance between populations divided by the diversity only depends on the mutation rate and the effective stabilizing strength. It is decoupled from plenty genomic details such as the number of QTL, details of the genotype–phenotype map or recombination. This allows us to determine the strength of constraining selection from phenotypic measurements. However, this method is not yet extended to the analysis of adaptive pressures.

On the sequence level, recent studies, so called direct coupling analyses [29, 76–79], showed that the detection of biophysical conservation is possible from the evolutionary process. These use sophisticated models for pair-wise interactions, which are localized in the correlations of a few positions. However, broad correlations have been observed and suggested to be related to conserved functions such as protein stability, catalytic power or allosteric mechanisms, which are associated with the broad genomic basis of a conserved trait [80–82]. Furthermore, models and measures of sequence correlation used equilibrium assumptions of the evolutionary processes. This generates biases [29] if applied to strongly adaptive systems like viruses as it has been done by [6, 83]. Accurate models of broad correlations as well as correlations under strong adaptive pressures through time dependent-selection are still missing.

To bring the points together, the description of the evolution of molecular phenotypes lacks the knowledge of the genomic basis. The dynamics is highly correlated due to clonal interference and complex fitness interactions. Recent theoretical findings brought the evolutionary dynamics to the phenotypic level decoupled from many microscopic degrees of freedom. However, they have not addressed the evolution in fitness seascapes or the impact of phenotypic selection on sequence correlations. Neither, the co-evolution of quantitative traits in asexual populations has yet been described.

The aim of this thesis is to build minimal fitness models for studying the evolution of quantitative traits. We want to study their evolution and the co-evolution under adaptive pressures and ask

1. Can we reveal universal properties of these processes that allow to describe the evolution by a reduced number of key parameters?

2. How can we determine these parameters from evolutionary data, can we detect the evolutionary conservation and adaptation?

3. What implications are there for the predictability of the evolutionary process?

4. How does the evolution of a quantitative trait shape its underlying QTL, can we identify the effectively lower dimensionality of trait evolution? When do mutations compensate fluctuations of others, does the response pattern show the signatures of adaptation?

5. What are the consequences of phenotypic interference, i.e. the co-evolution of a large set of traits in asexual evolution? What do the scalings tell us about possible system sizes?

We use methods and results from statistical physics such as the Fokker-Planck equations for the trait dynamics, non-equilibrium measures, or scaling laws derived for the complex systems. We support our results by numerical simulations of the evolutionary process, which we describe in Appendix A.

Thesis organisation

In Chapter 2, we recapitulate the phenotypic diffusion equations for the dynamics with linked QTL. We identify statistics for selection that do not depend on details of the fitness landscape, given a certain local smoothness of the landscape. We study various types of fitness landscapes to model evolution and learn qualitatively, how thermodynamic non-equilibrium on the cellular level shapes the landscape for protein evolution to stabilize the evolution of proteins.

In Chapter 3, we study for the first time the asexual evolution of molecular phenotypes in adaptive fitness seascapes on the phenotypic level. We build a minimal model for fitness seascape with a randomly moving fitness peak. Answering question 1, we identify universality in the time-dependent divergence/diversity ratio that decouples from many genomic details and the mode of driving. We develop a new method that allows to distinguish the constraining from the directional selection by phenotypic measurements alone. Classical tests neither used time-resolved measurement nor had a neutral gauge to infer adaptation on phenotypic levels alone. Our methods directly measures the macro-evolutionary fitness flux (question 2) decoupled from micro-evolutionary driving, e.g. imposed by seasonal changes. Furthermore, we see that predictability of the evolutionary process can be conserved on phenotypic level over macro-evolutionary timescales (question 3). In a follow-up publication, we applied the derived method to the divergence of gene expression levels across the *Drosophila* genus. This allowed for the first time to detect system-wide adaptation from the phenotypic measurements. Wide adaptation was observed in sequence data of *Drosophila*, but could not yet been related to phenotypic adaptation.

Having seen the short-term constraints in the divergence pattern, we study in Chapter 4 their impact on the trait's constituting sequence. We add a minimal model of external driving of some of their sites. Adaptation or genetic drift of a site generates fluctuations of the trait value, which other QTL compensate. This generates a simple, but broad correlation pattern. Each trait confers a single rank to the correlation matrix, such that the correlations of a site with all other sites are just determined by the product of the pairwise trait effects, their driving rate, and the curvature of the fitness landscape. It is decoupled from their overall evolutionary rates and the details of the dynamics of all other sites (again question 1). From sequence data alone, we can hence read off the number of co-evolving traits and the genotype–phenotype map (questions 4). The asymmetry of the response matrix identifies sites under adaptation (question 2). To address question 3 again, short-term predictability of the process arises not in the response of an individual site but in their collective compensatory response, which is in fact the short-term phenotypic level of Chapter 3. The method derived in this section has a broad applications for biological systems. The large amount of available sequence data allows to reconstruct phylogenies and hence to measure the time-resolved correlations. It can be obtained on various evolutionary modes, as we show in two follow-up papers applying it to PDZ binding domains and to a antigenicity-stability model for hemagglutinin of the human influenza virus.

In Chapter 5, we discuss for the first time the asexual evolution of biophysical phenotypes on the genomic scale, where mutational variants of all traits compete under clonal interference. Here, we combine the diffusion equation for the traits of each gene with the traveling fitness

wave theory for the genomic scale. Each gene has traits evolving in a non-linear biophysical fitness landscape, which we discuss in Chapter 2. We build a minimalistic model of housekeeping evolution to quantify the cost of complexity. In this evolutionary mode, frequent trait mutations of weak selective effect generate a stationary fitness distribution, a fitness wave showing a universal fitness variance (question 1). This fitness wave of the integral effect of all genes is stable in time and hence fitness statistics are constant on the genomic scale (question 3), whereas on the phenotypic level noise generates strong fluctuations in each gene. The non-linear phenotypic selection entails a dramatic feedback on the mutational influx to the fitness wave. Therefore, phenotypic interference generates a dramatic and so far unknown super-linear genetic cost of the system size (question 5). We find that recombination resolves this burden even with low rates through a first order phase transition. It hence offers a new and feasible pathway for the evolution of sex. We compare the recombination rates of various species with the critical recombination rate. All considered species show recombination rates slightly above this critical threshold.

Chapter 2

Evolutionary dynamics and equilibrium of quantitative traits

In this chapter, we first review the diffusion dynamics for the population mean and diversity of a quantitative trait under genetic drift and mutations in a given fitness landscape. We then derive the impact of trait selection onto genomic selection and recall the fixation probabilities of mutations. Finally, we identify appropriate fitness landscapes to model the evolution of biophysical phenotypes, which underly non-equilibrium cellular thermodynamics. In all parts we discuss consequences of the trait equilibrium, which include typical selection coefficients or the trait fitness variance in a population.

2.1 Diffusion equations for trait mean and diversity

In this section, we build our model for phenotypic evolution. We then retrieve the dynamics of the trait mean and diversity on the phenotypic level under mutations, selection and genetic drift or genetic draft with the rest of the genome. We discuss implications of the evolutionary equilibrium in these landscapes.

Our model for quantitative traits, Figure 2.1A, is based on a simple additive map from genotypes to phenotypes. The trait value E of an individual depends on its genotype, the sequence of alleles $(a_1, \ldots, a_\ell)$ at ℓ constitutive genomic sites. We study a linear mapping from genotype to phenotype,

$$E(a_1, \ldots, a_\ell) = E_{\min} + \sum_{i=1}^{\ell} E_i \sigma_i, \qquad \text{with } \sigma_i = \begin{cases} 1, & \text{if } a_i = a_i^*, \\ 0, & \text{otherwise.} \end{cases} \tag{2.1}$$

Here, the trait has a minimum value $E_{\min}$ and $E_i > 0$ is the contribution of a given site i to the trait value, i.e. its mutational effect. We assume a two-allele genomic alphabet and a_i^* denotes the allele conferring the larger phenotype at site i. The extension to a four-allele alphabet is straightforward. The genotype-phenotype map (2.1) defines the allelic trait average Γ_0 and the

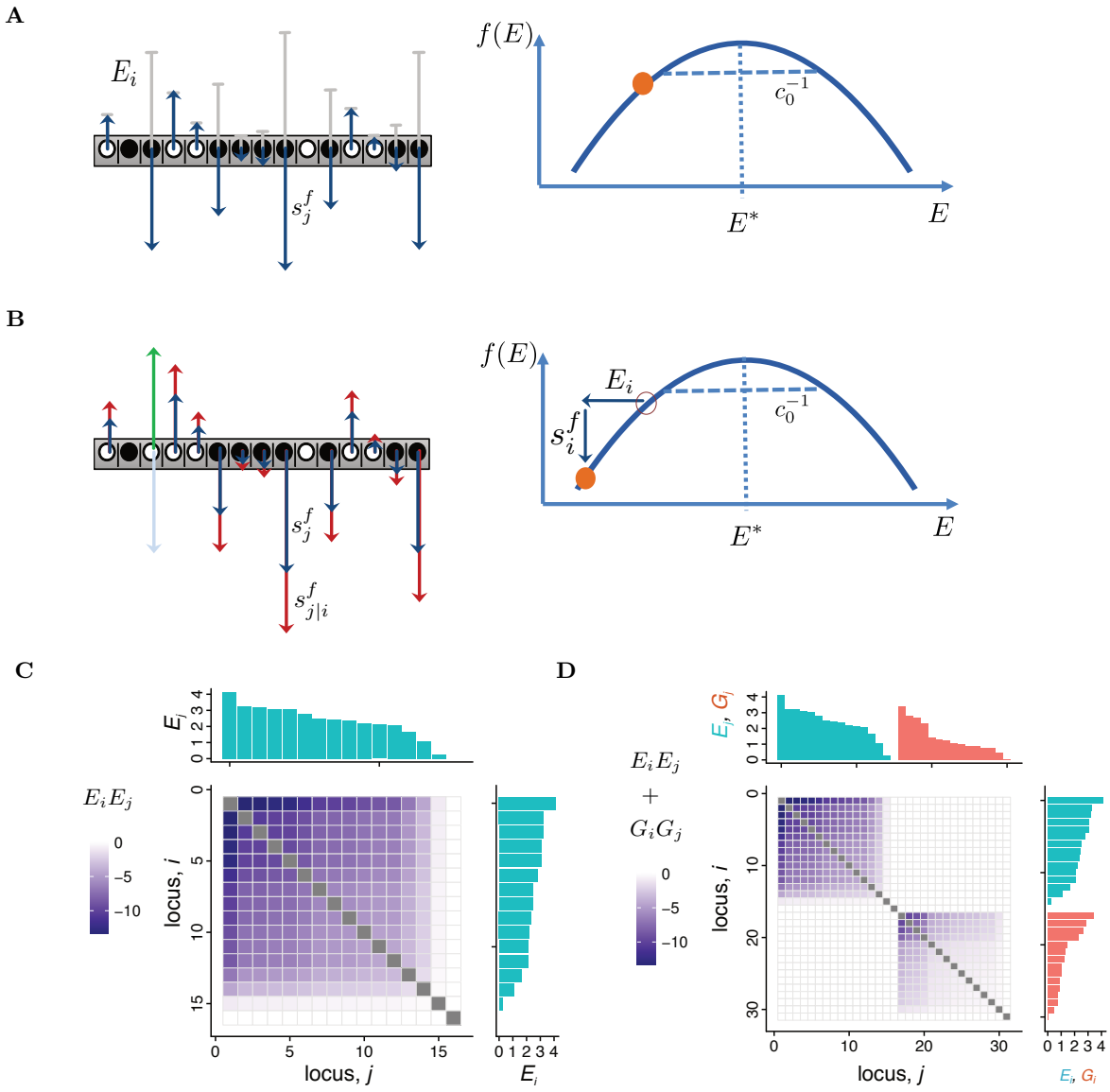

Figure 2.1. Molecular model and epistatic pattern of quantitative traits. **A** Linear model of the QTL–phenotype mapping: Each site $i \in \ell$ confers two alleles $a_i = 0, 1$ ($\circ$ or $\bullet$) with trait effect E_i (grey bars) to the linear quantitative trait $E = E_{\min} + \sum_{i=1}^{\ell} a_i E_i$. The trait fitness $f(E)$ is non-linear in the trait value E and hence determines the trait selection on loci, $s_j^f \approx E_j f'(E)$ (blue arrows) dependent on the genetic background, particularly the position E (orange dot) on the fitness landscape. **B** Phenotypic selection entails broad epistasis between sites: A primary, here for the trait deleterious mutation at a site i (green arrow) changes the trait value $E \to E - E_i$ shifting to steeper part of the fitness landscape (orange dot). This triggers compensatory mutations by fortifying the selection on all trait sites by $s_{j|i}^f$ (red arrows). **C** The epistasis score between two particular sites is determined by the matrix $\omega_{ij} = 2Nc_0E_iE_j$ (color code). It is approximately proportional to the trait effect of the primary mutation E_i (blue bars in rows & columns), to the compensatory trait effect E_j (blue bars in columns), and to the (local) curvature of the fitness landscape $c_0 = -f''(E)$. Hence, it has a simple rank 1 form generated by $\ell + 1$ parameters instead of ℓ^2 in direct-coupling models. **D** Another quantitative trait (red bars) generates an additive epistatic effect conferring another rank to the matrix; here without epistatic overlap.

trait span E_0^2,

$$\Gamma_0 = E_{\min} + \frac{1}{2}\sum_{i=1}^{\ell} E_i, \qquad E_0^2 = \frac{1}{4}\sum_{i=1}^{\ell} E_i^2, \tag{2.2}$$

which are the mean and the variance of the trait for random sequences. The linear genotype-phenotype map (2.1) has been chosen here for concreteness. Such linear maps are approximately realized for some molecular traits, such as transcription factor binding energies [84]. However, many other systems have nonlinearities, which are commonly referred to as *trait epistasis*. It can be argued that simple forms of trait epistasis will leave many of our results intact, which is indicated at few places, but a systematic inclusion of trait epistasis is beyond the scope of this thesis. At the same time, the fitness land- and seascapes introduced below depend on the trait in a nonlinear way; hence, they always contain *fitness epistasis.*

Quantitative traits have a sufficient number of constitutive loci to be generically polymorphic in a population, although most individual genomic sites are monomorphic. The distribution $\mathcal{W}(E)$ of trait values in a given population is often approximately Gaussian [45, 53, 85]. Hence, it is well characterized by its mean and variance,

$$\begin{aligned} \Gamma \equiv \overline{E} &= \int \mathrm{d}E\, E\, \mathcal{W}(E), \\ \Delta \equiv \overline{(E-\Gamma)^2} &= \int \mathrm{d}E\, (E-\Gamma)^2\, \mathcal{W}(E), \end{aligned} \tag{2.3}$$

where overbars denote averages over the trait distribution $\mathcal{W}(E)$ within a population. The variance Δ is called the trait diversity; in the language of quantitative genetics, this quantity equals the total heritable variance including epistatic effects.

We consider the evolution of the trait E under genetic drift or genetic draft, genomic mutations, and natural selection, which is given by a trait-dependent fitness landscape $f(E)$ or fitness seascape $f(E,t)$. Variants of these functions are in detail discussed in Section 2.3. At a given evolutionary time, the trait distribution in a population has mean $\Gamma(t)$ and diversity $\Delta(t)$. As shown previously[1] [53], the evolutionary dynamics of a quantitative trait in a fitness seascape can be described in good approximation by diffusion equations for the distributions $Q(\Gamma, t \,|\, F_1)$ and $Q(\Delta, t \,|\, F_2)$ of its mean and its diversity,

$$\frac{\partial}{\partial t} Q(\Gamma, t \,|\, F_1) = \left[\frac{g^{\Gamma\Gamma}}{2N} \frac{\partial^2}{\partial \Gamma^2} - \frac{\partial}{\partial \Gamma} \left(m^{\Gamma} + g^{\Gamma\Gamma} \frac{\partial F_1(\Gamma, t)}{\partial \Gamma} \right) \right] Q(\Gamma, t \,|\, F_1), \tag{2.4}$$

$$\frac{\partial}{\partial t} Q(\Delta, t \,|\, F_2) = \left[\frac{g^{\Delta\Delta}}{2N} \frac{\partial^2}{\partial \Delta^2} - \frac{\partial}{\partial \Delta} \left(m^{\Delta} + g^{\Delta\Delta} \frac{\partial F_2(\Delta, t)}{\partial \Delta} \right) \right] Q(\Delta, t \,|\, F_2), \tag{2.5}$$

with evolutionary forces discussed in detail in the following. These equations are projections of the Kimura diffusion equation [5,86] from the genotypes on the phenotype space. In Appendix B we show how this dynamics can easily be extended to multiple traits without further difficult notions if the mutational effects between traits are not strongly correlated.

[1] The citation also refers to the next paragraph.

The distributions $Q(\Gamma, t \,|\, F_1)$ and $Q(\Delta, t \,|\, F_2)$ are time-dependent probability densities of the trait mean and the variance, which describe an ensemble of populations evolving in the same fitness seascape $f(E,t)$. These dynamics involve selection forces from fitness seascape components

$$F_1(\Gamma, t) = f(\Gamma, t) + f''(\Gamma, t) \times \int \mathrm{d}\Delta \, \Delta \, Q(\Delta, t \,|\, F_2), \tag{2.6}$$

$$F_2(\Delta, t) = \Delta \times \int \mathrm{d}\Gamma \, f''(\Gamma, t) \, Q(\Gamma, t \,|\, F_1), \tag{2.7}$$

which are projections of the mean population fitness

$$\overline{f}(t) \equiv \int \mathrm{d}E \, f(E,t) \, \mathcal{W}(E,t) = f(\Gamma, t) + \frac{1}{2} \Delta f''(\Gamma, t) + \ldots \tag{2.8}$$

onto the marginal variables Γ and Δ. Derivatives $f'(.)$ are supposed to act on the first function argument. Selection drives the mean trait uphill a fitness landscape and constraints the trait diversity under stabilizing selection $f''(\Gamma, t) < 0$. Stochasticity by genetic drift enters through the diffusion coefficients

$$g^{\Gamma\Gamma} = \langle \Delta \rangle \equiv \int \mathrm{d}\Delta \, \Delta \, Q(\Delta, t \,|\, F_2), \qquad g^{\Delta\Delta} = 2\Delta^2. \tag{2.9}$$

The population size N acts as 'inverse temperature'. If a population is larger, its evolution is more deterministic because the effect of randomness in the reproduction is comparatively smaller. Mutation coefficients

$$m^{\Gamma} = -2\mu(\Gamma - \Gamma_0), \qquad m^{\Delta} = 4\mu(E_0^2 - \Delta) - \Delta/N \tag{2.10}$$

drive the trait mean towards a randomized sequence and generate trait diversity. These coefficients depend on the effective population size N and the point mutation rate μ. Under strong interference with the rest of the genome, N has been identified as being still determined by the coalescence rate. We just need to replace it by the (externally given) coalescence time $2N \to \tilde{\sigma}^{-1}$ in the trait dynamics [54]. It is the same variable that has been identified to determine the threshold of neutrality $\tilde{\sigma}$ for the selection of arising mutations [68] and will be the relevant parameter when studying the phenotypic interference in Chapter 5. Interference within the trait is captured by the trait dynamics (2.4) and (2.5).

The diffusion equations (2.4) and (2.5) are coupled through the fitness components (2.6) and (2.7) and through the diffusion coefficient $g^{\Gamma\Gamma}$. If we neglect direct selection on the trait mean by setting $F_1(\Gamma, t) = 0$, Equation (2.4) describes a *quasi-neutral* diffusion of the trait mean, which depends the full drift term $g^{\Gamma\Gamma} = \langle \Delta \rangle$ under selection (see Section 3.3). The quasi-neutral dynamics defines a characteristic timescale

$$\tilde{\tau} \equiv \frac{2NE_0^2}{\langle \Delta \rangle}. \tag{2.11}$$

In the special case of a time-independent fitness landscape $f(E)$, the diffusive dynamics of the trait mean and the diversity leads to evolutionary equilibria of a Boltzmann form [53],

$$Q_{\rm eq}(\Gamma \,|\, F_1) = \frac{1}{Z_\Gamma}\, \tilde{Q}_0(\Gamma)\, \exp[2NF_1(\Gamma)], \tag{2.12}$$

$$Q_{\rm eq}(\Delta \,|\, F_2) = \frac{1}{Z_\Delta}\, Q_0(\Delta)\, \exp[2NF_2(\Delta)], \tag{2.13}$$

where Z_Γ and Z_Δ are normalization constants. The equilibrium distributions under selection build on the quasi-neutral distribution $\tilde{Q}_0(\Gamma) \sim \exp[-2\mu N(\Gamma - \Gamma_0)^2/\langle\Delta\rangle]$ of the trait mean, where selection may shapes $\langle\Delta\rangle$, and on the neutral diversity distribution $Q_0(\Delta)$. We note that the evolutionary equilibrium in a static fitness landscape is limited to the marginal distributions $Q_{\rm eq}(\Gamma \,|\, F_1)$ and $Q_{\rm eq}(\Delta \,|\, F_2)$, while the joint distribution $Q(\Gamma, \Delta|f)$ reaches a non-equilibrium stationary state [53]. In the limit of low mutation rates, the Boltzmann distribution (2.12) describes an asymptotic selection-drift equilibrium $Q_{\rm eq}(E|F_1) \sim Q_0(E)\exp[2Nf(E)]$; the trait values E are predominantly monomorphic in a population and they change by substitutions at individual trait loci [16, 53, 87].

Some relations of a trait equilibrium obtained from (2.4), which needs to be integrated over Γ, and (2.5) will provide useful when considering typical selection coefficients and the fitness diversity,

$$\langle f'(\Gamma)\rangle = -\frac{\langle m^\Gamma\rangle}{g^{\Gamma\Gamma}} = \frac{1}{2N}\frac{\langle\Gamma\rangle - \Gamma_0}{E_0^2}[1 + \mathcal{O}(\mu N c)], \tag{2.14}$$

$$\langle f'(\Gamma)^2\rangle = \frac{\langle m^{\Gamma^2}\rangle}{g^{\Gamma\Gamma^2}} + \frac{\mu}{Ng^{\Gamma\Gamma}} - \frac{\langle f''(\Gamma)\rangle}{2N} = \langle f'(\Gamma)\rangle^2 - \frac{\langle f''(\Gamma)\rangle}{2N}\left[1 + \mathcal{O}(c^{-1}, \mu N)\right], \tag{2.15}$$

where we used the approximations of a mutation–drift balance of the trait diversity for $g^{\Gamma\Gamma} = \langle\Delta\rangle = 4\mu N E_0^2[1 - \mathcal{O}(\mu N c)]$ [53], which generalizes to the mutation–draft balance [54]. We abbreviated the local curvature $c := -2NE_0^2\langle f''(\Gamma)\rangle$ of the fitness landscape in units of the genetic drift and the neutral sequence variation. Furthermore, we assumed that higher orders of the landscape $f'''(\Gamma)$ do not shape the variance of Γ in $\langle m^{\Gamma^2}\rangle$ such that it is given by the results of a quadratic fitness landscape, namely $\langle\Gamma^2\rangle - \langle\Gamma\rangle^2 = E_0^2/(2c)\left[1 + \mathcal{O}(c^{-1/2}, \mu N)\right]$ [53]. This term is negligible in (2.15). Moreover the corrections are supposedly small, because $c \gtrsim 1$ determines a regime of effective trait selection [53] and $\mu N < 1$ is small since it is the neutral single site polymorphism. We discuss types of fitness landscapes in detail in the Section 2.3. In anticipation of that section it is worth mentioning that in a quadratic fitness landscape (2.24) this curvature is by definition constant, $f''(E) = -c_0$, while in a biophysical fitness landscape (2.25), e.g. modeling protein folding or binding, the scaling is mainly given by the mutation-selection balance of Equation (2.4): $\langle f''(\Gamma)\rangle \approx \langle k_B T f'(\Gamma)\rangle = -m^\Gamma/(g^{\Gamma\Gamma}k_B T)$.

The form of the phenotypic evolution equations is approximately decoupled from details of the trait's molecular determinants. The dynamics of (2.4) and (2.5) do not depend on the distribution of effects in the genotype-phenotype map (2.1). Recombination between the trait loci induces a crossover between the selection on entire genotypes and the selection on individual

alleles [53,88,89]. Genetic linkage affects the form of the diffusive dynamics of Δ. The form of the dynamics for Γ remains invariant even under strong linkage with the rest of the genome, so that the statistics of Γ depends on recombination only through the diffusion coefficient $g^{\Gamma\Gamma} = \langle\Delta\rangle$. On the one hand, these effects are small for within-trait recombination over a wide range of evolutionary parameters, as shown by simulations reported in Chapter 3 and reference [53]. it was shown how strong linkage with the rest of the genome constrains $\langle\Delta\rangle$ [54] and we study the consequences to collective trait dynamics and adaptation in asexual evolution in Chapter 5.

2.2 Selection and dynamics of QTL

Here, we discuss the effect of the phenotypic selection on the QTL. We use these not only to study QTL correlations in Chapter 4, but they provide some generic properties of trait selection in various types of fitness landscapes. Understanding the selection strength of new trait variants is crucial for the phenotypic fitness wave in Chapter 5. We assume a regime, where the fitness landscape is sufficiently smooth. By this we mean that new variants are not pushed over a fitness optimum. The quantitative traits we consider have a biased mutational target for deleterious mutations, which warrants this condition by pushing populations at least mildly to the flank of fitness landscapes. With this, we derive selection coefficients, and 2nd order selection between sites. We find an universal typical scale of selection coefficients imposed by the scale, which is given by the inverse coalescence time. We shortly recapitulate how these determine substitution and fixation for independent mutations and under interference selection both needed in Chapter 4.

The impact of the trait selection on the single site selection coefficient of a quantitative trait locus j, Figure 2.1A, is approximately given by the gradient of the fitness landscape and the trait effect E_j,

$$s_j^f(E,t) = f(E+E_j,t) - f(E,t) = E_j f'(E,t) + \mathcal{O}(E_j^2 f''(E,t)), \tag{2.16}$$

For small effect mutations we can omit the second term if we are not directly at a fitness peak, i.e. $E_j \lesssim f'(E)/f''(E)$. This is reasonable for quantitative trait mutations encoded in multiple sites. We neglect this term from now on. The average mutation effect in a population with Gaussian distributed $\mathcal{W}(E)$ reads $\overline{s}_j^f(t) \approx E_j \left[f'(\Gamma(t),t) + \frac{1}{2}\Delta(t) f'''(\Gamma(t),t)\right]$. Unsurprisingly, quantitative traits generate a directional selection towards higher trait fitness. With marginalized trait statistics, the average selection coefficient across individuals and population is $\langle\overline{s}_j^f(t)\rangle \approx E_j \left[\langle f'(\Gamma,t)\rangle + \frac{1}{2}\langle\Delta\rangle\langle f'''(\Gamma,t)\rangle\right]$. For sufficiently un-rugged landscapes, i.e. $\langle\Delta\rangle \lesssim \langle f'(\Gamma,t)\rangle/\langle f'''(\Gamma,t)\rangle$, the second term can be neglected which we do in the following. Under trait equilibrium and mutation–drift dominated $\langle\Delta\rangle$ we use (2.14) omitting the $\mathcal{O}(c^{-1},\theta)$

and find that typical selection coefficients are of order of the coalescence rate,

$$|\langle \overline{s}_j^f \rangle| = \frac{|E_j \langle m^\Gamma \rangle|}{g^{\Gamma\Gamma}} \approx \frac{|E_j|}{\epsilon} \frac{1}{2N}, \tag{2.17}$$

where $\epsilon := E_0^2/|\langle \Gamma \rangle - \Gamma_0|$ defines a typical trait effect scale. Comparing with Equations (2.2) and (2.10), it relates the average squared effect of QTL mutations $\sum_{i=1}^{\ell} E_i^2/\ell = 4E_0^2/\ell$ with the average directional effect $(\langle \Gamma \rangle - \Gamma_0)/(2\ell)$. The efficacy of trait site selection is in a transient regime. Trait dynamics balance such that the majority, but not all trait sites confer the beneficial allele. This has important implications for phenotypic evolution: a) Quantitative trait selection alone does not constrain the dynamics of a particular site significantly; these underly fluctuations even in constant environments and some sites offer beneficial mutational targets. b) Under interference selection in a traveling fitness wave, quantitative traits generate a constant mutational influx with selection coefficients generically smaller than the width of the fitness wave, as we will learn in detail in Chapter 5.

Nonlinear fitness landscapes generate fitness epistasis with epistatic selection coefficients between sites i and j given by their trait effects in second order of $f'(E)$, cp. Figure 2.1B,

$$\begin{aligned} s^f_{j|i}(E,t) &\equiv s^f_j(E+E_i) - s^f_j(E) \approx E_j f'(E+E_i,t) - E_j f'(E,t) \approx E_i E_j f''(E,t) \\ &= \frac{1}{2N}\omega_{ij}(E,t) \approx s^f_{i|j}(E,t), \end{aligned} \tag{2.18}$$

where $\omega_{ij}(E,t) := 2NE_iE_jf''(E,t)$ is a matrix measuring epistasis in dimensionless units and depicted in Figure 2.1C. We assumed again that trait effects are sufficiently small in smooth fitness landscapes, now also in higher derivatives $E_i, E_j \lesssim f'(E)/f''(E), f''(E)/f'''(E)$. This type of epistasis in product form has been identified by [90] in the context of Fisher's geometric model [31], however discussed there in the effects around fitness peaks. Our approximation is not valid close to peaks of the fitness landscape.

Traits under stabilizing selection have non-linear, downwards curved fitness landscapes, i.e. $f''(E,t) < 0$, such that the non-linearity generates negative epistasis for mutations with the same sign of trait effects. Quantitatively, it is proportional to both trait effects: the more destabilizing a mutation is, the stronger is the selective pressure for compensation. By taking the stationary ensemble of the trait distribution, we find the average epistatic effect for two mutations arising at equal time, i.e. on the same genetic background E,

$$\begin{aligned} \langle s^f_{j|i} \rangle &= \frac{1}{2N}\omega_{ij}, \qquad \text{with} \\ \omega_{ij} &:= \langle \omega_{ij}(\Gamma) \rangle = 2NE_iE_j\langle f''(\Gamma)\rangle \equiv -\frac{E_iE_j}{E_0^2}c, \end{aligned} \tag{2.19}$$

which scales for all sites with the average and hence local curvature of the fitness landscape $c = -2NE_0^2\langle f''(\Gamma)\rangle$. The epistatic matrix ω_{ij} (as well as $\omega_{ij}(E,t)$) is symmetric and generates broad epistasis across all trait sites. Nonetheless, it has a simple rank 1 given by the outer product of the vector of trait effects $\vec{E} = (E_1, \ldots, E_\ell)$ with itself. In Appendix B we see

that multiple quantitative traits generate additive epistasis. Hence each trait adds a rank to ω_{ij} as depicted in Figure 2.1D for two traits. The epistatic selection gets more predominant, the stronger the curvature of the fitness landscape is compared to its slope, i.e. $\langle s^f_{j|i}\rangle/\langle s^f_j\rangle \approx E_i\langle f''(\Gamma,t)\rangle/\langle f'(\Gamma,t)\rangle$.

In addition to the selection through a focal trait, s^f_j, there is possibly additional external selection $s_j(t)$ through pleiotropic interaction with Mendelian or other quantitative phenotypes,

$$s^{\mathrm{tot}}_j(t) = s^f_j(t) + s_j(t). \tag{2.20}$$

Time dependence of $s_j(t)$ reflects external adaptive pressures, which are supposed to change over much longer timescales than trait fluctuations in $s^f_j(t)$ equilibrating quickly through the collective dynamics of all trait sites. Generically, a mutation can therefore be beneficial or deleterious in its trait effect and beneficial or deleterious with respect to the external pressures. This single site selection changes the dynamics of sites and demands to adapt the null-model of neutral trait ($f(E) = 0$) evolution from [53] by reducing $E_0^2 \approx \frac{1}{4}\sum_i E_i^2\rho_i^{\mathrm{eq}}/\mu$ with non-adaptive substitution rates $\rho_i^{\mathrm{eq}} \leq \mu$, which we discuss in detail in Chapter 4. Hence, it reduces the timescale of trait evolution, Equation (2.11). We use this external selection (2.20) in Chapter 4 to model adaptive pressures on trait sites, which trigger compensatory mutations.

Fixation probabilities of mutations. Since individual quantitative trait sites are mostly monomorphic, $\mu N < 1$, we do not consider the particular dynamics of finite site frequencies but restrict ourself to substitution dynamics here. The selection coefficient determines the chance of a mutation to fix in the evolutionary process. For independently arising mutations, i.e. in the low mutation rate regime $\mu N\ell < 1$, with fitness effect s the fixation probability is in the diffusion limit $s \ll 1$ independent of the particular replication mechanism and follows the Kimura-Otha substitution rate [31–34]

$$G(s) = \frac{2s}{1-\exp(-2Ns)} + \mathcal{O}(s). \tag{2.21}$$

However quantitative traits can generically be polymorphic, $\mu N\ell > 1$, meaning that various mutational variants coexist and compete for fixation. Since a lot of traits are in a localized part of the genome, recombination cannot break linkage quickly enough [52]. Furthermore, other parts of the genome can be genetically linked to the trait and generate interference effects. A mutation that has fitness effects smaller than the width of the fitness distribution within a population, which is mainly scaling with $\sim\tilde{\sigma}$, shows strongly reduced fixation probabilities. For Gaussian fitness distributions, so called traveling waves that arise under large mutational input as reviewed in [91], the fixation probability reads [69, 92]

$$G(s) = \frac{1}{N}\exp(s/\tilde{\sigma}), \qquad |s| \lesssim \tilde{\sigma}, \tag{2.22}$$

where N is the population size and $\tilde{\sigma} > 1/(2N)$ is the neutrality threshold [68] also identified as coalescence rate [71]. Mutations under strong selection that exceed the width of the fitness

wave, $|s| \gg \tilde{\sigma}$, again follow Equation (2.21). Intermediate selection follows a more complex form [69].

The marginal equilibrium of a site in a time-constant fitness landscape is well known, e.g. in 2-state systems in physics, from substitution probabilities. The state probability of an allele with selection s being fixed reads [92, 93],

$$\lambda_{\mathrm{eq}}(s) = 1 - \lambda_{\mathrm{eq}}(-s) = \frac{G(s)}{G(s) + G(-s)} = \frac{1}{1 + \exp(-s/\tilde{\sigma})}, \tag{2.23}$$

with coalescence rate $\tilde{\sigma} = 1/(2N)$ for independent evolution (2.21) and $\tilde{\sigma} \gg 1/(2N)$ in a fitness wave (2.22).

2.3 Modeling biophysical fitness landscapes

The evolutionary process depends highly on the underlying fitness landscape $f(E, t)$. Here we discuss the fitness landscapes used in this thesis and their differences and similarities in their balancing point. We use a quadratic fitness seascape to describe phenotypic adaptation in Chapter 3. The sequence correlations in Chapter 4 do not depend on the details of the fitness landscape as long as the landscape stabilizes the evolution. We use biophysical fitness landscapes to model protein traits of genes in the co-evolution model in Chapter 5. These are thermodynamically modeled to be proportional to functional states of a protein, e.g. being folded with a ligand bound. We argue how non-equilibrium thermodynamics shape the fitness landscape and stabilize the evolutionary process in a stability–affinity model. All fitness landscapes generate typical selection coefficients of the same order of magnitude and universal scaling of the fitness variations in a population.

The detailed functionality of the fitness land- or seascape $f(E, t)$ is a key input to the trait dynamics (2.4) and (2.5) and determines hence its equilibrium distributions (2.12) and (2.13). Previous work has shown that biophysical interactions shape the evolutionary process [76, 77, 80, 81], where the authors studied the pairwise couplings of sites. On the trait level, non-equilibrium processes not only drive changes of $f(E, t)$ on macroevolutionary timescales. Furthermore, cell biology is far from equilibrium [18], and thermodynamic non-equilibrium processes on cell-cycle timescales shape the functionality of proteins. This becomes important in the co-evolution of functionally linked traits. Therefore it is worth to study the underlying biophysics that influence the fitness of biophysical traits. In this section, we discuss the advantage and disadvantage of various fitness landscapes to model the protein evolution and discuss how thermodynamic non-equilibrium determines the functional form of a fitness landscape from cell-physical principles. These short-term non-equilibria originate from physical processes in a cell and must not be confused with the non-equilibrium of a fitness seascape that originates from environmental or co-evolutionary fluctuations that change fitness in the long term, i.e. on evolutionary scales.

Quadratic fitness landscape. Classically, constraining selection has been extensely analyzed in quadratic fitness landscapes [31, 45, 51, 53, 94–98]

$$f(E,t) = f^* - c_0\big(E - E^*\big)^2, \tag{2.24}$$

as depicted in Figure 2.2A. These landscapes can be seen as second order expansions of an arbitrary fitness landscape and are hence minimalistic non-linear models. They are a good basis to model gene expression levels to describe stabilizing selection around a single fitness peak and they provide many universal results such as decoupling from genomic details, e.g. the distribution of trait effects or rates of recombination [53]. In Chapter 3, we use this type of landscape and generalize it to a fitness seascape with a time-dependent fitness peak $E^*(t)$ as a minimal model for stabilizing selection together with adaptation to reveal universality. The process decouples again from microscopic details and from details of the driving of the landscape. The adaption just depends on the stabilizing strength and mean square peak-displacements. On the same principle, these landscapes are a good proxy for studying the co-evolution of trait sites in Chapter 4, because they are generated by the same (local) constraint from its curvature.

Stability model. While these quadratic models provide a good minimalistic scheme for stabilizing selection, they cannot describe the detailed scaling behavior with solutions on differently curved parts of biophysical fitness models like a mesa-landscape. A minimal example for a single biophysical trait is a free energy between 2-states, for instance a bound/unbound ligand in binding domains or folded/misfolded proteins, which we discuss here as an example. In thermodynamic equilibrium at temperature T, a protein is folded with probability $p_+(G) = 1/[1 + \exp(-G/k_BT)]$, where G is the Gibbs free energy difference[2] between the unfolded and the folded state and k_B is Boltzmann's constant. A minimal biophysical fitness model takes the mesa-shaped form

$$f(G) = f_0\, p_+(G) = \frac{f_0}{1 + \exp(-G/k_BT)}, \tag{2.25}$$

see Figure 2.2B, with a single selection coefficient capturing functional benefits of folded proteins and metabolic costs of misfolding [99–101]. Similar fitness models based on binding affinity have been derived for transcriptional regulation [15–17]; the rationale of biophysical fitness models has been reviewed in references [87, 102]. A key characteristic of these biophysical traits is that the sequence space is sparser in the high-fitness regime, because a folding protein sequence or a binding sequence requires a specialized sequence offering more mutational targets for deleterious than for beneficial mutations. Therefore, mutations push the trait down the fitness edge until it gets balanced by stronger selection on steeper slopes of the landscape, cp. (2.14). We use this balance in Chapter 5 as minimal model of protein evolution to quantify the genetic cost of biophysical traits. In contrast to a quadratic landscape with constant curvature, this type of landscape may comprises gene loss, if deleterious mutations cannot be balanced, due to a maximal slope of selection. This is characterized by a protein selection $f_0 \lesssim \tilde{\sigma}$ and will be discussed in Chapter 5. Biophysical trait selection hence provides two landmarks of selection:

[2] where the notation is not to be confused with fixation probabilities $G(.)$, which we denote as functions.

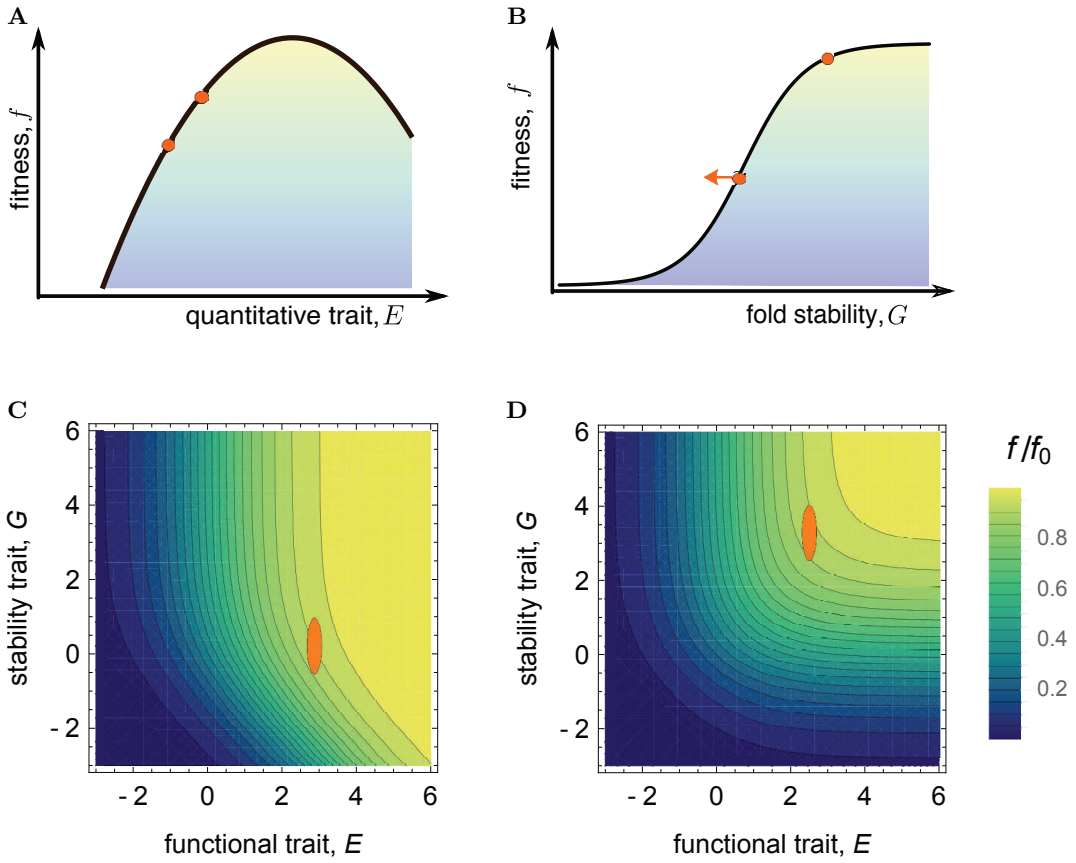

Figure 2.2. Models of phenotypic fitness landscapes. A Quadratic fitness landscape $f(E)$, Equation (2.24), as a minimal model for stabilizing selection on a quantitative trait E penalizing deviations from an optimal trait value E^*. Mutations, genetic drift, or genetic draft push populations down the landscape until selection gets strong enough to balance with left orange dot indicating a population with stronger deleterious effects. The curvature generates the selective constraints. **B** Minimal biophysical fitness model. The fitness of an individual trait, $f(G)$, is a sigmoid function of its fold stability G. This function has a high-fitness region of stable, functional proteins, an inflection point at intermediate fitness marking marginally functional proteins, and a low-fitness region of dysfunctional proteins. The mutation-selection dynamics on this landscape generates high-fitness equilibria ($\tilde{\sigma} \ll f_0$, red dot) and unstable states at lower fitness ($\tilde{\sigma} \gtrsim f_0$, red dot with arrow), depending on the fitness difference f_0 between functional and dysfunctional proteins and the coalescence rate $\tilde{\sigma}$. **C, D** Thermodynamic fitness landscapes $f(G, E)$ of the stability-affinity model, Equations (2.26) – (2.27), are shown as functions of the stability G and affinity E. Stable populations, characterized by stationary trait means and variances, are marked by red ellipsoids. **C** Thermodynamic equilibrium. **D** Non-equilibrium, e.g driven by active degradation of folded proteins, decorrelates the traits thermodynamically and generates more independent selection on stability G. In the high-fitness part, this landscape becomes approximately additive in G and E.

characteristic single site selection, which is almost neutral $s \sim \tilde{\sigma}$ as discussed in the previous section, and the larger, mesoscopic trait selection scale given by the height of the plateau $f_0 \gtrsim \tilde{\sigma}$ which can still be efficient though the collective dynamics of all trait sites.

Stability-affinity model. This model extends the minimal protein model by explicitly including protein function, which we assume to be mediated through binding to a molecular target. By that, proteins can be in three thermodynamic states: functional, i.e. folded and target-bound $(++)$, folded and unbound $(+-)$, and unfolded $(--)$. We assume ordinary proteins such that unfolded proteins cannot bind their target, which implies that the fourth state of unfolded proteins localized to their target $(-+)$ is suppressed by the entropy loss of localization.

In *thermodynamic equilibrium,* the statistics of this ensemble is governed by two quantitative traits, which are defined as free energy differences: the fold stability $G \equiv G_{--} - G_{+-}$ and the reduced binding affinity $E \equiv G_{+-} - G_{++}$, which includes the entropy loss of localization and depends on the ligand concentration. The equilibrium state probabilities p_{++}, p_{+-}, and p_{--} are given by Boltzmann statistics depending on the traits G and E; in particular,

$$p_{++}(G,E) = \frac{1}{1 + \mathrm{e}^{-E/k_BT} + \mathrm{e}^{-(E+G)/k_BT}}. \tag{2.26}$$

Equilibrium models of this kind are well known in protein biophysics [55, 56]. From this equilibrium, the thermodynamic fitness landscape is modeled

$$f(G,E) = f_0\, p_{++}(G,E) \tag{2.27}$$

analogous to Equation (2.25) [57, 58, 103]. This landscapes is plotted in Figure 2.2C. Assuming uncorrelated mutational effects in both traits, the 2d-dynamics are an uncomplicated extension of the evolution of a single trait, see Appendix B. They show an evolutionary instability: selection is acting effectively 1-dimensional and may be mapped onto Equation (2.25). It works on the binding trait E but not independently on stability G, e.g. $f(G,E) \approx f_0(1-\mathrm{e}^{-E/k_BT}(1+\mathrm{e}^{-G/k_BT}))$ in a stable regime $E, G \gtrsim k_BT$. In fact, proteins can compensate destabilizing mutations by stronger functional binding, keeping $E + G$ constant. While this is a clear result of the thermodynamic equilibrium not taking into account dynamical details determining the state probability, $p_{++}(G,E)$, this is not a biologically meaningful process. It keeps the protein folded only by an extreme free energy benefit through the ligand binding. Folded but unbound proteins would hardly exist. Though, there exist proteins that fold only with a ligand bound, they are strongly outnumbered.

In principle, this instability could be resolved by a limited density of available encoding sequences for such trait values through the non-linear mutational influx m^Γ in (2.4), which relates in fact to a maximal reachable E in (2.1). However, this change is rather insensitive at dynamics near a fitness cliff, as discussed in Chapter 5. Substantial lifetimes of unfolded or functional states, depending exponentially on the trait $\sim \mathrm{e}^{E/k_BT}$, are still in reach by this linear entropy-like 'force'. Furthermore such strong constraints would be a fatal target for deleterious mutations and the evolutionary process could have developed work-arounds, e.g. by

longer binding domains. Therefore it cannot directly explain, how the vast majority of ordinary proteins is able to fold and bind a ligand according to demand. This problem unveils the core of the problem with this biophysical model: it assumes thermodynamic equilibrium, while it is well-known that biological processes are on cell level far from equilibrium [18]. Ligand fluctuations, regulatory networks, or changing cellular environments need proteins being ready to change their state on timescales of the cell cycle. While this problem is partially resolved by catalysts, there are also ubiquitous mechanism for active protein degradation. Any source of thermodynamic non-equilibrium would reduce the dependence of the folding trait G from its binding E and hence stabilizes the evolutionary process, cp. Figure 2.2D, with stronger curved iso-fitness lines as in Figure 2.2C.

Active protein degradation. We discuss now a minimalistic thermodynamic non-equilibrium model produced by active protein degradation. This affects a wide range of proteins, for example through the ubiquitin-proteasome pathway [104]. It ensures that regulatory proteins are rapidly cleared once their function ends (at a particular point of the cell cycle). Consider a simple model, which has a constant rate K^- of active degradation and a rate $K_G^+ = K_G^0 \mathrm{e}^{G/k_BT}$ for the folding process. Here we do not model details of the pathways of protein synthesis from and degradation into amino acid constituents, which would only affect the total protein concentration but not their state probabilities. In a marginal steady state considering folding only, proteins are folded with probability

$$\tilde{p}_+(G) = \frac{1}{1+\nu_G \mathrm{e}^{-G/k_BT}}, \tag{2.28}$$

where $\nu_G = K^-/K_G^0$. Hence, this model retains the sigmoid form of the fitness landscape given in Equation (2.25) and shown in Figure 2.2B; evolutionary conclusions remain invariant. Apart from details of the gene-loss dynamics for very unstable proteins, it follows the same scaling laws as the single trait evolution (2.25).

For the 3-state thermodynamics, we assume a single degradation rate K^- for the processes $(++) \to (--)$ and $(+-) \to (--)$, a rate $K_G^+ = K_G^0 \mathrm{e}^{G/k_BT}$ for the folding process $(--) \to (+-)$, and a rate $K_E^+ = K_E^0 \mathrm{e}^{E/k_BT}$ for the binding process $(+-) \to (++)$. In this model, the folding and binding processes decouple, and we obtain the non-equilibrium steady-state probability

$$p_{++}(G,E) = \frac{1}{\big(1+\nu_G \mathrm{e}^{-G/k_BT}\big)\big(1+(1+\nu_E)\mathrm{e}^{-E/k_BT}\big)}, \tag{2.29}$$

with $\nu_G = K^-/K_G^0$ and $\nu_E = K^-/K_E^0$. From this, we again build thermodynamic fitness landscapes, Figure 2.2D,

$$f(G,E) = f_0\, p_{++}(G,E) \tag{2.30}$$

analogous to Equation (2.25) and (2.27). The non-equilibrium landscape generates a stabilizing selection on the protein stability G. In the plateau of large fitness, $G \gtrsim 1$ and $E \gtrsim 1$, selection decouples and evolution is (selectively) independent between these traits, $f(G,E) \approx f_0(1 - \nu_G \mathrm{e}^{-G/k_BT} - (1+\nu_E)\mathrm{e}^{-E/k_BT})$. As derived in Appendix B, a stationary state again follows the same scaling laws as the single trait evolution (2.25). However, with 2 'independent' co-evolving

traits. We use this landscape in Chapter 5, but break it down to two traits in the stable regime to study the scaling. Both evolve independently in a sigmoid fitness landscape. Nonetheless, the particular non-equilibrium model (2.29) is of importance to understand evolutionary stability. For instance it would, in contrast to equilibrium models, explain the position of the wild-type of a GB1 protein outside the dense state-space regime as reported in [103].

It is worth mentioning that the minimalistic biophysical model (2.25) cannot generate sign epistasis since it has no local optimum, such as peaked fitness models [90]. However, in the 2-dimensional models (2.27) and (2.30) pleiotropic mutations can cross a local maximum, if they have opposite effects in both traits. This effect gets stronger the stronger the non-equilibrium fortifies selection on the stability trait.

For modeling local stabilizing selection of quantitative traits and the broad epistatic interaction of its sites, the particular choice of the landscape is not important as long as it is non-linear. If biophysical traits with their scaling and stability conditions are to be modeled, e.g. for protein function and stability, thermodynamical considerations have to be taken into account carefully. Equilibrium leads to effectively 1-dimensional evolution with evolutionary instabilities; these are taken care for in non-equilibrium models generating independent selection on all traits in the stable part of the landscape. Thermodynamic equilibrium and non-equilibrium are mappable to a simplified 1-dimensional-biophysical model such that the difficulty is just in counting the independent degrees of freedom. These should be inferable from our correlation measure in Chapter 4.

All phenotypic fitness landscapes have in commonon on balancing points distant from the peak and, if trait-selection alone is not constraining the diversity $\langle\Delta\rangle$, that typical selection coefficients $s \sim \tilde{\sigma}$ (2.17) are of the size of the coalescence rate $\tilde{\sigma}$. (with $\tilde{\sigma} = 1/2N$ without external interference). Hence, single mutations are close to neutrality. On the other hand, the mesoscopic trait evolution defines a second selection scale which determines that overall trait selection is stabilized, if it is larger than $\tilde{\sigma}$. This scale is $c_0 E_0^2$ in (2.24) or f_0 in the biophysical landscapes (2.25), (2.27), and (2.30). Moreover, we find universal behavior for the fitness statistics in biophysical landscapes at stable balancing points $G/k_BT \gtrsim 0$, where $f''(G) \approx f'(G)/k_BT$. With using (2.15) and (2.14), each independent trait generates a fitness diversity $\langle\Delta_f\rangle \approx \langle\Delta\rangle\langle f'^2(\Gamma)\rangle = \frac{\langle\Delta\rangle}{(2N)^2}(1/\epsilon^2 + 1/(\epsilon k_BT)) \sim \mu\ell/N$, which gets largely independent of the selection parameter f_0 (but log-corrections in ϵ). A quadratic fitness landscape (2.24) generates the same scaling, if far on the flank of the landscape (2.15) $\langle f'^2(\Gamma)\rangle \gtrsim c_0/(2N)$ such that the balance point is far off the fitness peak. These results generalize to interference selection $1/(2N) \to \tilde{\sigma}$ and are a key scaling ingredient for the width of a fitness distribution in Chapter 5.

Though these landscapes generally show the same scaling behaviors, the map from the free energy changes of mutations to fitness effects of focal protein needs to be studied from its cell-biological properties.

Chapter 3

Adaptive evolution of molecular phenotypes

In this Chapter, we study the adaptive evolution of a quantitative trait under time-dependent selection, which arises from environmental changes or through fitness interactions with other co-evolving phenotypes. We analyze a model of trait evolution under mutations and genetic drift in a single-peak fitness seascape. The fitness peak performs a constrained random walk in the trait amplitude, which determines the time-dependent trait optimum in a given population. We derive analytical expressions for the distribution of the time-dependent trait divergence between populations and of the trait diversity within populations. Based on this solution, we develop a method to infer adaptive evolution of quantitative traits. Specifically, we show that the ratio of the average trait divergence and the diversity is a universal function of evolutionary time, which predicts the stabilizing strength and the driving rate of the fitness seascape. From an information-theoretic point of view, this function measures the macro-evolutionary entropy in a population ensemble, which determines the predictability of the evolutionary process. Our solution also quantifies two key characteristics of adapting populations: the cumulative fitness flux, which measures the total amount of adaptation, and the adaptive load, which is the fitness cost due to a population's lag behind the fitness peak.

3.1 Introduction

In this chapter, we focus on the adaptive evolution of molecular traits, which involves mutations, genetic drift, and (partial) recombination of the trait loci. The adaptive dynamics take place on macro-evolutionary timescales and can generate large trait changes — in contrast to micro-evolutionary processes based on standing trait variation in a population. Adaptive trait changes are driven by time-dependent selection on the trait values. Specifically, we consider the trait evolution in a single-peak *fitness seascape* [59, 85, 105], which has a moving peak described by a stochastic process in the trait coordinate. The time-dependence of the optimal trait value

can have extrinsic or intrinsic causes; for example, the optimal expression level of a gene is affected by changes in the environment of an organism and by expression changes of other genes in the same gene network. These fitness seascape models have two fundamental parameters: the *stabilizing strength* and the *driving rate*, which measure the width and the mean square displacement of the fitness peak per unit of evolutionary time. In an ensemble of populations with independent fitness peak displacements, these dynamics describe lineage-specific adaptive pressure. We discuss specific seascape models with continuous or punctuated adaptive pressure; that is, the fitness peak performs a constrained (Ornstein-Uhlenbeck) random walk or a Poisson jump process in the trait coordinate. These stochastic processes define minimal non-equilibrium models for the adaptive evolution of a quantitative trait.

Here we focus on *macro-evolutionary* fitness seascapes, which have low driving rates compared to the diffusion of the trait by genetic drift and describe persistent selection on a quantitative trait [59,106]. We show that this kind of selection generates two complementary evolutionary forces. On short timescales, a single fitness peak acts as stabilizing selection, which constrains the trait diversity within a population as well as its divergence between populations. On longer timescales, the population trait mean follows the moving fitness peak, which generates an adaptive component of the trait divergence. In the limit case of a static fitness landscape, we recover the evolutionary equilibrium of quantitative traits under stabilizing selection, which has been the subject of a previous publication [53]. The evolution in a quadratic fitness landscape is described by an Ornstein-Uhlenbeck dynamics of the trait mean [94–97], which should not be confused with the Ornstein-Uhlenbeck process of the fitness peak in a stochastic seascape.

We also discuss the regime of *micro-evolutionary* fitness seascapes, which describe rapidly changing selection on a quantitative trait. Such fitness changes are ubiquitously generated by ecological fluctuations. They lead to micro-evolutionary adaptation of the trait from its standing variation in a population but do not generate directional selection on evolutionary timescales. We show that micro-evolutionary fitness seascapes can be mapped to effective fitness landscapes that describe relaxed stabilizing selection.

Our model of adaptive trait evolution contains different sources of stochasticity: mutations establish trait differences between individuals within one population, reproductive fluctuations (genetic drift) and fitness seascape fluctuations generate trait differences between populations with time. In macro-evolutionary fitness seascapes, these stochastic forces act on different timescales and define different statistical ensembles, similar to thermal and quenched fluctuations in the statistical thermodynamics of disordered systems. In Section 2.1, we derived stochastic evolution equations for the trait mean and the trait diversity in a fitness seascape. This we combine in Section 3.2 with the dynamics of the position of the fitness peak, which establish a joint dynamical model for the trait and the underlying fitness seascape over macro-evolutionary timescales. In Section 3.3, we discuss the analytical solution of these models for a stationary ensemble of adapting populations. This ensemble has a time-independent trait diversity within populations, as well as a trait divergence between populations that depends on their divergence time. In Section 3.4, we evaluate two important summary statistics of adaptive processes. The *genetic load*, which is defined as the difference between the maximum fitness and the mean

population fitness, is shown to include a specific adaptive component, which results from the lag of the population behind the moving fitness peak. The cumulative *fitness flux* measures the amount of adaptation in a population over a macro-evolutionary period: it is zero at evolutionary equilibrium and increases monotonically with the driving rate of selection [60]. Furthermore, we determine the *predictability* of trait values in one population given its distribution in another population, which is obtained by a suitably defined entropy of the population ensemble under divergent evolution.

The statistical theory provides a new method to infer selection on a quantitative trait from diversity and time-resolved divergence data. Given these data in a family of evolving populations, we use the divergence-diversity ratio $\Omega(\tau)$ for different divergence times τ to determine the stabilizing strength and the driving rate of the underlying fitness seascape. These selection parameters, in turn, quantify the amount of conservation and adaptation in the evolution of the trait. The divergence-diversity ratio is universal: it depends on the stabilizing strength and the driving rate of the fitness seascape as well as on the evolutionary distance between populations, but it is largely independent of the trait's constitutive sites, of the amount of recombination between these sites, and of the details of the fitness dynamics. In contrast to most sequence evolution tests, the Ω test does not require the gauge of a neutrally evolving "null trait". We discuss this test along with probabilistic extensions in Section 3.5.

This chapter contains some necessarily technical derivations of our main results. For readers who are not interested in technical issues, it offers a fast track: the section summaries 3.2.2, 3.3.4, 3.4.4, the description of the Ω test in Section 3.5, its application to gene expression of *Drosophila* in 3.6, and the concluding Section 3.7 can be read as a self-contained unit.

3.2 Stochastic seascape models

In this section, we introduce simple stochastic models for the dynamics of selection, which promote fitness landscapes to fitness seascapes. We then combine the dynamics of trait and selection to a joint, non-equilibrium evolutionary model.

In particular, we discuss the evolution in a trait fitness seascapes $f(E,t)$ that changes on macro-evolutionary timescales. This process is illustrated in Figure 3.1: At a given evolutionary time, the population has a trait mean $\Gamma(t)$, diversity $\Delta(t)$, and is positioned at a distance $\Lambda(t) \equiv \Gamma(t) - E^*(t)$ from the optimal trait value. The trait distribution follows the moving fitness peak, building up a trait divergence

$$D^{(1)}(t,\tau) = (\Gamma(t) - \Gamma(t-\tau))^2 \tag{3.1}$$

between an ancestral population at time $t-\tau$ and its descendent population at time t in a given lineage. In the same way, we can define the trait divergence between two descendent populations at time t that have evolved independently from a common ancestor population at time $t-\tau/2$,

$$D^{(2)}(t,\tau) = (\Gamma_1(t) - \Gamma_2(t))^2. \tag{3.2}$$

In a suitably defined ensemble of parallel-evolving populations, the expectation values of these divergences, $\langle D^{(\kappa)}(\tau)\rangle$ ($\kappa = 1, 2$), depend only on the divergence time τ. The asymptotic divergence for long times is just twice the trait variance across populations,

$$\lim_{\tau\to\infty}\langle D^{(\kappa)}(\tau)\rangle = 2\langle(\Gamma - \langle\Gamma\rangle)^2\rangle \qquad (\kappa = 1, 2). \tag{3.3}$$

In particular, the quantity E_0^2 defined in (2.2) is the trait variance in an ensemble of random genotypes, which results from neutral evolution (with averages $\langle\ldots\rangle_0$ marked by a subscript) at low mutation rates, $E_0^2 = \lim_{\mu\to 0}\langle(\Gamma - \langle\Gamma\rangle_0)^2\rangle_0$. For finite times, however, the statistics of the single-lineage divergence $D^{(1)}$ and the cross-lineage divergence $D^{(2)}$ differ from each other in an adaptive process. As we will discuss in detail below, this is a manifestation of the non-equilibrium evolutionary dynamics in a fitness seascape. In contrast, evolutionary equilibrium in a fitness landscape dictates $\langle D^{(1)}(\tau)\rangle_{\rm eq} = \langle D^{(2)}(\tau)\rangle_{\rm eq}$ by detailed balance.

For a generic fitness seascape $f(E, t)$, the diffusion equations (2.4) and (2.5) do not have a closed analytical solution. At the same time, we are often not interested in the detailed history of fitness peak displacements and the resulting trait changes. To describe generic features of adaptive processes, we now introduce solvable stochastic models of the seascape dynamics and link broad features of these models to statistical observables of adapting populations.

In this chapter, we restrict our analysis to single-peak fitness seascapes of the form (2.24), Figure 2.2A. Despite its simple form, it covers a broad spectrum of interesting selection scenarios [2]. For constant trait optimum E^*, it is a time-honored model of *stabilizing selection*. [2, 16, 25, 31, 46, 51, 85, 107–109]. Nearly all known examples of empirical fitness landscapes for molecular quantitative traits are of single-peak [110] or mesa-shaped [15, 17, 107, 111, 112] forms. Mesa landscapes describe directional selection with diminishing return: they contain a fitness flank on one side of a characteristic "rim" value E^* and flatten to a plateau of maximal fitness on the other side, cp. Section 2.1 and Figure 2.2B. Furthermore, trait values on the fitness plateau tend to be encoded by far fewer genotypes than low-fitness values. This differential coverage of the genotype-phenotype map turns out to generate an effective second flank of the fitness landscape, which makes our subsequent theory applicable to mesa landscapes as well [2]. We refer to the scaled parameter

$$c = 2NE_0^2c_0 \tag{3.4}$$

as the *stabilizing strength* of a fitness landscape. This dimensionless quantity has a simple interpretation: it equals the ratio of the neutral trait variance E_0^2 and the weakly deleterious trait variance around the fitness peak, which, by definition, produces a fitness drop $\leq 1/(2N)$ below the maximum f^*. As shown in reference [53], the mutation-selection-drift dynamics of a quantitative trait in a single-peak fitness landscape leads to evolutionary equilibrium with a characteristic equilibration time

$$\tau_{\rm eq}(c) \;=\; \frac{1}{\mu + c\tilde{\tau}^{-1}(c)} \simeq \begin{cases} \mu^{-1} & \text{for } c \lesssim 1, \\ (c\tilde{\tau}(c))^{-1} & \text{for } c \gtrsim 1, \end{cases} \tag{3.5}$$

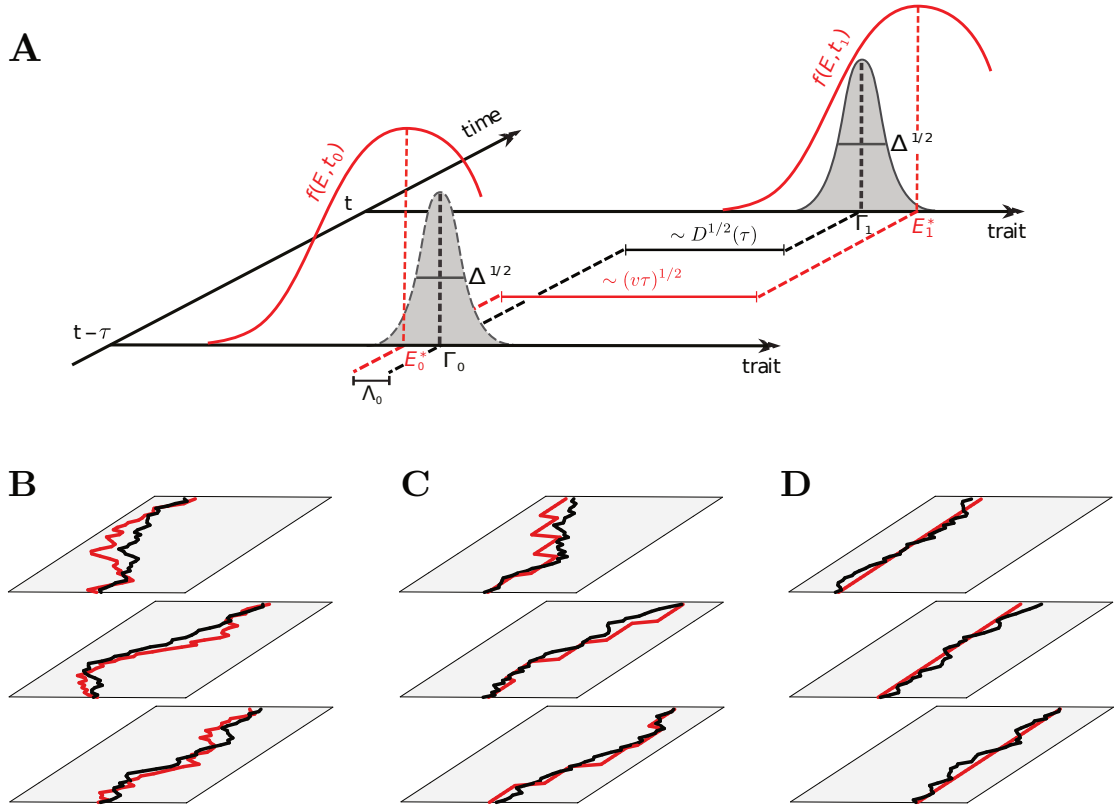

Figure 3.1. Adaptive evolution of a quantitative trait. A Evolution of the distribution of trait values $\mathcal{W}(E,t)$ (gray curves) in a given population subject to a single-peak fitness seascape $f(E,t)$ (red curves). At a given time t, the population has a trait distribution $\mathcal{W}(E,t)$ with mean $\Gamma(t)$ and diversity $\Delta(t)$, and is positioned at a distance $\Lambda(t) = \Gamma(t) - E^*(t)$ from the fitness peak. The population follows the moving fitness peak and builds up a trait divergence $D^{(1)}(t,\tau) = (\Gamma(t) - \Gamma(t-\tau))^2$ between the ancestral state at time $t-\tau$ and the descendent state at time t. The divergence $D^{(2)}(t,\tau)$ between two descendent populations with a common ancestor at time $t-\tau/2$ can be defined in an analogous way; see Equations (3.1) and (3.2). **B–D** Evolutionary population ensembles, each represented by three sample populations. In a given population, a realization of a single-peak fitness seascape specifies a lineage-specific optimal trait value that depends on evolutionary time, $E^*(t)$ (red line). The population mean trait, $\Gamma(t)$ (black line), adapts to the moving fitness peak with additional lineage-specific fluctuations due to mutations and genetic drift. The adaptive process is shown for three cases of fitness seascapes: **B** Diffusive fitness seascape: incremental changes in the optimal trait value reflect adaptive pressure caused by continuous ecological changes. The function $E^*(t)$ follows an Ornstein-Uhlenbeck random walk in the trait coordinate. **C** Punctuated fitness seascape: sudden changes in the optimal trait value reflect adaptive pressure caused by major, discrete ecological events. The function $E^*(t)$ is described by a Poisson jump process in the trait coordinate. We show that both types of fitness seascapes lead to a solvable, non-equilibrium joint statistics of Γ and E^*. **D** Fitness landscape: each population has a time-independent optimal trait value E^* and reaches an evolutionary (selection-mutation-drift) equilibrium [53].

where $\tilde{\tau}(c)$ is the quasi-neutral drift time defined in Equation (2.11).

For time-dependent $E^*(t)$, Equation (2.24) becomes a fitness seascape model [59, 85, 105]. At any given evolutionary time, this model describes stabilizing selection of strength c towards an optimal trait value $E^*(t)$. In addition, the changes of $E^*(t)$ over macro-evolutionary periods introduce directional selection on the trait and generate adaptive evolution. The form (2.24) of a fitness seascape assumes the stabilizing strength c to remain constant over time. As discussed in Section 3.2.1, this assumption leads to an important computational simplification: only the trait mean Γ adapts to the moving fitness peak, while the diversity Δ remains at evolutionary equilibrium. However, generalizing our model to a time-dependent stabilizing strength $c(t)$ is straightforward and is briefly discussed below. We consider two minimal models of seascape dynamics:

1) Diffusive fitness seascapes. In this model, the fitness optimum $E^*(t)$ performs an Ornstein-Uhlenbeck random walk with diffusion constant υ_0, average value G and stationary mean square deviation r_0^2. The scaled parameters

$$\upsilon = \frac{\upsilon_0}{E_0^2}, \qquad r^2 = \frac{r_0^2}{E_0^2}, \tag{3.6}$$

will be called the *driving rate* and the *driving span* of a fitness seascape. Different realizations of this random walk with the same set of parameters are shown in Figure 3.1B. The distribution of optimum trait values, $\mathcal{R}(E^*, t)$, follows a diffusion equation,

$$\frac{\partial}{\partial t}\mathcal{R}(E^*, t) = \upsilon E_0^2 \frac{\partial}{\partial E^*}\left[\frac{\partial}{\partial E^*} + \frac{1}{r^2 E_0^2}(E^* - G)\right]\mathcal{R}(E^*, t). \tag{3.7}$$

This dynamics leads to a seascape ensemble, which is characterized by an expected peak divergence

$$\left\langle (E^*(t) - E^*(t+\tau))^2 \right\rangle = 2r^2 E_0^2 \left(1 - \mathrm{e}^{-\tau/\tau_{\mathrm{sat}}(\upsilon, r^2)}\right) \tag{3.8}$$

with the saturation time

$$\tau_{\mathrm{sat}}(\upsilon, r^2) = \frac{r^2}{\upsilon}, \tag{3.9}$$

and by an equilibrium distribution

$$\mathcal{R}_{\mathrm{eq}}(E^*) = \frac{1}{\sqrt{2\pi r^2 E_0^2}} \exp\left[-\frac{1}{2}\frac{(E^* - G)^2}{r^2 E_0^2}\right] \tag{3.10}$$

of optimal trait values. Diffusive seascapes models of this form describe continuous adaptive pressure due to incremental ecological changes that affect the optimal trait value $E^*(t)$. We assume that typical optimal trait values fall into the neutral trait repertoire given by Equation (2.2), which implies that the scaled driving span r^2 is at most of order 1.

2) Punctuated fitness seascapes. This model has discrete, large fitness peak shifts. Individual shifts of the optimal trait value may result from discrete ecological events such as major

migrations and speciations. Lineage-specific shifts in large phylogenies have been studied in references [94, 95, 97]; however, these shifts are assumed to be caused by known external events. Here we introduce a stochastic model to describe a priori unknown shifts. The simplest such model is a Poisson jump process with jump rate $\tau_{\text{sat}}^{-1}(\upsilon, r^2) = \upsilon/r^2$, by which successive values of E^* are drawn independently from the distribution $\mathcal{R}_{\text{eq}}(E^*)$, given by (3.10). Different realizations of this process are shown in Figure 3.1C. The Poisson jump process is described by the evolution equation

$$\frac{\partial}{\partial t}\mathcal{R}(E^*, t) = \frac{\upsilon}{r^2}\left[\mathcal{R}_{\text{eq}}(E^*) - \mathcal{R}(E^*, t)\right]. \tag{3.11}$$

It has the same time-dependent expected peak divergence (3.8) and the same equilibrium distribution (3.10) as the diffusion process (3.7) with same driving parameters (3.6). The difference between the jump process and the diffusion process lies in the anomalous scaling of higher moments,

$$\begin{aligned}\left\langle (E^*(t) - E^*(t+\tau))^k \right\rangle &\sim E_0^k r^{k-2}\upsilon\tau \\ &\quad \text{for } k = 2, 4, \ldots \text{ and } \tau \ll \tau_{\text{sat}}(\upsilon, r^2).\end{aligned} \tag{3.12}$$

This scaling is shared by simple models of turbulence; see, e.g., reference [113].

In both types of fitness seascape, we distinguish two dynamical selection regimes:

- *Macro-evolutionary* fitness seascapes are defined by the condition $\tau_{\text{sat}}(v, r^2) \gtrsim \tau_{\text{eq}}(c)$. As discussed in detail below, such seascapes keep the trait mean always close to equilibrium and induce an adaptive response linear in the driving rate υ. The limit $\upsilon \to 0$ describes an ensemble of *quenched* population-specific fitness *landscapes* with a distribution of optimal trait values given by Equation (3.10); see Figure 3.1D.

- *Micro-evolutionary* fitness seascapes have $\tau_{\text{sat}}(\upsilon, r^2) \lesssim \tau_{\text{eq}}(c)$ and delineate a regime of reduced adaptive response, where the evolution of the trait mean gradually decouples from that of the fitness seascape. In the asymptotic fast-driving regime ($\upsilon \gg r^2/\tau_{\text{eq}}(c)$), the adaptation of the trait is completely suppressed. In this regime, we can average over the fitness fluctuations and describe the macro-evolution of the trait in terms of an effective fitness landscape with an optimal trait value $\mathcal{E}$.

3.2.1 Joint dynamics of trait and selection

We now combine the diffusive dynamics of quantitative traits in a given fitness seascape, which is given by Equations (2.4) and (2.5), and the seascape dynamics (3.7) or (3.11) into a stochastic model of adaptive evolution. The statistical ensemble generated by this model is illustrated in Figure 3.1B–D: Each population evolves in a specific realization of the fitness seascape, which is given by a history of peak values $E^*(t)$. Its trait mean $\Gamma(t)$ follows the moving fitness peak with fluctuations due to mutations and genetic drift. The ensemble of populations contains, in addition, the stochastic differences between realizations of the fitness seascape. The statistics of

this ensemble involves combined averages over both kinds of fluctuations, which are denoted by angular brackets $\langle ... \rangle$.

The population ensemble can be described by a joint distribution of mean and optimum trait values, $Q(\Gamma, E^*, t) = Q(\Gamma, t \,|\, E^*)\mathcal{R}(E^*, t)$. Using Equations (2.4) and (3.7) together with the projection of the fitness seascape,

$$F_1(\Gamma \,|\, E^*) = f^* - \frac{c}{NE_0^2}\langle\Delta\rangle - \frac{c}{E_0^2}\big(\Gamma - E^*\big)^2, \tag{3.13}$$

given by Equations (2.6) and (2.24), we obtain the evolution equation for the joint distribution in a diffusive seascape,

$$\begin{aligned}\frac{\partial}{\partial t}Q(\Gamma, E^*, t) = \Bigg[&\frac{g^{\Gamma\Gamma}}{2N}\frac{\partial^2}{\partial\Gamma^2} - \frac{\partial}{\partial\Gamma}\left(m^\Gamma - g^{\Gamma\Gamma}\frac{2c}{E_0^2}(\Gamma - E^*)\right) \\ &+ \frac{\upsilon}{E_0^2}\frac{\partial^2}{\partial E^{*2}} + \frac{\upsilon}{r^2}\frac{\partial}{\partial E^*}(E^* - G)\Bigg] Q(\Gamma, E^*, t),\end{aligned} \tag{3.14}$$

with $g^{\Gamma\Gamma} = \langle\Delta\rangle$ and $m^\Gamma = -2\mu(\Gamma - \Gamma_0)$. Note that the differential operator in Equation (3.14) is asymmetric: the trait optimum E^* follows an independent stochastic dynamics, but the trait mean Γ is coupled to E^*. This asymmetry reflects the causal relation between selection and adaptive response: the trait mean $\Gamma(t)$ follows the moving fitness peak, as shown in Figure 3.1B,C. As a consequence, the joint evolution equation (3.14) leads to a non-equilibrium stationary distribution $Q_{\rm stat}(\Gamma, E^*)$, although the marginal seascape dynamics (3.7) reaches an equilibrium state. In the fitness landscape limit ($\upsilon \to 0$), the evolution of the trait mean reaches evolutionary equilibrium; in the opposite limit ($\upsilon \to \infty$), this dynamics can be described by an effective equilibrium. In Section 3.3.1, we will obtain explicit solutions for the non-equilibrium distribution $Q_{\rm stat}(\Gamma, E^*)$ and its equilibrium limits. Time-dependent conditional probabilities (propagators) in the stationary ensemble will be discussed in Section 3.3.2 and in Appendix C. The case of a punctuated fitness seascape is also treated in Appendix C, where we solve the Langevin equations for Γ and E^* to obtain the first and second moments of $Q(\Gamma, E^*, t)$.

The trait diversity evolves under the projected fitness function

$$F_2(\Delta \,|\, c) = -\frac{c}{NE_0^2}\,\Delta, \tag{3.15}$$

given by Equations (2.24) and (2.7). In a fitness seascapes with a constant stabilizing strength c, this function is time-independent. The dynamics of the trait diversity (2.5) decouples from the adaptive evolution of the trait mean and leads an evolutionary equilibrium $Q_{\rm eq}(\Delta \,|\, c)$ of the form (2.13). As detailed in Section 3.3.3, the equilibrium assumption for the trait diversity holds for most adaptive processes in a fitness seascape of the form (2.24). However, we can generalize our seascape models to include a time-dependent stabilizing strength $c(t)$. This leads to generic adaptive evolution of both, Γ and Δ, which is described by a coupled non-equilibrium stationary distribution $Q_{\rm stat}(\Gamma, \Delta, E^*, c)$.

3.2.2 Discussion

Figure 3.1 illustrates our model of natural selection: *fitness seascapes* that have a peak moving in trait space on macro-evolutionary timescales. The peak displacement follows a stochastic process that models broad classes of evolutionary change. *Diffusive* seascapes describe continuous changes in the optimal trait value, which are ubiquitously generated by ecological fluctuations. *Punctuated* seascapes capture large-scale changes caused by discrete events, such as speciations or neo-functionalization of genes [114]. Of course, such models are highly idealized representations of biological reality. Their strength lies in their simplicity: minimal seascapes have just two important evolutionary parameters, the stabilizing strength c and the driving rate v, which are defined in Equations (3.4) and (3.6). These parameters can be inferred from data, as we show below in Section 3.5. If this inference results in useful, testable information about real systems, the underlying models can be justified *a posteriori*.

In a diffusive fitness seascape, the diffusion equation (3.14) describes the joint dynamics of mean and optimal trait. However, the role of its two variables are asymmetric: the mean trait follows the fitness peak, but the fitness peak moves in an autonomous way. This asymmetry leads to a non-equilibrium evolutionary dynamics, as discussed in the next section.

3.3 Adaptive evolution in a single-peak fitness seascape

In this section, we develop the key analytical results of this chapter. We provide an explicit solution for the non-equilibrium joint distribution of mean and optimal trait in a diffusive seascape, $Q_{\mathrm{stat}}(\Gamma, E^*)$; the case of punctuated seascapes is treated in Appendix C. These solutions describe a stationary ensembles of adapting populations. We derive an expression for the expected time-dependent trait divergence in these ensembles, which holds for both seascape models. Finally, we juxtapose the adaptive behavior of the trait mean with the equilibrium statistics of the trait diversity, which emerges in good approximation for most fitness seascape of constant stabilizing strength. Our analytical results are supported by simulations for diffusive and punctuated fitness seascapes.

3.3.1 Stationary distribution of mean and optimal trait

In a diffusive fitness seascape, the evolution equation (3.14) has a stationary solution of bivariate Gaussian form,

$$Q_{\mathrm{stat}}(\Gamma, E^*) = \frac{1}{Z} \exp\left[-\frac{1}{2} \begin{pmatrix} \hat{\Gamma} \\ \hat{E}^* \end{pmatrix}^T \mathbf{\Sigma}^{-1} \begin{pmatrix} \hat{\Gamma} \\ \hat{E}^* \end{pmatrix} \right], \tag{3.16}$$

where $\hat{\Gamma} \equiv \Gamma - \langle\Gamma\rangle$ and $\hat{E}^* \equiv E^* - \mathcal{E}$. This distribution is specified by its expectation values

$$\begin{aligned} \begin{pmatrix} \langle\Gamma\rangle \\ \langle E^*\rangle \end{pmatrix} &\equiv \int \mathrm{d}\Gamma \mathrm{d}E^* \begin{pmatrix} \Gamma \\ E^* \end{pmatrix} Q_{\mathrm{stat}}(\Gamma, E^*) \\ &= \begin{pmatrix} w(c)\,\mathcal{E} + (1 - w(c))\,\Gamma_0 \\ \mathcal{E} \end{pmatrix}, \end{aligned} \tag{3.17}$$

and the covariance matrix

$$\begin{aligned} \mathbf{\Sigma} &= \begin{pmatrix} \langle\hat{\Gamma}^2\rangle & \langle\hat{\Gamma}\hat{E}^*\rangle \\ \langle\hat{\Gamma}\hat{E}^*\rangle & \langle\hat{E}^{*2}\rangle \end{pmatrix} \\ &\equiv \int \mathrm{d}\Gamma \mathrm{d}E^* \begin{pmatrix} \hat{\Gamma}^2 & \hat{\Gamma}\hat{E}^* \\ \hat{\Gamma}\hat{E}^* & \hat{E}^{*2} \end{pmatrix} Q_{\mathrm{stat}}(\Gamma, E^*) \\ &= E_0^2 \begin{pmatrix} (1/2c)\,w(c) + r^2 w(c) w(c, \upsilon, r^2) & r^2 w(c, \upsilon, r^2) \\ r^2 w(c, \upsilon, r^2) & r^2 \end{pmatrix}. \end{aligned} \tag{3.18}$$

The distribution $Q_{\mathrm{stat}}(\Gamma, E^*)$ depends on the parameters that characterize the fitness seascape: the stabilizing strength c, the driving rate υ, and the relative driving span r^2, which are defined in Equations (3.4) and (3.6). Together with the effective population size N and the point mutation rate μ, these parameters determine the characteristic timescales of evolution in a fitness seascape, the equilibration time $\tau_{\mathrm{eq}}(c)$ and the saturation time of fitness fluctuations, $\tau_{\mathrm{sat}}(\upsilon, r^2)$; see Equations (3.5) and (3.9). The function

$$w(c, \upsilon, r^2) \equiv \frac{c\langle\delta\rangle}{c\langle\delta\rangle + 2\theta + N\upsilon/r^2} = \frac{\tau_{\mathrm{eq}}^{-1}(c) - \mu}{\tau_{\mathrm{eq}}^{-1}(c) - \mu + \tau_{\mathrm{sat}}^{-1}(\upsilon, r^2)}, \tag{3.19}$$

and its equilibrium limit $w(c) \equiv w(c, \upsilon = 0, r^2)$ govern the coupling between the mean and optimal trait. The mutation rate μ is the inverse of the neutral timescale $\tau_{\mathrm{eq}}(0) = \mu^{-1}$. These functions depend on the scaled diversity $\langle\delta\rangle \equiv \langle\Delta\rangle/E_0^2$, which is given in reference [53], Equations (68) – (73), and is restated below in Equation (3.39). For traits under substantial selection ($c \gtrsim 1$), we can distinguish two dynamical regimes: In macro-evolutionary fitness seascapes, where $\tau_{\mathrm{sat}}(\upsilon, r^2) \gtrsim \tau_{\mathrm{eq}}(c) \approx 2N/(\langle\delta\rangle c)$, this coupling remains close to the equilibrium value $w(c) \approx 1$; micro-evolutionary fitness fluctuations, which have $\tau_{\mathrm{sat}}(\upsilon, r^2) \lesssim \tau_{\mathrm{eq}}(c)$, induce a partial decoupling of mean and optimal trait.

We can also express this crossover in terms of the average square distance between trait mean in the population and optimal trait of the underlying fitness seascape,

$$\langle\Lambda^2\rangle \equiv \int \mathrm{d}\Gamma \mathrm{d}E^* \,(\Gamma - E^*)^2\, Q_{\mathrm{stat}}(\Gamma, E^*). \tag{3.20}$$

The analytical solution for the scaled quantity $\langle\lambda^2\rangle \equiv \langle\Lambda^2\rangle/E_0^2$ follows from Equations (E.13)

and (3.18),

$$\langle\lambda^2\rangle(c,\upsilon,r^2) \simeq \begin{cases} \langle\lambda^2\rangle_{\rm eq}(c,r^2) + \upsilon\tau_{\rm eq}(c)\dfrac{w(c)}{2}\left[1+\mathcal{O}\left(\dfrac{\tau_{\rm eq}}{\tau_{\rm sat}}\right)\right] \\ \qquad\qquad\qquad\qquad \text{(macroevolutionary seascapes)}, \\ \langle\lambda\rangle_{\rm eq}(c,0) + r^2\Big[1-\mathcal{O}\Big(\dfrac{\tau_{\rm sat}}{\tau_{\rm eq}}\Big)\Big], \\ \qquad\qquad\qquad\qquad \text{(microevolutionary seascapes)}, \end{cases} \tag{3.21}$$

where

$$\begin{aligned} \langle\lambda^2\rangle_{\rm eq}(c,r^2) &= \frac{w(c)}{2c} + (\langle\lambda^2\rangle_0 + r^2)(1-w(c))^2 \\ &\simeq \frac{1}{2c} \qquad \text{for } c \gg 1 \end{aligned} \tag{3.22}$$

is the equilibrium average in a fitness landscape. The non-equilibrium contribution reflects the lag between the population and the moving fitness peak. In macro-evolutionary seascapes, this term remains small, which indicates that the trait distribution $\mathcal{W}(E)$ closely follows the displacements of the fitness peak. In micro-evolutionary seascapes, the mean square distance $\langle\lambda^2\rangle$ becomes comparable to the driving span r^2; that is, the population no longer adapts to the moving fitness peak in an efficient way.

The distribution $Q_{\rm stat}(\Gamma,E^*)$ describes a stationary state that is manifestly out of equilibrium, i.e., it does not have detailed balance. Its probability current

$$\begin{aligned} \mathbf{J}_{\rm stat}(\Gamma,E^*) &= -\begin{pmatrix} \dfrac{g^{\Gamma\Gamma}}{2N}\dfrac{\partial}{\partial\Gamma} - m^\Gamma + g^{\Gamma\Gamma}\dfrac{2c}{NE_0^2}(\Gamma-E^*) \\ \upsilon E_0^2\dfrac{\partial}{\partial E^*} + \dfrac{\upsilon}{r^2}(E^*-G) \end{pmatrix} Q_{\rm stat}(\Gamma,E^*) \\ &\simeq \begin{cases} \left[-2\upsilon c\begin{pmatrix} \hat\Gamma - \hat E^*(1+1/(2cr^2)) \\ (\hat\Gamma - \hat E^*) \end{pmatrix}\left(1+\mathcal{O}\left(\dfrac{\tau_{\rm eq}}{\tau_{\rm sat}}\right)\right)\right] Q_{\rm stat}(\Gamma,E^*) \\ \qquad\qquad \text{(macroevolutionary seascapes)}, \\ \left[\dfrac{c\langle\delta\rangle}{N}\begin{pmatrix} \hat E^* \\ -2cr^2\hat\Gamma \end{pmatrix}\Big(1-\mathcal{O}\Big(\dfrac{\tau_{\rm sat}}{\tau_{\rm eq}}\Big)\Big)\right] Q_{\rm stat}(\Gamma,E^*) \\ \qquad\qquad \text{(microevolutionary seascapes)}, \end{cases} \end{aligned} \tag{3.23}$$

expresses the adaptive motion of the trait mean following the displacements of the fitness peak. The probability current shows a crossover similar to the adaptive part of $\langle\Lambda^2\rangle$ in (3.21): it increases linearly for low driving rates and saturates to a constant in the regime of micro-evolutionary fitness fluctuations.

Remarkably, the joint statistics of mean and optimal trait can be associated with evolutionary equilibrium in the limits of low and high driving rates. In the first case, we obtain the equilibrium

distribution

$$\begin{aligned} Q_{\rm eq}(\Gamma, E^*) &= \lim_{\upsilon\to 0} Q_{\rm stat}(\Gamma, E^*) \\ &= \tilde{Q}_0(\Gamma)\, \exp[2NF_1(\Gamma|E^*)]\, \mathcal{R}(E^*) \\ &= \frac{1}{Z_\Gamma\sqrt{2\pi r^2 E_0^2}} \exp\left[-\frac{2\theta}{\langle\Delta\rangle}(\Gamma-\Gamma_0)^2 - \frac{c}{E_0^2}(\Gamma-E^*)^2 - \frac{1}{2r^2E_0^2}(E^*-\mathcal{E})^2\right], \end{aligned} \tag{3.24}$$

which is the product of a Boltzmann distribution (2.12) and a *quenched* weight of the trait optimum E^* given by (3.10). This distribution satisfies detailed balance; that is, the probability current $\mathbf{J}_{\rm stat}(\Gamma, E^*)$ vanishes in the limit $\upsilon \to 0$. In the opposite limit, we obtain the distribution

$$\begin{aligned} Q_\infty(\Gamma, E^*) &= \lim_{\upsilon\to \infty} Q_{\rm stat}(\Gamma, E^*) \\ &= \tilde{Q}_0(\Gamma)\, \exp[2NF_1(\Gamma|\mathcal{E})]\, \mathcal{R}(E^*) \\ &= \frac{1}{Z_\Gamma\sqrt{2\pi r^2 E_0^2}} \exp\left[-\frac{2\theta}{\langle\Delta\rangle}(\Gamma-\Gamma_0)^2 - \frac{c}{E_0^2}(\Gamma-\mathcal{E})^2 - \frac{1}{2r^2E_0^2}(E^*-\mathcal{E})^2\right]. \end{aligned} \tag{3.25}$$

In this limit, the fast fluctuations of the fitness peak — and the associated current $\mathbf{J}_{\rm stat}(\Gamma, E^*)$ given by (3.23) — decouple from the macro-evolutionary dynamics of the mean trait. The latter is governed by the effective fitness landscape

$$F_1(\Gamma|\mathcal{E}) = \int F_1(\Gamma|E^*)\, \mathcal{R}(E^*)\, dE^*, \tag{3.26}$$

which is obtained by averaging over the ensemble (3.10) of fitness peak positions and it describes stabilizing selection towards the average peak position $\mathcal{E}$. Accordingly, the scaled average square distance $\langle\lambda^2\rangle$, as given by Equation (3.21), is the sum of the equilibrium variance $\langle\lambda^2\rangle_{\rm eq}(c, 0)$ and the driving span r^2. We can extend the notion of an effective fitness landscape to micro-evolutionary seascapes with a large but finite driving rate ($c \gg 1$, $\upsilon \gg r^2/\tau_{\rm eq}(c)$). Such seascape models still generate stabilizing selection on the trait mean towards the mean peak position $\mathcal{E}$, but with a reduced effective stabilizing strength

$$c_{\rm eff} \approx c\left[1 - \frac{2c^2r^2\tau_{\rm sat}(\upsilon, r^2)}{\tau_{\rm eq}(c)}\right]. \tag{3.27}$$

Similar effective landscapes resulting from micro-evolutionary seascapes have been observed in phenomenological models [115].

As shown in Appendix C, the dynamics of the trait in a punctuated seascape leads to a stationary population ensemble that has the same first and second moments as in the case of a diffusive seascape. In particular, the average square displacement between mean and optimal trait, Equation (3.21), as well as the averages of divergence, genetic load, and fitness flux described in the following sections coincide for both kinds of seascapes.

The properties of the stationary ensemble of mean and optimal trait in a fitness seascape

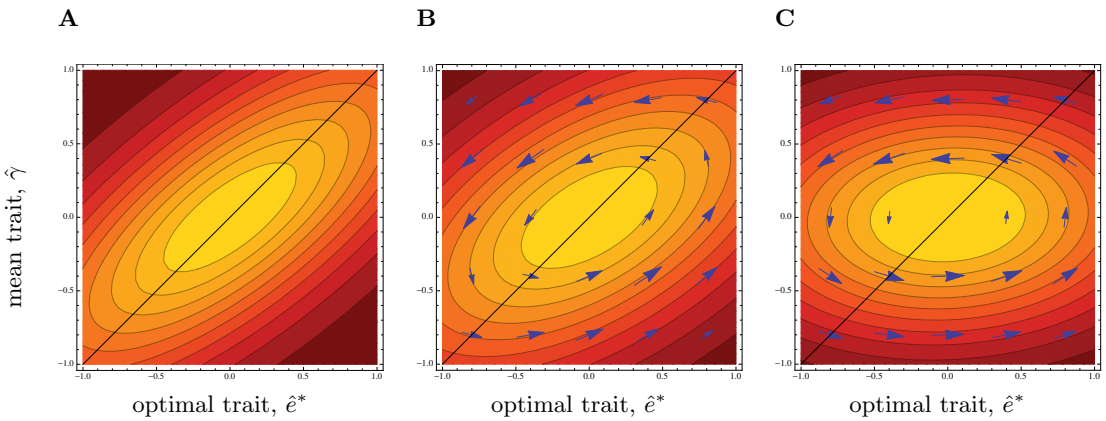

Figure 3.2. Stationary distribution of mean and optimal trait in a fitness seascape. The distribution $Q_{\rm stat}(\Gamma, E^*)$ is shown **A** in the equilibrium limit ($c = 1$, $\upsilon = 0$, $r^2 = 1$), **B** for an intermediate driving rate ($\upsilon = 1.5r^2/\tau_{\rm eq}$), and **C** in the deep micro-evolutionary regime ($\upsilon = 50r^2/\tau_{\rm eq}$); see Equations (3.16), (3.24), and (3.25). The probability current $\mathbf{J}(\Gamma, E^*)$, which is given by Equation (3.23), is marked by arrows. With increasing driving rate, the correlation between Γ and E^* is seen to decrease.

are summarized in Figures. 3.2 and 3.3. The stationary distribution $Q_{\rm stat}(\Gamma, E^*)$ is shown in Figure 3.2 for given parameters c, r^2, and for different values of the driving rate: in the equilibrium limit ($\upsilon \to 0$), for an intermediate value of υ, and in the fast-driving regime ($\upsilon \gg r^2/\tau_{\rm eq}(c)$). The non-equilibrium probability current $\mathbf{J}_{\rm stat}(\Gamma, E^*)$ is marked by arrows. The crossover between micro- and macro-evolutionary fitness seascapes is plotted in Figure 3.3 for the scaled average square distance $\langle \lambda^2 \rangle$ as a function of the driving rate υ. Our analytical results are tested by numerical simulations of the underlying Fisher-Wright process [116] in a fitness seascape (2.24) with diffusive and punctuated peak displacements. The details of the numerical methods for the population simulations are discussed in Appendix A.

3.3.2 Time-dependent trait divergence

In the previous work [53], it was shown that the variance of the trait mean across populations, $\langle \hat{\Gamma}^2 \rangle$, and the average trait diversity $\langle \Delta \rangle$ uniquely characterize the stabilizing strength c in a fitness landscape. The ensemble variance $\langle \hat{\Gamma}^2 \rangle$ is just the half of the asymptotic trait divergence $\lim_{\tau\to\infty} \langle D(\tau) \rangle \equiv \lim_{\tau\to\infty} \langle (\Gamma(t+\tau) - \Gamma(t))^2 \rangle$. As it is clear from the previous subsection, the stationary distribution $Q_{\rm stat}(\Gamma)$ and its statistics is compatible with different values of the seascape parameters and, hence, cannot uniquely characterize them. Instead, we use the time-dependent statistics of the stationary ensemble to infer the parameters of the fitness seascape. A fundamental time-dependent observable is the joint propagator $G_\tau(\Gamma, E^* \,|\, \Gamma_a, E_a^*)$, which denotes the conditional probability for mean and optimal trait values Γ, E^* at time t, given the values Γ_a, E_a^* at time t_a; this function is analytically calculated in Appendix C. The resulting marginal propagator $G_\tau(\Gamma |\, \Gamma_a)$ serves as building block for the probabilistic analysis of individual evolutionary trajectories of cross-species trait data, which is discussed in a follow-up paper [3] and briefly reported in Section 3.6. Here we use the joint propagator to compute the time-dependent trait divergence between populations in one and two lineages, $\langle D^{(\kappa)} \rangle(\tau)$ ($\kappa = 1, 2$), as defined

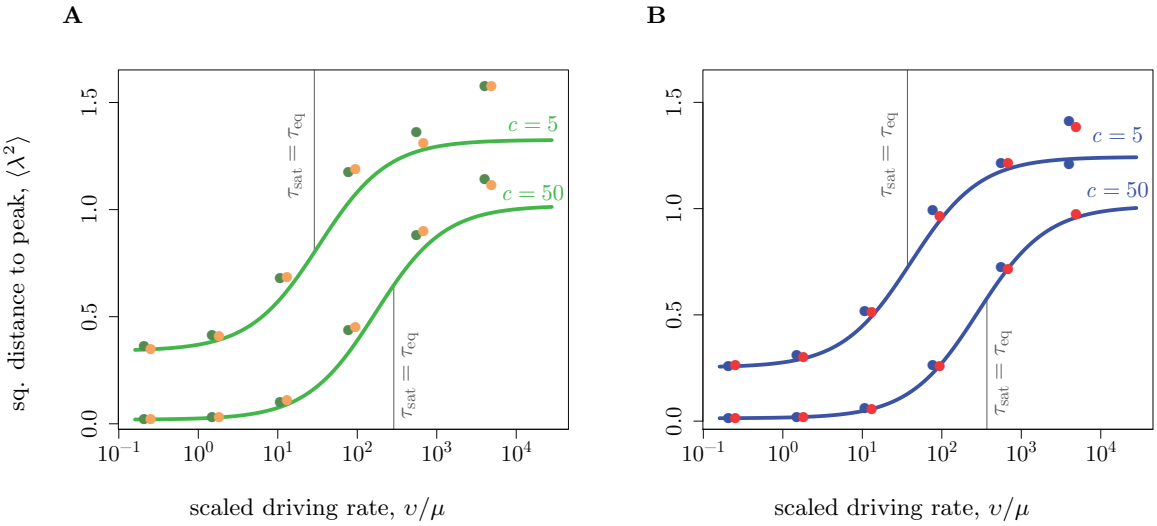

Figure 3.3. Adaptive lag between mean and optimal trait. The scaled average square distance $\langle\lambda^2\rangle$ is plotted against the scaled driving rate υ/μ for **A** non-recombining and **B** fully recombining populations for different stabilizing strengths c. The other parameters are $r^2 = 1$, $\theta = 0.0125$. This function increases from an equilibrium value for $\upsilon = 0$ to a micro-evolutionary limit value for $\upsilon \to \infty$ with a crossover for $\tau_{\rm sat}(\upsilon, r^2) \sim \tau_{\rm eq}(c)$, as given by Equation (3.21). The analytical results (lines) are compared to simulation results (with parameters $N = 100, \ell = 100$) for a diffusive seascape (green and blue dots) and for a punctuated seascape (orange and red dots).

in Equations (3.1) and (3.2). The average divergence between an ancestral and a descendent population in a single lineage can be written as an expectation value in the stationary ensemble,

$$\begin{aligned}
\langle D^{(1)}\rangle(\tau) &\equiv \langle(\Gamma(t) - \Gamma(t_a))^2\rangle \\
&\equiv \int \mathrm{d}\Gamma\, \mathrm{d}\Gamma_a\, (\Gamma - \Gamma_a)^2 \times \left(\right. \\
&= \int \mathrm{d}E_a^*\, \mathrm{d}E^*\, \mathrm{d}\Gamma_a\, \mathrm{d}\Gamma\, (\Gamma - \Gamma_a)^2\, G_\tau(\Gamma, E^* \,|\, \Gamma_a, E_a^*)\, Q_{\rm stat}(\Gamma_a, E_a^*),
\end{aligned} \tag{3.28}$$

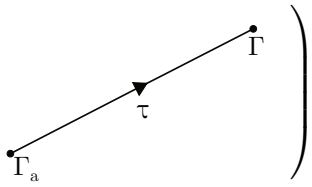

where $\Gamma_a \equiv \Gamma(t_a)$, $\Gamma \equiv \Gamma(t)$, $E_a^* \equiv E^*(t_a)$, $E^* \equiv E^*(t)$, and $\tau = t - t_a$. In a similar way, the average divergence between two descendent populations evolved from a common ancestor

population is given by

$$\begin{aligned}
\langle D^{(2)}\rangle(\tau) &\equiv \langle(\Gamma_1(t)-\Gamma_2(t))^2\rangle_{\substack{\Gamma_1(t_a)=\Gamma_2(t_a)\\ E_1^*(t_a)=E_2^*(t_a)}} \\
&\equiv \int \mathrm{d}\Gamma_a\,\mathrm{d}\Gamma_1\,\mathrm{d}\Gamma_2\,(\Gamma_1-\Gamma_2)^2\,\times \left(\quad\right) \\
&= \int \mathrm{d}E_a^*\,\mathrm{d}E_1^*\,\mathrm{d}E_2^*\,\mathrm{d}\Gamma_a\,\mathrm{d}\Gamma_1\,\mathrm{d}\Gamma_2\,(\Gamma_1-\Gamma_2)^2\,G_{\tau/2}(\Gamma_1,E_1^*\,|\,\Gamma_a,E_a^*) \\
&\qquad \times G_{\tau/2}(\Gamma_2,E_2^*\,|\,\Gamma_a,E_a^*)\,Q_{\mathrm{stat}}(\Gamma_a,E_a^*),
\end{aligned} \tag{3.29}$$

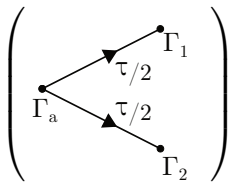

where $\Gamma_a \equiv \Gamma_1(t_a) = \Gamma_2(t_a)$, $E_a^* \equiv E_1^*(t_a) = E_2^*(t_a)$, $\Gamma_i \equiv \Gamma_i(t)$, $E_i^* \equiv E_i^*(t)$ $(i = 1, 2)$, and $\tau \equiv 2(t - t_a)$. The resulting scaled divergences $\langle d^{(\kappa)}\rangle(\tau) \equiv \langle D^{(\kappa)}\rangle(\tau)/E_0^2$ $(\kappa = 1, 2)$ can be calculated using the results of Appendix C. We obtain

$$\begin{aligned}
\langle d^{(\kappa)}\rangle(\tau;c,\upsilon,r^2) &= \frac{\tau_{\mathrm{eq}}(c)}{\tilde{\tau}(c)}\Big[1-e^{-\tau/\tau_{\mathrm{eq}}(c)}\Big] \\
&+ \upsilon\,w(c,\upsilon,r^2)w(c,-\upsilon,r^2)\left[\tau_{\mathrm{sat}}(\upsilon,r^2)\big(1-\mathrm{e}^{-\tau/\tau_{\mathrm{sat}}(\upsilon,r^2)}\big)-\tau_{\mathrm{eq}}(c)\left(1-\mathrm{e}^{-\tau/\tau_{\mathrm{eq}}(c)}\right)\right] \\
&- 2(\kappa-1)\frac{\upsilon}{\tau_{\mathrm{eq}}^{-1}(c)+\tau_{\mathrm{sat}}^{-1}(\upsilon,r^2)}\,w(c,-\upsilon,r^2)^2\left[\mathrm{e}^{-\tau/(2\tau_{\mathrm{sat}}(\upsilon,r^2))}-\mathrm{e}^{-\tau/(2\tau_{\mathrm{eq}}(c))}\right]^2,
\end{aligned} \tag{3.30}$$

where the equilibration time $\tau_{\mathrm{eq}}(c)$, the saturation time $\tau_{\mathrm{sat}}(\upsilon, r^2)$, and the coupling factor $w(c, \upsilon, r^2)$ are given by equations (3.5), (3.9), and (3.19). The difference between the two divergence measures is a consequence of the non-equilibrium adaptive dynamics, which violate detailed balance. Equation (3.30) is valid for diffusive and for punctuated fitness seascapes. It contains the three characteristic timescales defined in the previous section: the *drift time* $\tilde{\tau}(c)$ is the scale over which the diffusion of the trait mean, in the absence of any fitness seascape, generates a trait divergence of the order of the neutral trait span E_0^2; the *equilibration time* $\tau_{\mathrm{eq}}(c)$ governs the relaxation of the population ensemble to a mutation-selection-drift equilibrium in a fitness landscape of stabilizing strength c; the *saturation time* $\tau_{\mathrm{sat}}(\upsilon, r^2)$ is defined by the mean square displacement of the fitness peak reaching the driving span r^2. Here, we focus on fitness seascapes with substantial stabilizing strength and with a driving span of order of the neutral trait span ($c \gtrsim 1$, $r^2 \sim 1$). This selection scenario is biologically relevant: it describes adaptive processes that build up large trait differences by continuous diffusion or recurrent jumps of the fitness peak.

In macro-evolutionary seascapes, the equilibration time and the non-equilibrium saturation time are well-separated, $\tau_{\mathrm{eq}}(c) \ll \tau_{\mathrm{sat}}(\upsilon, r^2)$. This results in three temporal regimes of the trait divergence:

1. *Quasi-neutral regime,* $\tau \lesssim \tau_{\rm eq}(c)$. The scaled divergence takes the form

$$\langle d^{(\kappa)} \rangle(\tau) = 2\langle \hat{\gamma}^2 \rangle_{\rm eq} \left(1 - e^{-\tau/\tau_{\rm eq}}\right) \tag{3.31}$$

$$\simeq \frac{\langle \delta \rangle}{N} \tau \left(1 + O(\tau/\tau_{\rm eq})\right) \qquad (\kappa = 1, 2) \tag{3.32}$$

with $\tau_{\rm eq}(c)$ given by Equation (3.5). Its linear initial increase is caused by phenotypic diffusion with the quasi-neutral diffusion constant $\Delta/(2N)$, as given by Equations (2.4) and (2.9). This diffusion, in turn, is generated by genetic drift and mutations at the trait loci, which evolve under linkage disequilibrium imposed by stabilizing selection on the trait diversity Δ, as discussed in reference [53] and section 3.3.3. The quasi-neutral increase of the divergence is bounded by stabilizing selection acting directly on the trait mean; this force becomes important for divergence times of order $\tau_{\rm eq}(c)$. In the absence of directional selection, it generates a constrained equilibrium divergence

$$2\langle \hat{\gamma}^2 \rangle_{\rm eq}(c) = \frac{w(c)}{c}. \tag{3.33}$$

The quasi-neutral regime (3.32) should be compared with genuinely neutral trait evolution,

$$\langle d^{(\kappa)} \rangle_0(\tau) = \frac{\langle \delta \rangle_0}{\mu N} \left(1 - e^{-\mu\tau}\right), \tag{3.34}$$

which follows from Equation (3.31) in the limit $c = 0$. The neutral asymptotic behavior for short divergence times reduces to a well-known result of classical quantitative genetics [51, 117, 118], $\langle D^{(\kappa)} \rangle_0 = 2V_m(\tau/2)$ with $V_m = \langle \Delta \rangle_0 / N \approx 4\mu E_0^2$. The saturation for divergence times of order $1/\mu$ follows the saturation of the genetic divergence at the ℓ constitutive loci.

2. *Adaptive regime,* $\tau_{\rm eq}(c) \lesssim \tau \ll \tau_{\rm sat}(v, r^2)$. The scaled trait divergence follows

$$\langle d^{(\kappa)} \rangle(\tau) = \left[2\langle \hat{\gamma}^2 \rangle_{\rm eq} \left(1 - \upsilon\, \tilde{\tau}\, \kappa\, w(c)^2\right) + \upsilon\, w(c)^2\, \tau\right] \left[1 + O\left(e^{-\tau/\tau_{\rm eq}}, \tau/\tau_{\rm sat}\right)\right]$$

$$\simeq \left[2\langle \hat{\gamma}^2 \rangle_{\rm eq} + \upsilon\, (\tau - \kappa\tau_{\rm eq}(c))\right] \times \left[1 + O\left((\theta c)^2, e^{-\tau/\tau_{\rm eq}}, \tau/\tau_{\rm sat}\right)\right] \qquad (\kappa = 1, 2) \tag{3.35}$$

In this regime, the trait divergence is the sum of an (asymptotically constant) equilibrium component and an adaptive component, which increases with slope υ. In a macroevolutionary fitness seascape, this slope is, by definition, smaller than the slope in the initial quasi-neutral (3.32), which allows for a clear delineation of the two regimes in empirical data. This feature will be exploited in our selection test for quantitative traits, which will be discussed in Section 3.5.

3. *Saturation regime,* $\tau \gtrsim \tau_{\rm sat}(\upsilon, r^2)$. On the largest timescales, the divergence

$$\langle d^{(\kappa)} \rangle(\tau) \approx 2\langle \hat{\gamma}^2 \rangle_{\rm eq} + 2r^2 w(c) w(c, \upsilon, r^2) \big(1 - e^{-\tau/\tau_{\rm sat}}\big) \qquad (\kappa = 1, 2) \tag{3.36}$$

approaches its non-equilibrium saturation value

$$\langle \hat{\gamma}^2 \rangle_{\rm stat}(c, \upsilon, r^2) = 2\langle \hat{\gamma}^2 \rangle_{\rm eq} + 2r^2 w(c) w(c, \upsilon, r^2), \tag{3.37}$$

which equals the Γ-variance of the stationary distribution $Q_{\rm stat}(\Gamma, E^*)$, and is primarily determined by the driving span r^2. In empirical data, this regime is often well beyond the depth of the phylogeny and, hence, not observable.

In micro-evolutionary seascapes, the saturation of fitness fluctuations occurs faster than the equilibration of the trait under stabilizing selection, i.e., $\tau_{\rm sat}(\upsilon, r^2) \lesssim \tau_{\rm eq}(c)$. Hence, there is a direct crossover from the quasi-neutral to the saturation regime. For fast micro-evolutionary fitness fluctuations, $\tau_{\rm sat}(\upsilon, r^2) \ll \tau_{\rm eq}(c)$, the constraint on the trait equals that in an effective fitness landscape with stabilizing strength $c_{\rm eff}$ given by Equation (3.27). In this regime, time-dependent trait divergence data alone can no longer resolve adaptive evolution in a fitness seascape from equilibrium in the corresponding effective fitness landscape; this requires additional information on the trait diversity.

Figure 3.4 and Figure C.1A show the scaled divergence $\langle d^{(1)} \rangle(\tau)$ for selection parameters c and υ covering macro-evolutionary and micro-evolutionary fitness seascapes. The analytical expression of Equation (3.30) is seen to be in good agreement with numerical simulations for diffusive and punctuated fitness fluctuations.

3.3.3 Stationary trait diversity

As discussed in Section 3.2, our diffusion theory predicts that the movements of the optimum trait in a single-peak fitness seascape of the form (2.24) only affects the evolution of the trait mean in the population and not the trait diversity. The statistics of the trait diversity remains similar to the case of evolution under stabilizing selection, which is characterized by a time-invariant fitness function, $F_2(\Delta) = -c_0\,\Delta$. The resulting equilibrium distribution $Q_{\rm eq}(\Delta)$ is the product of the neutral mutation-drift equilibrium $Q_0(\Delta)$, which is given in Equations (53) and (55) of [53] and a Boltzmann factor from the scaled fitness landscape, $Q_{\rm eq}(\Delta) = Q_0(\Delta)\,\exp[-c_0\,\Delta]$. These distributions determine the average diversity

$$\langle \Delta \rangle \equiv \int \mathrm{d}\Delta\, \Delta\, Q_{\rm eq}(\Delta) \tag{3.38}$$

and its neutral counterpart $\langle \Delta \rangle_0$, as well as the scaled expectation values $\langle \delta \rangle \equiv \langle \Delta \rangle / E_0^2$ and $\langle \delta \rangle_0 \equiv \langle \Delta \rangle_0 / E_0^2$. The selective constraint on the trait diversity enters the diffusion coefficient of the trait mean in Equation (2.4), which sets the drift timescale $\tilde{\tau}(c) = (1/2\mu)(\langle \delta \rangle_0 / \langle \delta \rangle(c))$, as given by Equation (2.11). The distributions $Q_0(\Delta)$ and $Q_{\rm eq}(\Delta)$ can be written in closed analytical form; unlike in the case of the trait mean, these distributions depend directly on the

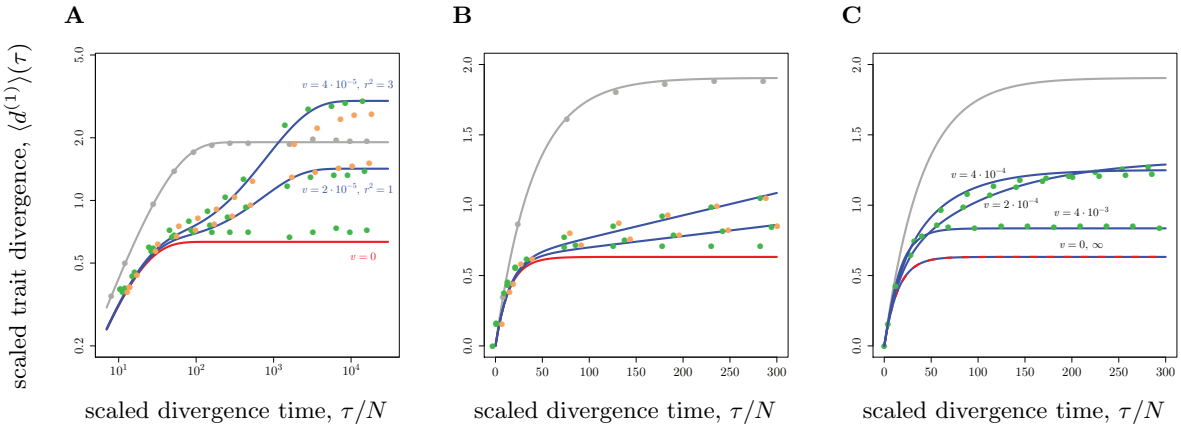

Figure 3.4. Time-dependence of the trait divergence. The scaled average divergence $\langle d^{(1)}\rangle(\tau)$ is shown as a function of the scaled divergence time τ/N for three cases: neutral evolution ($c = 0$; grey lines), conservation in a static fitness landscape ($c = 1$, $\upsilon = 0$; red line), and adaptation in a macro-evolutionary fitness seascape ($c = 1$, $\upsilon > 0$; blue lines). Other parameters: $\theta = 0.0125$, $N = 100$, $\ell = 100$, $\mathcal{E} = 0.7\ell$. The analytical results of Equation (3.30) (lines) are compared to simulation results for asexual evolution in diffusive and punctuated fitness seascapes (green and orange dots, respectively). The corresponding results for fully recombining genomes are shown in Appendix Figure C.1. **A** Logarithmic plot and **B** linear plot for macro-evolutionary seascapes, $\tau_{\rm sat}(\upsilon, r^2) > \tau_{\rm eq}(c)$. These plots show three evolutionary regimes: For $\tau \lesssim \tau_{\rm eq}$, the trait evolution is dominated by genetic drift and mutations. For $\tau \gtrsim \tau_{\rm eq}$, the seascape data show an adaptive divergence component proportional to $\upsilon\tau$; the landscape data saturate to an equilibrium divergence set by stabilizing selection. For $\tau \sim \tau_{\rm sat}$, the seascape data saturate to a non-equilibrium asymptotic value of twice the driving span r^2. **C** Micro-evolutionary seascapes $\tau_{\rm sat}(\upsilon, r^2) < \tau_{\rm eq}(c)$. There is a single cross-over from the quasi-neutral regime for smaller values of τ to the saturation regime for larger values of τ. The divergence $\langle d^{(1)}\rangle(\tau)$ equals that in an effective fitness landscape of stabilizing strength $c_{\rm eff} < c$. The limit $\upsilon \to \infty$ has $c_{\rm eff} = c$; i.e., the function $\langle d^{(1)}\rangle(\tau)$ becomes identical to the case $\upsilon = 0$ (blue–red dashed line).

rate of recombination in the population [53]. We obtain the scaled neutral expectation value $\langle\delta\rangle_0 = 4\theta(1 - 4\theta + O(\theta^2))$, which is independent of the recombination rate, and the selective constraint

$$\frac{\langle\delta\rangle(c)}{\langle\delta\rangle_0} = \begin{cases} 1 - 4\theta c + \mathcal{O}((\theta c)^2) & \text{for } \theta c \ll 1, \\ (4\theta c)^{-1/2} + \mathcal{O}((\theta c)^{-1}) & \text{for } \theta c \gg 1 \end{cases} \tag{3.39}$$

in non-recombining populations. We note that this constraint depends only on the product θc; therefore, it remains weak over a wide range of parameters ($c \lesssim 1/\theta$), which includes strong selection effects on the trait mean [53]. The full crossover function and the corresponding expressions for fully recombining populations are given in Equations (68) – (73) of reference [53].

The numerical simulations reported in Figure 3.5 show that the average diversity in diffusive and punctuated fitness seascapes is well represented by the equilibrium value throughout the crossover from macro- to micro-evolutionary driving rates, and over a wide range of stabilizing strengths. Theoretically, the results of the diffusion theory are valid for adaptive processes unless recurrent selective sweeps reduce the trait diversity within the population. Such sweeps are more prominent in punctuated fitness seascapes due to sudden changes of the trait optimum. We expect a significant reduction in trait diversity due to the large and frequent jumps of the trait optimum in punctuated fitness seascapes with very strong stabilizing selection. This regime is beyond the scope of this chapter.

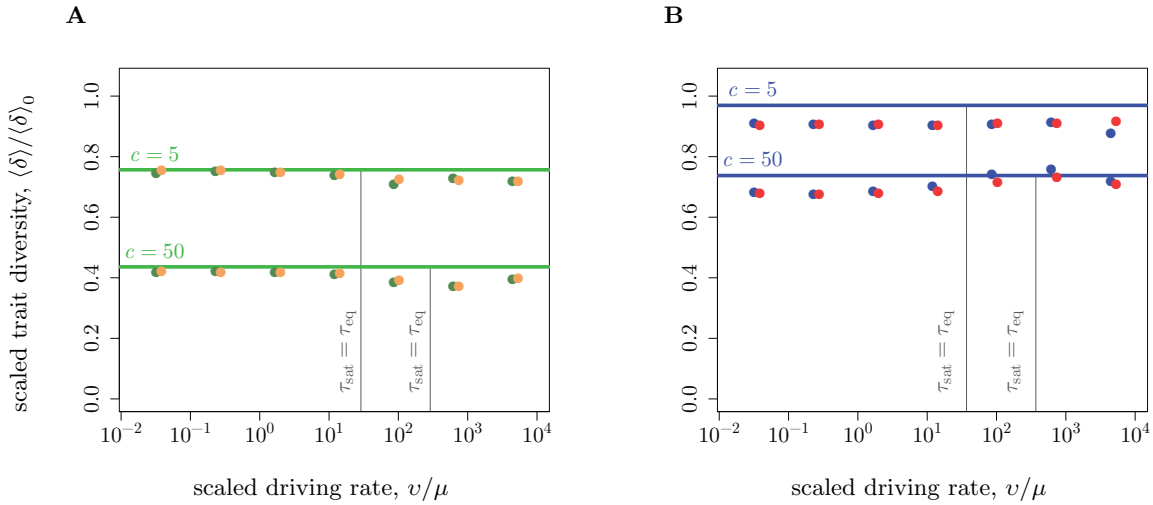

Figure 3.5. Equilibrium trait diversity. The figure shows the average trait diversity $\langle\delta\rangle$ (in units of the neutral average $\langle\delta\rangle_0$) in a fitness seascape as a function of the scaled driving rate v/μ for different values of the stabilizing strength ($c = 5, 50$, top to bottom); other parameters are as in Figure 3.4. The equilibrium predictions of diffusion theory (lines), which do not depend on v, are compared to simulation results of the adaptive process of **A** non-recombining and **B** fully recombining populations in diffusive (green/orange dots) and punctuated seascapes (blue/red dots). The simulation results confirm evolutionary equilibrium of the trait diversity.

3.3.4 Discussion

In this section, we have derived an explicit expression for the joint distribution of mean and optimal trait, $Q_{\rm stat}(\Gamma, E^*)$, in a diffusive fitness seascape; the first and second moments of this distribution remain the same for punctuated fitness fluctuations. Importantly, the distribution $Q_{\rm stat}(\Gamma, E^*)$ results from a genuine non-equilibrium dynamics. Mathematically, it is distinguished from evolutionary equilibrium by a non-vanishing probability current, which is shown in Figure 3.2. Biologically, the deviation from equilibrium reflects the lag of a population that follows a moving fitness peak. This lag can be measured by an increased distance between mean and optimal trait, as shown in Figure 3.3.

The non-equilibrium calculus also produces an analytic expression for the average time-dependent trait divergence between populations, $\langle D\rangle(\tau)$, which will play a key role in the inference of selection discussed below. In a macro-evolutionary fitness landscape, this function displays two important regimes, which are shown in Figure 3.4B. In the *quasineutral regime*, which occurs for short divergence times, $\langle D\rangle$ grows linearly with τ at a rate proportional to the average trait diversity $\langle\Delta\rangle$, as given by Equation (3.32). This resembles the well-known short-time behavior for neutral evolution [51, 117, 118]; however, the diversity is reduced by stabilizing selection. In the *adaptive regime*, which occurs for larger divergence times, the function $\langle D\rangle(\tau)$ depends on both stabilizing and directional selection acting directly on the trait mean, as shown in Equation (3.35). This separation of regimes is characteristic of quantitative traits. For genome evolution, negative and positive selection set nucleotide substitution rates, which affect the divergence to first order in time.

Finally, the trait diversity in a minimal seascape remains at an approximate equilibrium over a wide range of evolutionary parameters, as shown in Figure 3.5. This feature reflects the

properties of the moving fitness peak, which changes its position but retains its width. It is another difference to genome evolution, where selective sweeps can drastically deplete sequence diversity.

3.4 Fitness and entropy of adaptive processes

The distributions of the trait mean and diversity determine the fitness statistics of an ensemble of populations in the stationary state. These statistics can quantify the cost and the amount of adaption for the evolution of molecular traits. We also evaluate the predictability of the trait evolution in an ensemble of populations after diverging from a common ancestral population.

3.4.1 Genetic load

The genetic load of an individual population is defined as the difference between the maximum fitness and the mean fitness [119–122],

$$\mathcal{L}(t) \equiv f^* - \overline{f}(t). \tag{3.40}$$

For a quantitative trait in a quadratic fitness seascape of the form (2.24), we can decompose the load into contributions of the trait mean and diversity,

$$\mathcal{L}(t) = f^* - c_0\big(\Gamma(t) - E^*(t)\big)^2 - 2c_0\Delta(t). \tag{3.41}$$

In the stationary population ensemble (3.16), the average scaled genetic load can be written as the sum of an equilibrium and an adaptive component,

$$\begin{aligned} \langle 2N\mathcal{L}\rangle(c,\upsilon,r^2) &= c\big[\langle\lambda^2\rangle(c,\upsilon,r^2) + \langle\delta\rangle(c)\big] \\ &= c\big[\langle\lambda^2\rangle_{\mathrm{eq}}(c,r^2) + \langle\delta\rangle(c)\big] + c\big[\langle\lambda^2\rangle(c,\upsilon,r^2) - \langle\lambda^2\rangle_{\mathrm{eq}}(c,r^2)\big] \\ &\equiv 2N\mathcal{L}_{\mathrm{eq}}(c,r^2) + 2N\mathcal{L}_{\mathrm{ad}}(c,\upsilon,r^2); \end{aligned} \tag{3.42}$$

these components can be computed analytically from Equations (3.21) and (3.22). A simple form is obtained for fitness seascapes of substantial stabilizing strength ($c \gtrsim 1$),

$$2N\mathcal{L}_{\mathrm{eq}} \simeq \frac{1}{2} + \mathcal{O}(1/c, \theta c), \tag{3.43}$$

$$2N\mathcal{L}_{\mathrm{ad}}(c,\upsilon,r^2) \simeq \begin{cases} \upsilon\,\tilde{\tau}(c)\left[1 + \mathcal{O}\left(\dfrac{\tau_{\mathrm{eq}}}{\tau_{\mathrm{sat}}}\right)\right], & \text{(macroevolutionary seascapes)} \\ cr^2\Big[1 - \mathcal{O}\Big(\dfrac{\tau_{\mathrm{sat}}}{\tau_{\mathrm{eq}}}\Big)\Big], & \text{(microevolutionary seascapes),} \end{cases} \tag{3.44}$$

where the drift scale $\tilde{\tau}(c)$ is given by Equations (2.11) and (3.39). From these expressions, we read off three relevant properties of the genetic load.

First, the equilibrium load depends on c only via its diversity component; this dependence remains weak even for substantial stabilizing selection ($1 \lesssim c \lesssim 1/\theta$). The equilibrium load component related to the trait mean, $c\langle\lambda^2\rangle_{\mathrm{eq}}(c)$, becomes universal in this regime: the fluctuations of Γ are constrained to a fitness range of order $2N\mathcal{L}_{\mathrm{eq}} \simeq 1/2$ around E^*, irrespectively of the stabilizing strength and the molecular details of the trait [2]. This universality extends to simple nonlinearities in the genotype-phenotype map (2.1). For a d-component trait as in Fisher's geometrical model [31], the load formula generalizes to $2N\mathcal{L}_{\mathrm{eq}} \simeq d/2$ (similar results have previously been reported in references [123–125]). This is a direct evolutionary analogue of the equipartition theorem in statistical thermodynamics, which states that every degree of freedom that enters the energy function quadratically contributes an average of $k_BT/2$ to the total energy of a system at temperature T (the proportionality factor k_B is Boltzmann's constant) [2].

Second, the adaptive load component depends only weakly on c, via the drift scale $\tilde{\tau}(c)$. At a fixed value of Γ, the stochastic displacement of the fitness peak induces a fitness cost proportional to c; however, this effect is largely offset by an adaptive response that becomes faster with increasing c.

Third, the different regimes of adaptive trait evolution can be characterized in terms of the genetic load. The adaptive load is asymptotically linear in the driving rate and is subleading to the equilibrium load in the slow-driving regime ($v \lesssim \tilde{v}(c) \equiv 1/\tilde{\tau}(c)$). It becomes dominant for faster driving ($v \gtrsim \tilde{v}(c)$) and saturates in the micro-evolutionary regime ($v \gtrsim r^2/\tau_{\mathrm{eq}}(c)$). Figure 3.6A shows this dependence of the adaptive load on the driving rate.

3.4.2 Fitness flux

The fitness flux, $\phi(t)$, characterizes the adaptive response of a population evolving in a fitness land- or seascape,

$$\phi(t) = \int \mathrm{d}E\, f(E,t)\, \frac{\partial}{\partial t}\mathcal{W}(E,t). \tag{3.45}$$

The cumulative fitness flux, $\Phi(\tau) = \int_t^{t+\tau} \phi(t')\mathrm{d}t'$, measures the total amount of adaptation over an evolutionary period τ [19]. The evolutionary statistics of this quantity is specified by the fitness flux theorem [60]. According to the theorem, the average cumulative fitness flux in a population ensemble measures the deviation of the evolutionary process from equilibrium: this deviation equals the relative entropy of the actual process from a hypothetical time-reversed process [60,126]. It is substantial — i.e., the process is predominantly adaptive — if $\langle 2N\Phi\rangle \gtrsim 1$. Specifically, the cumulative fitness flux of a stationary adaptive process increases linearly with time, $\langle 2N\Phi(\tau)\rangle = \langle\phi\rangle\tau$ with $\langle 2N\phi\rangle > 0$.

For a quantitative trait in a quadratic fitness seascape of the form (2.24), we can decompose the fitness flux into contributions of the trait mean and the trait diversity,

$$\phi(t) = -2c_0\big(\Gamma(t) - E^*(t)\big)\frac{\mathrm{d}\Gamma(t)}{\mathrm{d}t} - 2c_0\frac{\mathrm{d}\Delta(t)}{\mathrm{d}t}. \tag{3.46}$$

In the stationary population ensemble (3.16), the average scaled fitness flux can be expressed in

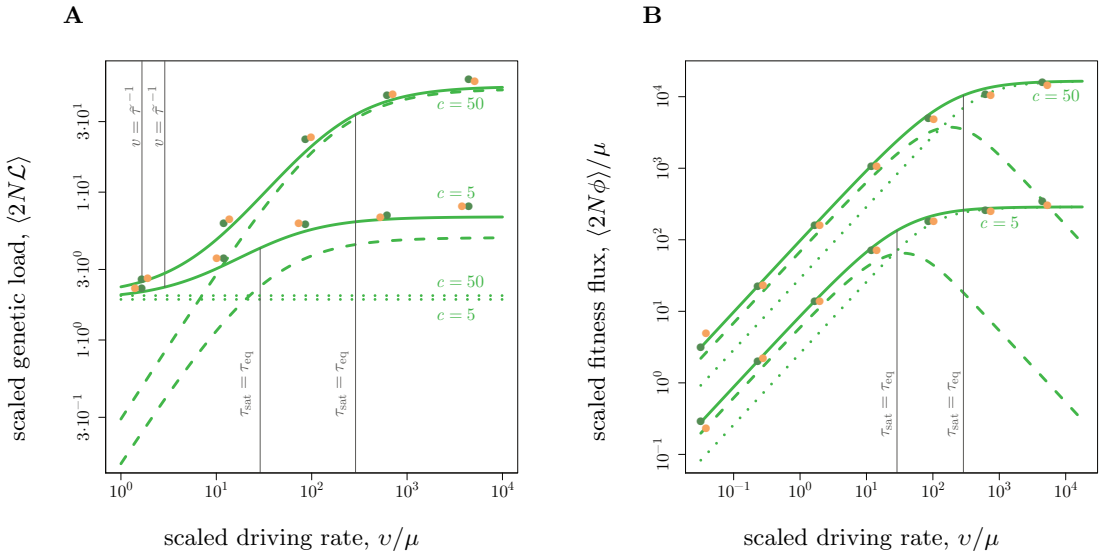

Figure 3.6. Genetic load and fitness flux. **A** Scaled genetic load $2N\mathcal{L}$ (full lines) and its constituents, the adaptive genetic load, $2N\mathcal{L}_{\rm ad}$ (dashed lines), and equilibrium genetic load, $2N\mathcal{L}_{\rm eq}$ (dotted lines), for stationary evolution of non-recombining populations in a fitness seascape. The load components are plotted against the scaled driving rate υ/μ for stabilizing strengths $c = 5, 50$; other parameters like in Figure 3.4. The analytical results of Equation (3.42) are compared to simulations for diffusive and punctuated fitness seascapes (green and orange dots). The corresponding data for fully recombining populations are shown in Figure C.1. The genetic load is dominated for $\upsilon \lesssim 1/\tilde{\tau}(c)$ by the equilibrium component and for $\upsilon \gtrsim 1/\tilde{\tau}(c)$ by the adaptive component; it saturates in the micro-evolutionary seascape regime ($\upsilon \gtrsim r^2/\tau_{\rm eq}(c)$). **B** The scaled fitness flux $\langle 2N\phi\rangle$ (solid line) and its components $\langle 2N\phi_{\rm macro}\rangle$ and $\langle 2N\phi_{\rm micro}\rangle$, as defined in Equations (3.53) and (3.54), are shown for the same parameters (all flux values are measured in units of $1/\mu$). In macro-evolutionary fitness seascapes, $\langle 2N\phi\rangle$ is an approximately linear function of the driving rate υ and the component $\langle 2N\phi_{\rm macro}\rangle$ is the dominant part. In micro-evolutionary seascapes, $\langle 2N\phi\rangle$ saturates and the component $\langle 2N\phi_{\rm micro}\rangle$ is the dominant part.

terms of the stationary probability current $\mathbf{J}_{\rm stat}(\Gamma, E^*)$,

$$\langle 2N\phi\rangle = -\frac{2c}{E_0^2}\int \mathrm{d}\Gamma \mathrm{d}E^*\,(\Gamma - E^*)J^{\Gamma}_{\rm stat}(\Gamma, E^*), \tag{3.47}$$

where $J^{\Gamma}_{\rm stat}(\Gamma, E^*)$ is the Γ–component of $\mathbf{J}_{\rm stat}(\Gamma, E^*)$. The fitness flux can be computed analytically from Equation (3.23),

$$\langle 2N\phi\rangle(c, \upsilon, r^2) = 2c\upsilon\, w(c, \upsilon, r^2). \tag{3.48}$$

In the regime of substantial stabilizing strength ($c \gtrsim 1$), we get

$$\langle 2N\phi\rangle(c, \upsilon, r^2) \simeq \begin{cases} 2c\upsilon\Big[1 - \mathcal{O}\Big(\dfrac{\tau_{\rm eq}}{\tau_{\rm sat}}\Big)\Big] & \text{(macroevolutionary seascapes)}, \\ \dfrac{4c^2r^2}{\tilde{\tau}(c)}\Big[1 - \mathcal{O}\Big(\dfrac{\tau_{\rm sat}}{\tau_{\rm eq}}\Big)\Big] & \text{(microevolutionary seascapes)}, \end{cases} \tag{3.49}$$

where the drift time $\tilde{\tau}(c)$ is given by Equations (2.11) and (3.39). The fitness flux depends linearly on the driving rate in a macro-evolutionary fitness seascape, and it saturates in the

regime of micro-evolutionary fitness fluctuations. Figure 3.6B shows this dependence of the fitness flux on the driving rate.

We can express the fitness flux in terms of correlation functions of the trait mean $\Gamma(t)$ and the lag $\Lambda(t)$, which results in a simple relation between fitness flux and adaptive load. Inserting the probability current of Equation (3.23) into the integral of Equation (3.47), we find

$$\begin{aligned}\langle 2N\phi\rangle &= \frac{2c^2\langle\delta\rangle}{E_0^2}\Big(\langle\Lambda^2\rangle - \langle\Lambda^2\rangle_{\rm eq}\Big) \\ &\quad + \frac{4c\theta}{E_0^2}\lim_{\tau\searrow 0}\Big(\langle\Lambda(t+\tau)(\Gamma(t)-\Gamma_0)\rangle - \langle\Lambda(t+\tau)(\Gamma(t)-\Gamma_0)\rangle_{\rm eq}\Big) \\ &= c\langle\delta\rangle\langle 2N\mathcal{L}\rangle_{\rm ad}(c,\upsilon,r^2)[1+\mathcal{O}(\theta)]. \end{aligned} \tag{3.50}$$

From this representation, we obtain the spectral decomposition of the fitness flux,

$$\langle 2N\phi\rangle(c,\upsilon,r^2) = \int_0^\infty \langle 2N\phi(\omega)\rangle\, d\omega \tag{3.51}$$

with

$$\langle 2N\phi(\omega)\rangle = 2c\upsilon\frac{c\langle\delta\rangle}{\pi/2}\frac{\omega^2}{(\tau_{\rm eq}^{-2}(c)+\omega^2)(\tau_{\rm sat}^{-2}(\upsilon,r^2)+\omega^2)}[1+\mathcal{O}(\theta/(c\langle\delta\rangle)]. \tag{3.52}$$

Using a cutoff frequency $\omega_c = k/\tau_{\rm eq}(c)$ with a constant k of order 1, we can now define a macro-evolutionary flux component,

$$\begin{aligned}\langle 2N\phi_{\rm macro}\rangle &= \int_0^{\omega_c}\langle 2N\phi(\omega)\rangle\, d\omega \\ &= 2c\upsilon\; w(c,\upsilon,r^2)\frac{(\tau_{\rm eq}^{-1}(c)+2\mu)\arctan[k] - (\tau_{\rm sat}^{-1}(\upsilon,r^2)+2\mu)\arctan\left[k\,\tau_{\rm sat}(\upsilon,r^2)/\tau_{\rm eq}(c)\right]}{(\pi/2)(\tau_{\rm eq}^{-1}(c)-\tau_{\rm sat}^{-1}(\upsilon,r^2))}, \end{aligned} \tag{3.53}$$

and the complementary micro-evolutionary component

$$\langle 2N\phi_{\rm micro}\rangle = \int_{\omega_c}^\infty \langle 2N\phi(\omega)\rangle\, d\omega = \langle 2N\phi\rangle - \langle 2N\phi_{\rm macro}\rangle. \tag{3.54}$$

In the regime of substantial stabilizing selection ($c \gtrsim 1$), the macro-evolutionary fitness flux in (3.53) reads

$$\langle 2N\phi_{\rm macro}\rangle(c,\upsilon,r^2) \simeq \begin{cases} 2c\upsilon\,\dfrac{2}{\pi}\arctan[k] & \\ \qquad\qquad\qquad\qquad \text{(macroevolutionary seascapes)}, & \\ 2c\upsilon\,\dfrac{\tau_{\rm sat}^2(\upsilon,r^2)}{\tau_{\rm eq}^2(c)}\,\dfrac{2}{\pi}\big(k-\arctan[k]\big) \sim \dfrac{1}{\upsilon}, & \\ \qquad\qquad\qquad\qquad \text{(microevolutionary seascapes)}. & \end{cases} \tag{3.55}$$

This fitness flux component quantifies the macro-evolutionary part of adaptation. In macro-evolutionary fitness seascapes ($\tau_{\rm sat}(v, r^2) \gtrsim \tau_{\rm eq}(c)$), it increases proportionally to the driving rate v and, for $k > 1$, it represents the main fraction of the total fitness flux $\langle 2N\phi \rangle$. In micro-evolutionary fitness seascapes ($\tau_{\rm sat}(v, r^2) \lesssim \tau_{\rm eq}(c)$), this component is suppressed: the macro-evolutionary fitness flux does not carry information on rapid fitness fluctuations. This cross-over of $\langle 2N\phi_{\rm macro} \rangle$ and of the complementary component $\langle 2N\phi_{\rm micro} \rangle$ is shown in Figure 3.6B.

The spectral decomposition of the fitness flux has important consequences for the analysis of macro-evolutionary adaptation. The detection of a substantial cumulative fitness flux $\langle 2N\Phi_{\rm macro}(\tau) \rangle > 1$ over a macro-evolutionary period τ is not confounded by the simultaneous presence of micro-evolutionary (for example seasonal) fitness fluctuations. Since the cumulative fitness flux is a measure of entropy production during adaptation, the spectral decomposition (3.51) also has an important information-theoretic interpretation: The difference $\langle 2N\phi_{\rm micro} \rangle = \langle 2N\phi \rangle - \langle 2N\phi_{\rm macro} \rangle$ is the average loss of information per unit time through temporal coarse-graining. This loss is a non-equilibrium analogue of the entropy production by spatial coarse-graining.

3.4.3 Predictability and entropy production

In reference [53], we quantified the evolutionary predictability of the molecular traits across an ensemble of populations by

$$\mathcal{P} \equiv \exp\big[\langle S(\mathcal{W}) \rangle - S(\langle W \rangle)\big], \tag{3.56}$$

with $S(\mathcal{W}) \equiv -\int \mathcal{W}(E) \log \mathcal{W}(E) dE$. This definition compares the ensemble-averaged "micro-evolutionary" Shannon entropy of the phenotype distribution within a population, $\langle S(\mathcal{W}) \rangle \equiv \int_{\mathcal{W}} S(\mathcal{W})\, Q(\mathcal{W})$, and the "macro-evolutionary" Shannon entropy of the mixed distribution, $S(\langle \mathcal{W} \rangle) \equiv S\big(\int_{\mathcal{W}} \mathcal{W}\, Q(\mathcal{W})\big)$, which is obtained by compounding the trait values of all populations into a single distribution. We have shown that the predictability is generically low in a neutral ensemble, but stabilizing selection in a single fitness landscape can generate an evolutionary equilibrium with predictability values $\mathcal{P}$ of order 1 [53].

Here we compute the predictability in a time-dependent ensemble of populations that descend from a common ancestor population. Similarly to reference [53], we evaluate Equation (3.56) for a distribution $Q_t(\mathcal{W})$ with the initial condition $Q_{t_a}(\mathcal{W}) = \delta(\mathcal{W} - \mathcal{W}_a)$ at time $t_a = t - \tau/2$. We obtain the time-dependent predictability

$$\mathcal{P}(\tau; c, v, r^2) \simeq \left(\frac{\langle \delta \rangle(c)}{\langle d^{(2)} \rangle(\tau; c, v, r^2)/2 + \langle \delta \rangle(c)} \right)^{1/2} = \left(\frac{1}{1 + \Omega^{(2)}(\tau; c, v, r^2)/4\theta} \right)^{1/2}. \tag{3.57}$$

Here, $\Omega^{(2)}(\tau; c, v, r^2) \equiv 2\theta \, \langle d^{(2)} \rangle(\tau; c, v, r^2)/\langle \delta \rangle$ denotes the ratio between trait divergence and diversity for the descendent populations. The trait statistics in a macro-evolutionary fitness seascape, given by Equations (3.30) and (3.39), entail the evolutionary predictability

$$\mathcal{P}(\tau; c, v, r^2) \;=\; \mathcal{P}_{\rm eq}(c) \left[1 - \frac{1}{2} v\, \tilde{\tau} \frac{\tau - 2\tau_{\rm eq}(c)}{2N} \left[1 + \mathcal{O}\left(\tau\, \tau_{\rm eq}(c) c v/N, \tau/\tau_{\rm sat}, \theta/(c\langle \delta \rangle) \right) \right] \right] \tag{3.58}$$

for $\tau \gtrsim \tau_{\rm eq}(c)$, with $\mathcal{P}_{\rm eq}(c) = (1 + w(c)/(2c))^{-1/2} = (1 + 1/(2c))^{-1/2}[1 + \mathcal{O}(\theta/(c\langle\delta\rangle))]$. There are two stochastic components that generate macro-evolutionary entropy and, hence, reduce the evolutionary predictability: fluctuations induced by genetic drift on short timescales $\tau \lesssim \tau_{\rm eq}(c)$ and fluctuations of the fitness peak over timescales $\tau \gtrsim \tau_{\rm eq}(c)$. Nevertheless, as shown by (3.58), the predictability of an adaptive process with substantial stabilizing selection can remain of order 1 over macro-evolutionary periods.

3.4.4 Discussion

In this section, we have introduced three simple summary observables of evolutionary processes: genetic load, fitness flux, and predictability. For quantitative traits, the statistics of these observables is universal; that is, it decouples from details of molecular evolution.

Genetic load is defined as the difference between the maximum of a fitness land- or seascape and the mean fitness in a population. Here we have evaluated the load associated with a quantitative trait. In evolutionary equilibrium under substantial stabilizing selection, the load takes the simple universal form $\mathcal{L} = 1/(4N)$, which generalizes to $\mathcal{L} = d/(4N)$ for a d-dimensional quantitative trait in a quadratic fitness landscape (see references [123–125] for similar results). This universal *strong*-selection behavior of the equilibrium load distinguishes quantitative traits from individual genetic loci, for which $\mathcal{L} \sim 1/N$ signals *weak* selection[1] (i.e., selection coefficients of order $1/N$). In fitness seascapes, there is an additional nonequilibrium load component, which is proportional to the driving rate υ and measures the fitness cost of adaptation. We still know little on how this type of load affects real populations. However, studies at the genetic level suggest it may play an important role in rapid asexual adaptation processes, which occur in microbial or viral populations [21, 68].

Fitness flux measures the fitness gain through adaptive changes per unit of evolutionary time; the cumulative fitness flux is the total adaptive fitness gain over an evolutionary period [60]. These universal measures serve to compare adaptive processes in different populations. In empirical studies, the fitness flux has been evaluated in systems as diverse as flies and influenza viruses [7, 19, 21]. Here we have shown that the fitness flux of a quantitative trait in a fitness seascape is proportional to stabilizing strength and driving rate, $\phi \approx 2c\upsilon$.

Predictability has been an important issue in laboratory evolution experiments, which can be repeated multiple times under similar conditions. For a quantitative trait, predictability can be defined in a straightforward way [53]: how much of the trait repertoire in an ensemble of parallel-evolving populations is already contained in the trait diversity of a single population? We have shown that fitness seascapes have antagonistic effects: stabilizing selection enhances, lineage-specific directional selection decreases predictability. Adaptive process in macro-evolutionary fitness seascapes can maintain substantial predictability values over macro-evolutionary periods. Parallel and convergent evolution at the functional level, paired with strongly divergent genome evolution has been observed in a number of recent experiments [20, 22, 23]. These experimental observations can be explained in a natural way, if we assume that many of these functions involve

[1] For a quantitative trait, $\mathcal{L} \sim 1/N$ holds over a broad range of stabilizing strengths [53]. Hence, this estimate cannot be used to infer weak selection, as claimed in reference [96].

a complex quantitative trait.

3.5 Inference of adaptive trait evolution

The statistical theory developed in this chapter suggests a new method to infer selection on quantitative traits. Our method is based on trait evolution in a single-peak fitness seascape, as defined in Equation (2.24), which is parametrized by its stabilizing strength c and its driving rate v.

Two main results are relevant for the inference of selection. First, evolution in a macro-evolutionary fitness seascape affects the population mean trait in complementary ways: it generates conservation on shorter scales and adaptation on longer scales of evolutionary time. These characteristics are measured by the expected trait divergence between populations, $\langle D^{(\kappa)}\rangle(\tau)$, which depends on the divergence time τ and on the selection parameters c and v in a characteristic way. The divergence can be measured either between an ancestral population and a descendent population ($\kappa = 1$) or between two descendent populations evolving from a common ancestor population ($\kappa = 2$). As discussed in Section 3.3.2 , these measures are generically distinct for adaptive processes[2]. Second, the expected trait diversity within populations, $\langle\Delta\rangle$, shows a weaker signal of conservation. Moreover, it decouples from the adaptive process in a single-peak fitness seascape over a wide range of evolutionary parameters, as discussed in Section 3.3.3.

3.5.1 Statistics of the divergence-diversity ratio Ω

Our test statistics is the time-dependent divergence-diversity ratio

$$\Omega^{(\kappa)}(\tau) = 2\theta\frac{\langle D^{(\kappa)}\rangle(\tau)}{\langle\Delta\rangle} \qquad (\kappa = 1, 2), \tag{3.59}$$

where $\theta = \mu N$ denotes the nucleotide diversity. This function depends on the divergence time τ and on the selection parameters c and v. The typical behavior of $\Omega^{(\kappa)}(\tau)$ for different evolutionary modes is shown in Figure 3.7 and can be summarized as follows:

- *Neutral evolution* ($c = 0$). The divergence-diversity ratio has an initially linear increase due to mutations and genetic drift, and it approaches a maximum value 1 with a relaxation time $\tau_0 = 1/\mu$,

$$\Omega^{(\kappa)}(\tau) \;=\; \Omega_0(\tau) \simeq \begin{cases} \mu\tau & \text{for } \tau \ll \tau_0 \\ 1 & \text{for } \tau \gg \tau_0 \end{cases} \qquad (\kappa = 1, 2). \tag{3.60}$$

  The function $\Omega_0(\tau)$, which does not depend on κ because of detailed balance, is shown as a grey line in Figure 3.7. Its linear short-term behavior reflects the classical quantitative

[2]The relative difference between $\langle D^{(1)}\rangle(\tau)$ and $\langle D^{(2)}\rangle(\tau)$ is small (Figure 3.7). This difference is conceptually important, however, because it manifests the violation of detailed balance in adaptive processes. Similar effects are ubiquitous in divergence data of trait adaptation across multi-branch phylogenies.

genetics result $\langle D^{(\kappa)} \rangle(\tau) \simeq V_m \tau$, where $V_m = \langle \Delta \rangle_0 / (2N)$ is often called the mutational variance of the trait [51, 117, 118].

- *Conservation in a fitness landscape* ($c \gtrsim 1, \upsilon = 0$). The divergence-diversity ratio approaches a smaller maximum value, $\Omega_{\rm stab}(c) < 1$, with a proportionally shorter relaxation time $\tau_{\rm eq}(c) = \Omega_{\rm stab}(c)/\mu$,

$$\Omega^{(\kappa)}(\tau) \;=\; \Omega_{\rm eq}(\tau; c) \simeq \begin{cases} \mu\tau & \text{for } \tau \ll \tau_{\rm eq}(c) \\ \Omega_{\rm stab}(c) & \text{for } \tau \gg \tau_{\rm eq}(c) \end{cases} \qquad (\kappa = 1, 2). \tag{3.61}$$

  The function $\Omega_{\rm eq}(\tau; c)$, which does not depend on κ by detailed balance, is shown as a red line in Figure 3.7. Over a wide range of evolutionary parameters, the maximum value depends on the stabilizing strength in a simple way, $\Omega_{\rm stab}(c) \sim 1/(2c)$, with corrections for weaker selection and for larger nucleotide diversity.

- *Adaptation in a macro-evolutionary fitness seascape* ($c \gtrsim 1, 0 < \upsilon \lesssim 1/\tilde{\tau}$). The divergence-diversity ratio acquires an adaptive component,

$$\begin{aligned} \Omega^{(\kappa)}(\tau) &= \Omega_{\rm eq}(\tau; c) + \Omega^{(\kappa)}_{\rm ad}(\tau; \upsilon) \\ &= \Omega_{\rm eq}(\tau; c) + \frac{\upsilon}{2} \left[\tau - \kappa \tau_{\rm eq}(c) \right] \qquad (\kappa = 1, 2), \end{aligned} \tag{3.62}$$

  with corrections for weaker selection and for τ approaching the non-equilibrium saturation time $\tau_{\rm sat} = r^2/\upsilon$. The functions $\Omega^{(\kappa)}(\tau)$ are shown as blue lines in Figure 3.7.

3.5.2 The Ω test for stabilizing and directional selection

Using the divergence-diversity ratio (3.59), we can infer selection on quantitative traits from diversity and *time-resolved* divergence data. In principle, comparative trait data from a single pair of species with divergence time $\tau \gtrsim \tau_{\rm eq}(c)$ determine stabilizing selection in a fitness landscape; data from three or more species determine stabilizing and directional selection in a fitness seascape. Following Equations (3.61) and (3.62), we then construct an approximate linear fit to the Ω ratio of these data,

$$\Omega(\tau) \approx \Omega_{\rm stab} + \Omega_{\rm ad}(\tau) = \Omega_{\rm stab} + \frac{\upsilon}{2}\tau. \tag{3.63}$$

We obtain simple estimates of stabilizing strength and driving rate,

$$c \approx \frac{1}{\Omega_{\rm stab}}, \qquad \upsilon \approx \frac{2\Omega_{\rm ad}(\tau)}{\tau}, \tag{3.64}$$

and we infer that a fraction

$$\omega_{\rm ad}(\tau) \;\equiv\; \frac{\Omega_{\rm ad}(\tau)}{\Omega(\tau)} = \frac{\Omega(\tau) - \Omega_{\rm stab}}{\Omega(\tau)} \tag{3.65}$$

of the observed trait divergence is adaptive, i.e., driven by directional selection.

The Ω test reflects generic characteristics of quantitative trait evolution, which are described by equations (3.60–3.62): The expected trait divergence $\langle D \rangle(\tau)$ always grows in a quasi-neutral linear way for divergence times $\tau \lesssim \tau_{\rm eq}(c)$; beyond this regime, it depends on both stabilizing and directional selection. This behavior has important consequences for applications. First, the Ω test is insensitive to selection if the species compared are too close. Second, cross-species comparisons that provide evidence for enhanced Ω values in a single lineage cannot distinguish directional from relaxed stabilizing selection. These limitations may partially explain the difficulties to infer system-wide evidence for directional selection on gene expression [127–129].

An important prerequisite for the wide applicability of the Ω test is its *universality*: the divergence-diversity ratio depends on the selection parameters c and v, but it decouples from the trait's genetic basis. In particular, it depends only weakly on the number and trait amplitudes of the constitutive sequence sites, additional single site adaptation through quick compensation by the integral trait sites as discussed in Chapter 4, and on the amount of recombination between these sites. All of these genetic factors are, in general, unknown. They act as confounding factors for an inference of selection based on non-universal observables [96]. The Ω statistics also decouples from details of the selection dynamics; it can be applied to continual as well as to punctuated adaptive processes. We have tested this universality by extensive numerical simulations, which are reported in Appendix A.

The Ω test is based on ensemble averages of trait divergence and diversity. Our statistical theory also specifies the deviations of individual evolutionary trajectories from the ensemble averages; these fluctuations are described by the propagator functions in Appendix C. We can use the propagator statistics to build a hidden Markov model for the inference of selection from noisy trajectories of individual traits. This method is essential in the analysis of trait divergence over phylogenies of species, which is described in detail in a follow-up paper [3].

3.5.3 Comparison with sequence-based inference of selection

The Ω test for selection on quantitative traits is related to a test for adaptive sequence evolution of the McDonald-Kreitman type [130]. This test evaluates the divergence-diversity ratio Ω for a sequence class under putative selection (e.g., nonsynonymous mutations in protein-coding sequence) and compares it to the analogous ratio Ω_0 for *bona fide* neutral changes (e.g., synonymous mutations). Positive selection in the query sequence is inferred if $\Omega > \Omega_0$. In this case, the amplitude ratio

$$\alpha = \frac{\Omega - \Omega_0}{\Omega} \tag{3.66}$$

estimates the fraction of nonsynonymous substitutions that are adaptive, i.e., driven by positive selection [131].

Comparing the two inference schemes reveals a number of important differences. Unlike the McDonald-Kreitman test, the Ω test for quantitative traits does not require a "null trait" that evolves near neutrality and takes the role of synonymous sequences. Indeed, no such neutral trait gauge is available in most cases. Instead, the Ω test compares data from three or more

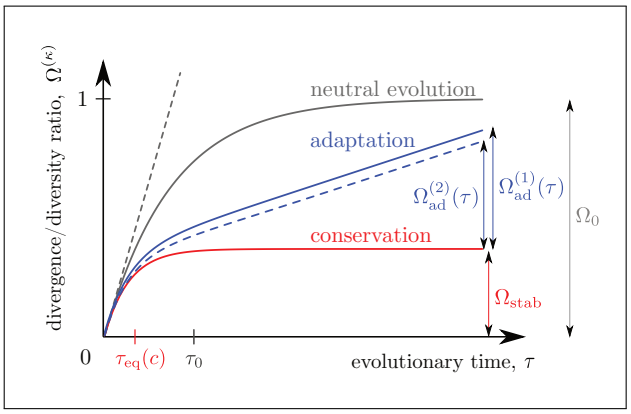

Figure 3.7. The universal divergence-diversity ratio $\Omega^{(\kappa)}$ ($\kappa = 1, 2$), as defined in Equation (3.59), for a quantitative trait evolving in a single-peak fitness land- or seascape. This ratio is plotted as a function of the scaled divergence time, τ. *Neutral evolution*: The function $\Omega_0(\tau)$ (grey line) is independent of κ and it reaches the saturation value 1 on times scales $\tau \gg \tau_0 = 1/\mu$ (grey curve; the short-time behavior $\Omega_0(\tau) \simeq \mu\tau$ given by classical quantitative genetics [51,117,118] is shown as dashed line). *Conservation in a fitness landscape*: The function $\Omega_{\rm eq}(\tau)$ is independent of κ and has a smaller saturation value $\Omega_{\rm stab}(c)$ reached faster than for neutral evolution, on timescales $\tau \gg \tau_{\rm eq}(c)$ (red curve). *Adaptation in a fitness seascape*: There is a linear surplus $\Omega_{\rm ad}^{(\kappa)}(\tau) \simeq v[\tau - \kappa\tau_{\rm eq}(c)]$, which measures the amount of adaptation (blue curves).

species, while the McDonald-Kreitman test requires only a single pair of species. Moreover, the Ω test includes the inference of the stabilizing strength, while the McDonald-Kreitman test leaves the strength of selection undetermined (large selection coefficients of beneficial alleles are an input assumption for the estimate (3.66)).

3.6 Pervasive adaptation in Drosophila

In a follow-up research project, we applied the inference method to the Drosophila genus. We could identify for the first time system-wide adaptation on the level of gene expression levels. The time-resolved divergence on macro-evolutionary timescales cannot be well explained by an equilibrium model or neutral evolution.

The *Drosophila* genus stayed a puzzle so far [129]: while extensive adaptation was inferred on genomic level [19,132,133], it was impossible to identify system-wide adaptation on the level of gene expression levels because the neutral gauge used in classical test, e.g. from synonymous sites, is not available on phenotypic level. Our Ω-test derived in this chapter opens new avenues to analyse this dataset. Hence, we applied the Ω-test in a follow-up research project [3]. The divergence of gene expression levels of thousands of genes could be temporarily resolved with the phylogenetic tree reconstructed from genomic information.

A 'simple' inference scheme is shown in Figure 3.8A. The observed gene expression divergence shows strong directive selection by adaptive pressures, cp. Figure 3.7 and Section 3.5.2. A more intricate maximum likelihood approach for the inference with the probabilistic propagators from Appendix C was also used in [3]. This allowed to infer that 54 % of genes showed a significant fitness flux time-integrated over the entire phylogeny ($\int 2N\phi(t)\mathrm{d}t > 1$) and 63 %

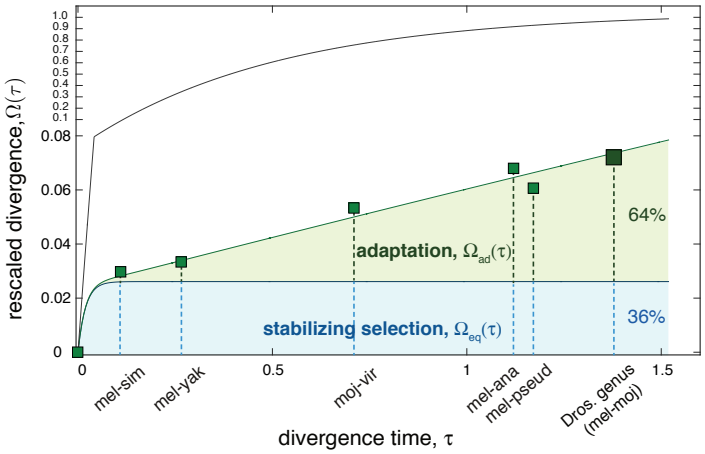

Figure 3.8. Pervasive adaptation inferred in *Drosophila*, taken from [3] The figure shows the average divergence curve of the Ω–test of gene expression levels across the *Drososphila* genus as a function of neutral divergence time in units of μ^{-1} [3]. The best fitted model (green) fits the data with substantial adaptation, which could not be fitted equivalently well by an equilibrium model. Blue shows the equilibrium divergence of the fitted model and grey the neutral expectation pattern.

adaptive divergence of total observed divergence, cp. Equation (3.65). Furthermore, alternative selection scenarios have been discussed and could be excluded as origination of the observed pattern; adaptation turned out to be by incremental, but continuous adaptation. Furthermore, the Ω-test allows also to analyze genes by functional classes and hence to identify functions under strong adaptation, as reported in [3].

3.7 Conclusion

In this chapter, we have developed a statistical theory for the evolution of a quantitative trait in a stochastic fitness seascape. The fitness model used for our analysis, a single-peak seascape with diffusive or punctuated peak displacements, covers a broad spectrum of biologically relevant evolutionary scenarios [2]. The two seascape parameters c and v quantify stabilizing and directional selection on the trait, which, in turn, govern the trait's fundamental evolutionary modes of conservation and adaptation. Our analysis shows that these modes are not mutually exclusive, but are joint features of dynamic selection models.

In a macro-evolutionary fitness seascape, conservation and adaptation are associated with different timescales: conservation is observed on shorter scales, while adaptive changes build up on longer scales of evolutionary time. Micro-evolutionary fitness fluctuations, on the other hand, lead to reduced genetic adaptation, which decouples from the macro-evolutionary dynamics of the trait. Rapid adaptive response to seasonal or other fluctuations of the environment often involves epigenetic modifications or phenotypic switching [115]. The evolutionary roles of these mechanisms are beyond the scope of this thesis. The spectral decomposition of the fitness flux, which has been introduced above, quantifies how the adaptive process is distributed on different scales of evolutionary time.

Our theory suggests new inference methods for selection on quantitative traits, which have important potential applications. At the sequence level, an increasingly complex picture of selection has emerged in recent years. Notably, we have acquired a growing repertoire of empirical genotype-fitness landscapes [134], which has generated important experimental and theoretical insights into the evolutionary dynamics on these landscapes. However, we still know little about the statistical properties of empirical phenotype-fitness maps, and next to nothing about phenotype-dependent seascapes. Systematic inference of selection on molecular quantitative traits, such as levels of gene expression and enzymatic activity, can contribute to close this gap. From applying this methods to the *Drosophila* genus, we could identify in a follow up publication a large degree of adaptation shaping the divergence of gene expression levels [3]. This allowed for the first time to detect adaptation on the phenotypic level and, hence, to unify the picture with observed broad adaptation on the sequence level. Eventually, fitness land- and seascapes for individual traits will need to be integrated into larger phenotype-fitness maps, which include fitness interactions between traits.

How the constraining selection shaping the divergence pattern impacts the co-evolution of QTL, even for multiple traits, will be the topic of Chapter 4.

Chapter 4

Epistatic pattern of molecular phenotypes

Correlations between genomic items have been observed in evolutionary systems and a dynamical origin of these is identified as fitness epistasis between these items. While theoretical models can well describe such interactions between pairs of sites, also broad correlation sectors have been observed in data. Here, we close the gap between so far local theory and experimental results by employing quantitative trait theory under stabilizing trait-selection. This non-linear phenotypic selection generates broad, but simple epistasis on the quantitative trait loci (QTL). These sectors can be identified with the mode of stabilizing selection on quantitative traits. We furthermore present a new method to make use of temporal distance information of mutations to appropriately measure correlations even with few mutations and far from evolutionary equilibrium. This allows us not only to identify the number of underlying traits by the rank of the correlation matrix, but also to re-identify the trait effects of QTL and strongly adaptive sites—the latter from break of detailed balance in the correlation measure. Hence, our model provides a new method to infer a-priori unknown genotype–phenotype–maps from sequence data as well as loci under strong adaptive pressure.

4.1 Introduction

The evolution of molecular phenotypes, such as protein stability, ligand binding properties or allosteric mechanisms is shaped by the collective dynamics of its multiple genomic sites [53]. These dynamics are caused by fitness interactions of these sites, i.e. fitness epistasis generated by non-linear phenotypic fitness landscapes. Recent studies, so called direct coupling analyses [29, 76–79], showed that the detection of biophysical constraints is possible from the evolutionary process: they could identify contact points of residues within and across proteins from the evolutionary sequences. These were explained by evolutionary models containing pairwise and hence local epistasis [76, 78, 79]. On the other hand, broad correlations have been detected

in sequence alignments across many protein families [80–82]. These sectors were identified with protein function, such as protein stability, catalytic power and allosteric mechanisms that supposedly underly quantitative traits. However, a sophisticated evolutionary model for these functions is still missing.

This motivated us to study a theory for the co-evolution of QTL. We find that the evolution of quantitative traits in non-linear fitness landscapes, particularly under stabilizing trait selection, generates these broad correlations. The underlying principle is depicted in Figure 4.1: a deleterious mutation at one trait locus is only occasionally compensated by a particular other site, but can be compensated by any other of the QTL. We see that broad correlations do not directly imply complicated epistatic interactions for traits with a significant input of deleterious mutations driving selection away from fitness optima. This leads to a smooth sequence landscapes of low rank in contrast to the very rugged fitness landscapes like in Kauffman NK models [135, 136] or house of cards models [137], or even phenotypic evolution around fitness peaks [90]. Though noise can be strong in the correlation of a given pair of sites, these correlations recover the smooth phenotypic fitness landscape on trait scales when taking all the QTL responses into account. We see that ubiquitous epistasis, which was associated to very limited predictability in rugged landscapes, actually can have a predictive power, e.g. in foreseeing compensatory mutations [10].

Furthermore, the methods and models developed so far use as a prerequisite the assumption of evolutionary equilibrium or maximum entropy principles, ignoring the phylogenetic relations [76,77,80,81]. It allows the inference of variational constraints in the evolutionary process, if this process is not too strongly driven by adaptation and data are evenly sampled across the phylogeny. However, it cannot identify the evolutionary mode, for instance to distinguish stabilizing selection from adaptation. Moreover, the equilibrium assumption faces a large bias if the analyzed sequences are not obtained from a well balanced phylogenetic tree underlying the data [29]. This is the case for strongly adaptive species. Nonetheless, such methods have been applied to infer mutational patterns in the somatic evolution of immune repertoires, epistatic interactions between deleterious mutations in the human immunodeficiency virus [6,83]. To address these issues, we extend the trait model to adaptive systems with fitness seascapes driving individual QTL [19, 59]. While fluctuations of undriven trait sites deleterious to the trait are generated by genetic drift or genetic draft, adaptation can significantly increase these rates, if strong adaptive pressure on a site overruns trait selection. Either cause triggers selection on compensatory mutations on other trait sites, but the compensatory response of driven sites is suppressed.

We introduce time-resolved observables such as pair-wise substitution rates that allow to quantify not only the trait effects, but also the adaptation of a site from the asymmetry of the response matrix. This short-term correlation measurements are also applicable to phylogenetic trees under very strong adaptive pressures [138] and can help to improve the predictability of evolution [7,10,11]. Such short-term time-ordered correlation measurements have been identified to detect the strength of non-equilibrium in Ising models with asymmetric couplings [139]. However here, the non-equilibrium equivalent would be the time-dependence of the external

magnetic field and constrained coupling constants with strengths dependent on the genetic background.

Finally, we generalize our approach to the correlation pattern of multiple co-evolving traits that generate multiple sectors but still lead to low-rank correlations; with this, it is possible to distinguish the effect of sites onto various functions. The compensation pressure of one trait can be seen as external driving onto the other trait. Therefore it will help to identify additional inter-protein relations from constrained inter-protein biophysics generated by broad binding domains, similar to how it is done with direct coupling analysis so far [79].

After we already discussed the average impact of trait selection onto single site selection and the epistasis generated by non-linear phenotypic fitness landscapes in Section 2.2, we now derive single site properties of trait plus external selection such as fixation probabilities and substitution rates in Section 4.2. This builds the fundament to derive deviations from these through the epistatic trait response in Section 4.3. In Section 4.4, we discuss how adaptation explains the asymmetry pattern of the response by relating it to the fitness flux. The analysis extends to the co-evolution of various quantitative traits in Section 4.5. With relating the epistatic pattern to Chapter 3, we can relate the response to predictability of compensation in Section 4.6. We guide the reader by keeping track of the key variables and results in Table 4.1. We support our analytical considerations by simulations performed with an Wright–Fisher–process containing (time-dependent) selection, stochastic mutations, and stochastic sampling of the successor generation (genetic drift) as detailed in Appendix A.

4.2 Effectively independent QTL dynamics

In this section, we derive the marginal single-site fixation probabilities of alleles in stationary states and the substitution rates under trait selection plus external selection, where the latter can be constant or causing adaptive pressures. On the one hand, these results serve as null-mode to analyze expected pairwise counts without explicitly triggered epistatic response. On the other hand, they are needed twofold for the correlation measurements: a) they determine the rate of a site as a primary mutation and b) the state probabilities of a site set its compensation probability. Hence, they need to be averaged over.

To study the co-evolution of quantitative trait sites, we model the evolution in a non-linear and time-independent phenotypic fitness landscape $f(E)$ with additional pleiotropic selection on some sites. The latter are fitness interactions with other Mendelian or polygenic traits. As discussed in Equation (2.20), the effective average selection on a site j is composed of its single site selection coefficient $s_j(t)$ and the average trait selection $s_j^f(t)$ set by the background mean field statistics of the other trait sites. Generically, this generates two polarizations for a mutation: first, it either raises or lowers the trait value, i.e. $\epsilon_j = +1$ or -1; second, it is either beneficial or deleterious with respect to the trait-external selection: $\epsilon_j \eta_j = +1$ or -1. Here,

[1] equilibrium
[2] macro-evolutionary driving

Table 4.1. Overview of important definitions and results. Here, we show the key definitions and results of the main text. The variables in in the text may have, context-dependent, explicit time-dependence t, or the rates have direction indices $\epsilon_j = \pm 1$ restricting on a subset of substitutions with respect to the trait value. The related count observables are introduced in Methods 4.8. The indexed variables relate to a single site j or pairs of sites i and j.

	Variable	Related observable	Description
Model parameters	μ, N		Mutation rate, population size
	$E, f(E), \ell,$ $E_0^2 = \frac{1}{4}\sum_i E_i^2$		Trait value, trait fitness, # of trait loci, neutral trait scale
	$c = 2NE_0^2\langle f''(\Gamma)\rangle$		Average stabilizing strength of trait
	E_j	From $\hat{N}_{ij}$ or N_{ij}^{pol}	Trait effect of site j
	s_j		Pleiotropic, trait-external selection (defined > 0 in adaptive model)
	γ_j		Driving rate of s_j
Single site variables	$s_j^f = E_j\langle f'(\Gamma)\rangle$		Average selection generated by trait
	$s_j^{\mathrm{tot}} = s_j^f + s_j$		Effective average single site selection
	$\rho_j \sim \begin{cases}\rho_j^{\mathrm{eq}}, & \text{eq.}^1\\ \gamma_j, & \text{driver}^2\end{cases}, \rho_j^{\mathrm{eq}}$	p_j, —	Resulting independent substitution rate, equilibrium substitution rate ($\gamma_j = 0$)
	$\alpha_j \approx \rho_j/\rho_j^{\mathrm{eq}} \geq 1$, $\alpha_j^{\mathrm{pol}} \geq 1$	From $\hat{N}_{ij}$ or N_{ij}^{pol}	Response asymmetry (equality if $\gamma_j = 0$)
	$\phi_j \approx \rho_j^{\mathrm{eq}} s_j(\alpha_j - 1)$	—	Fitness flux of site
Pairwise variables	$\rho_{ij}^0 = \rho_i\rho_j$	N_{ij}, $\langle N_{ij}^0\rangle \sim p_i p_j$	Null mode of independent evolution
	$\omega_{ij} = -c\frac{E_iE_j}{E_0^2}$	From $\hat{N}_{ij}$ or N_{ij}^{pol}	Epistasis matrix
	$\rho_{ij}(\tau) \approx \rho_{ij}^0 + \rho_i\rho_j^{\mathrm{eq}}\mathrm{e}^{-2\tau/\tau_{\mathrm{eq}}}$	N_{ij}, $\langle N_{ij}\rangle = N_{ij}^0 + \frac{\omega_{ij}}{3\alpha_j}$	Pairwise rates/counts
	$\hat{\rho}_{ij}(\tau) = \rho_{ij}(\tau) - \rho_{ij}^0$ $\approx \rho_{ij}^0\frac{\omega_{ij}^2}{\alpha_j}\mathrm{e}^{-2\tau/\tau_{\mathrm{eq}}}$	$\hat{N}_{ij} = N_{ij} - N_{ij}^0$, $\langle\hat{N}_{ij}\rangle \approx \frac{\omega_{ij}}{3\alpha_j}$	Epistatic response enhancement
	$\rho_{ij}^{\mathrm{pol}}(\tau) = \rho_{ij}^0\frac{\omega_{ij}}{\alpha_j^{\mathrm{pol}}}\mathrm{e}^{-\tau/\tau_{\mathrm{eq}}}$	N_{ij}^{pol}, $\langle N_{ij}^{\mathrm{pol}}\rangle \approx \frac{\omega_{ij}}{2\alpha_j^{\mathrm{pol}}}$	Polarized response rates/counts

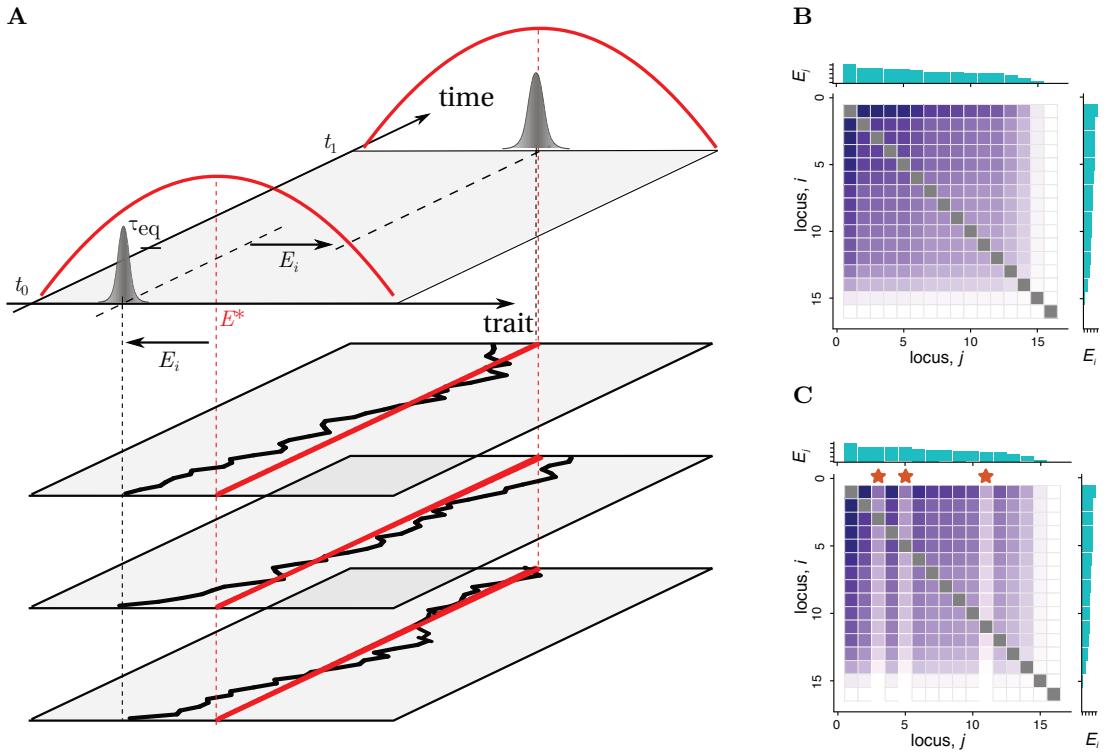

Figure 4.1. Compensatory trait dynamics and QTL correlations. The figure shows the compensatory dynamics on phenotypic level as well as the resulting response correlations. A primary substitution may arises through genetic drift/draft or through external adaptive pressures of the site i. **A** It brings the trait value out of equilibrium by its trait effect E_i at time t_0 and changes selection on all other QTL to compensate its effect. The compensatory process is stochastic and shows multiple microscopic pathways, however the mean effect follows simple dynamics. We derive the resulting time-dependent rates of pairwise substitutions of all pairs of sites, i.e. the dynamics in 2nd order in time. **B** (recapitulation of Fig. 2.1C) These dynamics generate broad epistasis and correlations between all trait loci (color code), which are in equilibrium just determined by the outer product of the trait effect vector $(E_1, \dots, E_\ell)$ (blue on top and right) and a global factor from the mean curvature of the fitness landscape. **C** In the response matrices, driver sites under external adaptive pressures (marked by stars) can be identified by their relatively small compensatory response. Asymmetry in the time-ordered correlation matrix is directly related to adaptation.

$\eta_j = \pm 1$ is the direction of external selection being parallel or anti-parallel to the effect of the focal trait.

For a quantitative analysis we specify a minimalistic model for each site that captures these properties: two environmental states $\eta_j(t) = \pm 1$ set external selection $s_j(t) = \eta_j(t) s_j$ with amplitude $s_j \geq 0$. In non-equilibrium, the external selection flips $\eta_j(t) \to -\eta_j(t)$ with rate γ_j. Nonetheless, the results show largely independence of this particular model specification. We know derive independent state probabilities and substitution rates under this model with trait mean field in local equilibrium, $\gamma_j = 0$, and under adaptation, $\gamma_j > 0$.

Single site equilibrium. In evolutionary *equilibrium*[3] selection is time-independent: single-site selection s_j and trait selection $f(E)$ are constant and thus is the average effective selection

[3]By equilibrium we mean the equilibrium of an undriven focal site together with an mesoscopic equilibrium on trait scale. These are marginal statistics of a high-dimensional steady state or even with driving on other trait sites.

coefficient $s_j^{\rm tot} = s_j + s_j^f$ (2.20). We denote the two equilibrium state probabilities by

$$\Lambda_{{\rm eq},j}^{\epsilon_j} := \Lambda_{\rm eq}(\epsilon_j s_j^{\rm tot}) \quad \text{with} \quad \epsilon_j = \begin{cases} +1, & \overline{\sigma_j} = 1 \\ -1, & \overline{\sigma_j} = 0 \end{cases} \tag{4.1}$$

for the fixed alleles $\overline{\sigma_j} = 0, 1$, cp. Equation (2.1), and with $\Lambda_{\rm eq}(.)$ from Equation (2.23).

The total rate of substitutions of a site j is in equilibrium

$$\check{\rho}_j^{\rm eq} \equiv \Lambda_{{\rm eq},j}^{-\epsilon_j} \mu N G(\epsilon_j s_j^{tot}) = \begin{cases} \mu 2N s_j / \sinh(2N s_j), & \text{(independent mutations)} \\ \mu/(2\cosh(s_j/\tilde{\sigma})), & \text{(strong interference, } s_j \lesssim \tilde{\sigma}), \end{cases} \tag{4.2}$$

where $G(.)$ is either obtained from (2.21) or (2.22). The stronger the site selection, the stronger fluctuations due to genetic drift or draft are constrained.

Single site adaptation. The marginal adaptive dynamics of a trait site is a generalization of [19], who treated a model with symmetric single site selection flips $s_j(t) = \pm|s_j|$ alone. However here, the time-constant average trait selection s_j^f can still constrain the dynamics. For instance for effective adaptive pressures, adaptive selection has to be larger than trait selection, $s_j \gtrsim |s_j^f|$. Therefore, we are in need of 4-state model (ϵ_j, η_j) with two allelic and selection states $\epsilon_j, \eta_j = \pm 1$, each. The transitions between the state probabilities $\Lambda_j^{\epsilon_j,\eta_j}$ are

- substitutions $\epsilon_j \to -\epsilon_j$ with rates $\mu N G_j^{\epsilon_j,\eta_j} := \mu N G(\epsilon_j(s_j^f + s_j\eta_j))$. These depend on the actual environment η_j and fixation probabilities $G(.)$ from either evolutionary mode (2.21) or (2.22).

- environmental changes flipping $\eta_j \to -\eta_j$ with rate γ_j.

We neglect double events $(\epsilon_j, \eta_j) \leftrightarrow (-\epsilon_j, -\eta_j)$.

We obtain the stationary state probabilities $\Lambda_{{\rm stat},j}^{\epsilon_j,\eta_j}$ from the eigenanalysis of the transition matrix, see Appendix D.1. The total substitution rates are obtained from summing over fixation states weighted by their probabilities,

$$\begin{aligned} \rho_{{\rm stat},j}^{\epsilon_j} &\equiv \sum_{\eta_j=\pm 1} \Lambda_{{\rm stat},j}^{-\epsilon_j,\eta_j} \mu N G_j^{\epsilon_j,\eta_j} \\ &= \frac{1}{2}\rho_j^{\rm stat} \equiv \sum_{\epsilon_j=\pm 1} \rho_{{\rm stat},j}^{\epsilon_j}. \end{aligned} \tag{4.3}$$

We find then the limits, well-known for $s_j^f \ll s_j$ or $s_j^f \gg s_j$ [19],

$$\rho_j^{\text{stat}} = \begin{cases} \rho_j^{\text{eq}}, & s_j \lesssim \max(|s_j^f|, 1/N) \text{ or } \\ & \gamma_j/\mu \lesssim N s_j \mathrm{e}^{-2Ns_j} \quad \text{(effectively unadaptive)}, \\ \gamma_j, & s_j \gtrsim \max(|s_j^f|, 1/N) \text{ and } \\ & N s_j \mathrm{e}^{-2Ns_j} \lesssim \gamma_j/\mu \lesssim N s_j \quad \text{(macro-evolutionary adaptation)}, \\ \mu N s_j, & s_j \gtrsim \max(|s_j^f|, 1/N) \text{ and } \\ & \gamma_j/\mu \gtrsim N s_j \quad \text{(micro-evolutionary adaptation)}, \end{cases} \tag{4.4}$$

where it is worth noting that average trait selection balances such that the condition on s_j is typical of order $1/N$ or $\tilde{\sigma}$ if draft dominates, see Equation (2.17). In Equation (4.4), $\rho_j^{\text{eq}} = \frac{\mu N(|s_j^f|-s_j)}{\sinh\left(2N(|s_j^f|-s_j)\right)} + \frac{\mu N(|s_j^f|+s_j)}{\sinh\left(2N(|s_j^f|+s_j)\right)}$ is the equilibrium limit $\gamma_j \to 0$. It deviated from $\check{\rho}_j^{\text{eq}}$ (4.2) by quenched disorder statistics across both selection states $\pm s_j$ with $\rho_j^{\text{eq}} = \check{\rho}_j^{\text{eq}}$ if $s_j = 0$. The exact results are reported in Appendix D.1. Adaptation generically triggers more substitutions.

4.3 Pairwise fixation rates

In this section, we take the independent rate derived in the previous section as the rate of a particular site acting as primary mutation. These cause a selective change that gets compensated by the ensemble of all trait sites on the trait equilibration timescales τ_{eq}. From this window of conditional selection, we derive the rate of observing a compensator substitution at a focal site. In particular, we introduce two time-dependent measures: the total pairwise fixation rate of mutations i and j and the polarized pairwise fixation rate. The latter is taking into account the sign of the trait-directions of mutations. If this information is known, it generates a stronger signal. Both response rates show a simple, but broad rank 1 form, which is mainly determined by the trait effects of the primary and the secondary mutation, cp. Figure 4.1B. Adaptation generates asymmetry, which we discuss in detail in Section 4.4.

In contrast to localized point epistasis, i.e. Mendelian epistasis, the epistatic effect $s_{j|i} \sim \omega_{ij}$ of a quantitative trait is only of short-term after the primary mutation, see Figure 4.2: when the mean trait is brought out of equilibrium by the primary mutation, $\langle\Gamma\rangle \to \langle\Gamma\rangle \pm E_i$, plenty of other QTL can already compensate this before a focal site j takes the opportunity. These compensatory pathways together are by a factor of order ℓ faster than the response time of locus j. Their average can be described on the mesoscopic trait scale by the trait equilibration $\langle\Gamma\rangle_{b_i}(\tau) - \langle\Gamma\rangle = E_i \mathrm{e}^{-\tau/\tau_{\text{eq}}}$, cp. the results of Chapter 3. This is valid because E_i's of quantitative traits are small compared to the trait scale and hence trigger a linear response. Here, $\langle . \rangle_{b_i}$ denotes the average compensatory dynamics of the genetic background conditioned on the primary

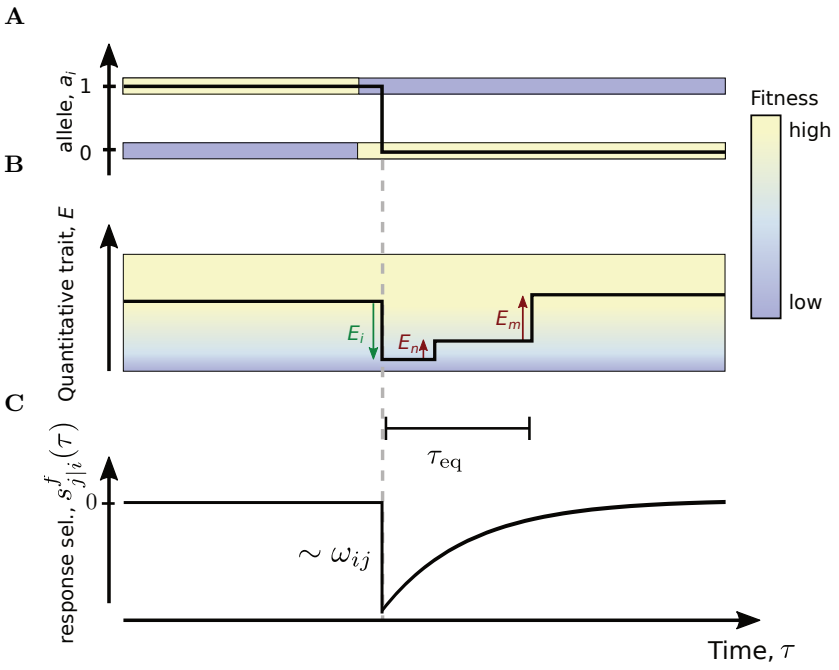

Figure 4.2. Trait epistasis under compensatory background dynamics. **A** Adaptive pressures pleiotropic to the trait visualized by time-dependent allelic fitness, genetic drift, or genetic draft generates a primary allele substitution on site i. **B** It changes the trait value by E_i (green arrow), which is on average deleterious for the trait and triggers compensation on timescale $\tau_{\rm eq}$ by other trait loci, here m and n. These restore the trait value by their effect sizes (red arrows). **C** The conditional response selection coefficient $\langle s^f_{j|i}(\tau)\rangle_{b_i} = \omega_{ij}/(2N)\mathrm{e}^{-\tau/\tau_{\rm eq}}$ (4.5) of a focal site j is negative, if a mutation has the same trait direction as the primary mutation. Dynamically, it decays through the average background compensation from all other trait sites on the trait equilibration time $\tau_{\rm eq} \approx 1/(c\mu)$ (3.5) derived in Chapter 3.

substitution at site i. This could be an ensemble of parallel evolution experiments starting conditioned with populations that just fixed the primary substitution or response statistics with various primary substitutions i spread on a phylogenetic tree, which is a temporal ensemble. The average decay of selection on site j reads then

$$\langle s^f_{j|i}\rangle_{b_i}(\tau) \approx \pm\frac{\omega_{ij}}{2N}\mathrm{e}^{-\tau/\tau_{\rm eq}}, \tag{4.5}$$

where τ is the time since substitution i and ω_{ij} is the characteristic epistatic matrix (2.19). This background meanfield hence changes temporarily the average effective selection at a site. With polarization ϵ_i of substitution i, a mutation with polarization ϵ_j at site j has the effective selection $\epsilon_j(s^{\rm tot}_j(t) + \epsilon_i\frac{\omega_{ij}}{2N}\mathrm{e}^{-\tau/\tau_{\rm eq}})$. The interaction of two particular sites has minor effects on the total trait scale and hence selection scale. Therefore the epistatic interaction ω_{ij} is generally small and we can expand the fixation probability $G^{\epsilon_j,\epsilon_i}_{j|i}(t,\tau) := G\Big(\epsilon_j\big(s^{\rm tot}_j(t) - \epsilon_i|\langle s^f_{j|i}\rangle_{b_i}(\tau)|\big)\Big)$ in ω_{ij},

$$G^{\epsilon_j,\epsilon_i}_{j|i}(t,\tau) = G^{\epsilon_j}_j + \big(G^{\epsilon_j}_j\big)'\epsilon_i\epsilon_j\omega_{ij}\mathrm{e}^{-\tau/\tau_{\rm eq}} + \frac{1}{2}\big(G^{\epsilon_j}_j\big)''\omega^2_{ij}\mathrm{e}^{-2\tau/\tau_{\rm eq}} + \mathcal{O}(\omega^3_{ij}), \quad \forall i,j, \tag{4.6}$$

where $(G_j^{\epsilon_j})^{(n)} = G^{(n)}(\epsilon_j s_j^{\rm tot}(t))$ is the n'th derivative of the unconditional fixation probability from either evolutionary mode (2.21) or (2.22). We obtain the total rate of observing these substitutions at time-distance τ assuming the stationary rate of the primary mutation to be independently given by (4.4),

$$\rho_{ij}^{\epsilon_j,\epsilon_i}(\tau) = \begin{cases} \rho_{{\rm eq},i}^{\epsilon_i}\Lambda_{{\rm eq},j}^{-\epsilon_j}\mu N G_{j|i}^{\epsilon_j,\epsilon_i}(\tau), & \text{(equilibrium)}, \\ \rho_{{\rm stat},i}^{\epsilon_i}\sum_{\eta_j=\pm1}\Lambda_{{\rm stat},j}^{-\epsilon_j,\eta_j}\mu N G_{j|i}^{\epsilon_j,\epsilon_i,\eta_j}(\tau), & \text{(adaptive)}, \end{cases} \qquad \forall i \neq j, \tag{4.7}$$

where we had to average over environmental backgrounds η_j (implicitly in the rate of $\rho_i^{\epsilon_i}$). We used, context-dependent, equilibrium fixation probabilities $G_{j|i}^{\epsilon_j,\epsilon_i}(\tau) = G\Big(\epsilon_j\big(s_j^{\rm tot} - \epsilon_i\epsilon_j|\langle s_{j|i}^f\rangle_{b_i}(\tau)|\big)\Big)$ or environmental dependent fixation probabilities $G_{j|i}^{\epsilon_j,\epsilon_i,\eta_j}(\tau) = G\Big(\epsilon_j\big(\eta_j s_j + s_j^f - \epsilon_i\epsilon_j|\langle s_{j|i}^f\rangle_{b_i}(\tau)|\big)\Big)$; we expand either of these according to Equation (4.6). Equation (4.7) is valid for different sites, $i \neq j$. The self-response $i = j$ deviates strongly: its state is conditioned after the primary substitution. Therefore, the polarization of the next mutation is predetermined and, moreover, single-site selection changes sign. We discuss it in Appendix D.1.

The total rate of observing any pairwise substitutions at sites i and j with temporal distance τ is obtained by summing over mutational polarizations,

$$\begin{aligned} \rho_{ij}(\tau) \equiv \sum_{\epsilon_j,\epsilon_i=\pm1} \rho_{ij}^{\epsilon_j,\epsilon_i}(\tau) &= \rho_i\rho_j + \rho_i\tilde{\rho}_j^{\rm eq}\omega_{ij}^2 {\rm e}^{-2\tau/\tau_{\rm eq}}\left[1 + \mathcal{O}(\omega_{ij}^2, \tau\mu)\right] \\ &=: \rho_{ij}^0\left[1 + (\omega_{ij}^2/\alpha_j){\rm e}^{-2\tau/\tau_{\rm eq}} + \mathcal{O}(\omega_{ij}^4, \tau\mu)\right], \end{aligned} \qquad \forall i \neq j, \tag{4.8}$$

where $\tilde{\rho}_j^{\rm eq} \approx \rho_j^{\rm eq}$, but a factor ~ 1 discussed for its consequences to the asymmetry of (4.8) in Appendix D.1, and $\rho_i = \rho_j^{\rm stat}$. The pairwise rate is enhanced for trait sites $E_i, E_j \neq 0$ compared to the null model of independent evolution, i.e.

$$\rho_{ij}(\tau) > \rho_{ij}^0 := \rho_i\rho_j, \qquad \forall i \neq j. \tag{4.9}$$

The compensatory response has an relative strength $\omega_{ij}^2 \sim (cE_iE_j)^2$ as we confirmed by simulations in Figure 4.3 with time-integrated observables, cp. Methods 4.8. Overall, is proportional to the equilibrium substitution rate $\rho_j^{\rm eq}$, which is the variability of site j constrained by its selection in a constant environmental state. On the other hand, independent rates are set by the total rate ρ_j including adaptive response: the asymmetry factor $\alpha_j = \rho_j/\rho_j^{\rm eq} \geq 1$ suppresses the relative response of j in substantial non-equilibrium, which we discuss extensively in the next section.

We introduce a polarized measure $\rho_{ij}^{\rm pol}(\tau)$ by taking the relative direction of trait effects of primary to compensatory mutation into account, i.e. $\epsilon_i\epsilon_j$. It measures the rate difference of parallel and anti-parallel substitutions with respect to the trait direction:

$$\begin{aligned} \rho_{ij}^{\rm pol}(\tau) &\equiv \sum_{\epsilon_j,\epsilon_i=\pm1} \epsilon_i\epsilon_j\rho_{ij}^{\epsilon_j,\epsilon_i}(\tau) \\ &= \rho_{ij}^0(\omega_{ij}/\alpha_j^{\rm pol}){\rm e}^{-\tau/\tau_{\rm eq}}\left[1 + \mathcal{O}(\omega_{ij}^2, \tau\mu)\right], \end{aligned} \qquad \forall i \neq j, \tag{4.10}$$

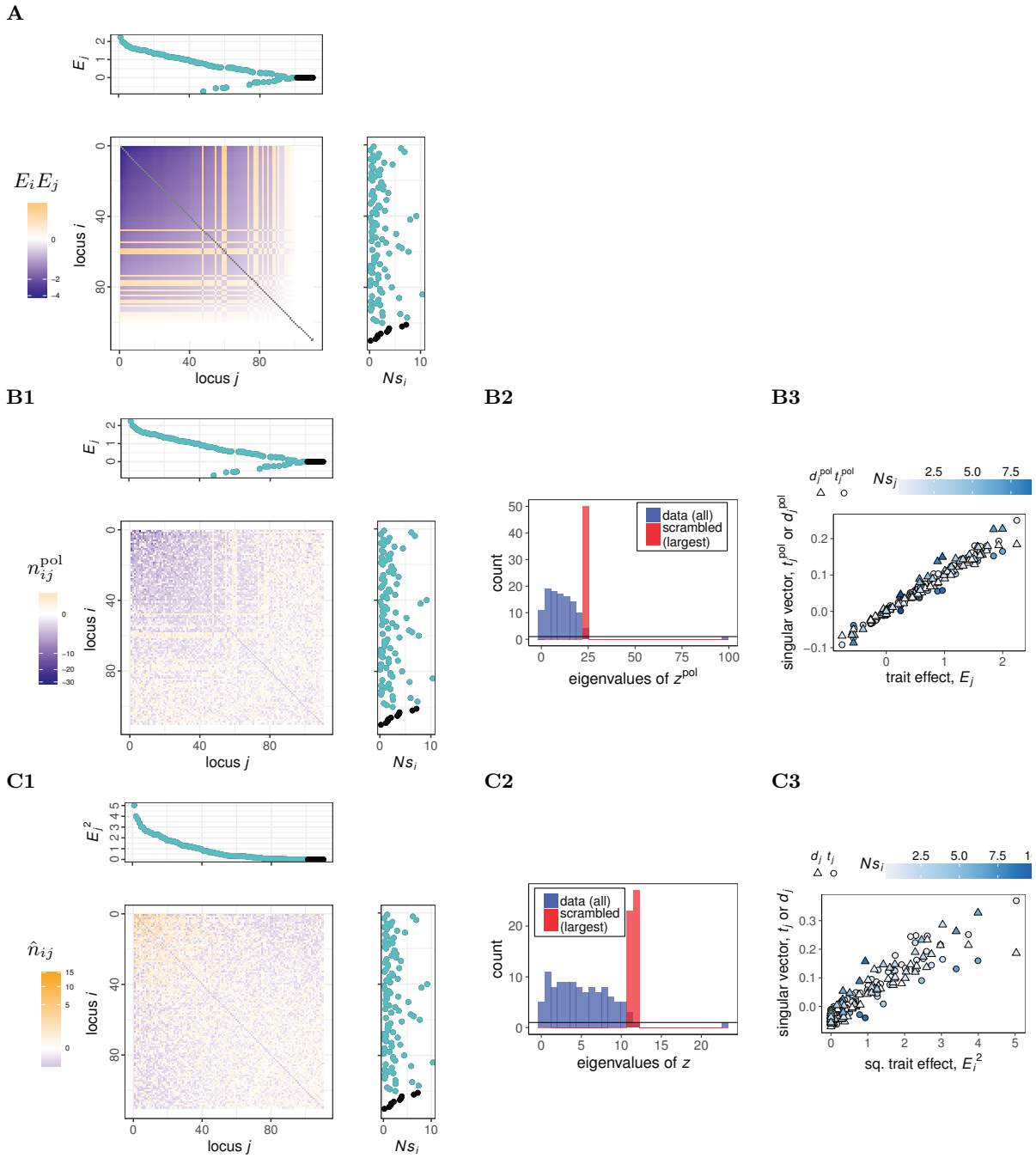

Figure 4.3. A quantitative trait generates broad correlations of low dimension. We simulate the evolution of a quantitative trait that generates the broad response pattern. **A** Simulation parameters: the trait effects E_i are shown on top (blue: trait sites, black: independent sites) and the epistasis $\omega_{ij} \sim -E_i E_j$ obtained from their outer product is shown as color matrix, cp. Figure 2.1C. Epistasis is not influenced by the single site selection coefficients s_i (right). The other parameters are $N = 1000, c = 100$, and $\gamma_i = 0.8\mu$ for all sites. **B1**–**C1** Enhancement of the response rates weighted by temporal proximity ($\tau_0 \sim 2$ substitutions), cp. Methods 4.8. The shown observables are: **B1**) the polarized response measured by $n_{ij}^{\mathrm{pol}} := N_{ij}^{\mathrm{pol}}/N_{ij}^0 \sim \rho_{ij}^{\mathrm{pol}}(0)$ (4.10) and **C1**) the total response with all substitutions measured by $\hat{n}_{ij} := \hat{N}_{ij}/N_{ij}^0 \sim \hat{\rho}_{ij}^{\mathrm{pol}}(0)$ (4.8). The simulations retrieve the trait pattern, which is noisy on pairwise level. Sites with $E_i < 0$ are visible with average negative sign in the polarized response. **B2**, **B3**, **C2**, **C3** A singular value decomposition on standard normalized data [138], see Methods 4.8, retrieves the trait effects of sites. **B2**,**C2** Spectrum of this significance matrix (blue) related to correlation matrices B1 and C1, respectively. Red: spectrum of first singular value of randomized process (null model) with correlations just by noise. Both measurements show a single significant singular value generated by the trait. **B3**,**C3** The singular vectors associated to the significant singular value show strong correlation with trait effects, i.e. $n_{ij}^{\mathrm{pol}} \sim E_i E_j \sim t_i^{\mathrm{pol}} d_j^{\mathrm{pol}}$ and $n_{ij} \sim E_i^2 E_j^2 \sim t_i d_j$. Here and in all other simulations, sites with less than 5 substitutions were excluded from the analysis. Data run to collect in total 40,000 substitutions.

with a factor $\alpha_j^{\rm pol} \geq 1$ suppressing the response of j in non-equilibrium. This we discuss together with α_j in detail in the next section. We verify this pattern by simulations in Figure 4.3. For trait sites $E_i, E_j \neq 0$, this rate is anti-correlated $\rho_{ij}^{\rm pol}(\tau) \sim -E_i E_j$. It is 0 if one site is not contributing to the trait. Since this response measures the first order in ω_{ij}, it gives a stronger signal than the correlations of all substitutions. However, the polarization is often a-priori unknown for biological data and, thus, this measure cannot be used.

Heterogeneous mutation rates μ_j would change total rates, i.e. $\rho_j \sim \mu_j$ and $\rho_j^{\rm eq} \sim \mu_j$, but not the relative effect imposed by trait epistasis. The key characteristics of the trait response measures (4.8) and (4.10) are

- **Time window for compensatory response.** An enhanced response is only observed on a short trait-equilibration timescale $\tau_{\rm eq}$. This is a dynamical consequence of the compensation by other trait sites, cp. Figure 4.2.

- **Generically broad, low rank correlations.** The rates are determined by broad matrices across all QTL. However, these show a simple, low rank pattern, cp. Figure 4.3: for the unpolarized rates (4.8), the independent model $\rho_{ij}^0 = \rho_i \rho_j$ without trait correlations is of rank 1 determined by single-site fixation rates only. The trait response itself adds another rank to the matrix, $\rho_i \tilde{\rho}_j^{\rm eq} \omega_{ij}^2$, since $\omega_{ij} \sim -E_i E_j$ is just determined by the outer product of trait effects. The simplicity of ω_{ij} also makes the polarized response $\sim \rho_{ij}^0 \omega_{ij}/\alpha_j$ to be of rank 1. Furthermore, co-evolving traits would add more independent ranks, as can be seen in Equation (4.16) discussed in detail in Section 4.5. Therefore, a quantitative traits generates broad and flat correlation patterns. This is an universal property that ℓ^2 epistatic correlations can be explained by ℓ parameters: each site's epistatic interaction with all other trait sites is characterized by its own trait effect. That allows the inference of trait effects, which we indeed retrieve in the presented simulations in Figures 4.3, 4.5, and D.2.

  A caveat concerns the diagonal elements of the response matrix as discussed in Appendix D.1. However, the impact of the diagonal to the full response matrix is localized and hence by a factor $\sim 1/\ell \ll 1$ smaller, which we can ignore in the further analysis.

- **Adaptation generates asymmetry,** which can even be inferred from these time-resolved correlations. This we discuss in detail in the following section.

4.4 Adaptation generates asymmetry

Here we discuss the asymmetry observed in both response rates, $\rho_{ij}(\tau)$ and $\rho_{ij}^{\rm pol}(\tau)$, cp. Figure 4.1C, which arises if the focal site for the secondary mutation is under strong adaptive pressure. Significant asymmetry in the correlation matrices means that the underlying process is in non-equilibrium. It is stronger, the farer the system is from equilibrium. We hence relate the strength of asymmetry to the fitness flux and discuss how it can be used to infer the genotype–phenotype map together with site-adaptation.

The symmetry properties of ρ_{ij} and ρ_{ij}^{pol} allow to distinguish strong non-equilibrium from equilibrium of particular sites: it measures how strong detailed balance $\rho_{ij}(\tau) = \rho_{ji}(\tau)$ and $\rho_{ij}^{\mathrm{pol}}(\tau) = \rho_{ji}^{\mathrm{pol}}(\tau)$ is broken. Using time-dependent observables for inferring non-equilibrium has been identified useful in Ising models with asymmetric couplings [139]. The asymmetry factors of the rates, α_j and α_j^{pol}, arise from constrained responses for adaptive sites and are functions of its selection parameters. Under Kimura-substitution[4] probabilities (2.21), they read

$$\alpha_j \approx \frac{\rho_j}{\rho_j^{\mathrm{eq}}} \geq 1 \tag{4.11}$$

$$\alpha_j^{\mathrm{pol}} = \frac{1 + b_1(s_j, s_j^f)\gamma_j/\mu}{1 + b_2(s_j, s_j^f)\gamma_j/\mu} \geq 1, \tag{4.12}$$

with equality to 1 in equilibrium and for low efficacy of selection $s_j \lesssim 1/(2N)$. This also includes the limit under interference selection described by (2.22). The full solutions are reported in Appendix D.1.

α_j compares the rate of site substitutions in equilibrium with the increased rate through adaptation in non-equilibrium, $\rho_j > \rho_j^{\mathrm{eq}}$; hence it is a measure of a site being busy with adaptation while response is determined by (short-term) equilibrium rates. We have inherited scaling behavior from Equation (4.4), which is shown in Appendix Figure D.1A,

$$\alpha_j \approx \begin{cases} 1, & s_j \lesssim \max(|s_j^f|, 1/N) \\ & \text{or } \gamma_j \lesssim \rho_j^{\mathrm{eq}} \quad \text{(ineffective driving)}, \\ \dfrac{\gamma_j}{\rho_j^{\mathrm{eq}}}, & s_j \gtrsim \max(|s_j^f|, 1/N) \\ & \text{and } \rho_j^{\mathrm{eq}} \lesssim \gamma_j \lesssim \gamma_j^{\mathrm{m}} \quad \text{(macro-evolutionary adaptation)}, \\ \dfrac{\mu N s_j}{\rho_j^{\mathrm{eq}}} \equiv \dfrac{\gamma_j^{\mathrm{m}}}{\rho_j^{\mathrm{eq}}}, & s_j \gtrsim \max(|s_j^f|, 1/N) \\ & \text{and } \gamma_j \gtrsim \gamma_j^{\mathrm{m}} \quad \text{(micro-evolutionary adaptation)}, \end{cases} \tag{4.13}$$

with the transition rate to micro-evolutionary seascapes $\gamma_j^{\mathrm{m}} \equiv \mu N s_j$, where adaptive fluctuations are too quick for the adaptation [106]. Asymmetry is visible for substantial single site selection $s_j \gtrsim s_j^f, 1/N$, if the rate of adaptation exceeds the equilibrium fluctuations of that site, $\gamma_j \gtrsim \rho_j^{\mathrm{eq}}$. The asymmetry factor increases with stronger driving, which is increasing either γ_j or s_j. We call such sites under measurable adaptive pressure driver sites and the rest trailer sites, which tend to compensate more if single site selection is not substantial. Under moderate, macro-evolutionary driving, the asymmetry factor scales $\alpha_j \sim \frac{\gamma_j}{2\mu} \mathrm{e}^{2N(s_j - |s_j^f|)}/(N s_j)$; under strong, micro-evolutionary driving $\gamma_j \gtrsim \gamma_j^{\mathrm{m}}$ it becomes independent of γ_j, $\alpha_j \sim \mathrm{e}^{2N(s_j - |s_j^f|)}$. Hence it can take large values even under moderate driving for strongly selected sites, because it would almost never compensate a deleterious mutation. We show this effect qualitatively for strong adaptive sites in simulations in Figure 4.4B,D and for mildly adaptive sites with comparable parameters to

[4] Under strong interference dynamics in the limit $s_j \lesssim \tilde{\sigma}$, Equation (2.22), the response is symmetric $\alpha_j/2 = \alpha_j^{\mathrm{pol}} = 1$: individual sites are under weak selection by definition, compared to the fitness distribution within a population.

Figure 4.3 in Appendix Figure D.1C.

The polarized asymmetry $\alpha_j^{\rm pol}$ is depicted in Appendix Figure D.1B. It also increases with driving strength, i.e. both, rate γ_j and selection s_j. Sites under strong adaptive pressures have again a suppressed compensatory response. The scaling regimes are

$$\alpha_j^{\rm pol} \approx \begin{cases} 1, & s_j \lesssim \max(|s_j^f|, 1/N) \\ & \text{or } \gamma_j \lesssim \rho_j^{\rm eq} \end{cases} \quad \text{(ineffective driving)},$$

$$\frac{\gamma_j}{\rho_j^{\rm eq}}, \quad \begin{array}{l} s_j \gtrsim \max(|s_j^f|, 1/N) \\ \text{and } \rho_j^{\rm eq} \lesssim \gamma_j \lesssim \gamma_j^{\rm m}\rho_j^{\rm eq}/\mu \end{array} \quad \text{(weak, macro-evolutionary adaptation)},$$

$$Ns_j \equiv \frac{\gamma_j^{\rm m}}{\mu}, \quad \begin{array}{l} s_j \gtrsim \max(|s_j^f|, 1/N) \\ \text{and } \gamma_j \gtrsim \gamma_j^{\rm m}\rho_j^{\rm eq}/\mu \end{array} \quad \text{(fast driving)}. \tag{4.14}$$

For substantial single site selection, the asymmetry factor gets significant again when exceeding the equilibrium substitution rate $\gamma_j \sim \rho_j^{\rm eq}$. It also compares the rate of adaptation with equilibrium fluctuations and allows for the same definition of driver/trailer sites like α_j. However, here the transition to the second regime without further scaling in γ_j is much lower than the micro-evolutionary regime at $\gamma_j \sim Ns_j\rho_j^{\rm eq} = \gamma_j^{\rm m} {\rm e}^{-2N(s_j - |s_j^f|)} \ll \gamma_j^{\rm m}$; it saturates to much lower values limited by its selection coefficient. Preliminary studies show that this asymmetry is qualitatively supported by these equations. This we show by simulations in Figure 4.4A,C for strong drivers and in Appendix Figure D.1C for mildly adaptive sites with comparable parameters to Figure 4.3.

The asymmetries α_j and $\alpha_j^{\rm pol}$ have important implications for time-ordered correlation measures: while all sites give a correlation signal independent of their particular selection as primary mutation, their compensatory response is basically 0 under strong adaptation. If selection of driving is large enough to overcome constraining trait selection and drift, their dependence on the driving rates is given by characteristic rates. These are particularly the mutation rate μ, the equilibrium fixation rate $\rho_j^{\rm eq}$, and the characteristic scale for the transition to micro-evolutionary seascapes $\gamma_j^{\rm m}$. This result is supposedly independent from the details of the underlying minimal model of driving. We call sites with substantial driving rates $\gamma_j > \rho_j^{\rm eq}$ driver sites and the rest trailer sites, which can be identified from their highly asymmetric response, see Figure 4.4A–D.

Fitness flux. The fitness flux measures the average fitness gain in response to external adaptive pressures. It also measures, similarly to the heat flux in statistical physics, the deviation from detailed balance [60]. In our non-equilibrium model for single-site driving, the stationary trait dynamics generates no fitness flux since it is under constant selection $f(E)$. Hence we can define a fitness flux ϕ_j for each site from its adaptive response to the single site driving γ_j; deleterious effects of this response onto the trait are on average compensated by trailer sites.

In the macro-evolutionary limit, when selection has enough time to adapt, the fitness flux is obtained from the enhancement of single-site rates and can therefore be linked to the total

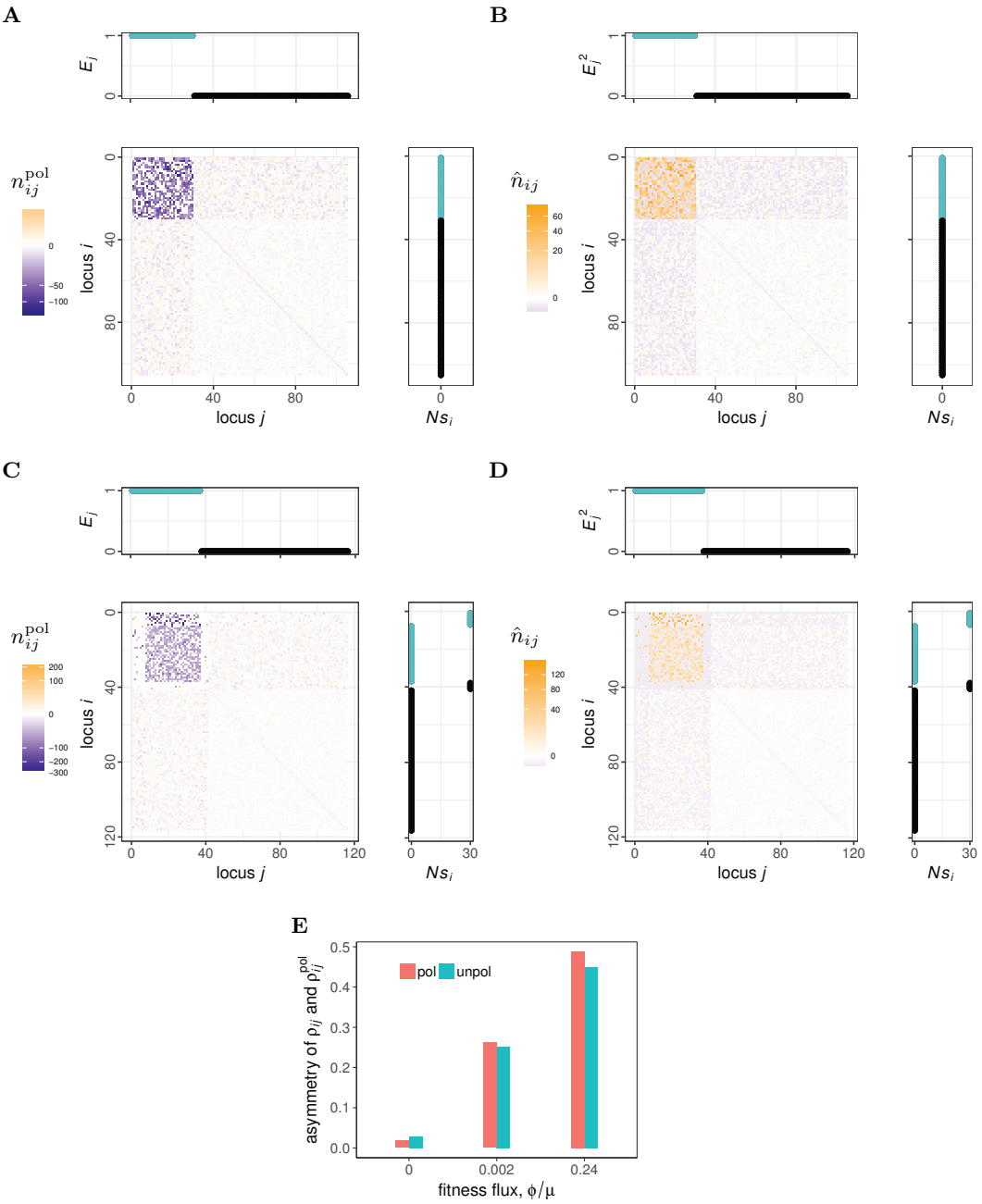

Figure 4.4. Adaptation generates asymmetric response correlations. We simulate with 40 trait sites ($E_i = 1$, blue) and 80 trait-independent sites ($E_i = 0$, black). Each set has 10 sites under substantial selection with $Ns_i = 30$. **A,B** Simulations without driving in evolutionary equilibrium. Sites s_i are excluded because they show no variability. **C,D** Contains driver sites (the set with $s_j \neq 0$), which have driving rates exponentially distributed with mean $\overline{\gamma}_i = 0.004\mu$. **A,C** show n_{ij}^{pol} similar to Figure 4.3B1. **B,D** shows $\hat{n}_{ij}$ similar to Figure 4.3C1. The other simulation parameters are the same. While the equilibrium matrices are symmetric apart from local noise, the non-equilibrium asymmetry of driver sites ($s_i \neq 0$ and $E_i \neq 0$) is clearly visible in the suppressed response as a compensatory mutation of panels C and D. **E** This asymmetry is clearly related to non-equilibrium and hence adaptation of some QTL. The panel shows the global asymmetry of the response matrices $\hat{n}_{ij}$ (blue) and n_{ij}^{pol} (red) against the observed cumulative fitness flux $\phi = \sum_{i\in\text{drivers}} \phi_i \approx \sum_{i\in\text{drivers}} \rho_i s_i$ for various simulation parameters (ϕ-scale non-linear). The first two measurements correspond to the matrices in panels A,B and C,D. We measure the asymmetry of a matrix as squared L2-norm of the asymmetric part divided by the full squared L2-norm, i.e. between 0 and 1. The asymmetry is monotonically increasing with the fitness flux: it is a measure for adaptation. However it saturates per driver site since their compensatory response is basically 0. In Figure D.1C,D we show the site-specific asymmetry for weaker driving.

count asymmetry

$$\phi_j \approx s_j(\rho_j - \rho_j^{\mathrm{eq}}) \approx s_j \rho_j^{\mathrm{eq}} (\alpha_j - 1) \geq 0, \tag{4.15}$$

where driving is captured by the asymmetry factor $\alpha_j \geq 1$. The fitness flux ϕ_j is 0 in equilibrium [60], where the response is symmetric, i.e. $\alpha_j = 1$. The same relation holds for the polarized asymmetry in the regime of weak macro-evolutionary adapation (4.14), $\gamma_j \gtrsim \gamma_j^{\mathrm{m}} \rho_j^{\mathrm{eq}}/\mu$, where $\alpha_j^{\mathrm{pol}} = \alpha_j$. In Figure 4.4D and Appendix Figure D.1D, we show that the asymmetry is indeed an increasing function of the fitness flux, though its quantitative scaling is out of numerical reach as discussed in the figure caption. In Appendix D.1, we generalize our pairwise rates from substitution rates to rates of finite allele frequencies for observing primary and secondary mutations [21]. This permits the application on phylogenetic trees, which we do in a follow up paper [138]. Distinct observation frequencies for driver- and trailer-mutations influence the symmetry of the null mode ρ_{ij}^0 only, but not the response asymmetry α_j, cp. Appendix D.1. Hence, they are not false positively related to adaptation: asymmetry in the correlation matrix is a pure pattern of adaptive sites.

Inference of the genotype–phenotype map and adaptation. The time-dependent rates[5] $\rho_{ij}(\tau)$ or $\rho_{ij}^{\mathrm{pol}}(\tau)$ can be measured if the temporal order and distance of mutations is known. This applies for instance to phylogenetic trees, even under strong adaptation biasing the tree. The causality information allows to infer both, epistasis and adaptation: for a particular site, the response rate by all other sites quantifies the trait effect E_j. The suppressed response $\rho_j/\rho_j^{\mathrm{eq}}$ reveals sites that are targets of adaptation. It measures the adaptive trait fluctuations in units of its (in principle unknown) variability without external pressure. Impressively, also the 2nd order measurement in $\rho_{ij}^{\mathrm{pol}}(\tau)$ can reveal more information of the adaptive process than classical sequence based tests such as the McDonald-Kreitman test [130], which compares substitution rates ρ_j with the null model of neutral evolution, $\rho_j^0 = \mu$. A symmetrized measure, e.g. $\rho_{ij}(\tau) + \rho_{ji}(\tau)$ or Pearson correlations, would not be able to distinguish adaptation from a smaller trait effect E_j.

4.5 Co-evolutionary quantitative traits

In this section, we extend the discussion to multiple co-evolving traits that shape the correlation pattern. We start by discussing 2 traits and extend the discussion to g co-evolving traits. We see that the polarized response $\rho_{ij}^{\mathrm{pol}}(\tau)$ produces as many ranks as traits co-evolve. From the singular modes associated to these ranks, all genotype-phenotype maps can be retrieved. In principle this is the same for $\hat{r}_{ij}(\tau)$ too, however with the caveat that a pair of highly pleiotropic traits can contribute an additional rank to the response pattern.

[5] And hence derived, time-integrated statistics such as $N_{ij} \sim \int \mathrm{d}\tau \rho_{ij}(\tau) \mathrm{e}^{-\tau/\tau_0}$ or $N_{ij}^{\mathrm{pol}} \sim \int \mathrm{d}\tau \rho_{ij}^{\mathrm{pol}}(\tau) \mathrm{e}^{-\tau/\tau_0}$ introduced in [138] and recapitulated in Methods 4.8.

Fitness is clearly not made up by a singular quantitative trait alone, but by a set of these. This is even the case when studying the evolution of single proteins maintaining stability and possibly different functions, cp. Section 2.3. Multiple correlation sectors associated with different functions have been observed in data [81] bringing the co-evolutionary pattern of various traits to high interest.

We start the discussion with the evolution of 2 co-evolving quantitative traits, E and G, which can be in general pleiotropic. We ignore functional epistasis between traits: we consider only fitness epistasis of sites through the non-linear selection of each individual trait. Nonetheless, the analysis is easily extended towards epistatic relation between traits, as we discuss in Appendix B. This can be relevant to study proteins as discussed in Section 2.3. As we derive in Appendix B, the epistatic selection coefficient between site i and j is a generalization of (2.19) by summing over the epistasis of all genes

$$\omega_{ij} = \omega_{ij}^E + \omega_{ij}^G = -2Nc_0^E E_i^E E_j^E - 2Nc_0^G E_i^G E_j^G. \tag{4.16}$$

We depicted the epistasis in Figure 4.5A for non-pleiotropic and Appendix Figure D.2 for highly pleiotropic traits. The superscript E or G stand for the corresponding parameters of the particular trait. The epistasis matrix is no longer of rank 1, but confers another rank for the 2nd trait. The pairwise substitution rates (4.8), (4.10), and (D.6) depend then on the generalized ω_{ij} (4.16).

We now define polarized rates ρ_{ij}^{pol} with respect to allelic state, they can be defined with respect to one of the traits or generalized to a measure taking the polarization of all traits into account. They show, $\rho_{ij}^{\text{pol}} \sim \omega_{ij}$, 1 rank per trait, which allows to retrieve the number of traits and the trait effects as we support by simulations in Figures 4.5B1–B3 and D.2B1–B3. We use a singular value decomposition described in Methods 4.8 and Appendix D.2 for the analysis, which we developed in [138].

The signal in the total rates $\rho_{ij} - \rho_{ij}^0 \sim \omega_{ij}^2$ is quadratic. The quadratic expansion of ω_{ij}^2 gives one rank for each within-trait dynamics, i.e. $\sim (c_0^E E_i^E E_j^E)^2$ and $\sim (c_0^G E_i^G E_j^G)^2$, and an additional across-trait rank for pleiotropic sites $\sim c_0^E c_0^G E_i^E E_i^G E_j^E E_j^G$, which we find in the simulations for highly pleiotropic traits D.2C1–C3. The latter captures pleiotropic information relevant for the dynamics: let a primary mutation be deleterious in both traits and a site j could compensate E, but would be deleterious in G, too. Then this site would show a weak response though it is beneficial for E. Therefore, these additional terms in principle allow to measure polarizations of site mutations between traits. However, if the degree of pleiotropy between traits is small, the additional rank is localized in the response matrix and it reduces to one significant rank per trait. This we show in Simulations 4.5C1–C3 for non-pleiotropic traits allowing us to retrieve the 2 traits and the trait effects from the singular value decomposition.

The results generalize to g co-evolving traits with epistatic matrix $\omega_{ij} = \sum_{g'=1}^{g} \omega_{ij}^{g'} = -\sum_{g'=1}^{g} 2Nc_0^{g'} E_i^{g'} E_j^{g'}$, cp. Appendix B. Here, the superscript stands for the parameters of the g'th trait. In principle, the polarized rates show g ranks and the total rates show g within-trait ranks and possibly up to $g(g-1)/2$ further ranks through broad pairwise pleiotropy. However,

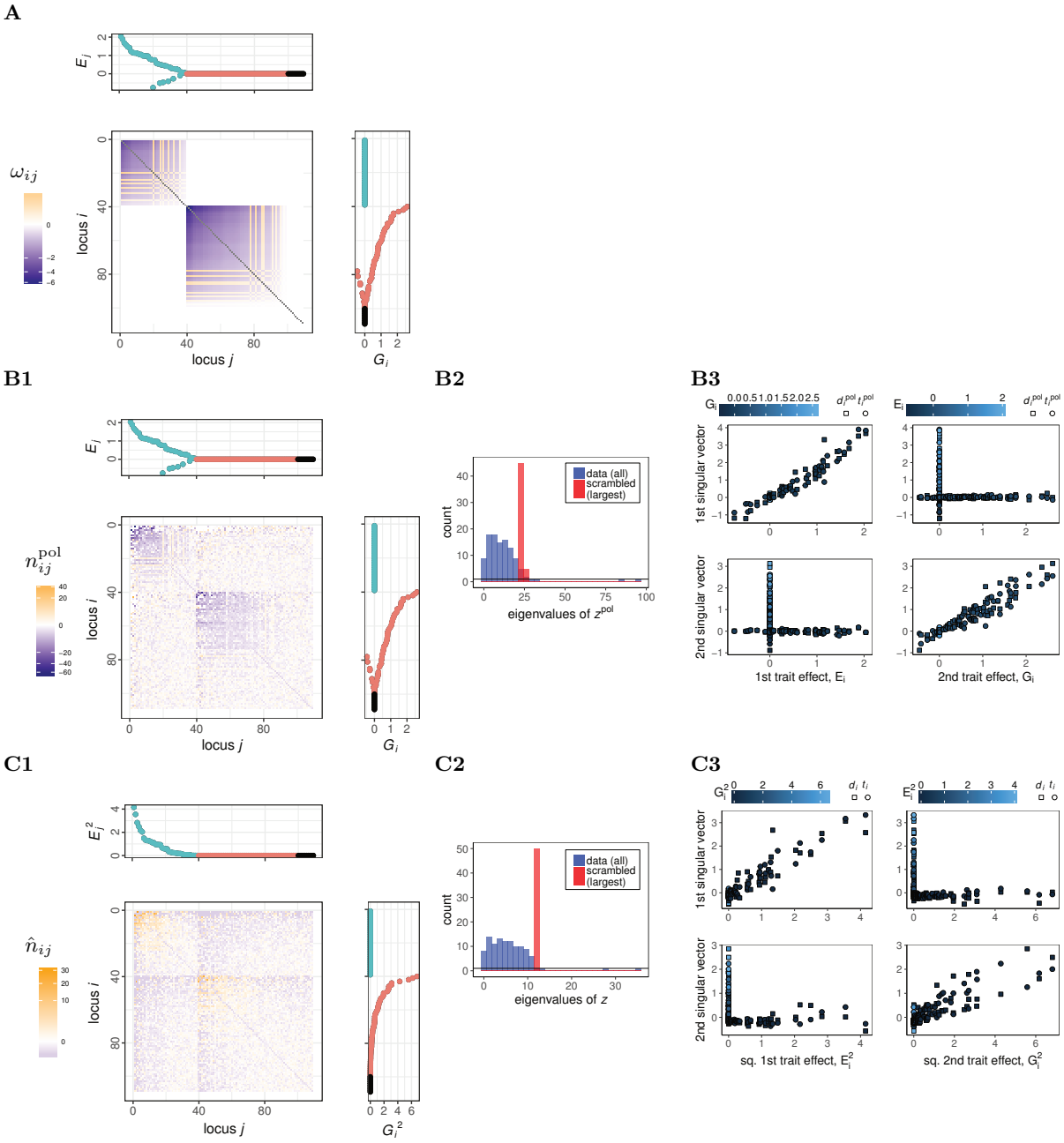

Figure 4.5. Epistasis and correlations generated by 2 quantitative traits Figure similar to Figure 4.3, however with two non-pleiotropic quantitative traits with trait effects E_i (blue trait in marginal plots) and G_i (red trait in marginal plots). **A**,**B1**,**C1** The right, marginal panels show now the 2nd trait component G_i (instead of s_i in Figure 4.3). Two non-pleiotropic traits generate two distinct epistatic sectors in ω_{ij}, Equation (4.16), and hence a similar, two-sector pattern in the response rates. **B2**,**C2** These sectors are each related to a significant singular value in the polarized and the unpolarized response: this number in principle allows to infer the number of traits in an evolutionary process. **B3**,**C3** The two singular vectors of the significant modes of the correlations well retrieve the trait effects. Here shown after a varimax rotation. It retrieves the orthogonal trait contributions and hence allows to infer both trait effects E_i and G_i independently. In Appendix Figure D.2, we show the corresponding results for two highly pleiotropic traits.

the degree of pleiotropy is limited in actual biological data [140] such that the number of ranks should scale with the number of traits determining selection. A difficulty in data analysis arises to distinguish for instance 3 traits from 2 pleiotropic traits under strong pleiotropy. However, it is in principle possible to retrieve the number of traits and site effects to each trait, since the cross-trait effects are clearly related to the within-trait effects.

To conclude, polarized rates ρ_{ij}^{pol} directly allow to infer the number of traits from the rank of the response matrix and the trait effects from the significant singular vectors. The same is valid for unpolarized rates $\hat{\rho}_{ij}$, if the traits are only locally pleiotropic. However, if there are more than 3 significant ranks observed and broad pleiotropy cannot be excluded a-priori, the degree of pleiotropy has to be studied carefully. As a bonus, in that case the polarization of the mutations in relation to the traits is measurable.

4.6 Trait constraints

In this section, we relate the sector generated by a trait to the constrained divergence discussed in Chapter 3. Unsurprisingly, the pairwise rates explain the stabilizing selection up to second order in time. This allows to relate the response matrices to predictability of the evolutionary process.

The compensatory effects have their origin in the selective constraints on trait level. These constraints on trait level were already discussed in context of the divergence curve, $\Omega^{(1)}(\tau) = 2\theta\frac{\langle D^{(1)}\rangle(\tau)}{\langle\Delta\rangle}$, Equation (3.59) and Figure 3.4 in Chapter 3. In the present model, the trait itself is not under adaptation and follows an equilibrium divergence ($\nu = 0$), $\Omega^{(1)}(\tau) \approx \frac{1}{c}\left(1 - \exp(-\tau/\tau_{\mathrm{eq}})\right)$. Here, we relate this divergence pattern to the pairwise correlation functions of trait sites.

We denote fixed site alleles by $\overline{\sigma}_i = 1, 0$ (2.1). In the substitution dynamics of site alleles, the rates ρ_i and conditional rates ρ_{ij}^{pol} weighted with trait effects generate the divergence,

$$\begin{aligned}\langle D(t,\tau)\rangle &= \left\langle \left(\Gamma(t+\tau) - \Gamma(t)\right)^2 \right\rangle = \left\langle \left(\sum_{i=1}^{\ell} E_i \left(\overline{\sigma}_i(t+\tau) - \overline{\sigma}_i(t)\right)\right)^2 \right\rangle \\ &= \sum_{i=1}^{\ell} E_i^2 \left\langle \Delta\overline{\sigma}_i^2 \right\rangle (t,\tau) + \sum_{j\neq i=1}^{\ell} E_i E_j \left\langle \Delta\overline{\sigma}_i \Delta\overline{\sigma}_j \right\rangle (t,\tau), \end{aligned} \tag{4.17}$$

with allele changes $\Delta\overline{\sigma}_i(t,\tau) := \left(\overline{\sigma}_i(t+\tau) - \overline{\sigma}_i(t)\right) = -1, 0, 1$. These have stationary cross-correlation functions

$$\begin{aligned}\left\langle \Delta\overline{\sigma}_i^2 \right\rangle_{\mathrm{stat}}(\tau) &= \int_0^\tau \mathrm{d}t' \rho_i^{\mathrm{stat}} + \mathcal{O}(\mu\tau)^2 = \rho_i^{\mathrm{stat}}\tau + \mathcal{O}(\mu\tau)^2, \\ \langle \Delta\overline{\sigma}_i \Delta\overline{\sigma}_j \rangle_{\mathrm{stat}}(\tau) &= \int_0^\tau \mathrm{d}t' \int_{t'}^\tau \mathrm{d}\tau' (\rho_{ij}^{\mathrm{pol}}(\tau', \tau'-t') + \rho_{ji}^{\mathrm{pol}}(\tau', \tau'-t')) + \mathcal{O}(\mu\tau)^3 \\ &= -(\rho_i\rho_j\tau^2)\frac{1}{2}\omega_{ij}(1/\alpha_i^{\mathrm{pol}} + 1/\alpha_j^{\mathrm{pol}}) + \mathcal{O}\left(\tau^3\mu^2/\tau_{\mathrm{eq}}\right), \quad \forall i \neq j, \end{aligned}$$

where the single-site change is linear and the cross-correlation quadratic in time. The quadratic

contribution of the former is negligible since a factor $1/\ell$ weaker than the integral cross-site compensation.

We restrict on $Ns_j \lesssim Ns_j^f$ for the majority of sites such that the asymmetry can be neglected, $\alpha_j^{\rm pol} \approx 1$, in the sum over sites. We then retrieve the stationary divergence in the integral over all sites

$$\begin{aligned}\langle D(\tau)\rangle_{\rm eq} &= \tau \sum_{i=1}^{\ell} E_i^2\rho_i - \tau^2 \frac{c}{2E_0^2} \sum_{j\neq i=1}^{\ell} \rho_i E_i^2 \rho_j E_j^2 + \mathcal{O}(\tau^3(\mu\ell)^2/\tau_{\rm eq}, \tau^2\mu^2\ell) \\ &= 4\mu\tau E_0^2\,(1-\tau/\tau_{\rm eq}) + \mathcal{O}(\tau^3(\mu\ell)^2/\tau_{\rm eq}, \tau^2\mu^2\ell),\end{aligned}$$

up to second order in time by the pairwise compensation. Higher orders in time would need higher order correlations, $\rho_{ijk}(\tau,\tau')$ and so forth, which we do not consider here. The mesoscopic trait dynamics is not strongly influenced by single-site driving, because of the quick compensation time through the integral effect of all sites. This is of course not valid, if most sites contributing to the trait are driver sites. However in this evolutionary mode, trait selection would be ineffective and irrelevant compared to the external selection.

The relation to the constrained trait-divergence allows to relate the response rates to the phenotypic predictability of the evolutionary process as discussed in [53], which is the short-term time-dependence of the predictability discussed in Section 3.4.3 ($v = 0$). The individual response of single sites is highly stochastic. However, the predictability is conserved on trait level. After a driver mutation, it is very likely that any of the multiple QTL will compensate its effect. This can improve predictions of the evolutionary process [7, 10, 11].

The macro-evolutionary adaptive Ω-test of Section 3 measures the directional v vs. constraining selection c of the trait itself. This test is insensitive to occasional single-site adaptive pressures, which get quickly compensated by the numerous trait sites. Substantial single-site constraints influence the trait diversity and the divergence in the same way. Therefore, they are not influencing the shape of the divergence curve. They are absorbed in an effective weaker trait scale $E_0^2 = \frac{1}{4}\sum_i E_i^2\rho_i/\mu$. This just demands for a reinterpretation of the parameter c in this model. Selection is not selection measured on the trait-scale of random sequences, but the expected trait variation without trait selection $E_0^2 = \lim_{c,\mu\to 0}\langle\hat{\Gamma}^2\rangle$, which is smaller through single-site constraints. The scale E_0^2 leaves the fitness flux of trait adaptation anyway invariant.

The pairwise correlation measure can also be generalized to the adaptive phenotype divergence discussed in Section 3. If the mean trait value follows a fitness peak moving with diffusion constant v_0, trait sites follow coherently. A self-consistent closure shows positive correlations $\langle\Delta\overline{\sigma}_i\Delta\overline{\sigma}_j\rangle_{\rm stat}(\tau) \sim c_0 v_0\mu\tau E_i E_j > 0$ on macro-evolutionary timescales $\tau > 1/(c\mu)$ arising from this coherent adaptation. The detection of this evolutionary mode from single sites would demand for long-term correlation measurements, which is not discussed in detail in this thesis.

4.7 Conclusions and outlook

In this chapter, we showed that the constrained evolution of quantitative traits generate a broad, but simple low rank epistatic correlation pattern. This pattern originates from the compensatory pressures induced by a primary mutation effecting all trait sites with their trait effects. The strength of these correlations is directly related to the strength of stabilizing selection on the trait, cp. Chapter 3. Correlation measurements allow hence to infer both, the number of traits constraining sequence evolution, which is in principle obtained from the number of significant ranks, and their underlying genotype–phenotype map. This follows a very simple procedure:

1. Observe pairwise mutations with their temporal distance and ordering, then
2. define an appropriate time-ordered and short-term count measure between pairs such N_{ij} or N_{ij}^{pol}, which we introduced in [138] and recapitulated in Methods 4.8, then
3. correct for the marginal measure $N_{ij}^{0} = \sum_{i'j'} N_{ij'} N_{i;j}$ [138] and Methods 4.8 and
4. perform a singular value decomposition on the significance matrix [138] to identify the number of significant traits. The right and the left singular vectors give the trait effects and the response asymmetry.

This procedure can be applied to multiple sequence alignments. From these, phylogenetic trees and hence the temporal distance of mutations can be reconstructed. Preliminary results show that we can apply the method and retrieve back known mutational effects in PDZ domains [private communication with Simone Pompei]. Here, the conserved trait is the binding energy with ligands [141]. The method can also help to detect inter-residue or inter-protein interactions [79], if generated by a broad trait, e.g. through binding domains.

Furthermore, time-resolved correlation measurements, such as the pairwise mutation counts weighted by proximity in time, allow the detection of external adaptation pressures. On trait sites, these entail a suppressed compensatory response. The asymmetry of the response matrix is proportional to the fitness flux. This is a big advantage over equal-time correlation measurements, which cannot distinguish adaptation from weaker constraining selection. We showed that weighting the counts with the relative polarization of the mutation pair improves, as expected, the signal strength. However, this is possible only, if the direction of trait effects is known a priori.

Though we concentrated in the main text on substitution dynamics, we showed that our method is also applicable to phylogenetic trees and hence to actual biological datasets. Strong adaptive pressures shape the phylogeny and bias classical methods. However, with time-dependent observables, this can be absorbed in the null mode of independent evolutionary rates of sites and does not influence the response pattern. This allows the inference of correlations and adaptation even on strongly adaptive systems, e.g. viral populations escaping the immune system, where classical tests assuming evolutionary are weak. Adaptation is a signature of a non-equilibrium system and implies asymmetry in the time-ordered correlation matrix. The asymmetry can be read off from such matrices and enables to detect target sites of strong

adaptation. In a follow-up paper, we infer a antigenicity-stability model for hemagglutinin of the human influenza virus [138]. The response asymmetry allows us to detect driver sites, which are closely related to known epitope sites exposed to the immune system [142]. The adaptive pressure from the immune system enforces deleterious mutations on these sites destabilizing a stability trait. Trailer mutations show higher fixation probabilities if they follow driver mutations. They compensate the deleterious driver effects. As discussed in Chapter 3, the compensatory trait response to adaptive pressures is trait-typical not predicable in a particular site, but for the collective trait sites and the trait effect of these. Gaining these information can help to improve evolutionary prediction [7, 10, 11].

Further research could study the impact of a trait fitness seascape $f(E,t)$ onto its sites. Supposedly, it will generate coherent adaptation on macro-evolutionary timescales of the fitness seascape changes, cp. Chapter 3. Nonetheless, the underlying pattern should have a similar complexity, given by the trait selection and trait effects. This trait-adaptation is distinguishable from single site adaptation if analyzed on different timescales.

4.8 Methods

4.8.1 Pairwise count matrices

We are interested in measuring trait epistasis together with the strength of adaptation in the data, which cannot be distinguished in classical equal time correlations from less constraining selection since the information about detailed balance is lost. On the other hand, the introduced time-dependent pairwise rates (4.8), (4.10), and (D.6) suffer strong under-sampling not only for pairs, but also in the time-resolution.

Therefore, we use in actual data analysis pairwise observational counts, which measure the short-term response similar to other bioinformatic measures introduced in the literature [143, 144]. We introduced these counts for the application on phylogenetic trees in [138]. Here, we rewrite these count measures for the application to substitution dynamics, which are of the same class but simplified. Under the substitution dynamics they are defined as

$$\begin{aligned} N_{ij} &= \int_0^T \mathrm{d}t \int_t^T \mathrm{d}\tau \rho_{ij}(t,\tau) \mathrm{e}^{-\tau/\tau_0}, \\ N_{ij}^{\mathrm{pol}} &= \int_0^T \mathrm{d}t \int_t^T \mathrm{d}\tau \rho_{ij}^{\mathrm{pol}}(t,\tau) \mathrm{e}^{-\tau/\tau_0}, \end{aligned} \tag{4.18}$$

which are extensive in observation time T and τ_0. τ_0 is to be chosen of the order of the trait equilibration time τ_{eq} and penalizes the counts for temporal distance to suppress long-term noise. The optimization with respect to τ_0 is discussed in Appendix D.2 and Figure D.4, e.g. obtained from optimizing the significance of the singular value decomposition presented in the next section. In simulations, substitutions fixing at the same time ($\tau = 0$) are averaged over the time-window since previous substitution event and all combinations of driver-/trailer-time-ordering.

If $\tau_0 \sim \tau_{\text{eq}}$ is well chosen, the expected counts are

$$\begin{aligned} \mathcal{N}_{ij} &:= \langle N_{ij} \rangle = \mathcal{N}_{ij}^0 \left(1 + \frac{\omega_{ij}^2}{3\alpha_j}\right), \\ \mathcal{N}_{ij}^{\text{pol}} &:= \langle N_{ij}^{\text{pol}} \rangle = \mathcal{N}_{ij}^0 \frac{\omega_{ij}}{2\alpha_j^{\text{pol}}}, \end{aligned} \tag{4.19}$$

with expectation value $\mathcal{N}_{ij}^0 = \langle N_{ij}^0 \rangle$ of the uncorrelated counts. As we showed in [138], these are estimated from the product $N_{ij}^0 = \Omega p_i p_j$ of the marginal counts $p_i = \frac{1}{\Omega}\sum_{j'} N_{ij'} = \frac{1}{\Omega}\sum_{i'} N_{i'j}$, and total count number $\Omega = \sum_{ij} N_{ij}$. The row- and column-sums are identical if only substitutions are considered. For a finite allele frequency analysis, these are different making $\mathcal{N}_{ij}^0$ asymmetric. We show the asymmetry of this null-mode in the underlying in Appendix D.1. The asymmetry of the null model does not generate false pattern of adaptation in α_j and α_j^{pol}. For long enough measurements, i.e. with suppressed noise, the trait signal ω_{ij} is supposed to by visible in observables $\hat{n}_{ij} = (N_{ij} - N_{ij}^0)/N_{ij}^0$ and $n_{ij}^{\text{pol}} = N_{ij}^{\text{pol}}/N_{ij}^0$. A probabilistic approach for noisy data, as needed for the simulations, is discussed in the next paragraph. By the law of large numbers, the variances $\langle (N_{ij} - \mathcal{N}_{ij})^2 \rangle \sim \mathcal{N}_{ij}^0$ and $\langle (N_{ij}^{\text{pol}} - \mathcal{N}_{ij}^{\text{pol}})^2 \rangle \sim \mathcal{N}_{ij}^0$ are both determined by the uncorrelated count number; corrections for small count numbers are discussed in detail in [138].

4.8.2 Rank reduction with singular value decomposition

To infer back the trait values from the correlation matrices we standard normalize the data with respect to the null expectation (uncorrelated evolution) [138], $z_{ij} = \frac{N_{ij} - N_{ij}^0}{\sqrt{N_{ij}^0}}$ and $z_{ij}^{\text{pol}} = \frac{N_{ij}^{\text{pol}}}{\sqrt{N_{ij}^0}}$, and use a singular value decomposition on these, $\tilde{z}_{ij} = \sum_{g'=1}^{g} \tilde{\lambda}^{(g')} \tilde{t}_j^{(g')} \tilde{d}_i^{(g')}$ and $\tilde{z}^{\text{pol}}$ equivalently. Here, g is the number of significant eigenvalues corresponding to the number of coevolving quantitative traits, cp. Section 4.5. Significance is tested against a null model generated by a randomly scrambling of site indices of mutations along the observed evolutionary trajectory, which can be mapped on a random matrix with expectations and variance from marginal counts p_i, for details see [138] and Appendix D.2. As shown in that appendix, the significance of a trait's singular value scales as $\tilde{\lambda} \sim \sqrt{\sum_{ij} N_{ij}} c^2/\ell^2$ or $\tilde{\lambda}^{\text{pol}} \sim \sqrt{\sum_{ij} N_{ij}} c/\ell$, whereas the most significant eigenvalue expected from noise scales $\sim \sqrt{\ell}$ [138], which hence tells how many data to collect to identify a trait of stabilizing selection c.

These matrices relate to Equations (4.19) through $(\hat{n}_{ij})_{\text{red}} \equiv \frac{\tilde{z}_{ij}}{\sqrt{N_{ij}^0}} = \frac{\omega_{ij}^2}{3\alpha_j}$+noise and through $\left(n_{ij}^{\text{pol}}\right)_{\text{red}} \equiv \frac{\tilde{z}_{ij}^{\text{pol}}}{\sqrt{N_{ij}^0}} = \frac{\omega_{ij}}{2\alpha_j^{\text{pol}}}$+noise, which are still of rank g. The noise level is reduced since the rank reduction considers the integral interaction of a site compared to all other sites. Hence, with Equation (4.16), $(\hat{n}_{ij})_{\text{red}} \sim \sum_{g'=1}^{g} c^{g'2} E_j^{g'2} E_i^{g'2}/\alpha_j$ retrieves back in each singular mode the squared trait effects in the right, driver singular vector, the constrained trait effect in the left, trailer singular vector, and the squared stabilizing strength in the singular value. Each singular mode stands for stabilizing selection of one trait. On the other hand, $\left(n_{ij}^{\text{pol}}\right)_{\text{red}} \sim$

$\sum_{g'=1}^{g} E_{g',j} E_{g',i} / \alpha_j^{\mathrm{pol}}$ retrieves similarly the first order of trait effects and stabilizing strength, for details see Appendix D.2. The asymmetry of the response matrices is obtained from the discrepancy of left- and right singular vectors.

Chapter 5

Phenotypic interference limits complexity

The evolution of microbial and viral organisms often generates clonal interference, a mode of competition between genetic clades within a population. In this chapter, we show that interference strongly constrains the genetic and phenotypic complexity of evolving systems. Our analysis uses biophysically grounded evolutionary models for an organism's quantitative molecular phenotypes, such as fold stability and enzymatic activity of genes. We find a generic mode of asexual evolution called *phenotypic interference* with strong implications for systems biology: it couples the stability and function of individual genes to the population's global speed of evolution. This mode occurs over a wide range of evolutionary parameters appropriate for microbial populations. It generates selection against genome complexity, because the fitness cost of mutations increases faster than linearly with the number of genes. Recombination can generate a distinct mode of sexual evolution that eliminates the superlinear cost. We show that positive selection can drive a transition from asexual to facultative sexual evolution, providing a specific, biophysically grounded scenario for the evolution of sex. In a broader context, our analysis suggests that the systems biology of microbial organisms is strongly intertwined with their mode of evolution.

5.1 Introduction

Asexually reproducing populations evolve under complete genetic linkage. Hence, selection on an allele at one genomic locus can interfere with the evolution of simultaneously present alleles throughout the genome. Linkage-induced interference interactions between loci include background selection (the spread of a beneficial allele is impeded by linked deleterious alleles), hitchhiking or genetic draft (a neutral or deleterious allele is driven to fixation by a linked beneficial allele), and clonal interference between beneficial alleles originating in disjoint genetic clades (only one of which can reach fixation). These interactions and their consequences for

genome evolution have been studied extensively in laboratory experiments [20,39], natural populations [21,38], and theory [64–71]. The most prominent global effect of interference is to reduce the speed of evolution, which has been observed in laboratory evolution experiments [35,36,40]. The fitness cost of interference, which has also been measured [37, 41], is the center piece of classic arguments for the evolutionary advantage of sex [31,62,145–147]. Much less clear is how interference affects the system-wide evolution of molecular phenotypes, such as protein stabilities and affinities governing gene regulation and cellular metabolism, which have generically non-linear fitness functions. This is the topic of the present chapter, which looks at the systems-biological consequences of interference evolution. We establish that interference generates a long-term degradation of an organism's molecular functions by the accumulation of deleterious mutations. This effect is strongly dependent on genome size: it becomes an evolutionary force constraining organismic complexity and driving the evolution of recombination.

Our analysis is based on simple biophysical models of molecular evolution [15,16,57,99–102], which we discussed in Seciton 2.3. In a minimal model, an individual's organism consists of g genes and each gene carries a single quantitative trait G, the stability of its protein. The trait is encoded in multiple sites of the gene sequence and is affected by mutations at these sites, most of which will make the protein less stable. Selection on a gene is described by a standard thermodynamic fitness landscape $f(G)$, which is a sigmoid function with a high-fitness plateau corresponding to stable proteins and a low-fitness plateau corresponding to unfolded proteins (Figure 2.2B). We also discuss an stability-affinity protein model with a two-dimensional fitness landscape $f(G, E)$; this model includes enzymatic or regulatory functions of genes, specifically the protein binding affinity E to a molecular target. The genome-wide mutation-selection balance in these fitness landscapes describes populations maintaining the functionality of their molecular traits; we refer to this state as *housekeeping evolution*. We analyze its long-term evolutionary forces on genome architecture that arise independently of short-term adaptive processes, such as the evolution of resistance.

Over a wide range of model parameters, we find that housekeeping evolution takes place in an evolutionary mode of *phenotypic interference*. In this mode, genetic and phenotypic variants in multiple genes generate standing fitness variation under complete genetic linkage, a so-called traveling fitness wave [64,66,67,69–71,73], cp. Figure 5.1. This traveling wave theory particularly applies to 'standing' fitness waves in housekeeping evolution [70, 73]. We show that phenotypic interference is a system-wide collective dynamics with a universal feedback between the global fitness wave and selection on individual phenotypic variants. This feedback generates a fitness cost, defined as the difference between the mean population fitness and the fitness maximum of fully functional genes, that increases quadratically with g (Figure 5.2). The fitness cost of interference quantifies its systems-biological effects: the maintenance of each gene degrades stability and function of all other genes by increasing the accumulation of deleterious mutations. The non-linear cost sets in already at a small number of genes, g_0, and generates strong selection against genome complexity in viable, asexually reproducing organisms. This distinguishes our biophysical models from classical models of mutational load, which predict a linear fitness cost up to a much larger error threshold g_m associated with mutational meltdown [61–64] (Figure 5.2).

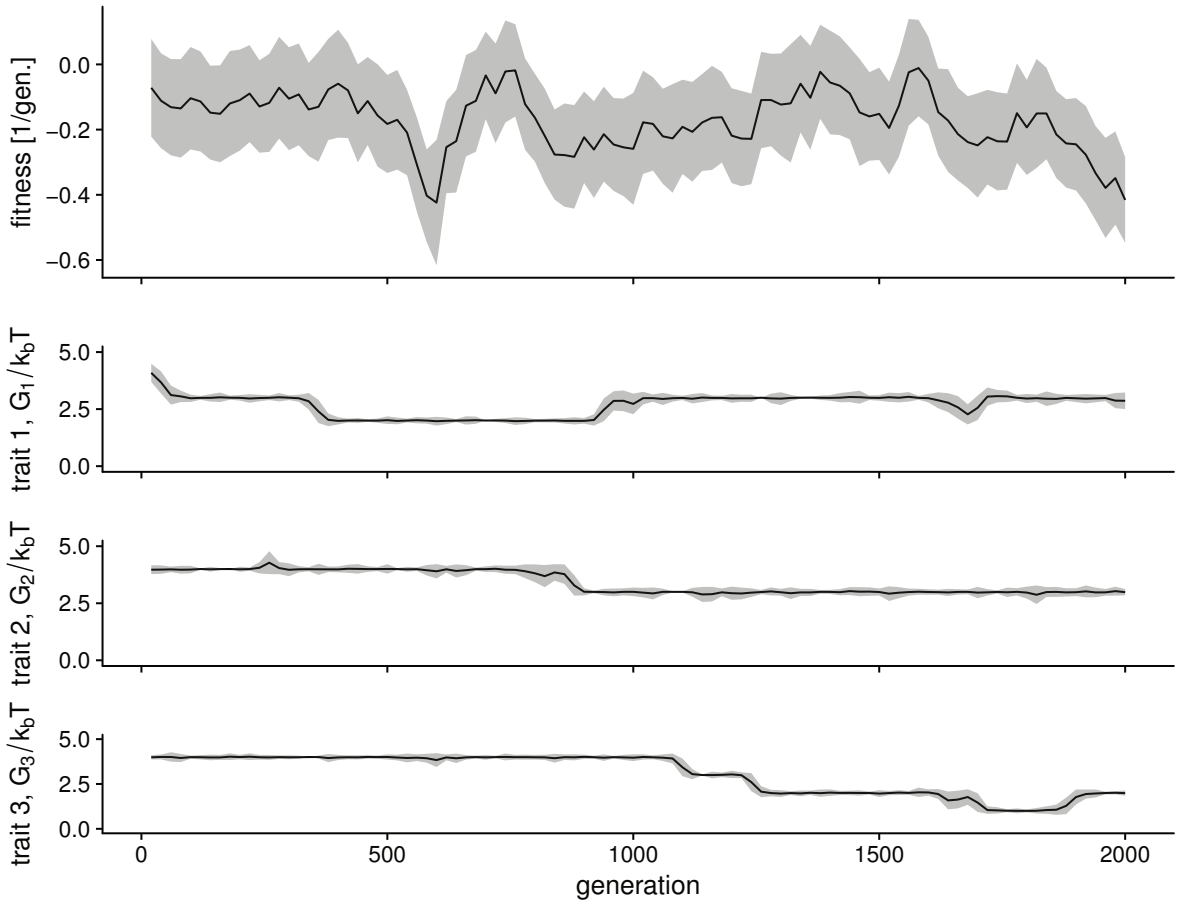

Figure 5.1. Phenotypic interference generates fitness wave. This figure shows example trajectories of population statistics in the housekeeping evolution of $g = 1000$ genes. The genome-wide fitness is depicted in the top panel (measured by deviations from its temporal average) and three example traits values are depicted in the three bottom panels. The line shows the population means, the ribbons show the square-root fitness diversity σ (top panel) or square-root trait diversities $\sqrt{\Delta G}$ (3 bottom panels). While each individual trait is noisy in units of its polymorphism and fluctuates in its class, the population fitness shows a rather stable evolution in units of its polymorphism. The polymorphism itself stays constant over time through the large supply of mutational variants from the 1000 genes. This makes the fitness wave theory [64, 66, 67, 69–71, 73] applicable on the level of genome-wide fitness statistics, whereas individual traits follows its noisy trajectory described by the dynamics from [53, 54]. Other simulation parameters: $f_0 = 0.2, N = 1000, u = 1.25 \times 10^{-3}$, $\epsilon_G/k_BT = 1$; see Appendix A for simulation details.

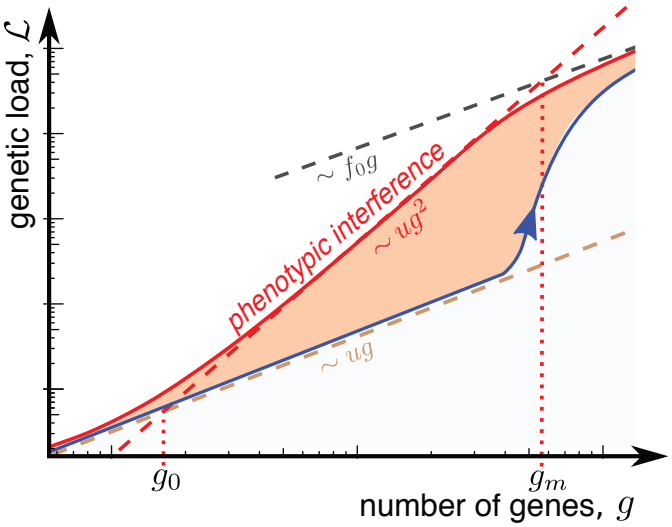

Figure 5.2. Fitness cost of phenotypic interference. The total genetic load $\mathcal{L}$ in a genome is shown as a function of the number of genes, g, for different models of genome evolution. Red line: Asexual evolution in the minimal biophysical model has an evolutionary regime of *phenotypic interference* where $\mathcal{L}$ increases quadratically with g; see Equation (5.2) and simulation data shown in Figure 5.4A. This regime arises from the competition of phenotypic variants within a population. The nonlinear scaling of $\mathcal{L}$ sets in at a small gene number g_0 and ends at a much larger value g_m, which marks the crossover to genomes with a large fraction of dysfunctional genes (grey line). Blue line: under asexual evolution in a model with discrete gene fitness effects, the onset of load nonlinearity and interference occurs at $g \sim g_m$ and is associated with the onset of Muller's ratchet [61,63,64]. Brown line: sexual evolution reduces $\mathcal{L}$ to a linear function of g, if the recombination rate is above the transition point R^* given by Equation (5.8).

Remarkably, the genome-wide steady state of evolution affords an analytic solution in our minimal model. We develop this solution in the following sections; then we turn to model extensions and biological consequences on genome complexity under asexual evolution. Housekeeping evolution in these models also provides a biophysically grounded rationale for the evolution of sex. We show that long-term selective pressure on the recombination rate induces a first-order phase transition to a mode of sexual evolution without genome-wide interference, and we obtain a simple estimate of the transition recombination rate R^* that can be directly compared to data.

The solution of the minimal model has two parts that will be discussed in order. First, the mean fitness variance of a single quantitative trait at evolutionary equilibrium depends in a simple way on a global evolutionary parameter, the coalescence rate $\tilde{\sigma}$. Second, for the steady state of housekeeping evolution, the fitness variances of all traits combine to the total standing fitness variation, which in turn sets the coalescence rate and leads to a closure of the derivation. We then discuss biological implications of phenotypic interference.

5.2 Evolution of a quantitative trait under interference selection.

Here we quickly recall and discuss the phenotypic statistics for a gene under interference selection, which we derived in Sections 2.2 and 2.3. We see that the coalescence rate $\tilde{\sigma}$ determines both, the mean selection coefficient and the fitness variance per gene. These decouple from the details of the underlying fitness landscape. We treat here the deterministic dynamics of the mean trait G under the average average trait diversity $\langle \Delta_G \rangle$. Mean trait fluctuations by genetic drift or draft leave the results invariant and are presented in Appendix E.2.

The stability G of a protein is the free energy difference between the unfolded and the folded state (Methods[1]). This trait gains heritable variation Δ_G by new mutations at a speed $u\epsilon_G^2$, where $u \equiv \mu\ell$ is the trait's total mutation rate and $\epsilon_G^2 = \frac{1}{\ell}\sum_i E_i^{G\,2} \equiv 4E_0^{G\,2}/\ell$ is the mean square stability effect of its sequence sites, cp. diversity dynamics Equation (2.5) and Methods. The trait loses variation by coalescence at a rate $\tilde{\sigma}$. These processes determine an equilibrium stability variation $\langle \Delta_G \rangle = u\,\epsilon_G^2/(2\tilde{\sigma})$. This type of relation is, rewritten to trait scales, the well known form for neutral sequence variation in models of genetic draft [148] and for neutral sequence variation in traveling fitness waves [92, 149]. It can be derived more generally from a diffusion theory for quantitative traits under selection [54]. However, in Appendix E we show a-posteriori for our solutions that genetic draft is constraining Δ_G strongly, such that selection does not shape it and it is effectively neutral. Next, we consider the mutation-selection equilibrium of a gene on the flank of the fitness landscape $f(G)$. We equate the rate of stability increase by selection, $\langle \Delta_G \rangle\, f'(G)$, with the rate of trait degradation by mutations, $u\epsilon_G$, using that most mutations in a functional trait are deleterious (Methods) and that the second term of $F_1(G)$ is negligible in (2.6) through strongly constrained $\langle \Delta \rangle$ under genetic draft. This relates the mean square selection coefficient at trait sites, $s^2 = \epsilon_G^2 f'^2(G)$, cp. Equation (2.16), and the fitness variance $\langle \Delta_f \rangle \approx \langle \Delta_G \rangle f'^2(G)$ to the coalescence rate, cp. Equation (5.11) in Methods,

$$s^2 = 4\tilde{\sigma}^2, \qquad \langle \Delta_f \rangle = 2u\tilde{\sigma}. \tag{5.1}$$

These relations are universal if deleterious mutations push evolution to the flank of non-linear fitness landscapes; that is, they do not depend on details of the fitness landscape and the trait effect distribution of sequence sites. Remarkably, trait fluctuations by genetic drift and genetic draft also leave their form invariant (Appendix E.2 and Figure E.1).

Equations (5.1) express a salient feature of selection on quantitative traits: the strength of selection on genetic variants is not fixed *a priori*, but is an emergent property of the global evolutionary process. A faster pace of evolution, i.e., an increase in coalescence rate $\tilde{\sigma}$, reduces the efficacy of selection [68, 69, 92]. In a downward curved part, i.e. stabilizing part of the fitness landscape, this drives the population to an equilibrium point of lower fitness and higher fitness gradients. The resulting equilibrium tunes typical selection coefficients to marginal relevance,

[1] Section 5.6

where mean fixation times $1/s$ are of the order of the coalescence time $1/\tilde{\sigma}$. This point marks the crossover between effective neutrality ($s \ll \tilde{\sigma}$) and strong selection ($s \gg \tilde{\sigma}$); consistently, most but not all trait sites carry their beneficial allele [68].

5.3 Housekeeping evolution of multiple traits.

The equilibrium scenario of housekeeping evolution builds on the assumption that over long timescales, selection acts primarily to repair the deleterious effects of mutations, because these processes are continuous and affect the entire genome. In contrast, short-term adaptive processes are often environment-dependent, transient, and affect only specific genes. Here we discuss a closed solution of the phenotypic interference dynamics for housekeeping evolution. In Appendix E.3, we extend this approach to scenarios of adaptive evolution and show that these do not affect our conclusions.

In a housekeeping equilibrium, the total fitness variation σ^2 is simply the sum of the fitness variances of individual genes, $\sigma^2 = g\langle\Delta_f\rangle$ (Figure E.2). Moreover, traveling wave theory shows that σ^2 and the coalescence rate $\tilde{\sigma}$ are simply related, $\sigma^2/\tilde{\sigma}^2 = \mathcal{C}_0 \log(N\sigma)$, where N is the population size and $\mathcal{C}_0 \sim 10^2$ [70, 71]. The traveling wave theory is applicable to our 'standing' housekeeping wave. It is not its net speed that matters [70, 73], but the large supply by mutational variants $\sigma \gtrsim s$. This condition is generically fulfilled for housekeeping phenotypes, cp. Appendix E. Together with Equation (5.1), we obtain the global fitness wave

$$\sigma^2 = 4\frac{u^2 g^2}{\mathcal{C}}, \qquad \tilde{\sigma} = 2\frac{ug}{\mathcal{C}}, \tag{5.2}$$

as well as corresponding characteristics of individual traits,

$$\frac{\langle\Delta_G\rangle}{\epsilon_G^2} = \frac{\mathcal{C}}{4g}, \qquad s^2 = 4\tilde{\sigma}^2 = 16\frac{u^2 g^2}{\mathcal{C}^2}, \tag{5.3}$$

in terms of the slowly varying parameter

$$\mathcal{C} = \frac{\sigma^2}{\tilde{\sigma}^2} \approx \mathcal{C}_0 \log(Nug). \tag{5.4}$$

As shown in Methods, this parameter has a simple interpretation: it estimates the complexity of the fitness wave, that is, the average number of genes with simultaneously segregating beneficial genetic variants destined for fixation. Fisher-Wright simulations of the minimal model confirm Equations (5.2–5.4); they reproduce the joint pattern of σ^2, $\tilde{\sigma}^2$, $\langle\Delta_G\rangle$, and s^2 and infer the wave complexity c (Figure 5.3).

These relations are the centerpiece of phenotypic interference theory. This evolutionary mode arises from the combination of (local) epistasis on trait sites through non-linear phenotypic selection, which is the key property distinguishing quantitative trait selection from Mendelian selection, together with linkage between phenotypes on the genomic scale. They show that the collective evolution of molecular quantitative traits under genetic linkage depends strongly

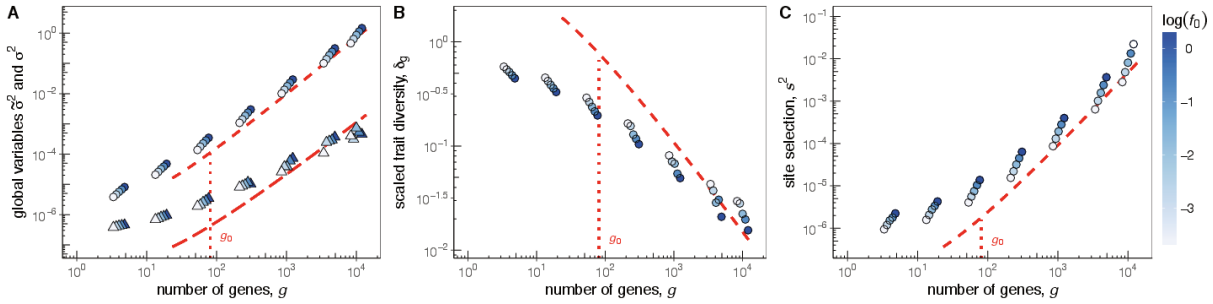

Figure 5.3. Global and local scaling under phenotypic interference. A Average total fitness variance, σ^2 (circles) and coalescence rate $\tilde{\sigma}^2$ (triangles) versus number of genes, g, for asexual evolution. Simulation data for different average gene selection coefficients f_0 (indicated by color) are compared to model results, $\sigma^2 \sim g^2/\mathcal{C}$ (short-dashed line) and $\tilde{\sigma}^2 \sim g^2/\mathcal{C}^2$ (long-dashed line) for $g > g_0 \sim 10^2$; Equations (5.2) and (5.4). **B** Average scaled trait diversity, $\langle \delta_G \rangle = \langle \Delta_G \rangle / \epsilon_G^2$, versus g. Simulation data (circles); model results, $\langle \delta_G \rangle \sim \mathcal{C}/g$ (dashed line; Equation (5.3)). Values $\langle \delta_G \rangle < 1$ indicate that individual proteins are in the low-mutation regime. **C** The mean square selection coefficient at sequence sites, s^2, versus g. Simulation results (circles); model results, $s^2 = 4\tilde{\sigma}^2 \sim g^2/\mathcal{C}^2$ (short-dashed line as in A; Equation (5.4)). The scaling $s^2 \sim \tilde{\sigma}^2$ is independent of f_0, signalling that site selection coefficients emerge from a feedback between global and local selection (see text). Other simulation parameters: $N = 1000, u = 1.25 \times 10^{-3}$, $\epsilon_G/k_BT = 1$; see Appendix A for simulation details.

on the number of genes that encode these traits. The dependence is generated by a feedback between the global fitness variation, σ^2, and mean square local selection coefficients at genomic sites, s^2. In Appendix E.1, we show that this feedback also tunes the evolutionary process to the crossover point between independently evolving genomic sites and strongly correlated fitness waves composed of multiple small-effect mutations.

5.4 Biological implications of phenotypic interference

The results so far where generic for solutions on the flank of a fitness landscape. We now discuss the implications for biophysical fitness landscapes (2.25) *and* (2.30)*. We show that the genetic load increases quadratically with the number of genes: an additional gene generates a deleterious burden on each other gene. We find dramatic cost of genome size for typical organisms. Moreover, genes will be lost, if the genetic load is larger than the plateau height of the fitness landscape. Finally, we show that recombination at low rates, of the order of the mutation rate, can resolve this cost by a first order phase transition. This opens an evolutionary feasible pathway for the evolution of sex with a comparatively low cost of horizontal gene transfer compared to the cost of phenotypic interference. A comparison with data shows that the considered species show recombination rates slightly above this threshhold.*

Interference selection against complexity. The feedback of phenotypic interference has an immediate consequence for the genetic load, which is determined by the average position of genes on the fitness landscape. We first consider stable and functional genes located in the concave part of the minimal model landscape $f(G)$ (Figure 2.2B). This part can be approximated by its exponential tail, where the load is proportional to the slope $f'(G)$. Equation (5.3) then

predicts a load $sk_BT/\epsilon_G \approx 2\tilde{\sigma}$ per gene, where we have used that typical reduced effect sizes ϵ_G/k_BT are of order 1 (Methods). This implies a superlinear scaling of the total equilibrium genetic load,

$$\mathcal{L}_{\rm int}(g) \approx 2g\tilde{\sigma} = 4\frac{ug^2}{\mathcal{C}}, \tag{5.5}$$

which sets on at a small gene number g_0 given by the condition $g_0 \approx \mathcal{C}/4$ (Figure 5.2, numerical simulations are shown in Figure 5.4A). The superlinearity of the genetic load is the most important biological effect of phenotypic interference. As detailed in Appendix E.3 and Figure 2.2, this scaling holds more generally for a sufficient number of quantitative traits evolving under genetic linkage; it does not depend on details of the fitness landscape and of the underlying biophysical processes. For example, active protein degradation, a ubiquitous process that drives the thermodynamics of folding out of equilibrium [104], does not affect our conclusions. Another example is the stability-affinity model, which has two quantitative traits per gene that evolve in a two-dimensional sigmoid fitness landscape $f(G, E)$ [57, 58]. We show that under reasonable biophysical assumptions, evolution in a stability-infinity model produces a 2-fold higher interference load than the minimal model, $\mathcal{L}_{\rm int}(g) \approx 8ug^2/\mathcal{C}$. Alternative models with a quadratic single-peak fitness landscape generate an even stronger nonlinearity of the load, $\mathcal{L}_{\rm int}(g) \sim g^3$. In contrast, a discrete model with a fitness effect f_0 of each gene shows a linear load up to a characteristic gene number $g_m = (f_0/u)\log(Nf_0)$ associated with the onset of mutational meltdown by Muller's ratchet [61, 63, 64].

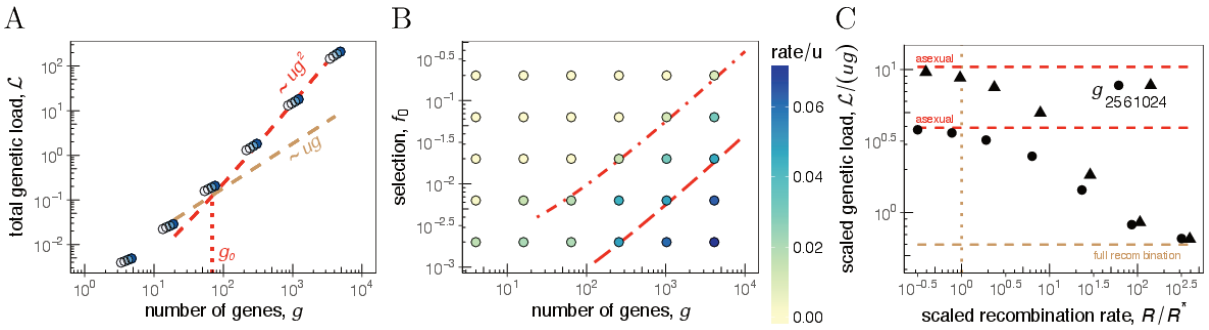

Figure 5.4. Genetic load, gene loss, and transition to sexual evolution. A Total genetic load $\mathcal{L}$ versus the number of genes g for asexual evolution. Simulation results (circles) for different values of f_0 (indicated by color, as in Figure 5.3); model results: interference load $\mathcal{L}_{\rm int} \sim ug^2/\mathcal{C}$ (red line; Equation (5.5)) for $g > g_0$ (dotted line) and null model $\mathcal{L} = ug$ (brown line) as in Figure 5.2. The superlinear behavior of $\mathcal{L}$ indicates strong selection against genome complexity. **B** Rate of gene loss (indicated by color, in units of u) as a function of the gene selection coefficient, f_0, and the number of co-evolving genes g. Genes with $f_0 \sim \tilde{\sigma}$ (long-dashed line, cf. Figure 5.3A) have appreciable loss rates; genes with $f_0 \gtrsim 10\tilde{\sigma}$ (dashed-dotted line) have negligible loss rates, i.e., are conserved under phenotypic interference. **C** Scaled genetic load, $\mathcal{L}/(ug)$, versus scaled recombination rate, R/R^*, for different genome sizes. The observed load rapidly drops from the superlinear scaling of phenotypic interference, $\mathcal{L} = 4ug^2/\mathcal{C}$ (asymptotic data: red lines), to the linear scaling of unlinked genes, $\mathcal{L} \sim ug$ (brown line). This signals a (fluctuation-rounded) transition to sexual evolution at the threshold recombination rate $R^* = 2ug/\mathcal{C}$ (dotted line, see Equation (5.8)). Other simulation parameters as in Figure 5.3; see Appendix A for simulation details.

The interference load builds up with a time lag given by the relaxation time to equilibrium,

$$\tau = \frac{1}{u} = 2\frac{g}{\mathcal{C}}\frac{1}{\tilde{\sigma}}. \tag{5.6}$$

Deleterious mutations in an organism's genes build up on a timescale τ, which exceeds the coalescence time $\tilde{\sigma}^{-1}$. Therefore, the load $\mathcal{L}_{\rm int}$ affects the long-term fitness of a population against competing lineages. Specifically, it generates strong long-term selection against genome complexity: the fitness cost for each additional gene, $\mathcal{L}'_{\rm int}(g)$, can take sizeable values even at moderate genome size. For example, in a "standard" microbe of the complexity of *E. coli*, a 10 % increase in gene number may incur an additional load $\Delta\mathcal{L} \approx 3 \times 10^{-2}$ under the stability-affinity model (with parameters $g = 5000, u = 10^{-6}, N = 10^8$). In comparison, the discrete model leads to a much smaller value $\Delta\mathcal{L} = 5 \times 10^{-4}$ for the same parameters.

It is instructive to compare the interference load of an extra gene with its physiological fitness cost $\mathcal{L}'_{\rm phys}(g)$, which is generated primarily by the synthesis of additional proteins (and is part of the overall fitness effect f_0). For a gene with an average expression level, $\mathcal{L}'_{\rm phys}(g) = \lambda/g$ with a constant $\lambda \sim 1$ reflecting the (re-)allocation of metabolic resources in the cell; see references [150, 151]. This cost acts as a selective force on changes of genome size, which take place within a coalescence interval $\tilde{\sigma}^{-1}$. Importantly, $\mathcal{L}'_{\rm phys}$ is much smaller than $\mathcal{L}'_{\rm int}$ for a standard microbe, suggesting a two-scale evolution of genome sizes. On short timescales, the dynamics of gene numbers is permissive and allows the rapid acquisition of adaptive genes; these changes are neutral with respect to $\mathcal{L}'_{\rm int}$. On longer timescales (of order τ), marginally relevant genes are pruned in a more stringent way, for example, by invasion of strains with more compact genomes.

Interference drives gene loss. The near-neutral dynamics of genome size extends to gene losses, which become likely when a gene gets close to the inflection point of the sigmoid fitness landscape (Figure 2.2B). The relevant threshold gene fitness, f_0^c, is set by the coalescence rate, which leads to

$$f_0^c \sim 2\tilde{\sigma} = \frac{4ug}{\mathcal{C}} \tag{5.7}$$

in the minimal model. Strongly selected genes ($f_0 \gg 2\tilde{\sigma}$) have equilibrium trait values firmly on the concave part of the landscape, resulting in small loss rates of order $u\exp(-f_0/2\tilde{\sigma})$; these genes can be maintained over extended evolutionary periods. Marginally selected genes ($f_0 \lesssim 2\tilde{\sigma}$) have near-neutral loss rates of order u [68], generating a continuous turnover of genes. According to Equation (5.7), the threshold f_0^c for gene loss increases with genome size, which expresses again the evolutionary constraint on genome complexity. The dependence of the gene loss rate on f_0 and $\tilde{\sigma}$ is confirmed by simulations (Figure 5.4B). The housekeeping coalescence rate $\tilde{\sigma} = 2ug/\mathcal{C}$ sets a lower bound for the fitness threshold f_0^c, adaptive evolution can lead to much larger values of $\tilde{\sigma}$ and f_0^c.

The transition to sexual evolution. Recombination breaks up genetic linkage at a rate R per genome and per generation (R is also called the genetic map length). Evolutionary models

show that recombination generates linkage blocks that are units of selection; a block contains an average number ξ of genes, such that there is one recombination event per block and per coalescence time, $R\xi/(g\tilde{\sigma}(\xi)) = 1$ [71, 91, 152]. Depending on the recombination rate, these models predict a regime of asexual evolution, where selection acts on entire genotypes ($\xi \sim g$), and a distinct regime of sexual evolution with selection acting on individual alleles ($\xi \ll g$). Here we focus on the evolution of the recombination rate itself and establish a selective avenue for the transition between asexual and sexual evolution. With the phenotypic interference scaling $\tilde{\sigma}(\xi) = 2u\xi/\mathcal{C}$ for $\xi \gtrsim \mathcal{C}$, as given by Equation (5.2), our minimal model produces an instability at a threshold recombination rate

$$R^* = \frac{2ug}{\mathcal{C}}. \tag{5.8}$$

This signals a first-order phase transition to sexual evolution with the genetic load as order parameter (Figure 5.4C). For $R < R^*$, the population is in the asexual mode of evolution ($\xi \sim g$), where interference produces a superlinear load $\mathcal{L}_{\text{int}} = 2ug^2/\mathcal{C}$. For $R > R^*$, efficient sexual evolution generates much smaller block sizes ($\xi \sim \mathcal{C}$). In this regime, the mutational load drops to the linear form $\mathcal{L} = ug \ll \mathcal{L}_{\text{int}}$, providing a net long-term fitness gain $\Delta\mathcal{L} \simeq \mathcal{L}_{\text{int}}$. However, the process of recombination itself entails a direct short-term cost $\mathcal{L}_{\text{rec}}$ [147]. If we assume that cost to be of order 1 per event, we obtain $\mathcal{L}_{\text{rec}} \sim R^* = \tilde{\sigma}$ close to the transition. This cost is much smaller than the gain $\Delta\mathcal{L}$ and remains marginal (i.e., $\mathcal{L}_{\text{rec}}/\tilde{\sigma} \sim 1$).

Together, our theory of phenotypic interference suggests a specific two-step scenario for the evolution of sex. Recombination at a rate of order R^* is near-neutral at short timescales, so a recombining variant of rate R^* arising in an asexual background population can fix by genetic drift and draft. Recombining strains acquire a long-term benefit $\Delta\mathcal{L} \sim gR^* = g\tilde{\sigma}$, so they can outcompete asexual strains in the same ecological niche. The threshold rate R^* is of the order of the genome-wide mutation rate ug, so even rare facultative recombination can induce the transition. This scenario builds on the basic biophysics of molecular traits but does not require *ad hoc* assumptions on adaptive pressure, on rate and effects of beneficial and deleterious mutations, or on genome-wide epistasis [147]. It is at least consistent with observed recombination rates in different parts of the tree of life: genome average values are always well above R^*; a high-resolution recombination map of the *Drosophila* genome shows low-recombining regions with values above but of order R^* [153, 154] (Table E.1).

5.5 Discussion

We have developed the evolutionary genetics of multiple quantitative traits in non-recombining populations. We find a specific evolutionary mode of phenotypic interference, which is characterized by a feedback between global fitness variation and local epistatic selection coefficients at genomic sites. This feedback generates highly universal features, which include the complexity of the evolutionary process and the scaling of coalescence rate and genetic load with gene number, as given by Equations (5.2)–(5.4).

Phenotypic interference produces strong selection against genome complexity in asexual populations, which implies selection in favor of recombination above a threshold rate R^* given by

Equation (5.8). The underlying genetic load originates from the micro-evolutionary interference of phenotypic variants within a population and unfolds with a time delay beyond the coalescence time, as given by Equation (5.6). Therefore, the interference load is a macro-evolutionary selective force that impacts the long-term fitness and survival of a population in its ecological niche.

Molecular complexity, the broad target of phenotypic interference, can be regarded as a key systems-biological observable. In our simple biophysical models, we measure complexity by number of stability and binding affinity traits in a proteome. More generally, we can define complexity as the number of (approximately) independent molecular quantitative traits, which includes contributions from an organism's regulatory, signaling, and metabolic networks that scale in a nonlinear way with genome size. Interference selection affects the complexity and architecture of all of these networks, establishing new links between evolutionary and systems biology to be explored in future work.

5.6 Methods

5.6.1 Biophysical fitness models

As discussed in the Introduction 2.3, in thermodynamic equilibrium at temperature T, a protein is folded with probability $p_+(G) = 1/[1 + \exp(-G/k_BT)]$, where G is the Gibbs free energy difference between the unfolded and the folded state and k_B is Boltzmann's constant. A minimal biophysical fitness model for proteins takes the form (2.25) $f(G) = f_0\, p_+(G) = \frac{f_0}{1+\exp(-G/k_BT)}$ with a single selection coefficient capturing functional benefits of folded proteins and metabolic costs of misfolding [99–101]. Similar fitness models based on binding affinity have been derived for transcriptional regulation [15–17]; the rationale of biophysical fitness models has been reviewed in references [87, 102]. In Appendix E.3, we introduce alternative fitness landscapes for proteins and show that our results depend only on broad characteristics of these landscapes. The minimal global fitness landscape for a system of g genes with traits $G_1, \ldots, G_g$ and selection coefficients $f_{0,1}, \ldots, f_{0,g}$ is taken to be additive, i.e., without epistasis between genes,

$$f(G_1, \ldots, G_g) = \sum_{i=1}^{g} \frac{f_{0,i}}{[1 + \exp(-G_i/k_BT)]}. \tag{5.9}$$

5.6.2 Evolutionary model

We characterize the population genetics of an individual trait G by its population mean Γ and its expected variance $\langle \Delta_G \rangle$. The trait mean follows the stochastic evolution equation (2.4)

$$\dot{\Gamma} = -u\kappa\epsilon_G + \langle \Delta_G \rangle f'(\Gamma) + \chi(t) \tag{5.10}$$

where we rewrite parameters from Chapter 2 to simplify the notation in this section: the mean trait dynamics is determined by its total mutation rate $u = \mu\ell$, the mean mutational effect is $(-\kappa)\epsilon_G = -(\Gamma - \Gamma_0)/\ell \approx \Gamma_0/\ell = \frac{1}{\ell}(E_{\min} + \sum_{i=1}^{\ell} E_i/2) < 0$, which we assume to be constant.

This means that the selection dynamics around $\Gamma \gtrsim 0$ take place far from the neutral sequence expectation Γ_0. The mean square trait effect of a mutation is $\epsilon_G^2 = \frac{1}{\ell}\sum E_i^2$, which determine the diversity $\langle \Delta_G \rangle = u\epsilon_G^2/(2\tilde{\sigma})$ [53,54]. We use effects $\epsilon_G \approx 1$–$3\, k_B T$, which have been measured for fold stability [155,156] and for molecular binding traits [15,157,158], and a mutational bias $\kappa = 1$, which is consistent with the observation that most mutations affecting a functional trait are deleterious.

5.6.3 Housekeeping equilibrium

The deterministic equilibrium solution ($\dot{\Gamma} = 0, \chi = 0$) of Equation (5.10) determines the dependence of $\langle \Delta_G \rangle$ and the associated fitness variance $\langle \Delta_f \rangle = \langle \Delta_G \rangle f'^2(G)$ on $\tilde{\sigma}$, as given by Equation (5.1); the same scaling follows from the full stochastic equation (Appendix E.2). The derivation of the global housekeeping equilibrium, Equations (5.2)–(5.4), uses two additional inputs: the additivity of the fitness variance, $\sigma^2 = g\langle \Delta_f \rangle$, which is confirmed by our simulations (Figure E.2), and the universal relation $\sigma^2/\tilde{\sigma}^2 = \mathcal{C}_0 \log(N\sigma)$ [70,71] in a travelling fitness wave, where the coalescence rate $\tilde{\sigma}$ is generated predominantly by genetic draft. Equations (5.2)–(5.4) determine further important characteristics of phenotypic interference:

(a) The complexity of the fitness wave, defined as the average number of beneficial substitutions per coalescence time, is $(v_+ g)/\tilde{\sigma} \sim ug/2\tilde{\sigma} = \mathcal{C}/4$, using that trait-changing mutations are marginally selected, Equation (5.1), and have nearly neutral fixation rates $v_+ \sim u/2$ per gene, cp. (2.17).

(b) The evolutionary equilibria of stable genes ($f_0 \gg \tilde{\sigma}$) are located in the high-fitness part of the minimal fitness landscape, $f \simeq f_0[1 - \exp(-G/k_B T)]$. These genes have an average fitness slope

$$f' = \left(\frac{\langle \Delta_f \rangle}{\langle \Delta_G \rangle} \right)^{1/2} = 2\tilde{\sigma}/\epsilon_G, \tag{5.11}$$

an average trait $\Gamma = -k_B T \log(2\tilde{\sigma} k_B T / f_0 \epsilon_G)$, and an average load $\mathcal{L}_{\rm int}(g)$ given by Equation (5.5).

(c) The scaling regime of Equations (5.2)–(5.4) sets in at a gene number g_0 given by the condition $g_0 = \mathcal{C}/4$; this point also marks the crossover from the linear load $\mathcal{L}_0(g) = ug$ to the nonlinear form $\mathcal{L}_{\rm int}(g)$. Notably, genes balance only a few $k_B T$ above the fitness edge as universally observed and predicted for biophysical traits, see review [101]; the position has only a log-dependence of evolutionary rates.

Chapter 6

Discussion

We used mathematical methods from physical diffusion equations for the evolution of quantitative traits, which have been derived under mutation-selection-drift- and mutation-selection-draft-dynamics [53, 54], and theories for interference selection [64–71] to analyze their universal pattern for various modes of phenotypic evolution. In particular we derived the phenotypic divergence in stochastic fitness seascape, QTL correlations under stochastic single-site seascapes, and the co-evolution of phenotypes on the systems biology level under strong genomic linkage. In all these modes, we identified universal behavior on the trait and systems biology level, where the higher level dynamics decouple from many stochastic degrees of freedom on the lower, constituting level.

In Chapter 2, we quantified that the phenotypic evolution balances in such a way that the phenotypic selection generate generically weak selection on its QTL. Typical selection coefficients are, independent of particular details of the fitness landscape, of the order of the inverse coalescence time, $s \sim \tilde{\sigma}$ (2.17), and evolve near neutrality. A single allele is evolutionary variable. However, the integral effect of all sites stabilizes the evolution through non-linear phenotypic fitness landscapes, which generate another scale of selection. This is indeed indirectly observed in biological data showing that biophysical traits have a beneficial mutational target site that is considerably smaller but still of the same order of magnitude as the deleterious target size [111, 159]. Therefore, a significant number of sites cannot be fixed in the most beneficial allele. This near-neutral selection has relevant implications for trait evolution: on the one hand, sites under constant trait selection are variable and hence fluctuate due to genetic drift or genetic draft triggering compensatory mutations. On the other hand, a substantial number of trait sites is available for compensation of trait fluctuations. This characteristic allowed us to identify universal and predictable dynamics on the trait level in Chapter 3 and to identify the compensation pattern in Chapter 4 also for sites without external adaptation. Furthermore, quantitative traits generically contribute to a smooth Gaussian fitness wave. In asexual evolution this is based on their large mutational input with typical selection coefficients smaller than the width of the fitness wave, i.e. the fitness variation in a population, $s^2 \sim \tilde{\sigma}^2 < \sigma^2$, which we used in Chapter 5.

In the Chapter 3, we introduced a minimalistic model for stochastic phenotypic seascapes

characterized by a randomly moving fitness peak. We again identified universal behavior in the adaptive response on the level of a quantitative trait: key observables such as the genetic load (3.44), the generated fitness flux (3.49), or the temporal divergence/diversity ratio (3.62) are mainly determined by the stabilizing parameter and driving rate, cp. Figure 3.7. They decouple from many genomic details such as the underlying genotype-phenotype map, the recombination map, or, as discussed in Chapter 4, localized single-site adaptation. Furthermore they do not depend on the particular driving mode of the seascape, but only on the average mean-square peak displacement on the macro-evolutionary timescale. Therefore, they are decoupled from micro-evolutionary, e.g. seasonal changes of the fitness seascape. These universal relations hence allow the inference of macro-evolutionary adaptation from the time-resolved divergence/diversity pattern discussed in Section 3.5. It is obtained from trait measurements alone and without the need of knowledge of a neutral gauge such as McDonald-Kreitman type tests require [130]. Moreover, the time information in the divergence permits to distinguish directional from less constraining stabilizing selection. We identified in [3] such pattern in the divergence of gene expression levels in the *Drosophila* genus (Figure 3.8). The model, which we developed in this thesis, allowed to quantify the macro-evolutionary fitness flux along the phylogeny without the need of sequence data.

On short, micro-evolutionary timescales, the trait dynamics imposes a constraining selection. In Chapter 4, we discussed the short-term response pattern of trait mutations on the sequence level. This arises from the first equilibration steps under stabilizing selection. We showed that this non-linear selection generates broad compensatory epistasis and hence response correlations between all QTL, Equations (4.8), (4.10), and Figure 4.3. In accordance with the fluctuation-dissipation theorem, we see that fluctuations arising from genetic drift/draft generate the same response pattern as driving particular sites out of equilibrium. The universality arises in a simple, one rank form of the $\ell \times \ell$ epistatic and response matrices. This generalizes to additional low ranks in the co-evolution with other traits. In other words, the driver impact of a trait site to all QTL is only determined by its trait effect and the response as a trailer mutation is also determined by its trait effect, but potentially suppressed if under single-site adaptation. This asymmetry in the correlation is just quantified by its adaptation rate (4.13) and (4.14). An asymmetric time-ordered correlation matrix is a key feature of ongoing adaptation in the underlying the QTL, see Figure 4.4. The response pattern decouples from details such as the site's independent substitution rate, e.g. through heterogeneous mutation rates or constraints by constant single-site selection. These findings permit to infer both, the genotype–phenotype map and the single-site adaptation, if the correlation is measured with respect to the time-order of mutations. Again, temporal information permits the distinction between stabilizing strength through the trait and adaptation without the need for a neutral gauge of the model. The 'null-mode' is obtained from independent substitution rates. Appropriate correlation measures furthermore allow for the application to strongly adaptive phylogenetic trees. Hence, the derived method is applicable to plenty of sequence data, from which the phylogenetic tree can be reconstructed. On the phylogenetic tree, mutational distances in time are well defined for the temporal correlation measures. Preliminary results support the theory [private communication with Simone Pompei]:

we identified the genotype–phenotype map in PDZ domains inferred from the time-resolved sequence correlations across species. This map is correlated to known trait effects of mutations in these domains. The trait effects are measured from mutagenesis experiments. The trait itself is the ligand binding energy of the domain [141]. We also apply the method to human influenza [138] discussed below in the outlook.

Finally, we discussed in Chapter 5 for the first time the system-wide co-evolution of biophysical phenotypes under asexual evolution. We found a so-far unknown evolutionary mode, which we called phenotypic interference. This is not unique to biophysical traits but generic for trait evolution under stabilizing selection: on the one hand, frequent coalescence through interference constrains the trait diversity and hence its efficacy of selection. On the other hand, quantitative traits generate mesoscopic epistasis in each gene caused by the non-linear selection of quantitative traits. It is the same type of epistasis that shaped the dynamics in the previous chapters. The epistasis generates a destructive feedback onto the coalescence rate $\tilde{\sigma}$ and the efficacy of selection of all other genes. It limits the complexity in asexual evolution: if the genome is increased by adding a gene, this imposes a long-term evolutionary cost onto all other genes through restricted selective repair opportunities of deleterious mutations. This entails a super-linear genetic cost (Figures 5.2 and 5.4A) with the number of co-evolving genes that gets pre-dominant at much smaller genomic sizes than classical studies of asexual evolution predicted [61–64] and which is supposedly substantial for standard organismic complexity. Smaller organisms should win the long-term evolutionary battle. However this cost can be overcome with a bit of horizontal gene transfer: recombination rates in the order of the mutation rate revert this feedback generating a strong benefit of recombination, i.e. a first order phase transition to the much lower cost of sexual evolution, Figure 5.4C. This implies a feasible pathway for the evolution of sex. Our detailed biophysical model allowed, to our knowledge for the first time, to quantify this critical recombination rate and a comparison with data showed that the analyzed species are slightly above this critical rate. Under phenotypic interference, universality arose on the systems biology level. A single gene behaves noisy under strong genetic draft. However, quantitative traits generate a large mutational input with on average small selection coefficients such that all the genes together generate a stationary stable traveling fitness wave [64, 66, 67, 69–71, 73]. The variance of this wave scales with the square of the genome-wide mutation rate and the coalescence rate is determined mainly by this genome-wide mutation rate. These results are independent of particular details of the phenotypic fitness landscapes or the trait effects of mutations.

To conclude, universalities arise in various modes of phenotypic evolution. These universalities generate simple pattern of the evolutionary process that can be used to infer the relevant parameters. Time-dependent observables allow us to relate observed trait divergence or sequence correlations to these parameters in time-dependent fitness seascapes. This way, we can quantify the strength of conservation as well as adaptation of the evolutionary process. Moreover, these universalities are closely related to the predictability of phenotypic evolution. Predictability is preserved by selection on mesoscopic scales, whereas individual trait sites tend to fluctuate generating a huge variety of micro-states. These findings can help to forecast and manipulate

the future outcome of evolutionary processes to fight quickly evolving diseases within patients and on global scales. Furthermore, fitness wave theories can learn from some genomic details that shape the rate and mean effect of arising mutations. Also with these details, universalities give rise to simple scaling laws that allow us to quantify the cost of phenotypic interference in asexual evolution. The theory offers an evolutionary feasible pathway for the evolution of sex.

In follow-up papers, we identify the macro-evolutionary seascape pattern in gene expression levels across the *Drosophila* genus and can quantify a substantial fitness flux along the phylogeny from the divergence pattern [3]. We discuss implications to universality and predictably in [2]. From sequence evolution, we infer in another follow-up paper an antigenicity-stability model for hemagglutinin of human influenza [138]. The asymmetry of the time-ordered correlation matrix shows epitope sites exposed to strong adaptive pressures and hence perturbing protein stability. Other sites can compensate for such effects and indeed show larger fixation probabilities if on the background of driver mutations. Such information could improve the predictability of the influenza evolution. In another follow-up paper, we study the genomic impact of a fitness wave for Mendelian traits, which corresponds to a linear genotype–fitness map [74]. In that case, a fitness wave balances such that significant sites are under no effective selection, which cannot be balanced on a higher-level trait selection scale. This entails a dramatic genomic melt-down on macro-evolutionary timescales. Hence, epistatic effects by quantitative trait selection and the genomic details need to be incorporated carefully into the discussion of traveling fitness wave theories to draw conclusions of long-term evolutionary processes outside the lab.

Acknowledgements

First of all, I want to thank my supervisor Michael Lässig for giving me the opportunity to work on these exciting projects and giving me ideas, guidance, and help. He always brought new paths and views, if a project seemed stuck. I thank my collaborators in this work, Daniel Klemmer, Armita Nourmohammad, and Simone Pompei. Working with you was very inspiring and enjoyable. I thank Daniel furthermore for the nice time sharing the office over all the years as well as Tom Röschinger, who joined more recently. I also thank the rest of our group and Johannes Berg's group for nice discussions and partially cooperations in other projects. Many thanks to Christa Stitz who always took care that administrative issues got resolved easily for us. I thank Stephan Schiffels for providing me with a c++ class that served as a basic for the Wright-Fisher simulations. Finally, I thank my family for their support, especially with the proofreading.

The work has been supported by the Bonn-Cologne graduate school for Physics and Astronomy.

Bibliography

[1] Torsten Held, Armita Nourmohammad, and Michael Lässig. Adaptive evolution of molecular phenotypes. *J Stat Mech: Theory Exp*, 2014(9):P09029, 2014.

[2] Armita Nourmohammad, Torsten Held, and Michael Lässig. Universality and predictability in molecular quantitative genetics. *Curr Opin Genet Dev*, 23(6):684 – 693, 2013. Equal contributions by AN and TH.

[3] Armita Nourmohammad, Joachim Rambeau, Torsten Held, Viera Kovacova, Johannes Berg, and Michael Lässig. Adaptive evolution of gene expression in drosophila. *Cell reports*, 20(6):1385–1395, 2017.

[4] Torsten Held, Daniel Klemmer, and Michael Lässig. Survival of the simplest: the cost of complexity in microbial evolution. *arXiv:1803.08473*, 2018. Equal contributions by TH and DK.

[5] M Kimura. Diffusion models in population genetics. *J Appl Probab*, 1(2):177–232, 1964.

[6] Andrew L Ferguson, Jaclyn K Mann, Saleha Omarjee, Thumbi Ndung'u, Bruce D Walker, and Arup K Chakraborty. Translating hiv sequences into quantitative fitness landscapes predicts viral vulnerabilities for rational immunogen design. *Immunity*, 38(3):606–617, 03 2013.

[7] Marta Łuksza and Michael Lässig. A predictive fitness model for influenza. *Nature*, 507(7490):57, 2014.

[8] Richard A. Neher, Trevor Bedford, Rodney S. Daniels, Colin A. Russell, and Boris I. Shraiman. Prediction, dynamics, and visualization of antigenic phenotypes of seasonal influenza viruses. *Proc Natl Acad Sci U S A*, 113(12):E1701–1709, mar 2016.

[9] Armita Nourmohammad, Jakub Otwinowski, and Joshua B Plotkin. Host-pathogen coevolution and the emergence of broadly neutralizing antibodies in chronic infections. *PLos Genet*, 12(7):e1006171, July 2016.

[10] Michael Lässig, Ville Mustonen, and Aleksandra M. Walczak. Predicting evolution. *Nature Ecology & Evolution*, 1:0077 EP –, 02 2017.

[11] Dylan H. Morris, Katelyn M. Gostic, Simone Pompei, Trevor Bedford, Marta Łuksza, Richard A. Neher, Bryan T. Grenfell, Michael Lässig, and John W. McCauley. Predictive modeling of influenza shows the promise of applied evolutionary biology. *Trends Microbiol*, 2017.

[12] Marta Łuksza, Nadeem Riaz, Vladimir Makarov, Vinod P. Balachandran, Matthew D. Hellmann, Alexander Solovyov, Naiyer A. Rizvi, Taha Merghoub, Arnold J. Levine, Timothy A. Chan, Jedd D. Wolchok, and Benjamin D. Greenbaum. A neoantigen fitness model predicts tumour response to checkpoint blockade immunotherapy. *Nature*, 551:517 EP –, 11 2017.

[13] Chikara Furusawa, Takaaki Horinouchi, and Tomoya Maeda. Toward prediction and control of antibiotic-resistance evolution. *Curr Opin Biotechnol*, 54:45 – 49, 2018. Analytical Biotechnology.

[14] Andrej Fischer, Ignacio Vázquez-García, and Ville Mustonen. The value of monitoring to control evolving populations. *Proc Natl Acad Sci U S A*, 112(4):1007–1012, 2015.

[15] U Gerland and T Hwa. On the selection and evolution of regulatory DNA motifs. *J Mol Evol*, 55(4):386–400, 2002.

[16] Johannes Berg, Stana Willmann, and Michael Lässig. Adaptive evolution of transcription factor binding sites. *BMC Evol Biol*, 4(1):42, 2004.

[17] V Mustonen, J Kinney, Curtis G. Jr Callan, and M Lässig. Energy-dependent fitness: A quantitative model for the evolution of yeast transcription factor binding sites. *Proc Natl Acad Sci U S A*, 105(34):12376–12381, 2008.

[18] F S Gnesotto, F Mura, J Gladrow, and C P Broedersz. Broken detailed balance and non-equilibrium dynamics in living systems: a review. *Rep Prog Phys*, 81(6):066601, 2018.

[19] Ville Mustonen and Michael Lässig. Adaptations to fluctuating selection in *Drosophila*. *Proc Natl Acad Sci U S A*, 104:2277–82, 2007.

[20] João Barroso-Batista, Ana Sousa, Marta Lourenço, Marie-Louise Bergman, Daniel Sobral, Jocelyne Demengeot, Karina B. Xavier, and Isabel Gordo. The first steps of adaptation of *Escherichia coli* to the gut are dominated by soft sweeps. *PLos Genet*, 10(3):e1004182, 03 2014.

[21] Natalja Strelkowa and Michael Lässig. Clonal interference in the evolution of influenza. *Genetics*, 192(2):671–682, 2012.

[22] Olivier Tenaillon, Alejandra Rodríguez-Verdugo, Rebecca L Gaut, Pamela McDonald, Albert F Bennett, Anthony D Long, and Brandon S Gaut. The molecular diversity of adaptive convergence. *Science*, 335(6067):457–461, January 2012.

[23] Erdal Toprak, Adrian Veres, Jean-Baptiste Michel, Remy Chait, Daniel L Hartl, and Roy Kishony. Evolutionary paths to antibiotic resistance under dynamically sustained drug selection. *Nat Genet*, 44(1):101–105, January 2012.

[24] Guy Sella and Aaron E Hirsch. The application of statistical physics to evolutionary biology. *Proc Natl Acad Sci U S A*, 102(27):9541–9546, 2005.

[25] N H Barton and J B Coe. On the application of statistical physics to evolutionary biology. *J Theor Biol*, 259(2):317–324, July 2009.

[26] Daniel Fisher, Michael Lässig, and Boris Shraiman. Evolutionary dynamics and statistical physics. *J Stat Mech Theor Exp*, 2013(01):N01001, 2013.

[27] Arup K Chakraborty and Andrej Kosmrlj. Statistical mechanical concepts in immunology. *Annu Rev Phys Chem*, 61:283–303, 2010.

[28] Harold P de Vladar and Nick H Barton. The contribution of statistical physics to evolutionary biology. *Trends Ecol Evol*, 26(8):424–432, 2011.

[29] Simona Cocco, Christoph Feinauer, Matteo Figliuzzi, Rémi Monasson, and Martin Weigt. Inverse statistical physics of protein sequences: a key issues review. *Rep Prog Phys*, 81(3):032601, 2018.

[30] Richard A Neher, Colin A Russell, and Boris I Shraiman. Predicting evolution from the shape of genealogical trees. *eLife*, 3:e03568, 2014.

[31] RA Fisher. *The genetical theory of natural selection*. Oxford University Press, USA, 1st edition, 1930.

[32] S Wright. Evolution in mendelian populations. *Genetics*, 16(2):97–159, 1931.

[33] P. A. P. Moran. The survival of a mutant gene under selection. *J Austral Math Soc*, 1(1):121126, 1959.

[34] M Kimura. On the probability of fixation of mutant genes in a population. *Genetics*, 47(6):713, 1962.

[35] J. A. G. M. de Visser, Clifford W. Zeyl, Philip J. Gerrish, Jeffrey L. Blanchard, and Richard E. Lenski. Diminishing returns from mutation supply rate in asexual populations. *Science*, 283(5400):404–406, 1999.

[36] Lília Perfeito, Lisete Fernandes, Catarina Mota, and Isabel Gordo. Adaptive mutations in bacteria: High rate and small effects. *Science*, 317(5839):813–815, 2007.

[37] Tim F Cooper. Recombination speeds adaptation by reducing competition between beneficial mutations in populations of *Escherichia coli*. *PLoS Biol*, 5(9):e225, 08 2007.

[38] Andrea J. Betancourt, John J. Welch, and Brian Charlesworth. Reduced effectiveness of selection caused by a lack of recombination. *Curr Biol*, 19(8):655–660, April 2009.

[39] Michael J. Wiser, Noah Ribeck, and Richard E. Lenski. Long-term dynamics of adaptation in asexual populations. *Science*, 342(6164):1364–1367, 2013.

[40] Michael J. McDonald, Daniel P. Rice, and Michael M. Desai. Sex speeds adaptation by altering the dynamics of molecular evolution. *Nature*, 531:233–236, 02 2016.

[41] Alejandro Couce, Larissa Viraphong Caudwell, Christoph Feinauer, Thomas Hindré, Jean-Paul Feugeas, Martin Weigt, Richard E. Lenski, Dominique Schneider, and Olivier Tenaillon. Mutator genomes decay, despite sustained fitness gains, in a long-term experiment with bacteria. *Proc Natl Acad Sci U S A*, 114(43):E9026–E9035, 2017.

[42] S. Schiffels, M. Lässig, and V. Mustonen. Rate and cost of adaptation in the Drosophila Genome. *ArXiv e-prints*, September 2014.

[43] S Wright. The analysis of variance and the correlations between relatives with respect to deviations from an optimum. *J Genet*, 30(2):243–256, 1935.

[44] M G Blumer. The genetic variability of polygenic characters under optimizing selection, mutation and drift. *Genet Res*, 19(1):17–25, 1972.

[45] Russell Lande. Natural selection and random genetic drift in phenotypic evolution. *Evolution*, 30(2):314–334, 1976.

[46] Nick H Barton. The maintenance of polygenic variation through a balance between mutation and stabilizing selection. *Genet Res*, 47(3):209–216, 1986.

[47] N H Barton and M Turelli. Evolutionary quantitative genetics: how little do we know? *Annu Rev Genet*, 23:337–370, 1989.

[48] Douglas Scott Falconer. *Introduction to quantitative genetics*. Halsted Press, 1989.

[49] S H Rice. A geometric model for the evolution of development. *J Theor Biol*, 1990.

[50] D L Hartl and C H Taubes. Compensatory nearly neutral mutations: selection without adaptation. *J Theor Biol*, 182(3):303–309, February 1996.

[51] Michael Lynch and Bruce Walsh. *Genetics and analysis of quantitative traits*. Sinauer Associates Inc, 1998.

[52] J M Comeron and M Kreitman. Population, evolutionary and genomic consequences of interference selection. *Genetics*, 161(1):389–410, 2002.

[53] Armita Nourmohammad, Stephan Schiffels, and Michael Lässig. Evolution of molecular phenotypes under stabilizing selection. *J Stat Mech Theor Exp*, 2013(01):P01012, January 2013.

[54] Daniel Klemmer and Michael Lässig. Quantitative traits in adaptively evolving populations. In preparation.

[55] R. Phillips, J. Kondev, J. Theriot, and N. Orme. *Physical Biology of the Cell*. Garland Science, 2013.

[56] Jacque Monod, Jeffries Wyman, and Jean-Pierre Changeux. On the nature of allosteric transitions: A plausible model. *J Mol Biol*, 12(1):88 – 118, 1965.

[57] Michael Manhart and Alexandre V Morozov. Protein folding and binding can emerge as evolutionary spandrels through structural coupling. *Proc Natl Acad Sci U S A*, 112(6):1797–1802, 2015.

[58] Nicolas Chéron, Adrian W.R. Serohijos, Jeong-Mo Choi, and Eugene I. Shakhnovich. Evolutionary dynamics of viral escape under antibodies stress: A biophysical model. *Protein Sci*, 25(7):1332–1340, 2016.

[59] Ville Mustonen and Michael Lässig. From fitness landscapes to seascapes: non-equilibrium dynamics of selection and adaptation. *Trends Genet*, 25(3):111–119, March 2009.

[60] V. Mustonen and M. Lässig. Fitness flux and ubiquity of adaptive evolution. *Proc Natl Acad Sci U S A*, 107:4248–53, 2010.

[61] H J Muller. The relation of recombination to mutational advance. *Mutat Res*, 106:2–9, 1964.

[62] Manfred Eigen. Selforganization of matter and the evolution of biological macromolecules. *Naturwissenschaften*, 58(10):465–523, 1971.

[63] I Gordo and B Charlesworth. The degeneration of asexual haploid populations and the speed of Muller's ratchet. *Genetics*, 154(3):1379–1387, 03 2000.

[64] Igor M. Rouzine, Éric Brunet, and Claus O. Wilke. The traveling-wave approach to asexual evolution: Muller's ratchet and speed of adaptation. *Theor Popul Biol*, 73(1):24 – 46, 2008.

[65] Philip J. Gerrish and Richard E. Lenski. The fate of competing beneficial mutations in an asexual population. *Genetica*, 102:127–144, Mar 1998.

[66] Michael M. Desai and Daniel S. Fisher. Beneficial mutation–selection balance and the effect of linkage on positive selection. *Genetics*, 176(3):1759–1798, 2007.

[67] Oskar Hallatschek. The noisy edge of traveling waves. *Proc Natl Acad Sci U S A*, 108(5):1783–1787, 2011.

[68] Stephan Schiffels, Gergely J Szöllősi, Ville Mustonen, and Michael Lässig. Emergent neutrality in adaptive asexual evolution. *Genetics*, 189(4):1361–1375, 2011.

[69] Benjamin H. Good, Igor M. Rouzine, Daniel J. Balick, Oskar Hallatschek, and Michael M. Desai. Distribution of fixed beneficial mutations and the rate of adaptation in asexual populations. *Proc Natl Acad Sci U S A*, 109(13):4950–4955, 2012.

[70] Richard A. Neher and Oskar Hallatschek. Genealogies of rapidly adapting populations. *Proc Natl Acad Sci U S A*, 110(2):437–442, 2013.

[71] Richard A. Neher, Taylor A. Kessinger, and Boris I. Shraiman. Coalescence and genetic diversity in sexual populations under selection. *Proc Natl Acad Sci U S A*, 110(39):15836–15841, 2013.

[72] Elisheva Cohen, David A. Kessler, and Herbert Levine. Front propagation up a reaction rate gradient. *Phys. Rev. E*, 72:066126, Dec 2005.

[73] Sidhartha Goyal, Daniel J. Balick, Elizabeth R. Jerison, Richard A. Neher, Boris I. Shraiman, and Michael M. Desai. Dynamic mutation–selection balance as an evolutionary attractor. *Genetics*, 191(4):1309–1319, 2012.

[74] Torsten Held, Daniel Klemmer, Fernanda Pinheiro, Simone Pompei, and Michael Lässig. Adaptive genome evolution by punctuated fitness waves. Equal contributions by TH, DK, FP, and SP. In preparation.

[75] L Kadanoff. Scaling and universality in statistical physics. *PhyA.*, 163:1–14, 1990.

[76] Martin Weigt, Robert A. White, Hendrik Szurmant, James A. Hoch, and Terence Hwa. Identification of direct residue contacts in proteinprotein interaction by message passing. *Proc Natl Acad Sci U S A*, 106(1):67–72, 2009.

[77] Faruck Morcos, Andrea Pagnani, Bryan Lunt, Arianna Bertolino, Debora S. Marks, Chris Sander, Riccardo Zecchina, José N. Onuchic, Terence Hwa, and Martin Weigt. Direct-coupling analysis of residue coevolution captures native contacts across many protein families. *Proc Natl Acad Sci U S A*, 108(49):E1293–E1301, 2011.

[78] Debora S. Marks, Lucy J. Colwell, Robert Sheridan, Thomas A. Hopf, Andrea Pagnani, Riccardo Zecchina, and Chris Sander. Protein 3d structure computed from evolutionary sequence variation. *PLoS One*, 6(12):1–20, 12 2011.

[79] Hendrik Szurmant and Martin Weigt. Inter-residue, inter-protein and inter-family coevolution: bridging the scales. *Curr Opin Struct Biol*, 50:26 – 32, 2018. Carbohydrates Sequences and topology.

[80] Steve W. Lockless and Rama Ranganathan. Evolutionarily conserved pathways of energetic connectivity in protein families. *Science*, 286(5438):295–299, 1999.

[81] Najeeb Halabi, Olivier Rivoire, Stanislas Leibler, and Rama Ranganathan. Protein sectors: Evolutionary units of three-dimensional structure. *Cell*, 138(4):774 – 786, 2009.

[82] Robert G Smock, Olivier Rivoire, William P Russ, Joanna F Swain, Stanislas Leibler, Rama Ranganathan, and Lila M Gierasch. An interdomain sector mediating allostery in hsp70 molecular chaperones. *Mol Syst Biol*, 6:414–414, 2010.

[83] John P Barton, Mehran Kardar, and Arup K Chakraborty. Scaling laws describe memories of host–pathogen riposte in the hiv population. *Proc Natl Acad Sci U S A*, 112(7):1965–1970, 02 2015.

[84] Yue Zhao and Gary D Stormo. Quantitative analysis demonstrates most transcription factors require only simple models of specificity. *Nat Biotechnol*, 29(6):480, 2011.

[85] H P de Vladar and N H Barton. The statistical mechanics of a polygenic character under stabilizing selection, mutation and drift. *J R Soc Interface*, 8(58):720–739, March 2011.

[86] W.J. Ewens. *Mathematical Population Genetics: I. Theoretical Introduction*. Interdisciplinary Applied Mathematics. Springer, 2004.

[87] Michael Lässig. From biophysics to evolutionary genetics: statistical aspects of gene regulation. *BMC Bioinf*, 8(Suppl 6):S7, September 2007.

[88] R A Neher and B I Shraiman. Competition between recombination and epistasis can cause a transition from allele to genotype selection. *Proc Natl Acad Sci U S A*, 106(16):6866–6871, April 2009.

[89] Boris Shraiman, Richard A Neher, Marija Vucelja, and Marc Mézard. Emergence of clones in sexual populations. *J Stat Mech*, P01008, 2013.

[90] Sungmin Hwang, Su-Chan Park, and Joachim Krug. Genotypic complexity of fisher's geometric model. *Genetics*, 206(2):1049–1079, 2017.

[91] Richard A. Neher. Genetic draft, selective interference, and population genetics of rapid adaptation. *Annu Rev Ecol Evol Syst*, 44(1):195–215, 2013.

[92] Daniel P. Rice, Benjamin H. Good, and Michael M. Desai. The evolutionarily stable distribution of fitness effects. *Genetics*, 200(1):321–329, 2015.

[93] Warren J Ewens. *Mathematical Population Genetics*. Springer, New York, 2004.

[94] Thomas F. Hansen. Stabilizing selection and the comparative analysis of adaptation. *Evolution*, 51(5):1341–1351, 1997.

[95] Marguerite A Butler and Aaron A King. Phylogenetic comparative analysis: a modeling approach for adaptive evolution. *Am Nat*, 164(6):683–695, 2004.

[96] T Bedford and D L Hartl. Optimization of gene expression by natural selection. *Proc Natl Acad Sci U S A*, 106(4):1133–1138, January 2009.

[97] Jeremy M. Beaulieu, Dwueng-Chwuan Jhwueng, Carl Boettiger, and Brian C. OMeara. Modeling stabilizing selection: Expanding the Ornstein-Uhlenbeck model of adaptive evolution. *Evolution*, 66(8):2369–2383, 2012.

[98] Harold P. de Vladar and Nick H Barton. Stability and response of polygenic traits to stabilizing selection and mutation. *Genetics*, 197(2):749–767, 2014.

[99] Peiqiu Chen and Eugene I. Shakhnovich. Lethal mutagenesis in viruses and bacteria. *Genetics*, 183(2):639–650, 2009.

[100] Richard A. Goldstein. The evolution and evolutionary consequences of marginal thermostability in proteins. *Proteins: Struct , Funct , Bioinf*, 79(5):1396–1407, 2011.

[101] Adrian W.R. Serohijos and Eugene I. Shakhnovich. Merging molecular mechanism and evolution: theory and computation at the interface of biophysics and evolutionary population genetics. *Curr Opin Struct Biol*, 26(0):84–91, 2014.

[102] Peter B. Chi and David A. Liberles. Selection on protein structure, interaction, and sequence. *Protein Sci*, 25(7):1168–1178, 2016.

[103] Jakub Otwinowski. Inferring protein stability and function from a high-throughput assay. *arXiv preprint*, 1802.08744, 2018.

[104] M Hochstrasser. Ubiquitin-dependent protein degradation. *Annu Rev Genet*, 30:405–439, 1996.

[105] M Kopp and J Hermisson. The genetic basis of phenotypic adaptation ii: the distribution of adaptive substitutions in the moving optimum model. *Genetics*, 183:1453–76, 2009.

[106] Ville Mustonen and Michael Lässig. Molecular evolution under fitness fluctuations. *Phys Rev Lett*, 100(10):108101, March 2008.

[107] Ville Mustonen and Michael Lässig. Evolutionary population genetics of promoters: predicting binding sites and functional phylogenies. *Proc Natl Acad Sci U S A*, 102(44):15936–15941, November 2005.

[108] N H Barton and H P de Vladar. Statistical mechanics and the evolution of polygenic quantitative traits. *Genetics*, 181(3):997–1011, 2009.

[109] Richard A. Neher and Boris I. Shraiman. Statistical genetics and evolution of quantitative traits. *Rev Mod Phys*, 83:1283–1300, Nov 2011.

[110] Frank Poelwijk, Philip Heyning, Marjon de Vos, Daniel Kiviet, and Sander Tans. Optimality and evolution of transcriptionally regulated gene expression. *BMC Syst Biol*, 5(1):128, 2011.

[111] C. Scott Wylie and Eugene I. Shakhnovich. A biophysical protein folding model accounts for most mutational fitness effects in viruses. *Proc Natl Acad Sci U S A*, 108(24):9916–9921, 2011.

[112] Rutger Hermsen, J. Barrett Deris, and Terence Hwa. On the rapidity of antibiotic resistance evolution facilitated by a concentration gradient. *Proc Natl Acad Sci U S A*, 2012.

[113] M. Lässig. Dynamical anomalies and intermittency in burgers turbulence. *Phys Rev Lett*, 84(12):2618–21, 2000.

[114] Michael Lynch and Allan Force. The probability of duplicate gene preservation by subfunctionalization. *Genetics*, 154(1):459–473, 2000.

[115] Olivier Rivoire and Stanislas Leibler. A model for the generation and transmission of variations in evolution. *Proc Natl Acad Sci U S A*, 111(19):E1940–E1949, 2014.

[116] M Möhle. Forward and backward diffusion approximations for haploid exchangeable population models. *Stoch Proc Appl*, 95:133–149, 2001.

[117] Ranajit Chakraborty and Masatoshi Nei. Genetic differentiation of quantitative characters between populations or species: I. mutation and random genetic drift. *Genet Res*, 39:303–314, 6 1982.

[118] Michael Lynch and William G. Hill. Phenotypic evolution by neutral mutation. *Evolution*, 40(5):915–935, 1986.

[119] J F Crow. Some possibilities for measuring selection intensities in man. *Hum Biol*, 30(1):1–13, 1958.

[120] J F Crow and M Kimura. Evolution in sexual and asexual populations. *Am Nat*, 99(909):439–450, 1965.

[121] J B S Haldane. The cost of natural selection. *J Genet*, 55(3):511–524, 1957.

[122] H J Muller. Our load of mutations. *Am J Hum Genet*, 2(2):111–176, 1950.

[123] D. L. Hartl and C. H. Taubes. Towards a theory of evolutionary adaptation. *Genetica*, 102-103:525–533, 1998.

[124] A Poon and S. P. Otto. Compensating for our load of mutations: freezing the meltdown of small populations. *Evolution*, 54:1467–1479, 2000.

[125] Olivier Tenaillon, Olin K Silander, Jean-Philippe Uzan, and Lin Chao. Quantifying organismal complexity using a population genetic approach. *PLoS One*, 2(2):e217, 2007.

[126] V Y Chernyak, M Chertkov, and C Jarzynski. Path-integral analysis of fluctuation theorems for general langevin processes. *J Stat Mech*, 8:080001, 2006.

[127] Philipp Khaitovich, Ines Hellmann, Wolfgang Enard, Katja Nowick, Marcus Leinweber, Henriette Franz, Gunter Weiss, Michael Lachmann, and Svante Pääbo. Parallel patterns of evolution in the genomes and transcriptomes of humans and chimpanzees. *Science*, 309(5742):1850–1854, 2005.

[128] Yoav Gilad, Alicia Oshlack, Gordon K Smyth, Terence P Speed, and Kevin P White. Expression profiling in primates reveals a rapid evolution of human transcription factors. *Nature*, 440(7081):242, 2006.

[129] Hunter B Fraser. Genome-wide approaches to the study of adaptive gene expression evolution. *Bioessays*, 33(6):469–477, April 2011.

[130] J H McDonald and M Kreitman. Adaptive protein evolution at the Adh locus in Drosophila. *Nature*, 351(6328):652–654, 1991.

[131] Nick G. C. Smith and Adam Eyre-Walker. Adaptive protein evolution in drosophila. *Nature*, 415:1022–1024, 02 2002.

[132] Ellen M. Leffler, Kevin Bullaughey, Daniel R. Matute, Wynn K. Meyer, Laure Ségurel, Aarti Venkat, Peter Andolfatto, and Molly Przeworski. Revisiting an old riddle: What determines genetic diversity levels within species? *PLoS Biol*, 10(9):1–9, 09 2012.

[133] Guy Sella, Dmitri A Petrov, Molly Przeworski, and Peter Andolfatto. Pervasive natural selection in the drosophila genome? *PLos Genet*, 5(6):e1000495, 2009.

[134] Ivan G. Szendro, Jasper Franke, J. Arjan G. M. de Visser, and Joachim Krug. Predictability of evolution depends nonmonotonically on population size. *Proc Natl Acad Sci U S A*, 110(2):571–576, 2013.

[135] Stuart A. Kauffman and Edward D. Weinberger. The nk model of rugged fitness landscapes and its application to maturation of the immune response. *J Theor Biol*, 141(2):211 – 245, 1989.

[136] Stefan Nowak and Joachim Krug. Analysis of adaptive walks on nk fitness landscapes with different interaction schemes. *J Stat Mech Theor Exp*, 2015(6):P06014, 2015.

[137] J. F. C. Kingman. A simple model for the balance between selection and mutation. *J Appl Probab*, 15(1):112, 1978.

[138] Simone Pompei, Torsten Held, and Michael Lässig. Adaptive traits of the human influenza. In preparation.

[139] H. Chau Nguyen, Riccardo Zecchina, and Johannes Berg. Inverse statistical problems: from the inverse ising problem to data science. *Adv Phys*, 66(3):197–261, 2017.

[140] Günter P. Wagner and Jianzhi Zhang. The pleiotropic structure of the genotype–phenotype map: the evolvability of complex organisms. *Nat Rev Genet*, 12(3):204–213, 03 2011.

[141] Richard N. McLaughlin Jr, Frank J. Poelwijk, Arjun Raman, Walraj S. Gosal, and Rama Ranganathan. The spatial architecture of protein function and adaptation. *Nature*, 491(7422):138–142, 11 2012.

[142] Björn F. Koel, David F. Burke, Theo M. Bestebroer, Stefan van der Vliet, Gerben C. M. Zondag, Gaby Vervaet, Eugene Skepner, Nicola S. Lewis, Monique I. J. Spronken, Colin A. Russell, Mikhail Y. Eropkin, Aeron C. Hurt, Ian G. Barr, Jan C. de Jong, Guus F. Rimmelzwaan, Albert D. M. E. Osterhaus, Ron A. M. Fouchier, and Derek J. Smith. Substitutions near the receptor binding site determine major antigenic change during influenza virus evolution. *Science*, 342(6161):976–979, 2013.

[143] Sergey Kryazhimskiy, Jonathan Dushoff, Georgii A. Bazykin, and Joshua B. Plotkin. Prevalence of epistasis in the evolution of influenza a surface proteins. *PLos Genet*, 7(2):1–11, 02 2011.

[144] Alexey D. Neverov, Sergey Kryazhimskiy, Joshua B. Plotkin, and Georgii A. Bazykin. Coordinated evolution of influenza a surface proteins. *PLos Genet*, 11(8):1–26, 08 2015.

[145] H. J. Muller. Some genetic aspects of sex. *Am Nat*, 66(703):118–138, 1932.

[146] Joseph Felsenstein. The evolutionary advantage of recombination. *Genetics*, 78(2):737–756, March 1974.

[147] A S Kondrashov. Classification of hypotheses on the advantage of amphimixis. *J Hered*, 84(5):372–387, 1993.

[148] John H. Gillespie. Genetic drift in an infinite population: The pseudohitchhiking model. *Genetics*, 155(2):909–919, 2000.

[149] Benjamin H. Good, Aleksandra M. Walczak, Richard A. Neher, and Michael M. Desai. Genetic diversity in the interference selection limit. *PLos Genet*, 10(3):e1004222, 03 2014.

[150] Matthew Scott, Carl W. Gunderson, Eduard M. Mateescu, Zhongge Zhang, and Terence Hwa. Interdependence of cell growth and gene expression: Origins and consequences. *Science*, 330(6007):1099–1102, 2010.

[151] Michael Lynch and Georgi K. Marinov. The bioenergetic costs of a gene. *Proc Natl Acad Sci U S A*, 112(51):15690–15695, 2015.

[152] Daniel B. Weissman and Nicholas H. Barton. Limits to the rate of adaptive substitution in sexual populations. *PLos Genet*, 8(6):1–18, 06 2012.

[153] Josep M. Comeron, Ramesh Ratnappan, and Samuel Bailin. The many landscapes of recombination in *Drosophila melanogaster*. *PLos Genet*, 8(10):1–21, 10 2012.

[154] S. Schiffels, V. Mustonen, and M. Lässig. The asexual genome of Drosophila. *ArXiv e-prints*, November 2017.

[155] Nobuhiko Tokuriki, Francois Stricher, Joost Schymkowitz, Luis Serrano, and Dan S. Tawfik. The stability effects of protein mutations appear to be universally distributed. *J Mol Biol*, 369(5):1318–1332, 2007.

[156] Konstantin B. Zeldovich, Peiqiu Chen, and Eugene I. Shakhnovich. Protein stability imposes limits on organism complexity and speed of molecular evolution. *Proc Natl Acad Sci U S A*, 104(41):16152–16157, 2007.

[157] Justin B Kinney, Anand Murugan, Curtis G Callan, and Edward C Cox. Using deep sequencing to characterize the biophysical mechanism of a transcriptional regulatory sequence. *Proc Natl Acad Sci U S A*, 107(20):9158–9163, 2010.

[158] Murat Tuğrul, Tiago Paixão, Nicholas H. Barton, and Gašper Tkačik. Dynamics of transcription factor binding site evolution. *PLos Genet*, 11(11):1–28, 11 2015.

[159] Guilhem Faure and Eugene V Koonin. Universal distribution of mutational effects on protein stability, uncoupling of protein robustness from sequence evolution and distinct evolutionary modes of prokaryotic and eukaryotic proteins. *Phys Biol*, 12(3):035001–035001, 05 2015.

[160] Crispin Gardiner. *Handbook of Stochastic methods: for physics, chemistry and the natural sciences*. Springer, 3rd edition, April 2004.

[161] Michael Lynch, Way Sung, Krystalynne Morris, Nicole Coffey, Christian R. Landry, Erik B Dopman, W Joseph Dickinson, Kazufusa Okamoto, Shilpa Kulkarni, Daniel L Hartl, and W Kelley Thomas. A genome-wide view of the spectrum of spontaneous mutations in yeast. *Proc Natl Acad Sci U S A*, 105(27):9272–9277, 2008.

[162] Peter D. Keightley, Rob W. Ness, Daniel L. Halligan, and Penelope R. Haddrill. Estimation of the spontaneous mutation rate per nucleotide site in a drosophila melanogaster full-sib family. *Genetics*, 196(1):313–320, 2014.

[163] Stephan Ossowski, Korbinian Schneeberger, José Ignacio Lucas-Lledó, Norman Warthmann, Richard M. Clark, Ruth G Shaw, Detlef Weigel, and Michael Lynch. The rate and molecular spectrum of spontaneous mutations in *Arabidopsis thaliana*. *Science*, 327(5961):92–94, 2009.

[164] Paul M. Harrison, Duncan Milburn, Zhaolei Zhang, Paul Bertone, and Mark Gerstein. Identification of pseudogenes in the *Drosophila melanogaster* genome. *Nucleic Acids Res*, 31(3):1033–1037, 2003.

[165] Evelyne Derelle, Conchita Ferraz, Stephane Rombauts, Pierre Rouzé, Alexandra Z Worden, Steven Robbens, Frédéric Partensky, Sven Degroeve, Sophie Echeynié, Richard Cooke, Yvan Saeys, Jan Wuyts, Kamel Jabbari, Chris Bowler, Olivier Panaud, Benot Piégu, Steven G Ball, Jean-Philippe Ral, François-Yves Bouget, Gwenael Piganeau, Bernard De Baets, André Picard, Michel Delseny, Jacques Demaille, Yves Van de Peer, and Hervé Moreau. Genome analysis of the smallest free-living eukaryote *Ostreococcus tauri* unveils many unique features. *Proc Natl Acad Sci U S A*, 103(31):11647–11652, January 2006.

[166] Jian Feng, Daniel Q. Naiman, and Bret Cooper. Coding DNA repeated throughout intergenic regions of the *Arabidopsis thaliana* genome: evolutionary footprints of RNA silencing. *Mol Biosyst*, 5:1679–1687, 2009.

[167] Douglas M Ruderfer, Stephen C Pratt, Hannah S Seidel, and Leonid Kruglyak. Population genomic analysis of outcrossing and recombination in yeast. *Nat Genet*, 38(9):1077–1081, September 2006.

[168] Anna-Sophie Fiston-Lavier, Nadia D. Singh, Mikhail Lipatov, and Dmitri A. Petrov. *Drosophila melanogaster* recombination rate calculator. *Gene*, 463(12):18 – 20, 2010.

[169] P A Salomé, K Bomblies, J Fitz, R A E Laitinen, N Warthmann, L Yant, and D Weigel. The recombination landscape in *Arabidopsis thaliana* F_2 populations. *Heredity*, 108(4):447–455, April 2012.

Appendix A

Numerical simulations with Wright-Fisher processes

We test our analytical results by simulations of a Wright-Fisher process [31, 32] for the evolution under neutral mutation-drift dynamics, in various fitness landscapes with stabilizing selection. We extend these landscapes to diffusive or punctuated fitness seascapes for sexual and asexual populations. For a single trait, we evolve a population of N individuals with genomes $\mathbf{a}^{(1)}, \ldots, \mathbf{a}^{(N)}$, which are bi-allelic sequences of length ℓ. A genotype $\mathbf{a}$ defines a phenotype $E(\mathbf{a}) = \sum_{i=1}^{\ell} E_i a_i$. The phenotypic effects E_i are drawn from various distributions. We generalize this approach to the co-evolution of multiple phenotypes below.

Generation sampling In each generation, the sequences undergo point mutations with a probability $\tau_{\text{gen}}\mu$ per generation, where τ_{gen} is the generation time. The sequences of next generation are then obtained by multinomial sampling; the general form of the sampling probability is proportional to $[1 + \tau_{\text{gen}} f(E(\mathbf{a}), t)]$, with the fitness seascape $f(E, t)$.

Recombination The evolutionary statistics of the trait mean depends indirectly on the recombination rate; this dependence arises because the mean diversity $\langle \Delta \rangle$ enters the quasi-neutral dynamics of Γ [53]. To simulate evolution with a finite recombination rate R, we recombine the genomes of pairs of individuals with probability $\tau_{\text{gen}} R$ at a single random crossover position of the genome. For the simulation of free recombination, we randomly shuffle the alleles $a_i^1, ..., a_i^N$ between the individuals at each genomic site i and in each generation. Simulations with recombination are presented in Figures C.1, C.2 (both for the adaptive ensemble), and 5.4C (for the phenotypic interference).

Adaptive ensemble

For a diffusive seascape, a new optimal trait value $E^*(t)$ is drawn before each reproduction step from a Gaussian distribution with mean $(1 - \tau_{\text{gen}} \upsilon / r^2) E^*(t) + \tau_{\text{gen}} (\upsilon / r^2) \mathcal{E}$ and variance $\tau_{\text{gen}} \upsilon E_0^2$. For a punctuated seascape, a new, uncorrelated fitness peak is drawn from the distribution

$R_{\rm eq}(E^*)$ with probability $\tau_{\rm gen}\upsilon/r^2$.

Universality is the (approximate) independence of a summary trait observable from details of the trait's genomic encoding and of its molecular evolution [2]. In Figure C.2, we report three universality tests for the divergence-diversity ratio $\Omega^{(1)}(\tau)$. First, simulations show that the Ω statistics depends only weakly on the recombination rate throughout the crossover between asexual evolution ($R = 0$) and free recombination ($R \to \infty$). Second, the Ω ratio is invariant under variations in the number of constitutive genomic sites, ℓ, at constant selection parameters c and υ. Third, this ratio is also invariant under variations of the phenotypic effect sizes E_i at these sites; this is tested by comparing simulations for two distributions of effect sizes.

QTL Epistasis

Here, we add adaptive pressure on single sites with selection coefficient $\eta_i s_i$ and flip probability $\tau_{\rm gen}\gamma_i$: $\eta_i \leftrightarrow -\eta_i$, $\eta_i = \pm 1$. For heterogeneous driver/trailer association of the sites we either implement heterogeneous s_i or heterogeneous γ_i. The particular values are shown in Figures 4.3, 4.4 and D.1C. The same underlying distributions in other figures are referred to these, but not shown if not influencing the response significantly. For 2 co-evolving traits, we add a second trait $G(\mathbf{a}) = \sum_{i=1}^{\ell} G_i a_i$. All traits evolve in a quadratic fitness landscape (2.24) such that the total fitness reads $f(\mathbf{a}) = f(E(\mathbf{a}); c_0^E) + f(G(\mathbf{a}); c_0^G) + \sum_i a_i \eta_i(t) s_i$ with c_0^E or c_0^G setting the curvature parameter of the particular fitness landscape. We discuss various kinds of distributions for E_i and G_i, which also define the degree of pleiotropy. The distributions are shown in the plots.

We measure for each substitution the time of fixation. However, we use the number of substitutions between two focal substitutions as time τ in the correlation analysis: this time-measure is comparable to the times available for reconstructed phylogenetic tree. If various new mutations fixed at the same time, we average over all possible time-orderings of their arising, which are not known. Furthermore, we give them a temporal distance by equal time-gaps between their arise since the preceding substitution event. Simulations are performed with parameters $N = 1000$, $N\mu = 0.0125$. We measure $40,000$ substitutions and count sites only, if they show more than 5 substitutions in the data (this concerns sites with strong single-site selection and very small γ_i only).

Phenotypic interference

Co-evolution of stability traits. Here each QTL segment is a subsequence $\mathbf{a}_i = (a_{i,1}, \ldots, a_{i,\ell})$ with binary alleles $a_{j,k} = 0, 1$ ($i = 1, \ldots, g$; $k = 1, \ldots, \ell$). A segment $\mathbf{a}$ defines a stability trait $G(\mathbf{a}) = \sum_{k=1}^{\ell} G_k a_k + G_{\rm min}$, where $G_{\rm min}$ is the smallest possible trait value. The resulting effect distribution of point mutations has as a second moment $\epsilon_G^2 = \sum_{\imath=1}^{\ell} G_k^2/\ell$ and a first moment $\kappa_0 \epsilon_G = \sum_{\imath=1}^{\ell} G_k(1 - 2\langle a_k \rangle)/\ell$, where $\langle a_k \rangle$ is the state-dependent probability of a mutation at site k being beneficial and brackets $\langle . \rangle$ denote averaging across parallel simulations or time. The genomic fitness is $f(\mathbf{a}) = \sum_{i=1}^{g} f(G(\mathbf{a}_i); f_{0,i})$ with $f(G; f_{0,i})$ given by Equation (2.25) and gene-specific amplitudes $f_{0,i}$.

Simulations are performed with parameters $N = 1000$, $N\mu = 0.0125$, each trait with genomic base of size $\ell = 100$, and each site with equal effect $G_k = 1$. The quantitative trait dynamics is insensitive to the form of the effect distribution [53]. To increase the performance of the simulations, we do not keep track of the full genome. We only store the number of deleterious alleles $n_i = \sum_{k=1}^{\ell} a_{i,k}$ for each trait, we draw mutations with rate $u = \mu\ell$, and we assign to each mutation a beneficial change $\mathcal{G}$ with probability n_i/ℓ and a deleterious change $-\mathcal{G}$ otherwise. This procedure produces the correct genome statistics for bi-allelic sites with uniform trait effects $G_i = \mathcal{G}$. Simulation data are shown with theory curves for $\kappa = 1$, which provide a good fit to all amplitudes; the input κ_0 is different by a factor of order 1 which includes fluctuation effects (Section E.2).

Housekeeping evolution. For the simulations in Figures 5.3 and 5.4A, where we are not explicitly interested in the loss of genes, we use an exponential approximation of the stable regime of the stability fitness landscape. The reason is a limited accessible parameter range in simulations constraining the values of f_0 and $\tilde{\sigma}$ due to finite N. We checked that the exponential approximation gives the same results as the full model in the regime $f_0/\tilde{\sigma} \gg 1$, where the gene loss rate in the biophysical landscape is negligible.

Loss rate measurements. In the biophysical landscape used in Fig 5.4B, a long-term stationary population is maintained by evolving 70% of the traits in a biophysical fitness landscape with selection f_0; the remaining 30% of the traits are modeled to be essential with selection $10f_0$. Gene loss is defined by the condition $G < -3.5k_BT$. To maintain a constant number of genes, lost genes are replaced immediately with an input trait value $G > 0$.

Appendix B

Coevolution of quantitative traits

In Section 2, we presented the dynamics of the population mean Γ and the diversity Δ of a single quantitative trait. We further showed the generated epistatic pattern ω_{ij}. In this appendix, we extend the dynamics and epistatic pattern to multiple co-evolving quantitative traits.

B.1 Dynamics of epistatic traits

In this section, we discuss the extension of the mean trait dynamics (2.4) to co-evolutionary dynamics of two traits. This can be biophysical related traits, evolving in a 2-dimensional fitness landscape $f(E, G)$ of Equations (2.27) or (2.30). However, we discuss the co-evolution in a generic fitness landscape.

The population genetics of the two-trait system is described by the population mean values Γ_G and Γ_E, the diversities Δ_{GG} and Δ_{EE}, and the covariance Δ_{GE}. Under mutations, genetic drift or draft, and selection given by the fitness landscape $f(G, E)$, the mean traits follow a stochastic evolution equation analogous to Equation (2.4). We present it here in the Langevin picture of the corresponding Fokker-Planck equation

$$\begin{pmatrix} \dot{\Gamma}_G \\ \dot{\Gamma}_E \end{pmatrix} = \begin{pmatrix} m^{\Gamma_G} \\ m^{\Gamma_E} \end{pmatrix} + \boldsymbol{g} \begin{pmatrix} \partial_G F_1(E,G) \\ \partial_E F_1(E,G) \end{pmatrix} + \begin{pmatrix} \chi_G \\ \chi_E \end{pmatrix}, \tag{B.1}$$

with $m^{\Gamma_{g'}}$ defined as (2.10) for each trait g' and $\boldsymbol{g} = \begin{pmatrix} \langle \Delta_{GG} \rangle & \langle \Delta_{GE} \rangle \\ \langle \Delta_{GE} \rangle & \langle \Delta_{EE} \rangle \end{pmatrix}$ similar to Equation (2.9). In the effective mean trait fitness,
$F_1(E,G) = f(E,G) + \mathcal{O}\left(\Delta_{GG}\frac{\partial^2 f}{\partial G \partial G}(E,G) + \Delta_{GE}\frac{\partial^2 f}{\partial G \partial E}(E,G) + \Delta_{EE}\frac{\partial^2 f}{\partial E \partial E}(E,G)\right)$, the higher orders are negligible if the diversities is strong enough constrained, which we assumne. Furthermore, the fluctuations of the dynamics have mean and variance

$$\begin{pmatrix} \langle \chi_G \rangle \\ \langle \chi_E \rangle \end{pmatrix} = \begin{pmatrix} 0 \\ 0 \end{pmatrix}, \qquad \begin{pmatrix} \langle \chi_G(t)\chi_G(t') \rangle & \langle \chi_G(t)\chi_E(t') \rangle \\ \langle \chi_G(t)\chi_E(t') \rangle & \langle \chi_E(t)\chi_E(t') \rangle \end{pmatrix} = \tilde{\sigma}\delta(t-t') \begin{pmatrix} \Delta_{GG} & \Delta_{GE} \\ \Delta_{GE} & \Delta_{EE} \end{pmatrix}. \tag{B.2}$$

In the scope of this work, we are not particularly interested in the co-evolution of trait diversities, i.e. the generalization of (2.5).

A stationary state under time-independent selection has the property

$$\begin{pmatrix} \langle \partial_G f(E,G) \rangle \\ \langle \partial_E f(E,G) \rangle \end{pmatrix} = -\mathbf{g}^{-1} \begin{pmatrix} \langle m^{\Gamma_G} \rangle \\ \langle m^{\Gamma_E} \rangle \end{pmatrix}. \tag{B.3}$$

Therefore, the gradient in both directions is just given by the mutational effects coupled through the (co-)diversities. If this polymorphism is not constrained by selection but genetic drift or draft, it is similar to (2.15) with the same implications for the mutational effects however coupled through $\langle \Delta_{GE} \rangle$. If this mutational covariance is small, the same statement holds for the expected squared slopes, cp. (2.15). However, as a stability condition, both directional derivates need to be large enough, which is the problem for the thermodynamics equilibrium of biophysical traits (2.27) discussed in the main text.

B.2 Selection on pleiotropic trait sites

For g co-evolving, possibly pleiotropic quantitative traits, the selection of a mutation in a fitness land- or seascape $f(E^1, \ldots, E^g, t)$ is approximately additive in the traits,

$$s_j^f(E^1, \ldots, E^g, t) \approx \sum_{g'=1}^{g} E_j^{g'} \partial_{E^{g'}} f(E^1, \ldots, E^g, t),$$

cp. (2.16) for $g = 1$. The epistatic selection

$$\begin{aligned} s_{j|i}^f(E^1, \ldots, E^g, t) &\approx \sum_{g'=1}^{g} E_j^{g'} \partial_{E^{g'}} f(E^1 + E_i^1, \ldots, E^g + E_i^g, t) - E_j^{g'} \partial_{E^{g'}} f(E^1, \ldots, E^g, t) \\ &\approx \sum_{g',g''=1}^{g} \underbrace{E_i^{g''} E_j^{g'} \frac{\partial^2 f}{\partial E^{g''} \partial E^{g'}}(E_1, \ldots E_g, t)}_{=:\omega_{ij}^{g',g''}(E^1,\ldots E^g,t)/(2N)} \end{aligned} \tag{B.4}$$

has in principle g^2 terms, if all traits have highly inter-functional epistasis between each trait pair. Each term is in its site-dependence just the outer product of the trait effects. In Chapter 4 we discuss the case without functional epistasis, i.e. additive selection across traits, where the Hessian matrix of $f(E_1, \ldots E_g) = f_1(E_1) + \cdots + f_g(E_g)$ is diagonal. The epistatic selection then reduces to

$$s_{j|i}^f(E^1, \ldots, E^g, t) \approx \sum_{g'} \underbrace{E_i^{g'} E_j^{g'} \frac{\partial^2}{\partial E^{g'2}} f_{g'}(E_{g'}, t)}_{=:\omega_{ij}^{g'}(E^{g'},t)/(2N)}, \tag{B.5}$$

which defines the average epistatic score for a particular gene $\omega_{ij}^{g'} := 2N \langle f''_{g'}(\Gamma^{g'}) \rangle$ averaged in a steady state for each trait.

Appendix C

Analytical theory of the adaptive ensemble

In Section 3.3.1, we obtained the Gaussian stationary distribution $Q_{\rm stat}(\Gamma, E^*)$ in a diffusive seascape from the underlying Fokker-Planck equation (2.4). Here we use a Langevin representation to compute the time-resolved trait divergence $\langle d^{(\kappa)}\rangle(\tau)$ ($\kappa = 1, 2$). This derivation, which reproduces mean and variance of the distribution $Q_{\rm stat}(\Gamma, E^*)$, applies to diffusive and punctuated fitness seascapes. We also compute the full propagator function $G_\tau(\Gamma, E^*|\Gamma_a, E_a^*)$ for macro-evolutionary diffusive seascapes. The propagator in a punctuated fitness seascape has the same mean and variance, but differs in higher trait moments.

Moments of the optimal trait. In a diffusive seascape, the fitness peak $E^*(t)$ follows an Ornstein-Uhlenbeck process with Langevin representation

$$\partial_t E^*(t) = -\frac{\upsilon}{r^2}(E^*(t) - G) + \eta(t), \tag{C.1}$$

where $\eta(t)$ is a Gaussian random variable with the statistics

$$\langle \eta(t)\rangle = 0, \quad \langle \eta(t)\eta(t')\rangle = 2\upsilon E_0^2\, \delta(t - t'). \tag{C.2}$$

Formally solving Equation (C.1),

$$E^*(t+\tau) = E^*(t)e^{-\tau/\tau_{\rm sat}} + \mathcal{E}(1 - e^{-\tau/\tau_{\rm sat}}) + \int_{t_1}^{t_2} {\rm d}t'\, e^{-(\tau - t')/\tau_{\rm sat}}\eta(t'), \tag{C.3}$$

and evaluating the noise correlations (C.2), we obtain the average peak value with an initial condition $E^*(t) = E_a$ and the autocorrelation function of the fitness peak in the stationary ensemble,

$$\begin{aligned} \langle E^*(t+\tau)\rangle(E_a) &= E_a e^{-\tau/\tau_{\rm sat}} + \mathcal{E}\big(1 - e^{-\tau/\tau_{\rm sat}}\big), & \text{(C.4)}\\ \langle E^*(t)E^*(t+\tau)\rangle &= \mathcal{E}^2 + E_0^2 r^2 e^{-\tau/\tau_{\rm sat}}. & \text{(C.5)} \end{aligned}$$

It is straightforward to check that Equations (C.4) and (C.5) are valid also for punctuated seascapes.

Moments of the trait mean. The Langevin equation for $\Gamma(t)$ reads

$$\partial_t \Gamma(t) = -2\mu(\Gamma(t) - \Gamma_0) - \langle\Delta\rangle \frac{2c}{E_0^2}(\Gamma(t) - E^*(t)) + \xi(t), \tag{C.6}$$

where $\xi(t)$ is a Gaussian noise with the statistics

$$\langle\xi(t)\rangle = 0, \quad \langle\xi(t)\xi(t')\rangle = \frac{\langle\Delta\rangle}{N}\,\delta(t-t'), \quad \langle\xi(t)E^*(t')\rangle = 0. \tag{C.7}$$

For diffusive seascapes, the last term in (C.7) is equivalent to $\langle\xi(t)\eta(t')\rangle = 0$, which implies that genetic drift and fitness seascape fluctuations are independent. The formal solution of Equation (C.6) reads

$$\begin{aligned}\Gamma(t+\tau) &= e^{-\tau/\tau_{\rm eq}}\Gamma(t) + (1-w(c))(1-e^{-\tau/\tau_{\rm eq}})\Gamma_0 \\ &\quad + \int_t^{t+\tau} \mathrm{d}t'\,(E^*(t')c\langle\delta\rangle + \xi(t'))\,e^{-(t+\tau-t')/\tau_{\rm eq}},\end{aligned} \tag{C.8}$$

where $w(c) = [1 + 2\theta/(c\langle\delta\rangle)]^{-1}$. In the case of a diffusive fitness seascape, we can insert the trajectory of the fitness peak $E^*(t)$ given by Equation (C.3),

$$\begin{aligned}\Gamma(t+\tau) &= \Gamma(t)e^{-\tau/\tau_{\rm eq}} + E^*(t)w(c,-\upsilon,r^2)\big(e^{-\tau/\tau_{\rm sat}} - e^{-\tau/\tau_{\rm eq}}\big) \\ &\quad +\Gamma_0(1-w(c))(1-e^{-\tau/\tau_{\rm eq}}) \\ &\quad +\mathcal{E}w(c,-\upsilon,r^2)\left[\big(1-e^{-\tau/\tau_{\rm sat}}\big) + \frac{\tau_{\rm eq}}{\tau_{\rm sat}}\big(1-e^{-\tau/\tau_{\rm eq}}\big)\right] \\ &\quad + \int_t^{t+\tau}\mathrm{d}t'\,\Big[\xi(t')e^{-(t+\tau-t')/\tau_{\rm eq}} \\ &\qquad\qquad +\eta(t')w(c,-\upsilon,r^2)\big(e^{-(t+\tau-t')/\tau_{\rm sat}} - e^{-(t+\tau-t')/\tau_{\rm eq}}\big)\Big];\end{aligned} \tag{C.9}$$

see e.g. Section 4 of [160]. Evaluating the noise correlations (C.7), we obtain

$$\langle\Gamma\rangle = w(c)\mathcal{E} + (1-w(c))\Gamma_0, \tag{C.10}$$

$$\begin{aligned}\langle\Gamma(t)\Gamma(t+\tau)\rangle &= \langle\Gamma\rangle^2 + \langle\hat{\Gamma}^2\rangle e^{-\tau/\tau_{\rm eq}} \\ &\quad +r^2E_0^2w(c,\upsilon,r^2)w(c,-\upsilon,r^2)(e^{-\tau/\tau_{\rm sat}} - e^{-\tau/\tau_{\rm eq}}),\end{aligned} \tag{C.11}$$

$$\begin{aligned}\langle\Gamma(t+\tau)E^*(t)\rangle &= \langle\Gamma\rangle\mathcal{E} + E_0^2r^2w(c,-\upsilon,r^2)e^{-\tau/\tau_{\rm sat}} \\ &\quad -H(\tau)E_0^2\,\upsilon\tau_{\rm eq}(c)w(c,\upsilon,r^2)w(c,-\upsilon,r^2)\big(e^{-\tau/\tau_{\rm eq}} - e^{-\tau/\tau_{\rm sat}}\big),\end{aligned} \tag{C.12}$$

where $w(c,\upsilon,r^2) = [1 + (2\theta + 2N\tau_{\rm sat}^{-1}(\upsilon,r^2))/(c\langle\delta\rangle)]^{-1}$ and $H(\tau)$ is the Heaviside step function, i.e. $H(\tau) = 1$ for $\tau > 0$ and $H(\tau) = 0$ otherwise. The relations (C.10) – (C.12) are also valid for punctuated seascapes, as can be shown by evaluating Equation (C.8) with the noise terms (C.4), (C.5), and (C.7). The time-reflection asymmetry of the cross-correlation (C.12) reflects the causal relation between Γ and E^*. The equal-time correlations reproduce the moments (3.18) obtained from the solution of the Fokker-Planck equation.

From the autocorrelation function (C.11), we immediately obtain the scaled divergence $\langle d^{(1)}\rangle$ reported in Equation (3.30). For the divergence between descendent populations, $\langle d^{(2)}\rangle$, we additionally use the fact that the fitness fluctuations in the different lineages are independent of each other. In a diffusive fitness seascape, we have

$$\langle \eta_i(t)\eta_j(t')\rangle = \delta_{i,j}\,\delta(t-t')\,2\upsilon E_0^2, \qquad i,j = 1,2, \tag{C.13}$$

which implies

$$\big\langle (E_1^*(t+\tau_1) - \langle E_1^*(t+\tau_1)\rangle)(E_2^*(t+\tau_2) - \langle E_2^*(t+\tau_2)\rangle)\big\rangle = 0; \tag{C.14}$$

the latter relation is valid also for punctuated seascapes.

Propagators. We recall the decomposition of the bivariate propagator,

$$G_\tau(\Gamma, E^*|\Gamma_a, E_a^*) = G_\tau(\Gamma|\Gamma_a, E_a^*, E^*)\, G_\tau(E^*|E_a^*), \tag{C.15}$$

which reflects the independence of the fitness peak dynamics from the trait mean.

The fitness peak propagator takes the standard form for an Ornstein-Uhlenbeck process and a Poisson jump process, respectively,

$$G_\tau(E^*|E_a^*) = \begin{cases} \dfrac{1}{\sqrt{2\pi\langle\hat{E}^{*2}\rangle(\tau,E_a^*)}} \exp\left[-\dfrac{(E^* - \langle E^*\rangle(\tau,E_a^*))^2}{2\langle\hat{E}^{*2}\rangle(\tau)}\right], & \text{(diffusive seascape)}, \\[2ex] e^{-\tau/\tau_{\rm sat}}\delta(E^*-E_a^*) + (1-e^{-\tau/\tau_{\rm sat}})R_{\rm eq}(E^*), & \text{(punctuated seascape)}, \end{cases} \tag{C.16}$$

see, e.g. reference [160]. In both cases, the propagator has the same mean and variance,

$$\langle E^*\rangle(\tau,E_a^*) = E_a e^{-\tau/\tau_{\rm sat}} + \mathcal{E}\big(1-e^{-\tau/\tau_{\rm sat}}\big), \qquad \langle\hat{E}^{*2}\rangle(\tau) = r^2E_0^2\big(1-e^{-\tau/\tau_{\rm sat}}\big), \tag{C.17}$$

in accordance with Equations (C.4) and (C.5).

For diffusive seascapes, we can also compute the Gaussian propagator of the trait mean for given fitness peak positions,

$$G_\tau(\Gamma|\Gamma_a, E_a^*, E^*) = \frac{1}{\sqrt{2\pi\langle\hat{\Gamma}^2\rangle(\tau)}} \exp\left[-\frac{1}{2}\frac{\big(\Gamma - \langle\Gamma\rangle(\Gamma_a, E_a^*, E^*, \tau)\big)^2}{\langle\hat{\Gamma}^2\rangle(\tau)}\right]. \tag{C.18}$$

If $\tau_{\rm eq} \lesssim \tau_{\rm sat}(\upsilon, r^2)$ and $\tau \lesssim \tau_{\rm sat}(\upsilon, r^2)$, we can approximate the stochastic trajectory of the trait optimum $E^*(t')$ in the time interval $t_a = t - \tau \leq t' \leq t$ by the most likely trajectory for given initial and the final values: $E^*(t') = E_a^* + ((t' - t_a)/\tau)(E^* - E_a^*)$. In this saddle-point approximation, we obtain the conditional trait moments

$$\begin{aligned}\langle\Gamma\rangle(\Gamma_a, E_a^*, E^*, \tau) &= \Gamma_a \mathrm{e}^{-\tau/\tau_{\rm eq}} + \big(E_a^* w(c) + \Gamma_0(1 - w(c))\big)\big(1 - \mathrm{e}^{-\tau/\tau_{\rm eq}}\big) \\ &\quad + \frac{E^* - E_a^*}{\tau}\, w(c)\left[\tau - \tau_{\rm eq}\big(1 - \mathrm{e}^{-\tau/\tau_{\rm eq}}\big)\right], \end{aligned} \tag{C.19}$$

$$\langle\hat{\Gamma}^2\rangle(\tau) = E_0^2 \frac{w(c)}{2c}\big(1 - \mathrm{e}^{-\tau/\tau_{\rm eq}}\big). \tag{C.20}$$

Equations (C.15) – (C.20) determine the joint propagator $G_\tau(\Gamma, E^*|\Gamma_a, E_a^*)$ for divergence times $\tau_{\rm eq} \lesssim \tau_{\rm sat}(\upsilon, r^2)$. In the large-time limit, $\tau \gg \tau_{\rm sat}(\upsilon, r^2)$, the propagator becomes independent of the initial condition and approaches the stationary distribution, $G_\tau(\Gamma, E^*|\Gamma_a, E_a^*) \simeq Q_{\rm stat}(\Gamma, E^*)$, given by Equations (3.16–3.18). In most biological experiments, the trait optimum values are hidden variables of the evolutionary process. In that case, the only observable propagator is the marginal propagator for the trait mean,

$$\begin{aligned} G_\tau(\Gamma|\Gamma_a) &\equiv \int dE_a^* dE^*\, G_\tau(\Gamma, E^*|\Gamma_a, E_a^*)\, \frac{Q_{\rm stat}(\Gamma, E_a^*)}{Q_{\rm stat}(\Gamma)} \\ &= \frac{1}{\sqrt{2\pi\langle D^{(1)}\rangle(\tau)}} \exp\left[-\frac{1}{2}\frac{(\Gamma - \langle\Gamma\rangle(\Gamma_a, \mathcal{E}, \tau))^2}{\langle D^{(1)}(\tau)\rangle}\right]. \end{aligned} \tag{C.21}$$

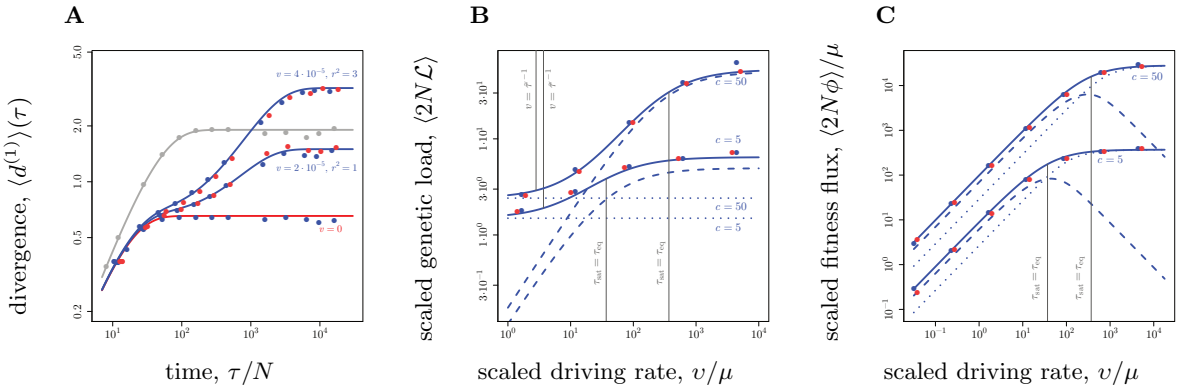

Figure C.1. Trait evolution under free recombination. **A** The scaled average divergence $\langle d^{(1)} \rangle(\tau)$ is shown as a function of the scaled divergence time τ/N for three cases: neutral evolution ($c = 0$; grey line), conservation in a static fitness landscape ($c = 1$, $v = 0$; red line), and adaptation in a macroevolutionary fitness seascape ($c = 1$, $v > 0$; blue lines). The analytical results of Equation (3.30) (lines) are compared to simulation results for evolution with free recombination in diffusive and punctuated fitness seascapes (blue and red dots, respectively). The analytical value of $\langle \delta \rangle$ is taken from Equation (69) of reference [53]; the other parameters are as in Figure 3.4. **B** Scaled genetic load $2N\mathcal{L}$ (full lines), adaptive load $2N\mathcal{L}_{\text{ad}}$ (dashed lines), and equilibrium load $2N\mathcal{L}_{\text{eq}}$ (dotted lines), plotted against the scaled driving rate v/μ. The other parameters are as in Figure 3.6A. **C** Scaled fitness flux $\langle 2N\phi \rangle$ and its components $\langle 2N\phi_{\text{micro}} \rangle$ and $\langle 2N\phi_{\text{macro}} \rangle$ (with decomposition constant $k = 2$), plotted against the scaled driving rate v/μ. The other parameters are as in Figure 3.6B.

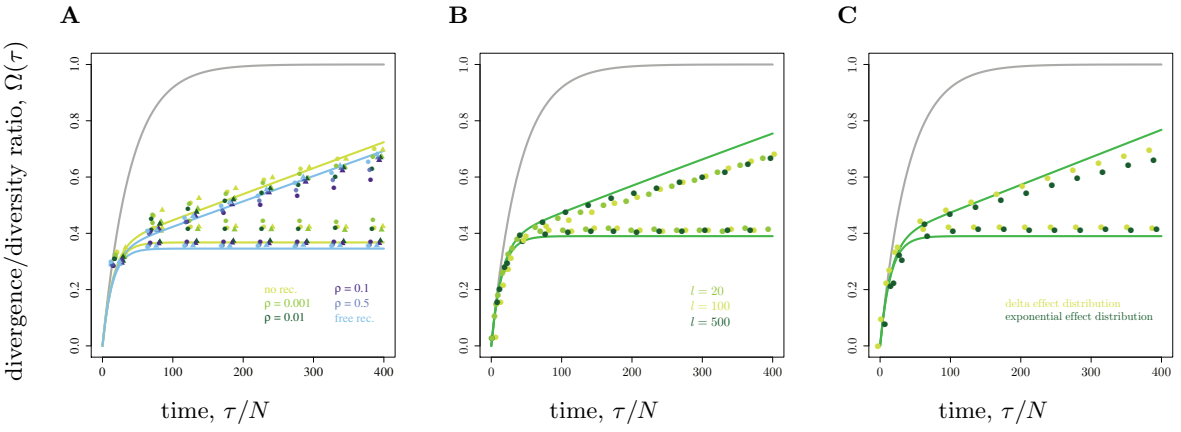

Figure C.2. Universality of the divergence/diversity ratio $\Omega(\tau)$. Numerical results for the evolution in fitness seascapes ($c = 1$, $v = 4 \cdot 10^{-5}$, upper lines and dots) and fitness landscapes ($c = 1$, $v = 0$, lower lines and dots) under different molecular conditions are compared to the analytical solutions for nonrecombining ($\rho = 0$) and free-recombining ($\rho \to \infty$) genomes. **A** Evolution with different recombination rates (color-coded dots for diffusive seascapes and triangles for punctuated seascapes). **B** Evolution with different numbers ℓ of constitutive sites in nonrecombining populations. **C** Evolution wih different effect distributions. The trait amplitudes E_i ($i = 1, \ldots, \ell$) are drawn from an exponential distribution with expectation value $1/\sqrt{2}$ and from a delta distribution (all sites have amplitude $E_i = 1$).

Appendix D

Detailed results of QTL epistasis and correlations

In this appendix, we collect the exact results and extensions for the QTL correlations and discuss the dimensional reduction of data. We start with the exact solution of single site state probabilities. We present the diagonal elements of the response matrix and the equilibrium asymmetry. We show the exact results for the polarized asymmetry and the response correlation under strong interference. We extend the correlation rates to finite frequencies of mutations, which do not change our conclusions in Chapter 4. Finally, we discuss how a dimension reduction of observed correlations retrieves the number of traits and trait effects.

D.1 Exact results for single site and pairwise substitution rates

Site state probabilities and substitution rates. Here, we present the exact results for the adaptive model in Section 4.2. These are particularly the marginal site statistics, i.e. the state probabilities $\Lambda_{\mathrm{stat},j}^{\epsilon_j,\eta_j}$ and the substitution rate ρ_j, which underly an interplay of the time-constant trait selection effect $N|s_j^f| \sim 1$, driving rate γ_j, and selection strength on driving Ns_j. The dynamics

$$\begin{aligned}\frac{\mathrm{d}}{\mathrm{d}t}\Lambda_j^{\epsilon_j,\eta_j}(t) = N\mu G\big(\epsilon_j(s_j^f+\eta_j s_j)\big)\Lambda_j^{-\epsilon_j,\eta_j}(t) + \gamma_j\Lambda_j^{\epsilon_j,-\eta_j}(t) \\ - \Big(N\mu G\big(-\epsilon_j(s_j^f+\eta_j s_j)\big)+\gamma_j\Big)\,\Lambda_j^{\epsilon_j,\eta_j}(t)\end{aligned} \tag{D.1}$$

is solved from the eigenanalysis of the transition matrix between all states (ϵ_j,η_j). We find for the stationary state probabilities

$$\Lambda_{\mathrm{stat},j}^{\epsilon_j,\eta_j} = \frac{1}{2}\Lambda_{\mathrm{eq},j}^{\epsilon_j,\eta_j}\frac{1+\frac{\gamma_j}{N\mu}\left(\frac{\Lambda_{\mathrm{eq},j}^{\epsilon_j,-\eta_j}}{G_j^{\epsilon_j,\eta_j}}+\frac{1}{G_j^{-\eta_j}}\right)}{1+\frac{\gamma_j}{N\mu}\left(\frac{1}{G_j^{-1}}+\frac{1}{G_j^{+1}}\right)}, \tag{D.2}$$

with $\Lambda_{\mathrm{eq},j}^{\epsilon_j,\eta_j} := \Lambda_{\mathrm{eq}}(\epsilon_j(s_j^f + \eta_j s_j))$, $G_j^{\epsilon_j,\eta_j} := G(\epsilon_j(s_j^f + \eta_j s_j))$, and $G_j^{\epsilon_j} := G_j^{\epsilon_j,+1} + G_j^{\epsilon_j,-1}$; $G(.)$ are obtained from Equation (2.21) or (2.22) and $\Lambda_{\mathrm{eq}}(.)$ from Equation (2.23). The equilibrium limit $\gamma_j \to 0$ has a factor 1/2 due to quenched disorder of the equilibrium solution (4.1) over both environmental states $\eta_j = \pm 1$.

The substitution rates (4.3) under Kimura substitution probabilities (2.21), which is the prerequisite for effective selection and hence strong driver sites, read

$$\rho_j = \rho_j^{\mathrm{eq}} \frac{1 + \frac{\gamma_j}{\mu} a_{j,1}}{1 + \frac{\gamma_j}{\mu} a_{j,2}} \tag{D.3}$$

$$= \begin{cases} \rho_j^{\mathrm{eq}}, & Ns_j \ll 1 \text{ or} \\ & \text{(effectively unadaptive)}, \\ \gamma_j, & Ns_j \gg N|s_j^f| \sim 1; \quad N|s_j^f| \mathrm{e}^{-Ns_j} \lesssim \gamma_j/\mu \lesssim Ns_j \\ & \text{(macro-evolutionary adaptation,)} \\ \mu N s_j, & Ns_j \gg N|s_j^f| \sim 1; \qquad\qquad \gamma_j/\mu \gtrsim Ns_j \\ & \text{(micro-evolutionary adaptation)}, \end{cases} \tag{D.4}$$

with

$$\rho_j^{\mathrm{eq}} = \mu \left(\frac{\Delta\sigma_j}{\sinh(2\Delta\sigma_j)} + \frac{\Sigma\sigma_j}{\sinh(2\Sigma\sigma_j)} \right) \tag{D.5}$$

being the quenched disorder equilibrium across both effective selection states $\Delta\sigma_j := N\left|s_j^f - s_j\right|$ and $\Sigma\sigma_j := N\left|s_j^f + s_j\right|$. The full solution of ρ_j has prefactors for the γ_j-terms in enumerator and denominator of (D.3),

$$a_{j,1} = \frac{\tanh(\Delta\sigma_j)\tanh(\Sigma\sigma_j)}{4\Delta\sigma_j\Sigma\sigma_j\left(\Delta\sigma_j \mathrm{csch}(2\Delta\sigma_j) + \Sigma\sigma_j \mathrm{csch}(2\Sigma\sigma_j)\right)} \times \left(2\Delta\sigma_j\Sigma\sigma_j\left(\coth(\Delta\sigma_j)\coth(\Sigma\sigma_j) - 1\right) + {\Delta\sigma_j}^2 \mathrm{csch}^2(\Delta\sigma_j) + {\Sigma\sigma_j}^2 \mathrm{csch}^2(\Sigma\sigma_j)\right)$$

and

$$a_{j,2} = \frac{2\Delta\sigma_j \coth(\Delta\sigma_j) + 2\Sigma\sigma_j \coth(\Sigma\sigma_j)}{4\Delta\sigma_j\Sigma\sigma_j \coth(\Delta\sigma_j)\coth(\Sigma\sigma_j)}.$$

The asymptotical behaviors are discussed in the main text.

Diagonal of response matrices. The self-response of a site deviates significantly from the broad pattern: a mutation on a site i brings compensation not only through the trait, but also conditions the response on its single-site selection. Hence, the self-response deviates from (4.7) and is in equilibrium

$$\rho_{ii}^{\epsilon_{i1}\epsilon_{i2}}(\tau) = \rho_{\mathrm{eq},i}^{\epsilon_{i1}} \delta_{\epsilon_{i1},-\epsilon_{i2}} \mu N G_{i|i}^{\epsilon_{i1}}(\tau),$$

with $G^{\epsilon_{i1}}_{i|i}(\tau) = G\Big(-\epsilon_{i1}\big(s_i^{\rm tot} - |\langle s^f_{i|i}\rangle_{b_i}(\tau)|\big)\Big)$. The Kronecker-delta $\delta_{\epsilon_{i1},-\epsilon_{i2}}$ takes care for the conditional state after the first substitution. $\langle s^f_{i|i}\rangle_{b_i}(\tau)$ is still given by (4.5). This equation yields in equilibrium[1]

$$\begin{aligned}\rho_{ii}(\tau) &= -\rho^{\rm pol}_{ii}(\tau)\\ &= \rho_{0\,ii}\Big(\cosh^2(\tilde\sigma_i) + \frac{\tanh(2\tilde\sigma_i)}{2\tilde\sigma_i}\underbrace{(-\omega_{ii})}_{>0}{\rm e}^{-\tau/\tau_{\rm eq}} + (\omega_{ii}^2/\alpha_j){\rm e}^{-2\tau/\tau_{\rm eq}} + \mathcal{O}(\omega_{ii}^3, \tau_{\rm eq}^3\mu^3)\Big),\end{aligned} \tag{D.6}$$

with both, even and odd orders of ω_{ij}. This result is obviously different to (4.8) and (4.10). For the single-site response, there is only one type of polarization available for compensation. This is not model specific, but also generalizes to a more general alphabet by a restricted state space of the site. A primary mutation changes possible beneficial/deleterious mutational targets. For non-adaptive strong selection $|Ns_i| > 1$, the response is significantly enhanced compared to the independent rate $\rho^0_{ii} \sim \rho_i^2$, because we expect after a (rare) deleterious substitution a quick self-compensation back to the beneficial state.

As a consequence, the diagonal breaks the simple low-rank form of the response matrices (4.8) and (4.10) by adding another rank, which cannot be absorbed in independent events $\rho^0_{ii} \sim \rho_i^2$. However, it impacts only ℓ of the ℓ^2 matrix element and has only a weak impact on retrieving the trait signal from the full matrix ρ_{ij}. It gives no significant singular mode in the SVD of $\hat\rho_{ij}$ or $\rho^{\rm pol}_{ij}$.

Equilibrium asymmetry. In the main text we omitted a factor $\alpha_j^{\rm eq} = \rho_j^{\rm eq}/\tilde\rho_j^{\rm eq} \sim 1$ in the response of the total mutation rates (4.8) causing a mild asymmetry even in equilibrium ($\rho^{\rm eq}_{ij}(\tau) \neq \rho^{\rm eq}_{ji}(\tau)$). The asymmetry factor

$$\alpha_j^{\rm eq} = \left(\coth^2\left(Ns_j^{\rm tot}\right) - \frac{\coth\left(Ns_j^{\rm tot}\right)}{Ns_j^{\rm tot}}\right)^{-1} \tag{D.7}$$

increases from 1 to 3 if selection comes close to neutrality $Ns_j^{\rm tot} \lesssim 1$, i.e. if the directional trait selection effect is cancelled by the single site selection. This particular neutral case also enters the quenched disorder statistics in the limit of weak adaptation of the adaptive model. Numerical studies show that it is well approximated by

$$\lim_{\gamma\to 0}\alpha_j^{\rm stat} \approx \alpha_j^{\rm eq}\big|_{s_j^{\rm tot}\left||s_j^f|-s_j\right|}, \tag{D.8}$$

[1] We do not present the non-equilibrium solution here, because already the equilibrium deviates strongly and we are not particularly interested in these single site rates.

see Figure D.3A. Only the distance from the neutral state $s_j^f = -s_j$ in the s_j^f-s_j plane is relevant. The full solution of the asymmetry is

$$\lim_{\gamma\to 0}\alpha_j^{\text{stat}} = \frac{\Delta\sigma_j \sinh(2\Sigma\sigma_j) + \Sigma\sigma_j \sinh(2\Delta\sigma_j)}{2\coth(\Delta\sigma_j)\coth(\Sigma\sigma_j)}\times \tag{D.9}$$
$$\left(\sinh^2(\Delta\sigma_j)\left(\Sigma\sigma_j\coth(\Sigma\sigma_j)-1\right)+\sinh^2(\Sigma\sigma_j)\left(\Delta\sigma_j\coth(\Delta\sigma_j)-1\right)\right)^{-1},$$

with $\Delta\sigma_j := N\left|s_j^f - s_j\right|$ and $\Sigma\sigma_j := N\left|s_j^f + s_j\right|$. It is slightly less asymmetric compared to (D.8) around $N|s_j^f| = Ns_j \approx 1$ as shown in Figure D.3B.

The mild breaking of detailed balance is no big concern, because strictly speaking the 'equilibrium dynamics' are in no equilibrium but a marginalized stationary state of the high-dimensional mutational space. The ensemble of all QTL compensates a substitution i before j may compensates. Therefore, the dynamics are not time-reversible. Nonetheless, the mild asymmetry is much weaker than the asymmetry from strong driver sites such that the asymmetry is still a good measure for external driving.

Polarized asymmetry. The full solution of the polarized asymmetry α_j, Equation (4.12), obtained from (4.10) reads

$$\alpha_j^{\text{pol}} = \frac{1+b_{j,1}\gamma_j/\mu}{1+b_{j,2}\gamma_j/\mu} \tag{D.10}$$
$$= 1 + \frac{\gamma_j}{\mu}(b_{j,1}-b_{j,2}) + \mathcal{O}(\gamma_j/\mu), \tag{D.11}$$

with

$$b_{j,1} = \frac{-2\sigma_j\sinh(2\sigma_j)\sigma_j^f\sinh\left(2\sigma_j^f\right) - {\sigma_j^f}^2\left(-2\cosh(2\sigma_j)\cosh\left(2\sigma_j^f\right)+\sinh^2(2\sigma_j)+2\right)+\sigma_j^2\sinh^2(2\sigma_j)}{2\left(\sigma_j^2-{\sigma_j^f}^2\right)\left(\sigma_j\sinh(2\sigma_j)\cosh\left(2\sigma_j^f\right)-\cosh(2\sigma_j)\sigma_j^f\sinh\left(2\sigma_j^f\right)\right)}, \tag{D.12}$$
$$b_{j,2} = \frac{2{\sigma_j^f}^2\left(\cosh(2\sigma_j)\cosh\left(2\sigma_j^f\right)-1\right)+\sigma_j\sinh(2\sigma_j)\left(-2\sigma_j^f\sinh\left(2\sigma_j^f\right)-\cosh\left(2\sigma_j^f\right)+\cosh(2\sigma_j)\right)}{2\left(\sigma_j^2-{\sigma_j^f}^2\right)\left(\sigma_j\sinh(2\sigma_j)\cosh\left(2\sigma_j^f\right)-\cosh(2\sigma_j)\sigma_j^f\sinh\left(2\sigma_j^f\right)\right)},$$

and $\sigma_j = 2Ns_j$ and $\sigma_j^f = 2Ns_j^f$. It is $\alpha_j^{\text{pol}} = 1$ in equilibrium and for weak single site selection (trailer regime), cp. (4.14). As Figure D.1B shows, the asymmetry increases the stronger the driving rate γ_j or the single site selection s_j. It gets less asymmetric, the stronger the average (time-independent) trait selection is. As discussed in Equation (4.14), it has two driver regimes. D_1) with moderate adaptation $\gamma_j \gtrsim \mu/b_{j,1}$, where $\alpha_j^{\text{pol}} \approx \gamma_j/(b_{j,2}\mu)$, and D_2^{pol}) with strong driving $\gamma_j \gg \mu/b_{j,k}$, $k=1,2$, where $\alpha_j^{\text{pol}} \approx \frac{b_{j,1}}{b_{j,2}}$.

Therefore, the asymmetry is a good measure for the strength of driving of a site and also related to the fitness flux generated by the site, cp. Section 4.4.

Response correlation under strong interference. Here, we consider the trait sites linked to the rest of the genome with strong interference in a fitness wave with fixation probabili-

ties (2.22) [69, 92]. These dynamics show pairwise rates

$$\begin{aligned}\rho_{ij}(\tau) &= \rho^0_{ij}(\tilde{\sigma})\left(1+\frac{1}{2}\omega_{ij}^2 \mathrm{e}^{-\tau/\tau_{\mathrm{eq}}}\right), \\ \rho^{\mathrm{pol}}_{ij}(\tau) &= \rho^0_{ij}(\tilde{\sigma})\omega_{ij}\mathrm{e}^{-\tau/\tau_{\mathrm{eq}}},\end{aligned} \qquad s_j^{tot} \lesssim \tilde{\sigma}, \tag{D.13}$$

where now $\omega_{ij} \sim \langle f''(\Gamma)\rangle/\tilde{\sigma}$. If the sites are under low efficacy of selection, they do not change the pattern of Equations (4.8) and (4.10). However, these rates show no asymmetry: mutations are by definition, $s \lesssim \tilde{\sigma}$, in the trailer regime. Strongly selected sites $s \gg \tilde{\sigma}$ still follow the fixation probability (2.21) and show the asymmetry of Equations (4.8) and (4.10). In conclusion, interference would not change the trait pattern in correlations but would weaken the asymmetry.

Finite allele frequency detection. So far, we focussed derived substitution dynamics for the response rates. However, the results can further be generalized to finite observed frequencies, x_D and x_T, of primary and secondary mutation to generalize it to the application to phylogenetic trees. We count a mutation if it reached frequency x_T clad by the first mutation with minimum frequency x_D. For these dynamics we generalize Equation (2.21) to finite frequency propagators [21]:

$$G(s|x) = \frac{1}{N}\frac{s}{1-e^{-Nxs}}. \tag{D.14}$$

These propagators change the rate of observations, but not the generic response process. Nonetheless, already in the null mode, i.e. without trait-correlations, these finite frequencies generate an asymmetry,

$$\rho^0_{ij}(\tau|x_D,x_T) = \rho^0_{ij}(x_D,x_T) = \rho_i(x_D)\rho_j(x_T) \neq \rho^0_{ji}(\tau|x_D,x_T). \tag{D.15}$$

For the response rate of a increasing mutation clade of site j in the background of i, Equation (4.8) generalizes to

$$\begin{aligned}\rho_{ij}(\tau|x_D,x_T) &= \rho_i(x_D)\rho_j(x_T) + \rho_i(x_D)\big(\rho_j^{\mathrm{eq}}(x_T)/\alpha_j^{\mathrm{eq}}(x_T)\big)\omega_{ij}^2\mathrm{e}^{-2\tau/\tau_{\mathrm{eq}}} + \mathcal{O}(\omega_{ij}^4,(\tau\mu)^3) \\ &=: \rho^0_{ij}(x_D,x_T)\left[1+\alpha_j(x_T)\omega_{ij}^2\mathrm{e}^{-2\tau/\tau_{\mathrm{eq}}} + \mathcal{O}(\omega_{ij}^4,(\tau\mu)^3)\right],\end{aligned} \tag{D.16}$$

The response with finite detection frequency can be mapped to the response under substitution dynamics with effective population size $N_T = x_T N$,

$$\rho_j^{\mathrm{eq}}(x_T) = x_T\rho_j^{\mathrm{eq}}\big|_{N\to N_T}, \tag{D.17}$$

$$\alpha_j^{\mathrm{eq}}(x_T) = \alpha_j^{\mathrm{eq}}\big|_{N\to N_T}. \tag{D.18}$$

where the r.h.s. variables are from equilibrium substitution dynamics, Equations (4.4) and (D.7).

If the null mode asymmetry is absorbed in the prefactor, the equilibrium response asymmetry $\alpha_j^{\mathrm{eq}}(x_T)$ is given by the weak asymmetry of (D.7) with effective population size Nx_T. Strong asymmetry is still a non-equilibrium property of the process. The asymmetry of the non-

equilibrium trait correlation of (D.16) is, similar to the substitution dynamics (4.11),

$$\alpha_j(x_T) = \alpha_j^{\mathrm{eq}}(x_T)\frac{\rho_j(x_T)}{\rho_j^{\mathrm{eq}}(x_T)} \sim \frac{\rho_j(x_T)}{\rho_j^{\mathrm{eq}}(x_T)}. \tag{D.19}$$

Reducing the threshold of trailer detection x_T on the one hand increases the number of mutations observed and hence improves the signal. On the other hand, a too low threshold counts too many neutral events and the trait signal gets weaker.

Finding such simple relations for polarized rates $\rho_{ij}^{\mathrm{pol}}(\tau)$ is still an open task. In principle they are algebraically calculable as function of the model parameters but yield unintuitive results; Nonetheless, they are still of factorizable rank 1 form due to factorizable $\rho_{ij}^0(x_D, x_T)$,

$$\rho_{ij}^{\mathrm{pol}}(\tau) = \rho_{ij}^0(x_D, x_T)\big[\underbrace{(\omega_{ij}/\alpha_j^{\mathrm{pol}}(x_T))}_{<0}\mathrm{e}^{-\tau/\tau_{\mathrm{eq}}} + \mathcal{O}(\omega_{ij}^3, (\tau\mu)^3)\big], \tag{D.20}$$

but show a stronger asymmetry due to the asymmetric rates in the null-mode prefactor $\rho_{ij}^0(x_D, x_T)$.

D.2 Singular value decomposition of trait sectors

Now we derive the singular value of a of a trait in the significance matrices z_{ij} and z_{ij}^{pol}. This approach applies for every selectively independent trait, each conferring a significant singular value. This singular mode can than be used to infer back the trait effects and the asymmetry of sites.

Significance of trait sectors. To optimize the signal strength of Equation 4.18, the parameter τ_0 has to be well chosen to discriminate in-causal long-term counts, i.e. noise. Performing the time integral leads to the optimization problem of $\tilde{\lambda} \sim \frac{\sqrt{\tau_{\mathrm{eq}}/\tau_0}}{k+\tau_{\mathrm{eq}}/\tau_0}$ with $k = 1, 2$ for polarized counts N_{ij}^{pol} and total counts N_{ij}, respectively, see Figure D.4. An optimal signal is achieved if $\tau_0 \sim \tau_{\mathrm{eq}}/k$. An overestimate of τ_0 yields to a more stable signal than the underestimation. In the following, we discuss particular results for $\tau_0 = \tau_{\mathrm{eq}}$. In the data analysis we use $\tau_0 \approx 3\tau_{\mathrm{eq}}$.

Given the expected count matrices, Equation (4.19), we can estimate the significance level of one trait through its singular value[2],

$$\langle z_{ij}\rangle \approx \frac{\mathcal{N}_{ij} - \mathcal{N}_{ij}^0}{\sqrt{\mathcal{N}_{ij}^0}} = \sqrt{\mathcal{N}_{ij}^0}\frac{\omega_{ij}^2}{3\alpha_j} = \tilde{\lambda}\tilde{d}_i\tilde{t}_j, \tag{D.21}$$

$$\langle z_{ij}^{\mathrm{pol}}\rangle \approx \frac{\mathcal{N}_{ij}^{\mathrm{pol}}}{\sqrt{\mathcal{N}_{ij}^0}} = \sqrt{\mathcal{N}_{ij}^0}\frac{\omega_{ij}}{2\alpha_j^{\mathrm{pol}}} = \tilde{\lambda}^{\mathrm{pol}}\tilde{d}_i^{\mathrm{pol}}\tilde{t}_j^{\mathrm{pol}}, \tag{D.22}$$

[2]For simplified notation without a trait index; it generalizes to g singular values for g traits, where these equation are applicable to each.

assuming weak correlation between fluctuations and signal. With normalized singular vectors

$$\tilde{d}_i = \frac{\sqrt{\rho_i} E_i^2}{\sqrt{\sum_k \rho_k E_k^4}}, \qquad \tilde{t}_i = \frac{\sqrt{\rho_i} E_i^2/\alpha_i}{\sqrt{\sum_k \rho_k (E_k^2/\alpha_k)^2}} \sim \frac{\sqrt{\rho_i} E_i^2}{\sqrt{\sum_k \rho_k E_k^4}}, \tag{D.23}$$

$$\tilde{d}_i^{\rm pol} = \frac{\sqrt{\rho_i} E_i}{\sqrt{\sum_k \rho_k E_k^2}}, \qquad \tilde{t}_i^{\rm pol} = \frac{\rho_i E_i/\alpha_i^{\rm pol}}{\sqrt{\sum_k \rho_k (E_k/\alpha_k^{\rm pol})^2}} \sim \frac{\rho_i E_i}{\sqrt{\sum_k \rho_k E_k^2}}, \tag{D.24}$$

we find the singular values

$$\tilde{\lambda} = \sqrt{\tau_0 T}\, \frac{c^2}{3(E_0^2)^2} \sqrt{\sum_k \rho_k E_k^4 \sum_{k'} \rho_{k'} (E_{k'}^2/\alpha_{k'})^2} \sim \sqrt{\Omega/\ell^2}\, \frac{c^2}{3} \frac{\sum_k E_k^4}{(E_0^2)^2} = \sqrt{\Omega/\ell^2}\, \frac{16c^2}{3\ell} \kappa_4, \tag{D.25}$$

$$\tilde{\lambda}^{\rm pol} = \sqrt{\tau_0 T}\, \frac{c}{2E_0^2} \sqrt{\sum_k \rho_k E_k^2 \sum_{k'} \rho_{k'} (E_{k'}/\alpha_{k'}^{\rm pol})^2} \sim \sqrt{\Omega/\ell^2}\, 2c. \tag{D.26}$$

In Equations (D.21) – (D.26), the trailer, $\tilde{t}_i$ and $\tilde{t}_i^{\rm pol}$, asymptotics become exact if sites are not driven strongly, such that the asymmetry factors in Equation (4.13) or (4.14) are $\alpha_j \approx \alpha_j^{\rm pol} \approx 1$. The variable κ_4 measures the kurtosis of the E_i-distribution across sites; it is $\kappa_4 = 1$ for a normal distribution. $\Omega = \sum_{ij} \mathcal{N}_{ij} \approx \sum_{ij} \mathcal{N}_{ij}^0 = \sum_{ij} \rho_i \rho_j \tau_0 T$ is the total number of observations determined by the measuring time T.

On the other hand, the expected noise level of pairwise observations is determined by the number of their pairwise counts, $\mathrm{var}\,(N_{ij}) = \mathcal{N}_{ij}/2$ and $\mathrm{var}\left(N_{ij}^{\rm pol}\right) = \mathcal{N}_{ij}/2$, where the given prefactors are for Gaussian distributed counts, which is approached for large N_{ij} by the law of large numbers. Therefore, the z-values z_{ij} and $z_{ij}^{\rm pol}$ are standard scores having variance 1/2. Random matrix theory predicts for independent distributed N_{ij} for each site-pair a maximum eigenvalue sharply distributed around $\tilde{\lambda}_{\rm noise}^{\rm max} = \sqrt{\ell}$ [138], which we see in the randomly scrambled trees. e.g. Figure 4.3B2,C2. Therefore we can detect traits with $\tilde{\lambda} \gtrsim \sqrt{\ell}$ from mutational counts alone and $\tilde{\lambda}^{\rm pol} \gtrsim \sqrt{\ell}$ if further the direction of mutations is known. It translates into a minimal size of the dataset of $\Omega \gtrsim \ell(\mu\ell\tau_{\rm eq})^4$ for the former and $\Omega \gtrsim \ell(\mu\ell\tau_{\rm eq})^2$ for the latter. This approach gives hence the number of significant traits, for which we next infer the site contributions.

Inference of trait effects. To relate the singular mode to the trait effects and asymmetries, we transform

$$\left(\frac{\hat{N}_{ij}}{N_{ij}^0}\right)_{\rm red} := \frac{\tilde{\lambda}\tilde{d}_i\tilde{t}_j}{\sqrt{N_{ij}^0}} = \frac{\omega_{ij}^2}{3\alpha_j} \equiv \lambda d_i t_j, \tag{D.27}$$

$$\left(\frac{N_{ij}^{\rm pol}}{N_{ij}^0}\right)_{\rm red} := \frac{\tilde{\lambda}^{\rm pol}\tilde{d}_i^{\rm pol}\tilde{t}_j^{\rm pol}}{\sqrt{N_{ij}^0}} = \frac{\omega_{ij}^2}{2\alpha_j^{\rm pol}} \equiv \lambda^{\rm pol} d_i^{\rm pol} t_j^{\rm pol}. \tag{D.28}$$

These are independent of the site's independent substitution rates ρ_i,

$$d_i = \frac{E_i^2}{\sqrt{\sum_k E_k^4}}, \qquad t_i = \frac{E_i^2/\alpha_i}{\sqrt{\sum_k (E_k^2/\alpha_k)^2}} \sim \frac{E_i^2}{\sqrt{\sum_k E_k^4}}, \tag{D.29}$$

$$d_i^{\mathrm{pol}} = \frac{E_i}{E_0}, \qquad t_i^{\mathrm{pol}} = \frac{E_i/\alpha_i^{\mathrm{pol}}}{\sqrt{\sum_k (E_k/\alpha_k^{\mathrm{pol}})^2}} \sim \frac{E_i}{E_0}. \tag{D.30}$$

The driver components give directly the trait effects, the trailer components further allow to infer the asymmetry and hence the strength of non-equilibrium of a site. The asymptotics are again exact close to equilibrium. The eigenvalues are reflecting the stabilizing strength $\lambda \sim \kappa_4 c^2$ and $\lambda^{\mathrm{pol}} \sim c$.

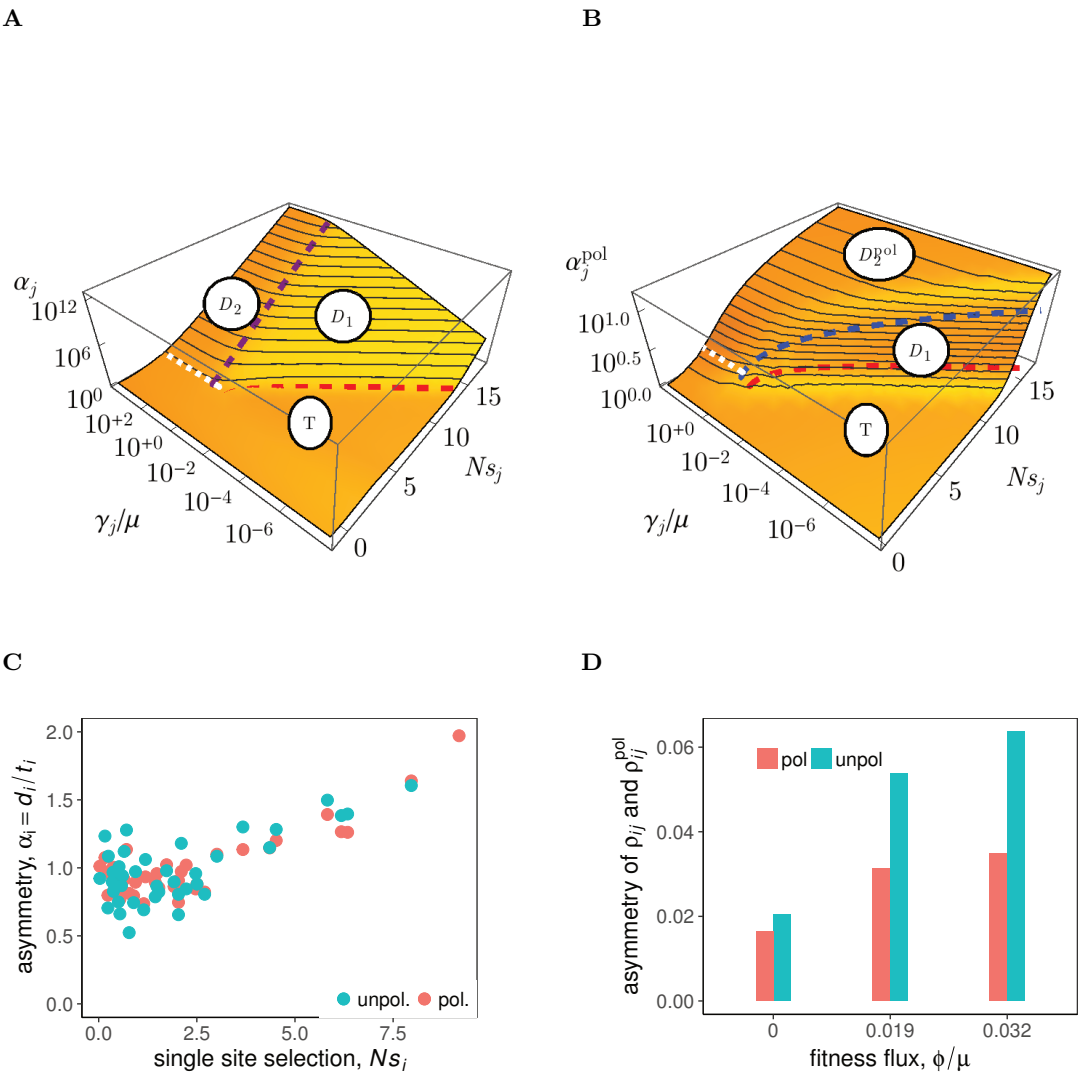

Figure D.1. Adaptation: breakdown of detailed balance generates asymmetric correlation response. **A** Asymmetry of site response, α_j, given by (4.11) with asymptotic behavior (4.13), and **B** its polarized counterpart, $\alpha_j^{\rm pol}$, given by (D.10) with asymptotic behavior (4.14). Both are shown as functions of their driving γ_j and selection strength s_j. They show the breakdown of detailed balance in non-equilibrium ($\gamma_j > 0$). $\alpha_j^{\rm pol} \approx \alpha_j \approx 1$ is symmetric for weak single site selection or weak driving rates, which we call trailer regime (T). It is separated from two distinguished regimes of asymmetry scaling, D_1 as a moderate driver regime and D_2 as an extreme driver regime, by red ($\gamma_j \sim \rho_j^{\rm eq}$) and white lines ($s_j \sim s_j^f$), respectively. The scaling in the two driver regimes changes, when **A**) going towards micro-evolutionary single-site seascape $\gamma_j \sim \gamma_j^{\rm m} \equiv \mu N s_j$ (purple line), or in **B**) $\gamma_j \sim \rho_j^{\rm eq} N s_j$ (blue line). **C** Simulations show indeed an increase in site's asymmetries α_j (blue) and $\alpha_j^{\rm pol}$ (red) with s_j. For trait sites having larger s_j, trait selection and drift are overcome such that a site is adaptable to fluctuating selection. However we have not yet reached the scaling regimes discussed in panels A,B. All $\ell = 40$ trait sites have same $\gamma_j = 0.8\mu$ and $E_j = 1$ but heterogeneous s_j. The simulations run with additional 80 non-trait sites with similar distributed single site selection, which show no visible asymmetry effect (not shown). All other parameters are like in Figure 4.3. **D** The global asymmetry of the response matrices is measured as the fraction of the L2 norm of the asymmetric part to the matrix compared to the L2 norm of the full matrix. It is plotted against the inferred fitness flux from the trait's driver site, $\phi_{fl} = \sum_{j\in \rm driver} \phi_j = \rho_i s_i$, which are defined by $Ns_j > 2.5, E_j > 0.5$. The simulations are similar to panel C, but varying $\gamma_j = 0, 0.8\mu, 8\mu$ (left, middle and right data points). The asymmetry generically increases with the fitness flux, it saturates since drivers are not expected to show compensatory response due to strong single site selection on simulation timescales. Sites with less than 5 mutations are excluded from the analysis, which excludes the driver sites in equilibrium showing no variation.

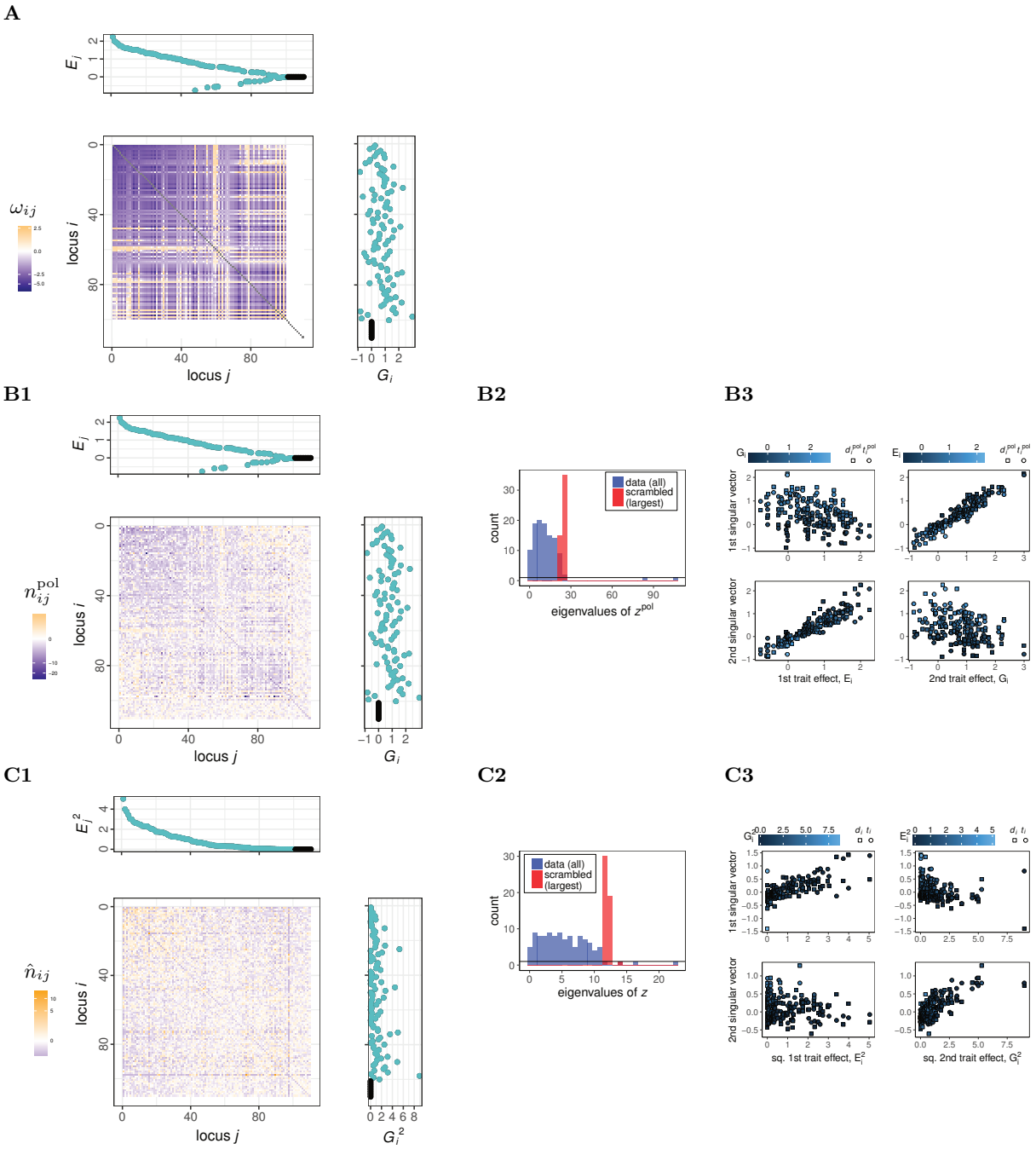

Figure D.2. Epistasis and correlations of 2 highly pleiotropic traits The Figure is similar to Figure 4.5 for non-pleiotropic traits. **A** Here, two pleiotropic quantitative traits have trait effects E_i (top marginal plot; defining ordering of sites) and G_i (right marginal plot). The trait effects are independently drawn. Blue sites contribute to the traits, black sites are neutral with respect to the trait. The epistatic matrix ω_{ij} (color) follows Equation (4.16). **A**,**B1**,**C1** The strong pleiotropy generates broad correlations without clear sectors, however still of small dimensionality. **B2**–**B3** In the linear response, the traits are each related to a significant singular mode. This number allows to infer the number of traits in B2 and the trait effects in B3. **C2** In the second order, another significant rank arises through strong pleiotropic interactions. **C3** The first two singular modes correlate with the trait effects. However, to carefully reconstruct trait effects, an appropriate rotation in the 3d significant subspace or a non-linear dimensional reduction is needed. All singular vectors in B3 and C3 are rotated with a varimax rotation amplifying the signal.

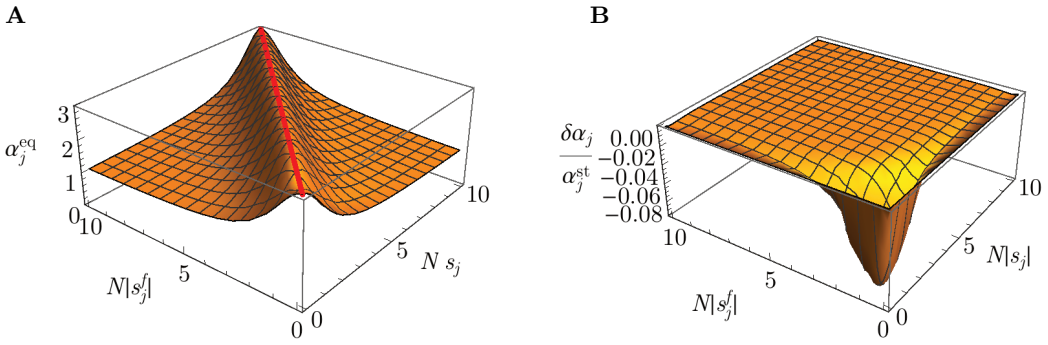

Figure D.3. Equilibrium asymmetry α_j^{eq} of response enhancement $\hat{\rho}_{ij}(\tau)$. **A** shows the full solution $\lim_{\gamma\to 0}\alpha_{\mathrm{stat},j}$, the red line shows the 'neutral hill' $|s_j^f| = s_j$. The symmetry breaking is, apart from very small deviations around $|Ns_j^f| = Ns_j \approx 1$, given by a shift of the solution (D.7) for $s_j = 0$: $|s_j|^f \to |s_j^f| - s_j$ and $|s_j| \to 0$. **B** shows the deviation from the shift-approximation and the full solution, i.e. $\delta\alpha_j = \lim_{\gamma\to 0}\alpha_j^{st} - \alpha_j^{eq}\big|_{s_j^{tot}=||s_j^f|-s_j|}$ from Equations (D.7) and (D.9).

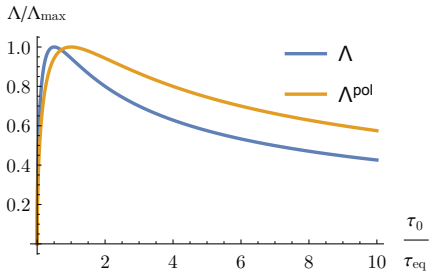

Figure D.4. Optimizing trait signal with τ_0 for unpolarized and polarized counts. The optimal discrimination time is $\tau_0 \sim \tau_{eq}$; however an overestimation is more stable than an underestimation.

Appendix E

Analytical theory and extensions of phenotypic interference

E.1 Trait diversity and cross-over scaling of the fitness wave

Equilibrium of trait diversity. We consider a quantitative trait G evolving by mutations, coalescence caused by genetic drift and genetic draft, and stabilizing selection in a fitness landscape $f(G)$. Mutations and coalescence alone generate an equilibrium of the trait diversity Δ_G,

$$\langle \Delta_G \rangle = \frac{u\epsilon_G^2}{2\tilde{\sigma}}, \tag{E.1}$$

as derived in the main text and References [53,54]. This expression is valid if stabilizing selection on the trait diversity can be neglected, i.e., if [53]

$$\frac{\mathcal{L}_\Delta}{\tilde{\sigma}} \equiv \frac{\langle \Delta_G \rangle |f''(\Gamma)|}{\tilde{\sigma}} \lesssim 1. \tag{E.2}$$

Here we show that this condition is self-consistently fulfilled throughout the phenotypic interference regime. Evaluating the expected fitness curvature in the high-fitness part of the minimal fitness landscape, Equation (2.25), where $f''(\Gamma) = -f'(\Gamma)/k_BT$, and in the mutation-coalescence equilibrium given by Equation (E.1), we obtain $f'' = -2\tilde{\sigma}/(\epsilon_g k_B T)$. By Equation (5.3), the condition (E.2) then reduces to

$$\frac{\langle \Delta_G \rangle}{\epsilon_G^2} = \frac{\mathcal{C}}{4g} \lesssim 1, \tag{E.3}$$

which is identical to the condition for phenotypic interference given in the main text. This relation expresses an important scaling property of the phenotypic interference regime: individual traits evolve in the low-mutation regime and are monomorphic at most times. In contrast, the the global trait diversity defines a polymorphic fitness wave,

$$\frac{4g\langle \Delta_G \rangle}{\epsilon_G^2} = \frac{\sigma^2}{\tilde{\sigma}^2} = \mathcal{C} \gtrsim g_0. \tag{E.4}$$

Cross-over scaling of the fitness wave. A travelling fitness wave maintained by mutations at genomic sites with a fixed selection coefficient s has two distinct scaling regimes [71, 91],

$$\sigma^2 = \begin{cases} sug, & (g \lesssim g_c), \\ \mathcal{C}\tilde{\sigma}^2 = (\frac{\mathcal{C}}{4})^{1/3}(s^2 ug)^{2/3}, & (g \gtrsim g_c), \end{cases} \tag{E.5}$$

which correspond to independently evolving sites and to an asymptotic fitness wave with strong interference selection, respectively. At the crossover point $g_c = \mathcal{C}s/(4u)$, the relation

$$\tilde{\sigma}(g_c) = \frac{2ug_c}{\mathcal{C}} = \frac{1}{2}s \tag{E.6}$$

is valid. Comparing this relation with the *generic* scaling under phenotypic interference, $\tilde{\sigma} = 2ug/\mathcal{C} = s/2$ as given by Equations (5.2) and (5.3), we conclude that the phenotypic fitness wave is locked in the crossover region of marginal interference. As discussed in the main text, this feature reflects the feedback between global and local selection in a phenotypic fitness landscape, which tunes selection coefficents to the g-dependent value $s = 4ug/\mathcal{C}$. Consistently, the phenotypic fitness wave has a fitness variance $\sigma^2 \sim g^2$, compared to the scaling $\sigma^2 \sim g^{4/3}$ of the asymptotic regime at fixed selection coefficients (up to log corrections).

E.2 Stochastic theory of phenotypic interference

In the main text, we derive the scaling relations of phenotypic interference, Equations (5.1) – (5.5), using the evolution equation for quantitative traits, Equation (5.10), in its deterministic limit ($\chi = 0$). Here we show that the full evolution equation generates the same scaling. We convert Equation (5.10) into an equivalent diffusion equation [53, 54] for the probability density $Q(\Gamma, t)$,

$$\frac{\partial}{\partial t} Q(\Gamma, t) = \left[\tilde{\sigma} \langle \Delta_G \rangle \frac{\partial^2}{\partial \Gamma^2} + \frac{\partial}{\partial \Gamma} \left(\kappa \epsilon_G u - \langle \Delta_G \rangle f'(\Gamma) \right) \right] Q(\Gamma, t), \tag{E.7}$$

with the average trait diversity $\langle \Delta_G \rangle$ given by Equation (E.1). The equilibrium probability distribution $Q_{\mathrm{eq}}(\Gamma)$ describes the stationary fluctuations of the population mean trait $\Gamma(t)$ of a stable gene around its long-term average $\langle \Gamma \rangle = \int \Gamma \, Q_{\mathrm{eq}}(\Gamma) \, d\Gamma$; these fluctuations are generated by genetic drift and (predominantly) genetic draft. In the biophysical fitness landscape, Equation (2.25), the equilibrium distribution can be evaluated analytically,

$$Q_{\mathrm{eq}}(\Gamma) = \frac{\left(\frac{f_0}{\tilde{\sigma}}\right)^{2\kappa \frac{k_B T}{\epsilon_G}} \exp\left(-\frac{2\kappa \Gamma}{\epsilon_G} - \frac{f_0}{\tilde{\sigma}} \mathrm{e}^{-\Gamma/k_B T} \right)}{k_B T \, \mathrm{Gamma}\left(2\kappa \frac{k_B T}{\epsilon_G} \right)}, \tag{E.8}$$

where Gamma and PolyGamma are standard transcendental functions. This function is plotted in Figure E.1A. The resulting average,

$$\frac{\langle \Gamma \rangle}{k_B T} = -\log\left(\frac{\tilde{\sigma}}{f_0}\right) - \mathrm{PolyGamma}\left(2\kappa \frac{k_B T}{\epsilon_G} \right), \tag{E.9}$$

shows that genes are slightly more stable than estimated from the deterministic average derived in the main text, $\Gamma/k_BT = -\log(2\kappa\tilde{\sigma}k_BT/f_0\epsilon_G)$. Through the nonlinearity of the fitness landscape, the fluctuations of the mean trait Γ induce fluctuations of the conditional average fitness variance, $\langle\Delta_f\rangle(\Gamma) = \langle\Delta_G\rangle f'^2(\Gamma)$. We obtain the equilibrium distribution

$$Q_{\rm eq}(\Delta_f) = \mathrm{Gamma}_{\rm gen}\left(\Delta_f;\ 2\kappa\frac{k_BT}{\epsilon_G}, \frac{1}{2}u\tilde{\sigma}\frac{\epsilon_G^2}{(k_BT)^2}, \frac{1}{2}, 0\right), \tag{E.10}$$

with $\mathrm{Gamma}_{\rm gen}$ denoting the generalized gamma distribution (Figure E.1B). The average fitness variance

$$\langle\Delta_f\rangle = 2\tilde{\sigma}u\kappa^2\left(1 + \frac{\epsilon_G}{2\kappa k_BT}\right) \tag{E.11}$$

differs from its deterministic counterpart, Equation (5.1) by a prefactor of order 1. Similarly, the Γ fluctuations induce fluctuations of the interference load of individual genes,

$$Q_{\rm eq}(\mathcal{L}_{\rm gene}) = \mathrm{Gamma}_{\rm dist}\left(\mathcal{L}_{\rm gene};\ 2\kappa\frac{k_BT}{\epsilon_G}, \tilde{\sigma}\right) \tag{E.12}$$

(Figure E.1C). The resulting dependence

$$\langle\mathcal{L}_{\rm gene}\rangle = 2\kappa\frac{k_BT}{\epsilon_G}\tilde{\sigma} \tag{E.13}$$

is identical to the deterministic case; the fluctuation effect on $\langle\Gamma\rangle$, Equation (E.9), is offset by the fluctuation load in a downward-curved fitness landscape. Also expected derivatives of the fitness functions $\langle f^{(n)}(\Gamma)\rangle = -\frac{1}{(k_BT)^n}\langle\mathcal{L}_{\rm gene}\rangle$ are not influenced by fluctuations.

E.3 Model extensions

In this section, we discuss alternative evolutionary models of quantitative traits under genetic linkage. The mode of phenotypic interference, which is characterized by a superlinear scaling of the genetic load with genome complexity, occurs in all cases, suggesting it is a generic property of this class of models. Specifically, we discuss housekeeping dynamics in extended models of protein evolution and we extend our analysis to adaptive processes

Stability-affinity model. Here we discuss the simplest stationary states of housekeeping evolution in the co-evolutionary model for biophysical traits discussed in the Introduction 2.3 for biophysical equilibrium and non-equilibrium. We use the dynamical model presented in Appendix B, with the parameter notation simplifying discussion of Chapter 5 , in the deterministic limit of the co-evolution equation of Appendix B ($\chi_G = \chi_E = 0$). The trait diversities Δ_{GG} and Δ_{EE} are given as in Equation (E.1), and we assume that pleiotropic sites have uncorrelated effects on both traits, i.e. $\Delta_{GE} = 0$; this has recently been observed in [103]. As in the main text, we set $\kappa_G = \kappa_E = 1$, which says that most random mutations reduce stability and affinity.

In *thermodynamic equilibrium*, Equation (2.27) with (2.26) or Figure 2.2C, the high-fitness part of the fitness landscape takes the asymptotic form $f(G,E) \simeq f_0[1-\mathrm{e}^{-E/k_BT}(1+\mathrm{e}^{-G/k_BT}+$

$\mathrm{e}^{-E/k_BT})] + O((e^{-E/k_BT}, e^{-G/k_BT})^3)$. The mutation-selection equilibrium leads to mean trait values

$$\begin{pmatrix}\Gamma_G\\ \Gamma_E\end{pmatrix} \approx \begin{pmatrix} k_BT \log\left(\frac{\epsilon_G}{\epsilon_E} - 1\right)\\ -k_BT \log\left(2\frac{\tilde{\sigma}}{f_0}\left(\frac{k_BT}{\epsilon_E} - \frac{k_BT}{\epsilon_G}\right)\right)\end{pmatrix}, \tag{E.14}$$

where only the E-component depends on the coalescence rate $\tilde{\sigma}$. Comparison with the minimal model, Equation (1), shows that in the stable part of the fitness landscape, the equilibrium stability-affinity model becomes an essentially one-dimensional problem for the affinity trait E [57]. The total fitness variance per gene, $\langle\Delta_f\rangle = 2(u_G + u_E)\tilde{\sigma}$, is of the universal form [1] with an effective mutation rate

$$u = u_G + u_E. \tag{E.15}$$

We conclude that housekeeping evolution in this model follows the same scaling as in the minimal model, Equations (5.1) – (5.8), with the parameter u given by Equation (E.15). However, the equilibrium model lacks evolutionary stability, because lack of folding stability ($G > 0$) can be compensated by a stronger binding affinity.

With *active degradation*, Equation (2.30) with (2.29) or Figure 2.2D, the high-fitness part of the fitness landscape takes the asymptotic form $f(G, E) \simeq f_0[1-(1+\nu_E)\mathrm{e}^{-E/k_BT}-\nu_G\mathrm{e}^{-G/k_BT}]+ \mathcal{O}((e^{-E/k_BT}, e^{-G/k_BT})^2)$. Hence, for stable genes ($f_0 \gg \tilde{\sigma}$), the evolutionary dynamics of the traits G and E becomes approximately independent. The traits of each gene are at a mutation-selection equilibrium of the universal form (5.1), generating a combined fitness variance $\langle\Delta_f\rangle = 2(u_G + u_E)\tilde{\sigma}$. Therefore, housekeeping evolution in this model also follows the same scaling as in the minimal model, Equations (5.1) – (5.8), with a total mutation rate per gene given by Equation (E.15) and an effective value of g that is twice the number of genes,

$$g_{\text{eff}} = 2g. \tag{E.16}$$

In particular, the system-wide interference load is about twice the value of the minimal model, $\mathcal{L}_{\text{int}} \approx 8ug^2/\mathcal{C}$, as used in the main text. This estimate disregards the additional contribution from the enhanced total mutation rate, Equation (E.15), which takes into account that $u_E \ll u_G$ for many binding domains.

The form invariance of housekeeping evolution in these models shows the robustness of the phenotypic interference mode. It also suggests that in more general contexts, we can define genomic complexity as the number of quantitative traits that evolve (approximately) independently; see the Discussion of Chapter 5.

Single-peak fitness model. A minimal model of stabilizing selection is a quadratic landscape (2.24), $f(E) = -c_0(E - E^*)^2$, Figure 2.2A. This model penalizes deviations from an optimal trait value E^*. In contrast to the biophysical landscape, there is no gene loss in a quadratic landscape, because there are no constraints on its slope. As long as mutations generate trait equilibria predominantly on one flank of the landscape, the basic scaling of phenotypic interference, Equations (5.1) – (5.4), is universal and, hence, the same as in the minimal model. The genetic load for a single gene, $\mathcal{L}_{\text{gene}} = -f(\Gamma) = u^2\epsilon_E^2/(4\Delta_E^2 c_0)$, has been derived in [53].

With Δ_E given by Equation (E.1), we find a system-wide interference load

$$\mathcal{L}_{\text{int}} = g\mathcal{L}_{\text{gene}} = \frac{4u^2g^3}{\mathcal{C}^2\epsilon_E^2 c_0}. \tag{E.17}$$

Hence, the single-peak model has an even stronger load nonlinearity than the biophysical fitness landscapes.

Phenotypic interference in adaptive evolution. Here we show that the phenotypic interference scaling extends to simple models of adaptive evolution. In the minimal biophysical model, we assume that protein stabilities are still at an evolutionary equilibrium of the universal form (5.1), generating a combined fitness variance $g\langle\Delta_f\rangle = 2gu\tilde{\sigma}$. However, the global fitness variance acquires an additional contribution from adaptive evolution of other system functions,

$$\sigma^2 = \mathcal{C}\tilde{\sigma}^2 = 2\tilde{\sigma}ug + \phi, \tag{E.18}$$

where ϕ is the *fitness flux* or rate of adaptive fitness gain [60]. Mathematically, this term quantifies the deviations of the adaptive evolutionary process from equilibrium (defined by detailed balance). Closure of the modified dynamics leads to an increased coalescence rate $\tilde{\sigma}$,

$$\tilde{\sigma} = \frac{2ug}{\mathcal{C}} + \frac{\phi}{2ug} + \mathcal{O}\left(\frac{\phi^2}{(ug)^3}\right). \tag{E.19}$$

However, the adaptive term remains subleading to the housekeeping term for large g; this is true even if we assume that ϕ is proportional to g. Hence, the total interference load, $\mathcal{L}_{\text{int}} = g\tilde{\sigma} = 2ug^2/\mathcal{C} + \phi/u + \ldots$, retains the leading nonlinearity generated by housekeeping evolution, as given by Equation (5.5). Only for very high fitness flux ($\phi \gg u^2g^2/\mathcal{C}$), coalescence becomes dominated by adaptation, leading to a substantial decrease in the efficacy of selection.

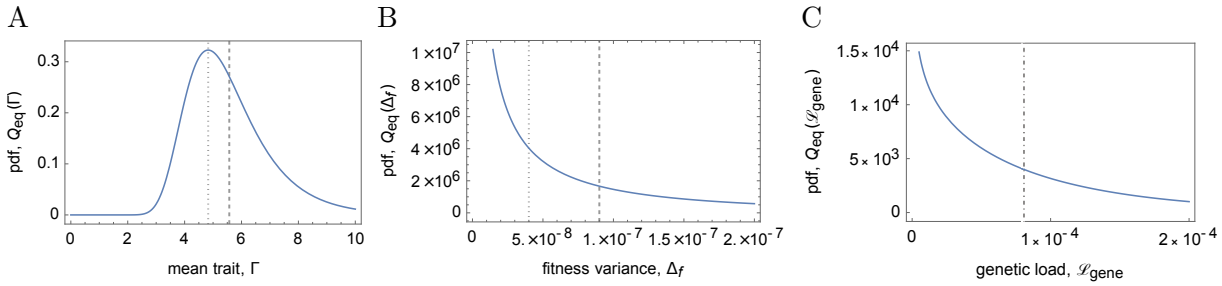

Figure E.1. Equilibrium distributions under stochastic evolution. The figure shows the probability density functions **A** of the mean population trait, $Q_{\rm eq}(\Gamma)$, **B** of the conditional expected fitness variance, $Q_{\rm eq}(\Delta_f)$, and **C** of the genetic load per gene, $Q_{\rm eq}(\mathcal{L}_{\rm gene})$; see Equations (E.8) – (E.12). These distributions measure deviations from long-term averages (dashed lines), which are generated by genetic drift and draft. The corresponding deterministic solutions are marked by dotted lines; both lines coincide in (C). All pdfs are shown for $\tilde{\sigma} = f_0/100 = 10^{-4}$; other parameters as in Figure 2. See Appendix E.2.

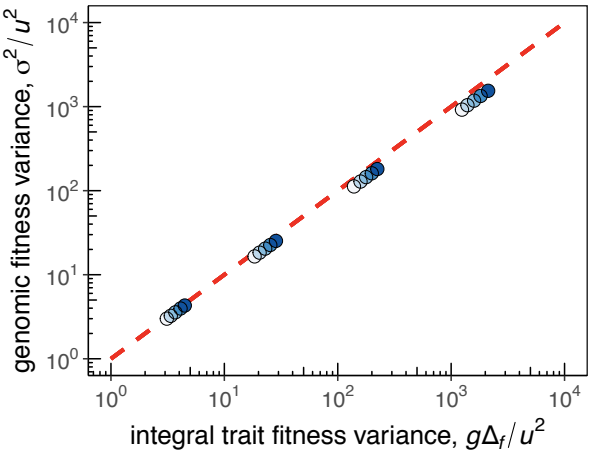

Figure E.2. Additivity of the genomic fitness variance. For housekeeping evolution in the minimal biophysical model, we plot the total fitness variance, σ^2, against the additive part $\Delta_{f,1}+\cdots+\Delta_{f,g}$. The additivity is used in the closure of the evolutionary dynamics, Equations (2) – (4).

	Saccharomyces cerevisiae	*Drosophila melanogaster*	*Arabidopsis thaliana*
μ	$3{\cdot}10^{-8}$ [161]	$3{\cdot}10^{-9}$ [162]	$7{\cdot}10^{-9}$ [163]
ℓ	1401 [164]	1500 [164]	2232 [165]
g	6563 [165]	14332 [164]	26990 [166]
R	$3{\cdot}10^{-2}$ [167]	$2{\cdot}10^{-3} - 1{\cdot}10^{-0}$ [153, 168]	$2{\cdot}10^{-0}$ [169]
R^*	$6{\cdot}10^{-5}$	$1{\cdot}10^{-3}$	$9{\cdot}10^{-3}$

Table E.1. Genome data and estimates of threshold recombination rates. Point mutation rate μ, average gene length ℓ (in basepairs), gene number g and recombination rate R per genome (map length) are shown for three recombining species. The parameter range for *D. melanogaster* describes local recombination rates in different parts of the chromosomes (in the same units) [153]. An upper bond of the threshold recombination rate R^* marking the transition to sexual evolution is obtained from Equation (5.8) (with $ug = \mu\ell g$ and $\mathcal{C} \approx \mathcal{C}_0 \approx 100$).

Erklärung

Ich versichere, dass ich die von mir vorgelegte Dissertation selbständig angefertigt, die benutzten Quellen und Hilfsmittel vollständig angegeben und die Stellen der Arbeit – einschließlich Tabellen, Karten und Abbildungen –, die anderen Werken im Wortlaut oder dem Sinn nach entnommen sind, in jedem Einzelfall als Entlehnung kenntlich gemacht habe; dass diese Dissertation noch keiner anderen Fakultät oder Universität zur Prüfung vorgelegen hat; dass sie – abgesehen von unten angegebenen Teilpublikationen – noch nicht veröffentlicht worden ist sowie, dass ich eine solche Veröffentlichung vor Abschluss des Promotionsverfahrens nicht vornehmen werde. Die Bestimmungen der Promotionsordnung sind mir bekannt. Die von mir vorgelegte Dissertation ist von Prof. Dr. Michael Lässig betreut worden.

Nachfolgend genannte Teilpublikationen liegen vor:

- Held, T., Nourmohammad, A., and Lässig, M. (2014). Adaptive evolution of molecular phenotypes. J Stat Mech: Theory Exp, 2014(9):P09029.
- Nourmohammad*, A., Held*, T., and Lässig, M. (2013). Universality and predictability in molecular quantitative genetics. Curr Opin Genet Dev, 23(6):684 693. *Equal contribution.

Promotionsbeginn: 01.04.2013

Promotionsende: 19.07.2018.

Ich versichere, dass ich alle Angaben wahrheitsgemäß nach bestem Wissen und Gewissen gemacht habe und verpflichte mich, jedmögliche, die obigen Angaben betreffenden Veränderungen, dem Dekanat unverzüglich mitzuteilen.

.....

Datum Unterschrift